



Brown, Stephen Alistair (2019) *Observations and modelling of the hydrogen Lyman lines in solar flares*. PhD thesis.

<https://theses.gla.ac.uk/40974/>

Copyright and moral rights for this work are retained by the author

A copy can be downloaded for personal non-commercial research or study, without prior permission or charge

This work cannot be reproduced or quoted extensively from without first obtaining permission in writing from the author

The content must not be changed in any way or sold commercially in any format or medium without the formal permission of the author

When referring to this work, full bibliographic details including the author, title, awarding institution and date of the thesis must be given

Enlighten: Theses

<https://theses.gla.ac.uk/>  
[research-enlighten@glasgow.ac.uk](mailto:research-enlighten@glasgow.ac.uk)

# Observations and Modelling of the Hydrogen Lyman Lines in Solar Flares

**Stephen Alistair Brown**

Astronomy and Astrophysics Group  
School of Physics and Astronomy  
Kelvin Building  
University of Glasgow  
Glasgow, G12 8QQ  
Scotland, U.K.



University  
of Glasgow

Presented for the degree of  
Doctor of Philosophy  
The University of Glasgow  
January 2019

---

This thesis is my own composition except where indicated in the text.  
No part of this thesis has been submitted elsewhere for any other degree  
or qualification.

**Copyright © January 2019 by Stephen Brown**

29 January 2019

---

*“The trick is to keep moving forward; to let go of the fear and the regret that slow us down, and keep us from enjoying a journey that will be over too soon. Yes, there will be unexpected bends in the road; shocking surprises we didn’t see coming - but that’s really the point, don’t you think?”*

**- Mary Alice Young**

**For Mum**

# Acknowledgements

If these past 4 (ish) years have taught me nothing else, it's that time always seems to speed up the older you get. It hasn't seemed like a long time, but perhaps that's down to the people who have made this ride an enjoyable one.

First and foremost, a heartfelt thanks goes to my supervisor, Lyndsay Fletcher. None of this would have been possible without her insight, knowledge, support and above-all, her approachability. From in-depth discussions about flare physics, to gripes with IDL, to my tendency to capitalise every second word I write, I could not have asked for a more helpful and encouraging supervisor.

Along this vein, props also need to be given to my secondary supervisor, Nic Labrosse. Always ready with some pearls of wisdom about radiative transfer, helpful comments on our latest manuscript, or just a good chat. It's been a pleasure working with you.

It takes an office to raise a postgraduate. It's hard to put into words the magic of Room 604 - it has to be lived. Every single person in that office has helped make every day hilarious, enjoyable, and on the difficult days, bearable. Shout outs to Room 614 and 616 also.

Thank you, Ben, for being the funniest (and kindest) person I know. Paul, for always being reliable company in the pub. Tony, for your snappy suits and macabre humour. Pete, for being a great office neighbour. Al, for literally knowing everything about everything. Duncan, for always reminding me of the importance of dressing well. Graham, for putting up with my incessant questioning whenever I've not understood something. Thanks also to Natasha, for always being on-hand with humor and advice.

To those still working hard; thank you for being the best company I could ask for, especially over this last stretch. I also thank the view from my office window, from which I've sat watching the snow fall, the leaves blow and the Sun shine when I should have been working. By extension, the entire community on level 6 deserves a mention. It will be hard to find another group of people as friendly, insightful and down-to-earth. Special thanks to Rachael for taking care of all things conference and admin-wise. Gail, thank you for your good-natured enthusiasm and for all the pub gossip.

Further afield, thank you to Adam Kowalski, for taking me under his wing at Goddard and helping me get to grips with RADYN and RH. Thank you to Jaime de la cruz Rodríguez, for easing my RH woes and providing helpful manuscript comments. Thank you to my Ma'ams in Greenbelt. Burlington crowd, you know who you are.

Thank you to Mum and Dad for the support. Neil, for making the last few months of writing practically possible. Donna et al for being there for me every step of the way. Last of all, thank you to Glasgow; a place I've called home for almost 9 years. I wouldn't have wanted it any other way.

# Abstract

The extent of dynamical processes in the lower atmosphere of the Sun during solar flares is not fully understood. While it is widely accepted that the majority of the associated flare energy is deposited in the Sun's chromosphere, it is less clear how this energy is transported and how it influences the configuration of material flows. Current models of chromospheric evaporation and condensation assume an upwards expulsion of high-temperature plasma, with an accompanying downwards flow at cooler temperatures. In this thesis, the validity of these assumptions are tested using a combination of observations and modelling, with particular focus given to the Lyman lines of hydrogen.

In Chapter 1, an outline of the Sun and its atmosphere is presented. The physical and observational properties of solar flares are described, considering several regions of the electromagnetic spectrum. In addition, an overview of observations relating to the dynamics of the chromosphere is provided.

In Chapter 2, the tools, data and numerical codes used in this work are described. The Solar Dynamics Observatory (SDO) and its Extreme Ultraviolet Variability Experiment (EVE) are introduced, which encompasses the observational domain of this work. The basics of radiative transfer are also described, before an outline of the numerical codes, RADYN and RH, are given.

Observations of Doppler shifted emission in the hydrogen Lyman lines throughout the course of 6 solar flares, facilitated by the EVE instrument, are presented in Chapter 3. Three independent methods for detection of these shifts are detailed, and examples of both redshifts and blueshifts are found. Possible interpretations of the cause of blueshifted emission are given. Regardless of flow direction, Doppler shifts

observed in the Lyman lines tend to indicate plasma speeds of around 20 – 30 km s<sup>-1</sup>. Due to its strong flare signal, the behaviour of the C III line is also investigated.

In Chapter 4, simulations output from the radiative hydrodynamic and radiative transfer code, RADYN, are used to model four variants of a solar flare. Parameters for the injected electron beam are varied, and the effects of this are assessed. The formation of the Lyman lines is investigated here, and the atmospheric variables output by each simulation are used to explain the resulting line shapes and their formation properties. These simulations suggest that the Lyman lines can be influenced by upflows, and several interesting cases of the atmospheric dynamics influencing these lines are presented.

In Chapter 5, an additional radiative transfer code, RH, is incorporated into our modelling to obtain model Lyman line profiles accounting for the effects of partial frequency redistribution. Both RADYN and RH line profiles are convolved with the EVE instrumental profile, and Doppler shifts in the degraded line profiles are measured. It is found that the presence of central reversals in the line core have the ability to critically obscure the flow direction perceived by an instrument such as EVE. The effects of frequency redistribution across the Lyman line profiles are investigated, along with the consequences of assuming statistical equilibrium. The potential capabilities of the Spectral Imaging of the Coronal Environment (SPICE) instrument on the upcoming Solar Orbiter are also explored.

In Chapter 6, recent EVE observations of an X9.3 class flare are presented, and Doppler shifts are measured in a wide sample of emission lines. A total of 14 lines are considered, and the relation between formation temperature and flow direction is investigated. It is generally found that many aspects of the dynamics of this flare fit the current paradigm of explosive evaporation.

In Chapter 7, concluding remarks are made. The key findings from this work, and the questions still unanswered, are noted. Finally, the direction of future work in this area is commented on.

# Contents

<b>Acknowledgements</b>	<b>iii</b>
<b>Abstract</b>	<b>vi</b>
<b>List of Figures</b>	<b>xi</b>
<b>List of Tables</b>	<b>xv</b>
<b>1 Introduction</b>	<b>1</b>
1.1 An Unusually Bright Night . . . . .	1
1.2 The Sun and its Atmosphere . . . . .	3
1.2.1 The Solar Interior . . . . .	3
1.2.2 The Photosphere and Extended Atmosphere . . . . .	4
1.2.3 The Solar Wind and the Sun-Earth Interaction . . . . .	9
1.3 Solar Flares . . . . .	11
1.3.1 Flare Initiation and Energy Release . . . . .	11
1.3.2 Physical Properties of Flares . . . . .	14
1.3.3 Observational Aspects of Solar Flares . . . . .	16
1.3.3.1 X-rays . . . . .	16
1.3.3.2 Ultraviolet . . . . .	17
1.3.3.3 Visible Light . . . . .	19
1.3.4 Dynamics Of The Flaring Chromosphere . . . . .	20
<b>2 Instrumentation, Concepts and Modelling Tools</b>	<b>24</b>
2.1 The Solar Dynamics Observatory . . . . .	24
2.1.1 The Extreme Ultraviolet Variability Experiment . . . . .	25
2.1.2 The Atmospheric Imaging Assembly . . . . .	28

2.2	Radiative Transfer in a One-Dimensional Atmosphere . . . . .	29
2.3	RADYN . . . . .	33
2.3.1	Development Of RADYN . . . . .	33
2.3.2	RADYN Code Description . . . . .	34
2.4	RH . . . . .	36
2.4.1	The Frequency Redistribution of Line Photons . . . . .	36
2.4.2	The RH Code . . . . .	38
<b>3</b>	<b>EVE Observations of the Lyman Lines During Flares</b>	<b>41</b>
3.1	Selection of Flare Data . . . . .	41
3.2	Methods for Doppler Shift Detection . . . . .	42
3.2.1	Single Gaussian Fitting . . . . .	43
3.2.2	Cross Correlation . . . . .	45
3.2.3	Intensity-Weighted Calculation of the Mean Wavelength . . . . .	49
3.2.4	Error Estimation . . . . .	50
3.2.4.1	Error Analysis Using EVE "Precision" Data . . . . .	50
3.2.4.2	An Empirical Approach . . . . .	52
3.3	Flows Observed with the EVE Instrument . . . . .	53
3.3.1	The 15th February 2011 Flare - Predominant Redshifts . . . . .	53
3.3.2	The 07th March 2011 Flare - Predominant Blueshifts . . . . .	58
3.3.3	The 03rd November 2011 Flare - Predominant Blueshifts . . . . .	63
3.3.4	The 07th March 2012 Flares - Predominant Blueshifts . . . . .	65
3.3.5	The 01st January 2014 Flare - Predominant Redshifts . . . . .	71
3.3.6	The 07th January 2014 Flare - Predominant Redshifts . . . . .	75
3.4	Imaging of Ejection Events with AIA . . . . .	79
3.4.1	An Eruption During the 7th March 2011 Flare . . . . .	79
3.4.2	An Eruption During the 1st January 2014 Flare . . . . .	80
3.5	More Interpretation of Upflow Signatures . . . . .	82
3.6	Summary of Flows Observed by the EVE Instrument . . . . .	83
<b>4</b>	<b>Flare Simulations and the Formation of the Lyman Lines</b>	<b>89</b>
4.1	The Preflare Atmosphere . . . . .	90

4.2	Flare Models . . . . .	91
4.2.1	The F10D3 Simulation . . . . .	94
4.2.2	The F10D8 Simulation . . . . .	96
4.2.3	The 3F10D8 Simulation . . . . .	96
4.2.4	The F11D3 Simulation . . . . .	99
4.3	Formation of the Lyman Lines in RADYN . . . . .	101
4.3.1	Line Formation in the F10D3 simulation . . . . .	102
4.3.2	Line Formation in the F10D8 simulation . . . . .	111
4.3.3	Line Formation in the 3F10D8 simulation . . . . .	115
4.3.4	Line Formation in the F11D3 simulation . . . . .	123
4.4	Summary of Results from Flare Simulations . . . . .	131
<b>5</b>	<b>Simulated Observations of Flows in the Flaring Chromosphere</b>	<b>133</b>
5.1	Model Line Profiles in RADYN and RH . . . . .	135
5.2	Simulated EVE Observations of Flows . . . . .	136
5.2.1	Velocities from the F10 ( $\delta = 3$ ) simulation . . . . .	139
5.2.2	Velocities from the F10 ( $\delta = 8$ ) simulation . . . . .	145
5.2.3	Velocities from the 3F10 ( $\delta = 8$ ) simulation . . . . .	149
5.2.4	Velocities from the F11 ( $\delta = 3$ ) simulation . . . . .	153
5.3	The Effects of Partial Redistribution on Model Lyman Line Profiles . . . . .	157
5.4	The Potential for Flow Measurements in Flares with Solar Orbiter's SPICE Instrument . . . . .	159
5.5	Closing Remarks on Interpreting Lyman Line Asymmetries . . . . .	165
<b>6</b>	<b>Comprehensive Dynamics of the X9.3 06th September 2017 Flare</b>	<b>166</b>
6.1	The 06th September 2017 X9.3 Event . . . . .	167
6.2	Selection of Spectral Lines and Doppler Velocity Measurements . . . . .	169
6.3	Doppler Velocity Profiles During The 06th September 2017 Flare . . . . .	175
6.4	The Variation of Flow Velocity with Line Formation Temperature . . . . .	180
<b>7</b>	<b>Conclusions</b>	<b>185</b>
	<b>Bibliography</b>	<b>193</b>

# List of Figures

1.1	AIA and HMI images of active region 12192 . . . . .	6
1.2	AIA images of coronal loops and coronal holes . . . . .	8
1.3	LASCO image of a CME . . . . .	10
1.4	Diagram of a solar flare . . . . .	13
1.5	Masuda's flare as observed by YOHKOH . . . . .	18
1.6	AIA and SOT images of a flare arcade and H $\alpha$ ribbons . . . . .	19
2.1	SDO/EVE spectrum during 15th February 2011 flare . . . . .	26
2.2	Comparison between unsubtracted and preflare-subtracted line profiles during the 07th March 2012 flare . . . . .	28
2.3	C III line profiles during the 07th March 2012 flare . . . . .	29
2.4	Diagram of radiative transfer within a plane parallel slab . . . . .	31
3.1	Gaussian fits to the Lyman and C III lines during the 07th March 2012 flare . . . . .	46
3.2	Visualisation of cross correlation . . . . .	47
3.3	Illustration of fitting the CCF results with a Gaussian . . . . .	48
3.4	Visualisation of the intensity weighted calculation of the mean wavelength . . . . .	49
3.5	The EVE "precision" errors compared to the observed variations in irradiance . . . . .	51
3.6	Ly- $\beta$ lightcurve of the 15th February 2011 flare . . . . .	54
3.7	Sun-as-a-star Doppler velocities obtained during the 15th February 2011 flare . . . . .	55
3.8	Flare-excess Doppler velocities obtained during the 15th February 2011 flare . . . . .	57

3.9	Ly- $\beta$ lightcurve of the 07th March 2011 flare . . . . .	59
3.10	Sun-as-a-star Doppler velocities obtained during the 07th March 2011 flare . . . . .	60
3.11	Flare-excess Doppler velocities obtained during the 07th March 2011 flare . . . . .	62
3.12	Ly- $\beta$ lightcurve of the 03rd November 2011 flare . . . . .	63
3.13	Sun-as-a-star Doppler velocities obtained during the 03rd November 2011 flare . . . . .	65
3.14	Flare-excess Doppler velocities obtained during the 03rd November 2011 flare . . . . .	66
3.15	Ly- $\beta$ lightcurve of the dual X-class 07th March 2012 flares . . . . .	67
3.16	Sun-as-a-star Doppler velocities obtained during the 07th March 2012 flares . . . . .	68
3.17	Flare-excess Doppler velocities obtained during the 07th March 2012 flares . . . . .	69
3.18	Ly- $\beta$ lightcurve of the 01st January 2014 flare . . . . .	72
3.19	Sun-as-a-star Doppler velocities obtained during the 01st January 2014	73
3.20	Flare-excess Doppler velocities obtained during the 01st January 2014 flare . . . . .	74
3.21	Ly- $\beta$ lightcurve of the 07th January 2014 flare . . . . .	75
3.22	Sun-as-a-star Doppler velocities obtained during the 07th January 2014	77
3.23	Flare-excess Doppler velocities obtained during the 07th January 2014 flare . . . . .	78
3.24	AIA 304 & 171 Å images of SOL2011-03-07 . . . . .	80
3.25	AIA 304 & 171 Å images of SOL2014-01-01 . . . . .	81
4.1	The preflare atmosphere used in RADYN simulations . . . . .	90
4.2	Atmospheric Evolution during the F10D3 Simulation . . . . .	95
4.3	Atmospheric Evolution during the F10D8 Simulation . . . . .	97
4.4	Atmospheric Evolution during the 3F10D8 Simulation . . . . .	98
4.5	Atmospheric Evolution during the F11D3 Simulation . . . . .	100
4.6	Ly- $\alpha$ contribution function (F10D3, $t = 20$ s) . . . . .	104

4.7	Ly- $\beta$ contribution function (F1oD3, $t = 20$ s) . . . . .	106
4.8	Ly- $\alpha$ contribution function (F1oD3, $t = 26$ s) . . . . .	107
4.9	Ly- $\beta$ contribution function (F1oD3, $t = 26$ s) . . . . .	109
4.10	Snapshots of each of the Lyman lines throughout the F1oD3 simulation	110
4.11	Ly- $\alpha$ contribution function (F1oD8, $t = 20$ s) . . . . .	112
4.12	Ly- $\alpha$ contribution function (F1oD8, $t = 26$ s) . . . . .	113
4.13	Snapshots of each of the Lyman lines throughout the F1oD8 simulation	114
4.14	Ly- $\alpha$ contribution function (3F1oD8, $t = 8$ s) . . . . .	116
4.15	Ly- $\alpha$ contribution function (3F1oD8, $t = 16.5$ s) . . . . .	118
4.16	Ly- $\alpha$ contribution function (3F1oD8, $t = 21$ s) . . . . .	119
4.17	Ly- $\alpha$ contribution function (3F1oD8, $t = 49$ s) . . . . .	121
4.18	Snapshots of each of the Lyman lines throughout the 3F1oD8 simulation	122
4.19	Ly- $\alpha$ contribution function (F11D3, $t = 9$ s) . . . . .	124
4.20	Ly- $\alpha$ contribution function (F11D3, $t = 20$ s) . . . . .	125
4.21	Ly- $\alpha$ contribution function (F11D3, $t = 45$ s) . . . . .	127
4.22	Ly- $\alpha$ contribution function (F11D3, $t = 47$ s) . . . . .	128
4.23	Dynamics of the F11D3 atmosphere around $t = 45$ s . . . . .	129
4.24	Snapshots of each of the Lyman lines throughout the F11D3 simulation	130
5.1	Instrumental Convolution of RADYN and RH Ly- $\alpha$ profiles . . . . .	137
5.2	Gaussian fits to degraded model Ly- $\alpha$ profiles . . . . .	139
5.3	Simulated Doppler velocities from the F1oD3 simulation . . . . .	140
5.4	Comparison between RADYN and RH profiles in the F1oD3 model . .	143
5.5	Simulated Doppler velocities from the F1oD8 simulation . . . . .	146
5.6	Comparison between RADYN and RH profiles in the F1oD8 model . .	148
5.7	Simulated Doppler velocities from the 3F1oD8 simulation . . . . .	150
5.8	Simulated Doppler velocities from the F11D3 simulation . . . . .	154
5.9	Comparison between RADYN and RH profiles in the F11D3 model . .	156
5.10	Snapshots of the Ly- $\beta$ line (3F1oD8 simulation) with SPICE instru- mental effects . . . . .	160
5.11	Doppler velocities in the Ly- $\beta$ line after convolution with SPICE in- strumentation . . . . .	162

---

5.12	Running measurement of the asymmetry in Ly- $\beta$ from SPICE . . . . .	163
5.13	Ly- $\beta$ convolved with a variety of instrumental profiles of differing FWHM values . . . . .	164
6.1	SDO/AIA Images of the 06th September 2017 X9.3 flare . . . . .	167
6.2	Full MEGS-B spectrum during the 06th September 2017 X9.3 flare . .	171
6.3	Multiple EVE Lightcurves during the X9.3 flare . . . . .	172
6.4	Emission line profiles throughout the X9.3 flare . . . . .	174
6.5	Sun as a star Doppler velocities during the X9.3 06th September 2017 flare . . . . .	176
6.6	Flare excess Doppler velocities during the X9.3 06th September 2017 flare . . . . .	178
6.7	Flare excess velocities during 06th September 2017 as a function of line formation temperature . . . . .	181
6.8	Sun as a star velocities during 06th September 2017 as a function of line formation temperature . . . . .	182

# List of Tables

1.1	Soft X-ray fluxes for GOES classifications . . . . .	15
3.1	Date, time and location information for each of the flares observed by EVE . . . . .	42
3.2	Summary of flare-excess flow velocities observed by EVE . . . . .	84
6.1	Formation temperatures and wavelength values for the emission lines observed in the 06th September 2017 flare . . . . .	170

# Chapter 1

## Introduction

### 1.1 An Unusually Bright Night

During the evening of 1st-2nd September 1859, the aurora borealis were observed as a diffuse, blood red glow to the north from Honolulu, Hawaii. On the same night, a similar red glow was seen smouldering in the sky south of Santiago, Chile, indicating a simultaneous extension of the southern hemisphere's auroral oval (Kimball 1960). This sort of occurrence is not common. The northern auroral oval is typically confined to the skies above Canada, Scandinavia and other less-temperate regions while that in the southern hemisphere usually only lights up the cold Antarctic night. While the previous few nights had been subject to unusually strong geomagnetic activity, this particular night resulted in the most equatorward extensions of the auroral ovals in observed history (Tsurutani et al. 2003). The intensity of the aurora was sufficient to allow those in the Rocky Mountains to read newsprint unaided by any other light source (Green et al. 2006). This exceptional night of auroral activity coincided with widespread disturbances in electromagnetic networks. Magnetometer needles were deflected off-scale, sparks were thrown from telegraph wires with enough vigour to set nearby material alight, and operators of telegraph systems received shocks from their equipment (Shea & Smart 2006).

Such a strong and widespread disturbance to the Earth's geomagnetic environment can only stem from the interaction between the Earth's magnetosphere and the

far-reaching influence of the Sun. Approximately 18 hours before this disturbance, Richard Carrington observed an dazzlingly bright feature persist for about five minutes above the sunspot region he was observing. His observation was soon verified by Richard Hodgson, who also happened to be observing the Sun simultaneously (Carrington 1859). Unbeknownst to them at the time, they had just recorded the first observation of a solar flare. Carrington initially speculated that it was an optical aberration caused by a stray ray of unfiltered sunlight due to its brightness.

This white light flare, visible to the naked eye, is now generally known as "The Carrington Event", and resulted in the liberation of a vast cloud of electrically-charged material from the Sun's atmosphere, carrying with it the magnetic field of the Sun. This cloud, known as a Coronal Mass Ejection (CME), arrived at the Earth's magnetosphere 17 hours and 40 minutes afterwards (Schwenn 2006). The subsequent reconfiguration of the Earth's magnetic field in response to the solar magnetic field embedded in the CME resulted in a remarkable geomagnetic storm. While Carrington himself was cautious about drawing any great conclusion between his observation and the resulting geomagnetic effects, this event arguably established the concept of solar variability and demonstrated the Sun-Earth interaction.

As time has passed, the advance of technology has allowed us to observe the Sun with increasingly high spatial and spectral resolution, along with more frequent cadence. From ground-based to space-borne observatories, the solar environment is now regularly observed across all regions of the electromagnetic spectrum. This has permitted the exploration of the solar flare phenomenon and its associated effects. We now know many things about flares and solar variability but there remain unanswered questions. Part of the problem with the current "standard model" of a flare lies in understanding how energy is transported through the solar atmosphere during these events. However, we do know that most of the energy that is not ejected (i.e. in the form of a CME) ends up being deposited in the lower layers of the Sun's atmosphere.

This thesis explores the response of the lower solar atmosphere during these dramatic and violent events. We do this by a combination of emission line spectroscopy, followed by simulations and modelling of flare-like events and the formation of

synthetic emission lines as a result. There are, and most likely will always be, puzzles to be solved regarding the behaviour of our nearest star, but if we are to understand how flares occur then we must examine the Sun across the entire electromagnetic spectrum and throughout its varied environments.

## 1.2 The Sun and its Atmosphere

The Sun is at the heart of our cosmic neighbourhood. It is a moderately-sized ( $R_{\odot} = 6.96 \times 10^8$  m) star with a mass ( $M_{\odot}$ ) of  $1.99 \times 10^{30}$  kg and spectral type G2V, placing it in the main-sequence epoch of its lifetime (Aschwanden 2005). The Sun is around halfway through this stage in its evolutionary track, and will remain a main-sequence star for a further 5 billion years, after which it will cease its current mode of energy production and become a red giant (Wolfson 2000).

It is a highly differentiated body, composed of numerous distinct layers and contrasting physical domains. Composed of plasma, it exhibits fluid rotation with a rotation period dependent on latitude. The rotation rate varies from about 25 days at the equator to 35 days at the poles (Beck 2000), and this differential rotation plays a key part in the initiation of the toroidal magnetic field and generation of solar activity. In this section, we briefly describe the solar interior and then outline the rich variety of regions that constitute the Sun's atmosphere.

### 1.2.1 The Solar Interior

The Sun maintains its hydrostatic equilibrium by the nuclear fusion of hydrogen into helium in its *core*. Two hydrogen nuclei first fuse to form a deuterium nucleus, which further fuses with an additional hydrogen nucleus to form  ${}^3\text{He}$ . Production of  ${}^4\text{He}$  is achieved through the fusion of two  ${}^3\text{He}$  nuclei, which liberates two protons (Priyalnik 2009). The reduction in mass of the bound nucleus compared to its initial constituents is liberated as energy. The overall conversion of four protons into the  ${}^4\text{He}$  nucleus is a highly efficient generator of energy, producing 26.73 MeV in total, and is facilitated by hydrogen being the most common chemical element (Stix 2004).

Here, the temperature is approximately 15 MK. The collective, continual fusion of protons in the Sun's core provides the outward pressure gradient required to balance the force of gravity exerted by the overlying layers.

Photons are also generated during these fusion reactions, and propagate outwards from the core and through the *radiative zone*. Here, the dominant mode of energy transport is via the propagation of these photons. This is not a quick process, as the opacity of the interior results in a very low mean free path of about 0.1 cm (Mitalas & Sills 1992). This means that the diffusion timescale of a photon from the core outwards is very long ( $\sim 170,000$  yr). Photons undergo successive scatterings, which reduce the energies of the gamma rays generated in the core.

At about  $0.7 R_{\odot}$ , the temperature gradient in the interior is high enough such that convection becomes possible. This is due to the high opacity caused by bound-bound and bound-free absorptions in partially ionised iron (E. Bailey et al. 2014). This region, the *convective zone*, primarily transports energy outwards through the atmosphere via mass motion (Priyalnik 2009). This process allows the composition of the interior in this zone to be thoroughly mixed, and stratification reduces. This more homogenous layer of the interior is more capable of producing magnetic flux, as the convective motions combine with the differential rotation to induce flows in the electrically conducting material (Solanki et al. 2006). The boundary between the radiative and convective zones is marked by the *tachocline*, where shear develops between the two zones as the interior transitions from solid-body to differential rotation and the initial amplification of the magnetic field occurs (Fan 2009; Charbonneau 2014).

### 1.2.2 The Photosphere and Extended Atmosphere

The Sun is not a perfect blackbody. Its spectrum is littered with a multitude of emission and absorption lines. However, as an approximation, the distribution its light closely matches that of a blackbody with a surface temperature of about 5800 K. From Wien's law,

$$\lambda_{max}T = 2.9 \times 10^{-3} \text{ mK} \quad (1.1)$$

It is clear that this temperature causes the blackbody function ( $B_{\lambda,T}$ ) to peak at a wavelength of 500 nm, in the green-yellow part of the visible spectrum (Pradhan & Nahar 2011). It is no coincidence that the human eye's sensitivity peaks at around this wavelength.

The effective surface of the Sun is the region at which the optical depth at this wavelength transitions from being prohibitively thick to thin. The dominant source of visible opacity here is through the photodetachment of electrons from  $\text{H}^-$  ions. The *photosphere* is the thin layer where the  $\text{H}^-$  opacity becomes low enough to render the solar material as transparent. This defines the visible surface of the Sun, and marks the boundary between its atmosphere and the interior (Pradhan & Nahar 2011). Densities here are still relatively high, with electron densities ( $n_e$ ) on the order of  $10^{17} \text{ cm}^{-3}$ . The plasma  $\beta$  here is about 14, where

$$\beta = \frac{P_{th}}{P_{mag}} = \frac{nk_B T}{B^2/2\mu_0} \quad (1.2)$$

and  $P_{th}$  and  $P_{mag}$  are the thermal and magnetic pressures respectively. Here,  $n$  is the particle density,  $k_B$  the Boltzmann constant,  $T$  the gas temperature,  $B$  the magnetic field strength and  $\mu_0$  the permeability of free space. The high  $\beta$  value indicates that the photospheric system is still dominated by the gas pressure and not magnetic effects (Aschwanden 2005).

The photosphere is not featureless, and is peppered with bright and dark regions. Granules are the visible manifestation of the top edges of convection cells, appearing bright in their cores and bounded by dark intergranular lanes. These granulation cells continuously change in form as hot material rises and cool material sinks, but have typical sizes on the order of 1 Mm (Nordlund et al. 2009). Bright features known as faculae are sometimes seen in the dark regions between adjacent cells, and are linked to strong magnetic fields (Keller et al. 2004). Less ubiquitous are large, localised dark regions on the photosphere known as sunspots. Dark due to their relatively low temperature, these blemishes on the Sun's disk indicate regions of

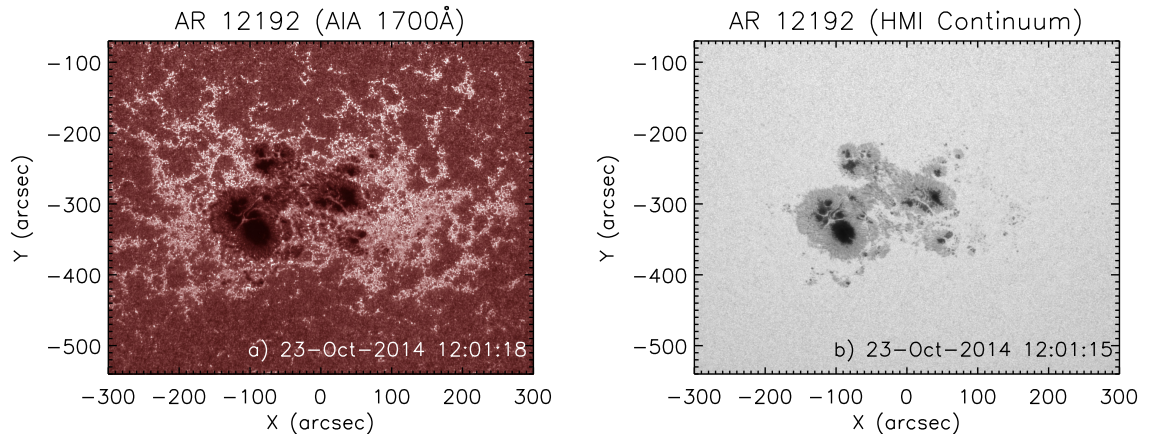


**Figure 1.1:** The most extensive active region of the current solar cycle, as observed by both the Atmospheric Imaging Assembly (AIA) (a) and the Helioseismic and Magnetic Imager (HMI) (b) instruments on board the Solar Dynamics Observatory (SDO). The AIA imagery shows continuum emission from the photosphere and temperature minimum region. The HMI continuum is obtained from imaging the Fe I absorption line (6173 Å).

intense magnetic field where convection is suppressed and the interior magnetic flux crosses the photospheric boundary (Zirin 1966; van Driel-Gesztelyi & Green 2015). When multiple sunspots are observed in close proximity, the grouping is known as an *active region* (Figure 1.1).

Observations of sunspots date back thousands of years, but have been heavily aided by the invention of the telescope (Wittmann & Xu 1987). Records of the number of individual and groups of sunspots on the photosphere at any given time (the International Sunspot Number) have been kept since the mid 1800s (Clette et al. 2014), and reveal an 11 year cyclical variation in the sunspot number, indicating a corresponding variability in the Sun’s magnetic activity. Accounting for a polarity switch between the two hemispheres, this solar cycle has an overall periodicity of 22 years (Hathaway 2015). The solar magnetic field plays a major role in flare physics, and will be discussed further in the following subsection.

Overlying the photosphere is the remarkably varied *chromosphere*. First photographed from the ground in 1860 during a total solar eclipse, it was later given its name in 1869 on the grounds of its brilliant red colour. This colour comes from the brightest line in the solar spectrum,  $H\alpha$ . Also observed in the chromosphere are *spicules*; jets of plasma that ascend into the upper chromosphere, rich in  $H\alpha$ . The chromosphere is a thin ( $\sim 2\,500$  km) layer of striking variety. The atmospheric temperature initially drops from the photospheric value until it reaches a minimum at an altitude of about 500 km, after which it begins to climb to 20 000 K in the space of about 2000 km (Bray & Loughhead 1974; Vernazza et al. 1981; Stix 2004). The density of the chromospheric plasma decreases with height, with  $n_e$  decreasing from about  $10^{12}$  to  $10^9$  over the first 2000 km (Bray & Loughhead 1974).

The chromosphere spans a wide range of temperatures, and has an active role in producing many of the Sun's emission lines. The hydrogen Lyman lines are formed in the upper chromosphere (Vernazza et al. 1981), and other strong lines such as Ca II H and K, and Mg II h and k (Stix 2004) are notable in the chromospheric radiation field. A semi-empirical pre-flare model of the photosphere and chromosphere, based on that of the quiet Sun "VAL3C" (Vernazza et al. 1981) model, is shown in Figure 4.1 and forms the basis of much of the work in Chapter 4.

Beyond an altitude of around 2 Mm, the solar atmosphere undergoes a dramatic change. As it becomes increasingly rarefied, the upper chromosphere gives way to the *transition region*. At this height, the temperature jumps drastically from the "cool" chromospheric regime and increases from  $10^4$  to  $10^6$  K in an extremely thin zone (Peter 2001; Stix 2004). This almost discontinuous region of the atmosphere demarcates the Sun's chromosphere from its extended *corona*.

The corona is the outermost region of the Sun's atmosphere. Much like the chromosphere, its presence is only made obvious via the occultation of light from the rest of the Sun's disk during a total solar eclipse. This is where the similarities with the chromosphere end, as it is a tenuous environment where the electron density is only  $10^9$  cm<sup>-3</sup> in the inner regions. At a temperature of 1 MK, the coronal plasma is composed wholly of ions and exhibits appreciable amounts of emission even in heavily ionised species such as Fe XVIII. The corona is also where the Sun appears

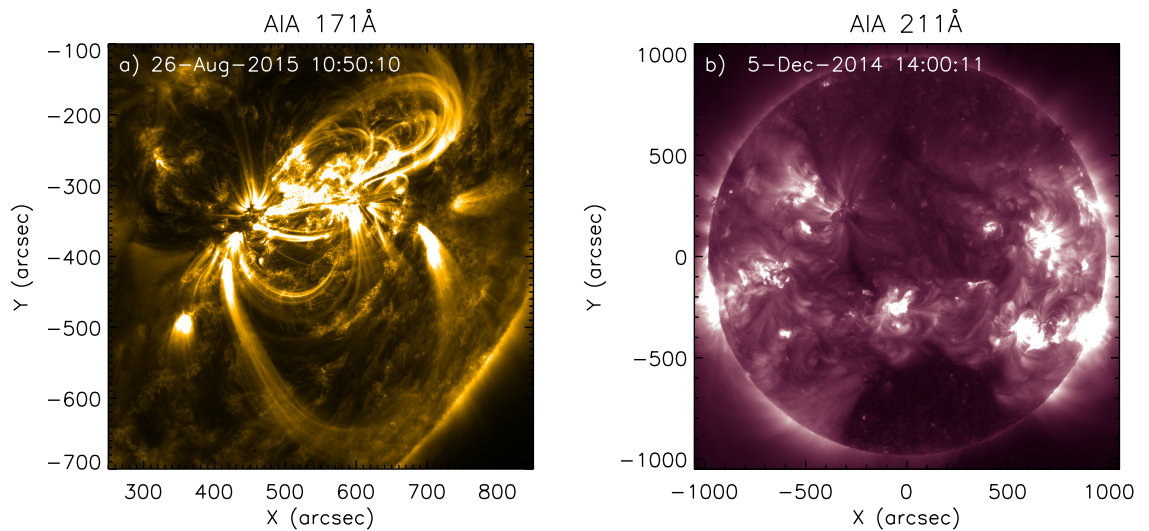


**Figure 1.2:** AIA images of hot, coronal loops above an active region (a), with bright chromospheric footpoints visible. The 171 Å AIA filter images the Fe ix ion, and traces out loops of plasma confined along the magnetic field. In contrast, a large coronal hole can be seen at the lower edge of the disk in the 211 Å filter (b), which images Fe xiv emission. Here, the magnetic field lines are open and particles are ejected into the solar wind.

brightest in X-rays (Aschwanden 2005). Here, the plasma  $\beta$  drops to lower than unity, which allows tubes of magnetic flux to expand outwards as the magnetic pressure is no longer balanced by the thermal pressure of the plasma (Stix 2004).

The ability of the magnetic field to dominate the coronal environment is not of little consequence. In the corona, a large fraction of the plasma has its location and dynamics constrained by the permeating magnetic field. Because of this, the density structure in the corona is not homogeneous, as parcels of plasma lie along the direction of lines of magnetic flux. The topology of the local field may vary, with regions of “closed” magnetic field originating from and returning to the solar surface over a relatively short distance, and areas of “open” field where the magnetic flux may extend a large distance into the heliosphere (Aschwanden 2005).

The tendency of coronal plasma to be confined by the magnetic field provides us with an advantageous position, where we can image the 2D projection of the

Sun's magnetic field via the emission from hot plasma. The corona above active regions generally hosts a large amount of plasma confined on closed magnetic field lines, which visibly appears as numerous glowing loops anchored in the Sun's chromosphere. These loops appear bright in the Soft X-ray (SXR) and extreme ultraviolet (EUV) regions (Figure 1.2a).

The corona also has structure beyond that of active regions, and the remainder of it that encompasses regions of closed magnetic field hosts other dynamic features. Nanoflares are small liberations of energy in the quiet corona that could provide part of the answer as to why the coronal temperature is so high (Klimchuk 2006; Viall & Klimchuk 2017). Beyond the regions of closed field, we find *coronal holes*, regions where the magnetic field is open and extends out into the further reaches of the heliosphere. These regions typically appear dark (Figure 1.2b) because they are devoid of plasma, as the field structure in these areas is so efficient at ejecting material outwards (Aschwanden 2005). Also observed in the coronal environment are *prominences*, dense strands of material at chromospheric temperatures ( $\sim 10^4$  K) which are suspended in the upper atmosphere by the magnetic field configuration (Parenti 2014). When viewed on-disk, these cool structures appear dark through absorption of the underlying emission and are known as *filaments*.

### 1.2.3 The Solar Wind and the Sun-Earth Interaction

The ability of localised coronal holes to channel plasma into the heliosphere adds to the overarching material flow of the *solar wind*. This continuous stream of ions and electrons propagates radially from the Sun, carrying with it the local magnetic field of the Sun (Parker 1958, 1965). Rotation of the Sun sweeps the radially propagating material into a spiral, with a proton density (at 1 AU) on the order of  $5 - 10 \text{ cm}^{-3}$  (Hundhausen 1970; Marsch 2006). The wind speed is closely related to solar latitude, with fast streams of the order  $750 \text{ km s}^{-1}$  originating from the polar regions and a slower wind of  $450 \text{ km s}^{-1}$  emanating from the equatorial zone (Owens & Forsyth 2013).

The solar wind is not the only mechanism by which material may be expelled

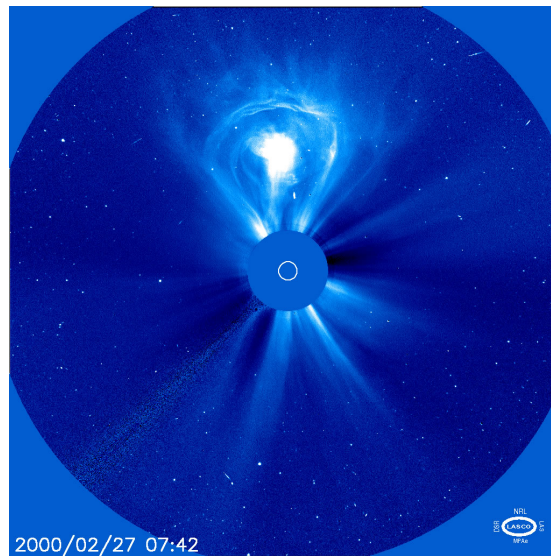


**Figure 1.3:** A CME observed on the 27th February 2000 by the Large Angle and Spectrometric Coronagraph (LASCO) C3 detector aboard SOHO. Visible are the dense front, the internal cavity and the central erupting prominence core. This image was obtained from the National Solar Observatory at <https://eclipse2017.nso.edu/coronal-mass-ejections-cme/>

from the Sun. Transient eruptions of much richer material take the form of *coronal mass ejections* (CME). These eruptions can liberate as much as  $10^{13}$  kg of coronal material in a single release. Often comprised of a leading edge, an interior cavity and a bright core comprising the original erupting filament (Figure 1.3), these ejecta can attain speeds of over  $2000 \text{ km s}^{-1}$  (Chen 2011).

From a combination of the solar wind and occasional CMEs, the Earth's magnetosphere is constantly bombarded by material that carries with it the magnetic field of the solar corona. The dynamic pressure of the solar wind causes compression of the dayside magnetosphere, while that on the night side is dragged out into a tail. Under intense solar wind conditions, the magnetopause can be pushed inwards to radii less than that of orbiting satellites, exposing them to the stream of charged particles (Pulkkinen 2007).

Interaction between the magnetosphere and the solar wind is maximised when the embedded magnetic field in the wind is directed southwards, which facilitates

*magnetic reconnection* (discussed further in §1.3) of the Earth's magnetic field with that of the solar wind. This results in open field lines being swept over the poles, after which a further reconnection in the magnetotail leads to particles being accelerated along Earth's field lines in a geomagnetic storm (Eastwood 2008). It is a process identical to this which led to the famous auroras observed during the nights around Carrington's historic observation.

It is now more clear than ever that the Sun and the Earth are not isolated systems. The magnetic environment of the Sun extends far beyond the inner regions of the corona, and Earth's magnetosphere is not invulnerable to its influence. It therefore becomes essential to understand the magnetic variability of the Sun.

## 1.3 Solar Flares

The presence of sunspots, active regions, and coronal loops reveal that the solar magnetic field can be highly localised into regions of greater strength. The field topology around active regions can be highly complex and can be thought of as a myriad of tubes of magnetic flux which connect regions of different polarity anchored in the photosphere.

Over time, the field can be subject to shear from the sub-photospheric motion and magnetic instabilities. Deformation of the field imparts energy to it, so a flux tube stores an increasing amount of magnetic energy as it becomes twisted and stretched. When regions of oppositely directed flux come together, the boundary between those two regions may reconfigure, resulting in outflows perpendicular to the inflowing direction and a new configuration of the magnetic field in a process called magnetic reconnection (Aschwanden 2005). This is the primary cause of the most energetic phenomena in the solar system, *solar flares*.

### 1.3.1 Flare Initiation and Energy Release

The standard model of a solar flare describes a rapid conversion of free magnetic energy into heating, particle acceleration and radiation via magnetic reconnection.

Detailed descriptions of all aspects of solar flares can be found in [Benz \(2008\)](#) and [Fletcher et al. \(2011\)](#), but we outline the salient points here. A simple 2-D picture is that of a magnetic loop, anchored in the lower atmosphere with an apex in the corona (Figure 1.4). Magnetic reconnection occurs at the boundary between two closely-spaced, oppositely directed field lines and the magnetic energy previously stored in the loop is liberated. In the standard model, this accelerates electrons and ions, which propagate away from the apex and down the loop towards the chromosphere. Outflows are also produced perpendicular to the direction in which the initial field lines came together, resulting in contraction of the loops below the *x-point* towards the chromosphere, and expulsion of closed field from above the *x-point* or current sheet.

The collisional thick target model (CTTM) explains hard X-ray (HXR,  $E \geq 20$  keV) brightenings at the chromospheric *footpoints* of the loop as due to accelerated electrons depositing their energy in the chromosphere via Coulomb collisions within the ambient plasma ([Brown 1971](#)). Bremsstrahlung is emitted as the electrons encounter increasingly dense plasma, while the precipitating protons and ions result in the emission of  $\gamma$ -rays ([Vilmer et al. 2011](#)). HXR emission may also be observed at the loop-top, as a result of acceleration close to the *x-point* where the outflowing plasma results in a density high enough for detectable bremsstrahlung to take place ([Masuda et al. 1994](#); [Fletcher 1995](#)).

As the chromosphere is heated, it expands upwards and fills the magnetic loops with hot plasma which emits in soft X-rays (SXR). Heating may either be gentle or explosive, and the nature of these two regimes along with the resulting dynamical effects are discussed further in §1.3.4. Extending the picture into 3-D, a surface of reconnection proceeds along a chain of coronal loops. This is observed as several *ribbons* of  $H\alpha$  emission, which move away from the polarity inversion line as reconnection occurs in the outer loops. This is accompanied by an *arcade* of SXR emission, as a multitude of loops begin to fill with heated plasma ([Fletcher et al. 2011](#)).

Particle beams are not the only mechanism by which the chromosphere may be heated during flares. It is difficult to reconcile inferred HXR emission intensities with a single heating mechanism of particle beams emanating from a solely coronal

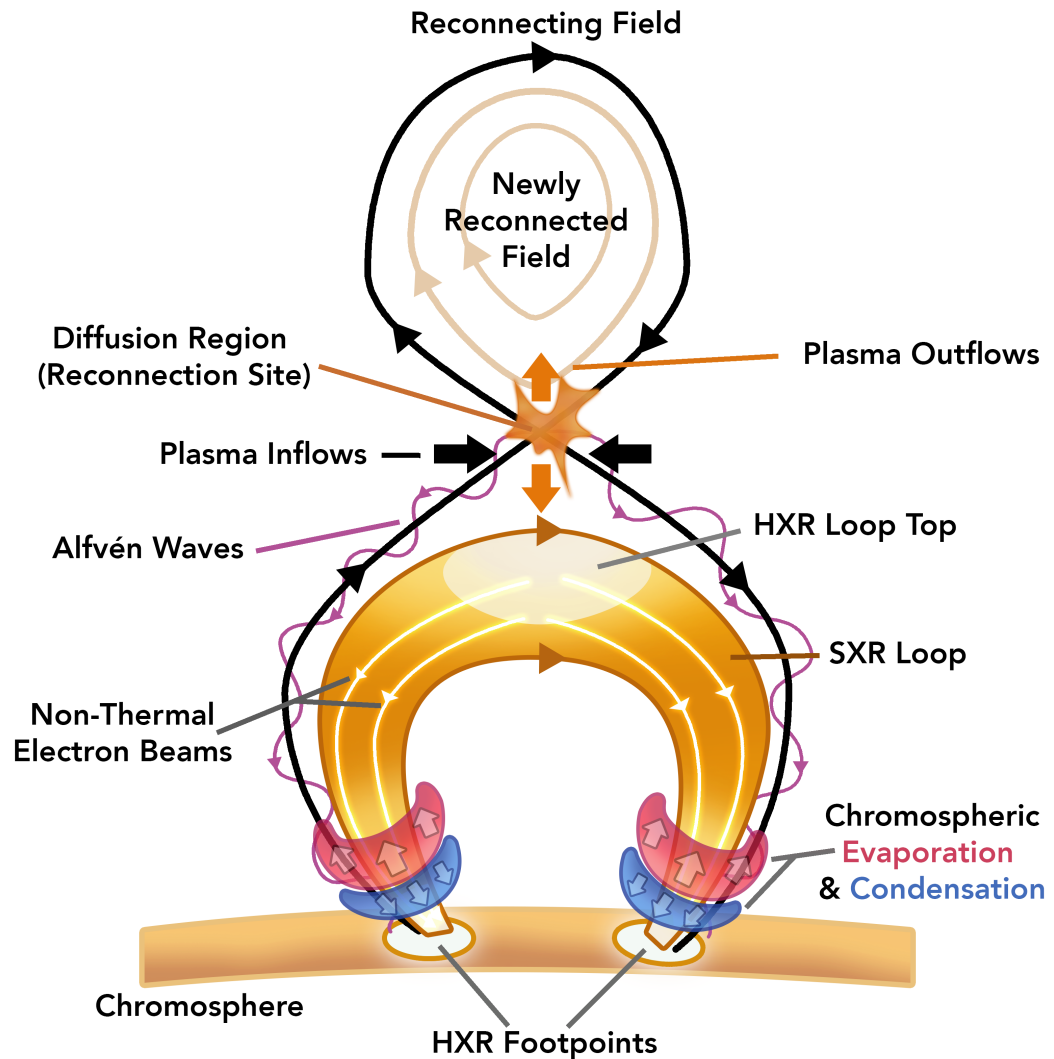


**Figure 1.4:** A 2-D picture of a solar flare. The reconnection accelerates electrons away from the diffusion region and generates Alfvén waves. Plasma above the point of reconnection is ejected. Flows are initiated in the chromosphere as it is heated.

acceleration region, as this requires a problematically high number and number flux of coronal electrons (Hoyng et al. 1976). In addition to heating by beams of particles, it is likely that some of the magnetic energy released during the reconnection is transported along the field lines and dissipated in the chromosphere by the propagation of Alfvén waves (Emslie & Sturrock 1982; Fletcher & Hudson 2008).

These waves are transverse oscillations of the field, initiated by the reconnection,

and with a propagation direction parallel to the field line. As an Alfvén wave encounters chromospheric densities, part of its energy should be dissipated into the chromospheric plasma, resulting in the wave being damped via ion-neutral friction (or Landau damping, [Bian & Kontar 2011](#)) and the chromosphere being heated ([Russell & Fletcher 2013](#)).

There still remain a myriad of mechanisms which have the potential to result in chromospheric heating. For a succinct summary and further references, Table 16.1 in [Aschwanden \(2005\)](#) proves a helpful resource. However, for this thesis we primarily consider heating via electron beams as the dominant heating mechanism (CTTM).

### 1.3.2 Physical Properties of Flares

While only constituting a fraction of the available magnetic energy, the energy released in flares can be in excess of  $10^{32}$  erg ([Fletcher et al. 2011](#); [Emslie et al. 2012](#)). Evaluating the total amount of radiated energy ( $E_{bol}$ ) correctly can be challenging as it requires simultaneous observations of the event across a vast range of wavelengths, but was done successfully for an event by [Milligan et al. \(2014\)](#), who found the radiated energy to be only 15% of that available. The definition of flare refers specifically to the radiation emitted, the majority of which is typically in the optical and ultraviolet regions of the spectrum.

Instead of attempting a measurement of  $E_{bol}$  for every flare, it is much easier to adopt a narrowband classification system for all events. The current system tiers flares by strength via the amount of SXR flux in the range 1-8 Å as observed by the Geostationary Operational Environmental Satellite (GOES, [Garcia 1994](#)). The most energetic class of flares are known as X-class, and are observed with SXR fluxes ( $F_{SXR}$ ) of greater than  $10^{-4}$  W m<sup>-2</sup>. The sequence then steps down through  $F_{SXR}$  via the M, C, B and A classes. Flux ranges for each classification are shown in Table 1.1.

The temporal profile of emission during flares can vary. As a general rule, many flare lightcurves allow a distinction between the flare *impulsive phase* and the *gradual phase*, however this is not always the case. There may also be signatures of pre-flare brightenings, although these are not always observable ([Fletcher et al. 2011](#)).

GOES Classification	Soft X-Ray Flux ( $\text{W m}^{-2}$ )
<b>X</b>	$\geq 10^{-4}$
<b>M</b>	$10^{-5} - 10^{-4}$
<b>C</b>	$10^{-6} - 10^{-5}$
<b>B</b>	$10^{-7} - 10^{-6}$
<b>A</b>	$\leq 10^{-7}$

**Table 1.1:** Ranges of  $F_{\text{SXR}}$  in the GOES 1-8 Å channel for each flare class. Data adapted from <http://www.swpc.noaa.gov/products/goes-x-ray-flux>

The impulsive phase is often easily seen in flare lightcurves. It is characterised by a sudden increase in emission, primarily in HXR, SXR,  $\gamma$ -rays, extreme ultraviolet and white light, along with the presence of microwave emission from the accelerated electrons as they produce synchrotron radiation (Svestka 1976; Fletcher et al. 2011). It should be noted however that the impulsive phase is not rigidly defined in multiwavelength observations, as impulsive behaviour may be observed in one wavelength range at a given time but not in others. For example, the impulsivity of the EUV emission need not begin at the same time as that of the HXR emission, although they may be correlated in time (Donnelly & Kane 1978). For a variation to be defined as impulsive, it should typically occur on a timescale of seconds to a minute (Dennis & Schwartz 1989).

The gradual phase describes the gentle decay of emission following the abrupt enhancement produced by the impulsive phase. The timescales for the gradual phase are typically on the order of minutes to tens of minutes, however on occasion this process can last for hours. The gradual phase is usually associated with the cessation of heating via non-thermal electrons, and encompasses the relaxation of the atmosphere as heat is redistributed in the chromosphere through a combination of conduction and mass flows (Berlicki et al. 2005). This process is made visible by the filling of magnetic loops by hot plasma, which is driven upwards as the chromospheric temperature increases.

Because the SXR emission in the gradual phase is dependent on the initial heating

of the chromosphere, there exists a causal link between the SXR and HXR emission. This link is evident in the time derivative of the SXR flux, as it closely tracks the HXR flux. Alternatively, the SXR flux at a given time is closely linked to the time-integrated HXR flux. This property, known as the *Neupert effect*, was observed to occur 80% of the time in a survey of 66 events (Dennis & Zarro 1993). Another survey by McTiernan et al. (1999) found that consistency with the Neupert effect was observed in 72% of the 33 flares studied in which the data were of appropriate quality to facilitate a comparison.

### 1.3.3 Observational Aspects of Solar Flares

Flares result in enhancements across the entire electromagnetic spectrum. Initially observed as a brilliant white flash in visible light, the advent of the space age has been accompanied by an ever-growing number of ground and space-based observatories which have extended our solar observations to spectral regions beyond visible light. For this work, we will mainly consider aspects at shorter wavelengths than that of visible light and outline some of their details below. For an extensive review, the reader is encouraged to consult Benz (2008) and Fletcher et al. (2011).

#### 1.3.3.1 X-rays

X-rays provide us with a wealth of information that encompasses much of the energetic properties of flares, going beyond the use of SXR measurements to classify flare strength. Soft X-ray emission ( $E \leq 10$  keV) during flares constitutes both a continuum component and emission from lines of highly-ionised species. The SXR continuum is generated via a combination of bremsstrahlung and radiative recombination, whereas the line emission results from radiative de-excitation of the upper levels of ions that have been almost stripped of their electrons (Svestka 1976).

Hard X-ray emission ( $20 \text{ keV} \leq E \leq 300 \text{ keV}$ ) is generally non-thermal in origin, resulting from bremsstrahlung emitted from the accelerated electron population as they encounter the “thick-target” ion population of the chromosphere. While bremsstrahlung is also generated by the thermal electrons, the photon flux in HXR

cannot be attributed to a purely thermal source. The HXR spectrum is therefore fitted with a power law distribution above a certain cutoff energy (Kane & Anderson 1970; Kontar et al. 2011; Holman et al. 2011).

The first spectral observations of the Sun in X-rays were made by the *Orbiting Solar Observatory* (OSO) missions, which were capable of producing lightcurves in the 1 – 8 Å band (Mosher et al. 1979). This band is now monitored continuously by the *Geostationary Operational Environmental Satellite* (GOES), which also has a solar X-ray imager. Imaging of both SXR and HXR emission was made possible by the *YOHKOH* satellite (Tsuneta et al. 1991; Kosugi et al. 1991), which revealed HXR emission in the high-altitude regions of loops in one flare (Figure 1.5). Its follow-up mission, *Hinode / X-Ray Telescope* (XRT), currently images the Sun in SXR and provides spatial detail about the distribution of the hottest plasma on the Sun (Golub et al. 2007).

The most energetic X-ray emission has been successfully observed for the past 16 years by the *Ramaty High-Energy Solar Spectroscopic Imager* (RHESSI). With a resolution of 2.3 arcsec up to 100 keV, it provides the most detailed maps of solar HXR emission ever achieved (Lin et al. 2002). Typically, X-ray emission is only appreciable around active regions, particularly in flare loops and footpoints

### 1.3.3.2 Ultraviolet

The ultraviolet (UV) region is one of the most energetically important during flare progression. Many of the radiative losses in the chromosphere originate in ultraviolet and extreme ultraviolet (EUV) lines. H Ly- $\alpha$  (121.6 nm) is the strongest emission line in the solar spectrum, and contributes significantly to the amount of energy radiated during a flare (Milligan et al. 2014). All of the higher order H Lyman lines, along with the Lyman continuum, display heightened levels of emission during flares. The He II line (30.4 nm) also plays an important role in radiating away the impulsive phase energy, (Tousey et al. 1973; Svestka 1976). Many other ions contribute to the emission in UV, such as C IV, Ca II, the O lines, and highly ionised species of Fe. The EUV emission can persist long after the initial energy deposition, as heated plasma fills the coronal loops which radiate away the energy (Figure 1.6a).

Early observations of flare EUV bursts were performed by the OSO missions, from

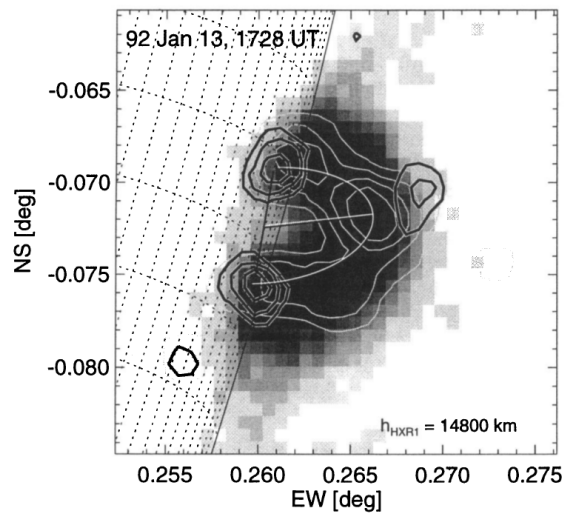


**Figure 1.5:** The famous “Masuda” flare observed on the 13th January 1992 by the YOHKOH Soft (SXT) and Hard (HXT) telescopes. The SXR loop is imaged in greyscale, with HXR contours showing high-energy X-ray emission in the 14 – 23 keV (white) and 23 – 33 keV (black) ranges. The footpoints and a loop-top source are clearly visible in HXR. This figure was taken from [Aschwanden et al. \(1996\)](#).

which a close correlation in time was revealed between the EUV emission and the HXR and microwave emission produced by the impulsive phase ([Castelli & Richards 1971](#); [Svestka 1976](#)). As UV is largely attenuated by Earth’s atmosphere, it was not until *Skylab* was launched with its UV spectroheliographs that imaging of the Sun in this region became feasible. More sophisticated EUV observations were made possible with the launch of the *Extreme Ultraviolet Imaging Telescope* (EIT) on board the *Solar and Heliospheric Observatory* (SOHO), which imaged the Sun in 4 EUV passbands with a pixel size of 2.6 arcsec ([Delaboudinière et al. 1995](#)).

More recent EUV observations were made possible with the *Transition Region and Coronal Explorer* (TRACE) satellite. TRACE allowed CCD imaging of the Sun at a pixel size of 0.5 arcsec in 7 UV and EUV passbands ranging from 171 to 1700 Å ([Handy et al. 1999](#)), and yielded observations of active region flows in the EUV ([Winebarger et al. 2001](#)) to motions of flare footpoints in the UV ([Fletcher et al. 2004](#)). Since the launch of *Hinode*, its *EUV Imaging Spectrometer* (EIS) instrument

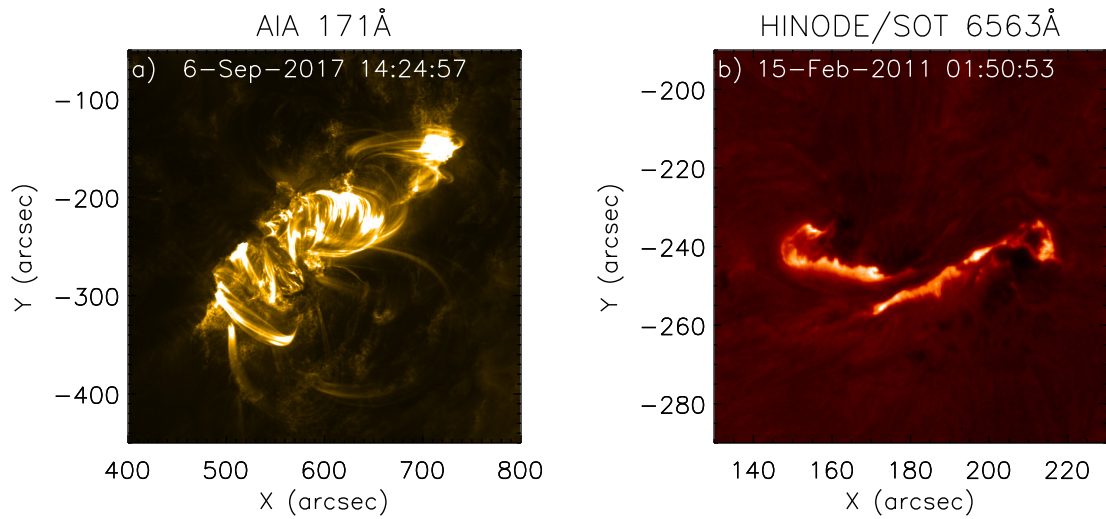


**Figure 1.6:** AIA images of a flare arcade in EUV after the 06th September 2017 flare (a), showing a chain of post-flare loops radiating away the deposited energy. Ribbons in  $H\alpha$  can be observed during the 15th February 2011 flare (b) by Hinode/SOT.

has allowed imaging spectroscopy of the Sun in many EUV lines, and includes those from numerous ionisation states of Fe (Culhane et al. 2007). Launched in 2013, the *Interface Region Imaging Spectrograph* (IRIS) spacecraft has also allowed imaging spectroscopy of the chromosphere and transition region in several EUV lines spanning a wide range of temperatures (De Pontieu et al. 2014).

Currently, the *Solar Dynamics Observatory* (SDO, Pesnell et al. (2012)) provides a fantastic wealth of imaging and spectroscopic data in the UV and EUV, which we discuss further in §2.1.

### 1.3.3.3 Visible Light

A major benefit of observing the Sun in visible light is that it can be done by both space and ground based observatories. Historically, the  $H\alpha$  line of hydrogen (656.3 nm), caused by the  $3 \rightarrow 2$  transition, has dominated observations in visible light because of its rich diagnostic potential. Early flare classification was based on the appearance of flares in the  $H\alpha$  line (Svestka 1976). The disk in  $H\alpha$  reveals bright active regions and dark filaments (non-limb prominences), with the remaining

“mottled” emission originating mainly in the chromosphere.

An excellent compilation of H $\alpha$  spectroheliograms can be found in [Zirin \(1966\)](#). During flares, the morphology of H $\alpha$  brightenings usually evolves from several bright “knots” to two extended ribbons ([Figure 1.6b](#)), which separate at a few km s<sup>-1</sup> ([Bruzek 1964](#)). The spreading of ribbons is interpreted to be a consequence of the magnetic reconnection in the corona progressing upwards through loops at increasingly higher altitudes, which have their footpoints anchored further from the polarity inversion line ([Qiu et al. 2002](#); [Fletcher et al. 2004](#)). The link between the reconnection process and the formation of the H $\alpha$  ribbons is strengthened by the observation of HXR footpoints along these ribbons ([Radziszewski et al. 2007](#); [Benz 2008](#)).

The “white-light” component of flare emission refers to the continuum enhancement observed in the visible region. Solar observations find that the white light emission corresponds to a blackbody temperature of roughly 9000 K ([Kretzschmar 2011](#)), while a survey of stellar flares obtained a blackbody-like component of T=9000-14000 K ([Kowalski et al. 2013](#)). Solar flare observations in white-light are rare, but have been facilitated by TRACE ([Metcalf et al. 2003](#); [Hudson et al. 2006](#)) and the *Solar Optical Telescope* on board HINODE ([Tsuneta et al. 2008](#); [Kerr & Fletcher 2014](#)).

#### 1.3.4 Dynamics Of The Flaring Chromosphere

In particular, this thesis will focus on the dynamics of the chromosphere during flares. For the energetics of flares to be understood, we must develop a clear picture on how this region of the atmosphere responds to an influx of energy. Fortunately, we have a wealth of information from other authors on the general process. There exist a multitude of observations of both *chromospheric evaporation*, an upwards expansion of chromospheric material into the corona, and *chromospheric condensation*, a downwards motion of the chromosphere.

There are two prescriptions as to how the heating proceeds. In the *gentle* case, the chromosphere is heated slowly enough that the heating timescale is comparable to the hydrodynamic timescales in the plasma. This allows the chromosphere time to

radiate some of the energy away, and it responds dynamically by expanding slowly upwards into the corona as the temperature increases (Antiochos & Sturrock 1978; Fisher et al. 1985b). In this case, chromospheric evaporation may be observed as blueshifted components in ions with a wide range of formation temperatures.

In the *explosive* case, a large amount of non-thermal electrons rapidly heat the plasma to coronal temperatures with a timescale that does not allow the chromosphere to radiate the energy away fast enough. In this case, the chromosphere evaporates rapidly, expanding into the corona with a greater velocity than in the gentle case. This high-velocity upflow is accompanied by a compression wave (chromospheric condensation), driven down into the lower chromosphere by the thermal pressure (Fisher et al. 1985a). These condensations are observed as redshifted components in chromospheric lines.

Observations of upflow signatures in flares are reported by many authors. Upflows of  $250 \text{ km s}^{-1}$  in the Ca XIX X-ray line were observed from YOHKOH by Wülser et al. (1994). Additional YOHKOH observations by Doschek et al. (1994) revealed upflows in the X-ray Ca XIX and Fe XXV lines, with velocities reaching as high as  $800 \text{ km s}^{-1}$ . Milligan & Dennis (2009) were able to perform a multiwavelength survey of Doppler shifted lines using HINODE/EIS data, who found that all ionisation stages of iron above Fe XIII ( $T \geq 2 \text{ MK}$ ) exhibited blueshifts, with the hottest ions implying upflows in excess of  $250 \text{ km s}^{-1}$ . These observations agree well with the high-velocity upflow aspect of the explosive evaporation scenario.

However, other observations do suggest instances of gentle evaporation in lower temperature lines. Schmieder et al. (1990) found weak upflows ( $4 - 12 \text{ km s}^{-1}$ ) and downflows of a similar magnitude in the C IV line in *Solar Maximum Mission* data. Berlicki et al. (2005) determined upflow velocities of about  $5 \text{ km s}^{-1}$  in the H $\alpha$  line using the *German Vacuum Tower Telescope*. Blue asymmetries in H $\alpha$  were again observed by Kuridze et al. (2015) in the late stages of an M1.1 event using the *Swedish Solar Telescope*.

As expected from the explosive evaporation model, downflows in the chromosphere during flares have also been observed. Perhaps one of the most well-known examples is that of the red asymmetry in H $\alpha$  which was found to be present 80%

of the time in a sample of 244 events (Švestka et al. 1962). Ichimoto & Kurokawa (1984) determined downflow velocities from H $\alpha$  asymmetries to be between 40 – 100 km s<sup>-1</sup>. Later observations of the H $\alpha$  red asymmetry have also been reported by Wülser et al. (1994) and Kuridze et al. (2015). Redshifts in many chromospheric lines such as Mg VI and O VI were observed by Milligan & Dennis (2009), with downflow velocities between  $\sim$ 30 – 60 km s<sup>-1</sup>. Downflows in O V were observed by Kamio et al. (2005) in SOHO data, which attained speeds of 87 km s<sup>-1</sup>. Despite it being the strongest line in the solar spectrum, there are few observations of Doppler shifted emission in the H I Ly- $\alpha$  line, but Lemaire et al. (1984) found it to exhibit a redshift corresponding to a speed of 12 km s<sup>-1</sup> during a flare.

The observations suggest that, certainly in the cases of explosive evaporation, there is a link between the formation temperature of a line and its corresponding flow velocity. Milligan & Dennis (2009) illustrate this relation, and their observations suggest that the “turnover” point between downflow and upflow lies at a temperature of around 1 – 2 MK. Kamio et al. (2005) speculated that they could not observe any flows in the Mg IX line because its formation temperature (1 MK) places it in the intermediate region between the upflowing and downflowing plasma.

In this thesis, we investigate the chromospheric dynamics by studying the response of the hydrogen Lyman lines. This series of emission lines, formed by transitions to the ground ( $n = 1$ ) state of neutral hydrogen (H I), are essential to describing the radiative losses of the flaring chromosphere. They should therefore provide a wealth of information about the velocity field in the chromosphere during flares. However, until recently there were no systematic studies of their Doppler shifts. While the *Laboratoire de Physique Stellaire et Planetaire* (LPSP) and *Solar Ultraviolet Measurements of Emitted Radiation* (SUMER) instruments aboard OSO-8 and SOHO were capable of observing these lines, the requirement of the slit to be positioned meant that flare observations of the Lyman lines were rare (Lemaire et al. 1984, 2004, 2015). Only with the launch of SDO has full-disk coverage of the Lyman series been possible (see §2.1.1).

From the temperature structure of the solar chromosphere outlined by Vernazza et al. (1981), the Lyman lines should be formed over a range of heights, with their

cores originating somewhere close to the top of the chromosphere and their wings at a deeper altitude. Their formation temperature in this model is roughly  $10^4$  K. Because the lines are optically thick and a photon may be reabsorbed and re-emitted many times, the core may form deeper in the atmosphere than the altitude from which the observed core photons are eventually emitted.

In the models described by [Fontenla et al. \(1990\)](#), a radiative hydrodynamic approach is taken to more accurately obtain the chromospheric temperature structure, which places the formation of the core of the Ly- $\alpha$  line between around  $10^{4.6}$  -  $10^{4.8}$  K. Regardless of the atmospheric model considered, the formation temperature of the Lyman lines still lies well below the temperature threshold for upflows in the explosive evaporation scenario. This forms the basis of our expectations that the Lyman series should exhibit redshifted emission during flares as a result of this region of the atmosphere being compressed.

In Chapter 2, we outline the observational instrumentation and numerical tools required to probe the velocity characteristics and formation of the Lyman lines. Chapter 3 describes the methods used to detect and measure Doppler shifts in the Lyman lines in observations of 6 solar flares. In Chapter 4, we simulate three flare models, and use these to examine the formation of the Lyman lines. In Chapter 5, we perform synthetic observations of Doppler velocities in the Lyman lines from flare simulations by emulating the instrumentation from Chapter 3. Chapter 6 briefly revisits the link between flow direction and line formation temperature, and we provide some final remarks in Chapter 7.

## Chapter 2

# Instrumentation, Concepts and Modelling Tools

### 2.1 The Solar Dynamics Observatory

To gain a complete understanding of any flows present in the plasma emitting in the Lyman lines, we require data encompassing the spectral, temporal and spatial domains. We cannot measure a Doppler shift without a spectrum, and we cannot measure a sustained flow signature without time-resolution. Nor can we fully interpret any flow measurements made without the spatial context that images provide. Fortunately, these data are readily available.

The Solar Dynamics Observatory (SDO) was launched on the 11th February 2010 as part of NASA's "Living With A Star" program. The overarching aim is to further understanding in solar variability, focussing towards that which affects life on Earth, with a goal of aiding future predictive capabilities ([Pesnell et al. 2012](#)).

It consists of a multiwavelength, full-disk narrowband imager (*The Atmospheric Imaging Assembly (AIA)*), a high-cadence EUV spectrograph (*The Extreme Ultraviolet Variability Experiment (EVE)*) and a imager capable of producing photospheric magnetograms and dopplergrams (*The Helioseismic and Magnetic Imager (HMI)*). We further describe the SDO instruments relevant to this work in the following subsections.

### 2.1.1 The Extreme Ultraviolet Variability Experiment

One of the primary aims of the SDO mission is to better understand variability in the EUV region of the spectrum. EUV flux can vary by a factor of hundreds in a matter of seconds during periods of strong solar activity, which heats Earth's upper atmosphere. Not only does this cause it to expand thermally and increase the aerodynamic drag on orbiting satellites, but it increases the amount of ionisation in the upper atmosphere, affecting the propagation of radio waves and disrupting telecommunication and positioning systems (Kane & Donnelly 1971; Pesnell et al. 2012). EVE's primary science objective is to quantify and monitor the variations in solar EUV output, and to examine the origins of its variation. The spectral irradiance is measured by two spectrographs, a pinhole camera and a photodiode, with an additional broadband spectrograph used for calibration (Woods et al. 2012).

The Multiple EUV Grating Spectrographs (MEGS) measure the spectral irradiance using a combination of grazing and normal incidence detectors. MEGS-A provided wavelength coverage for the 5 – 37 nm region with a full width half-maximum (FWHM) of around 0.1 nm until mid 2014, after which it has remained switched off due to suffering an electronic failure. The pinhole camera, MEGS-SAM, which provided measurements in the 0.1 – 5 nm range, has also remained off since this time as it required use of the MEGS-A CCD.

Still operational, the MEGS-B instrument provides data in a broad wavelength range encompassing 35 – 105 nm. To mitigate degradation of the detector by UV photons, its exposure window is usually limited to a total of 3 hours per day. The MEGS-B spectra have a cadence of 10 s, and a wavelength sampling of 0.02 nm. While the FWHM varies slightly with wavelength, above 40 nm it remains comfortably below 0.09 nm (Crotser et al. 2007). Additionally, MEGS-B houses a photodiode (MEGS-P) which is centred on the Ly- $\alpha$  line (Woods et al. 2012). The wavelength range spanned by MEGS-B covers the Lyman series of hydrogen, excluding Ly- $\alpha$  (91.2-102.6 nm). These emission lines are generated by transitions to the  $n=1$  state. Blueward of 91.2 nm, the Lyman continuum is also covered extensively, where emission is produced as a result of free-bound transitions to the ground state. A

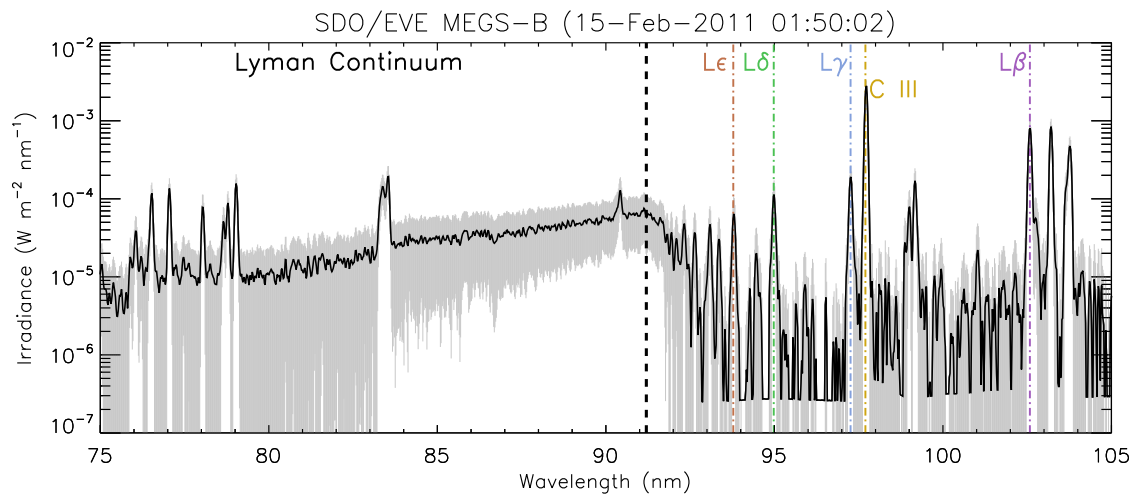


**Figure 2.1:** A “Sun as a star” spectrum (no preflare subtraction) obtained from EVE shortly after the onset of the X2.2 15th February 2011 flare. Formal “precision” irradiance errors are overplotted in light grey. The Lyman lines are observed as a series of prominent emission lines redward of the Lyman edge (thick dashed line at 91.2 nm) and are indicated by the dashed lines, while the Lyman continuum lies blueward of this limit. The C III line is also prominent in this region.

MEGS-B spectrum obtained during the 15th February 2011 flare is shown in Figure 2.1, in which the Lyman lines can be clearly seen.

The level 2 EVE spectral (EVS) data are pre-calibrated, and are corrected for dark current and curvature of the slit image on the detector.<sup>1</sup> These data are publicly available in the form of FITS files, containing wavelength, irradiance, time and error data, with the current release being version 6.<sup>2</sup> No further calibration or modifications to the data are performed in the work described in this thesis.

The spectra from EVE are obtained by integrating over the full disk of the Sun for a 10 s interval. Therefore, there is no spatial information in the spectral measurements and the spectra contain contributions from the entire disk. This presents a challenge for flare studies, where any flare-related enhancements are weak compared to the full-disk emission. In particular, this means that any Doppler shift in a given line

<sup>1</sup>[http://lasp.colorado.edu/eve/data\\_access/evewebdata/products/level2/EVE\\_L2\\_V6\\_README.pdf](http://lasp.colorado.edu/eve/data_access/evewebdata/products/level2/EVE_L2_V6_README.pdf)

<sup>2</sup>[http://lasp.colorado.edu/eve/data\\_access/evewebdata/products/level2/](http://lasp.colorado.edu/eve/data_access/evewebdata/products/level2/)

profile due to flare-associated motions will effectively be “washed-out” by intensity contributions and motions from across the rest of the Sun.

It therefore becomes necessary to find a way to isolate the contribution from the flare. For the observations in this thesis, this is done by first establishing a period of time before each flare which is classified as the “preflare”. This time-period is defined manually by inspection of the Ly- $\beta$  lightcurve for a given event. A preflare spectrum is obtained by time-averaging the full-disk spectrum over this period, which is then subtracted from each of the full-disk spectra during the subsequent flaring times.

These preflare-subtracted “flare excess” spectra are beneficial in that they contain emission purely from the flaring active region, but they are vulnerable to having a low signal to noise ratio (SNR) as the overall excess irradiance may be small compared to the preflare. Conversely, the full-disk “Sun as a star” spectra generally provide good signal for a given line profile, but at the expense of diminishing effects on the line associated with a flare. Comparisons between these two types of spectra during the 07th March 2012 X<sub>5.4</sub> flare are shown in Figures 2.2 and 2.3. In Figure 2.2, Ly- $\beta$  maintains a strong flare-excess signal even at late times, while the signal in the high-order Ly- $\epsilon$  decays more rapidly. The higher order lines generally show a weaker and shortlived flaring signal compared to those of Ly- $\beta$  and Ly- $\gamma$ .

The spectral region containing the Lyman lines also includes a particularly strong emission line from the C III ion. As in Figure 2.2, we show a comparison between the full-disk and preflare-subtracted C III line in Figure 2.3. Even at late times, the flare-excess C III line retains a prominent enhancement above the preflare average. Because its flare-excess signal is particularly strong, we included the C III line in our study as we expected it should be a reliable indicator of the motions associated with a given flare.

The full-disk and preflare-subtracted spectra from EVE data are used to measure line shifts in the Ly- $\beta$  (102.6 nm), Ly- $\gamma$  (97.3 nm), Ly- $\delta$  (95.0 nm), Ly- $\epsilon$  (93.8 nm) and the C III (97.7 nm) lines over the duration of six solar flares, which we detail further in chapter 3. Lyman lines of a higher order than Ly- $\epsilon$  are not considered as they are situated in increasingly close proximity to other lines, and their flare-excess signals are not strong enough to permit a reliable measurement of their line centroids.

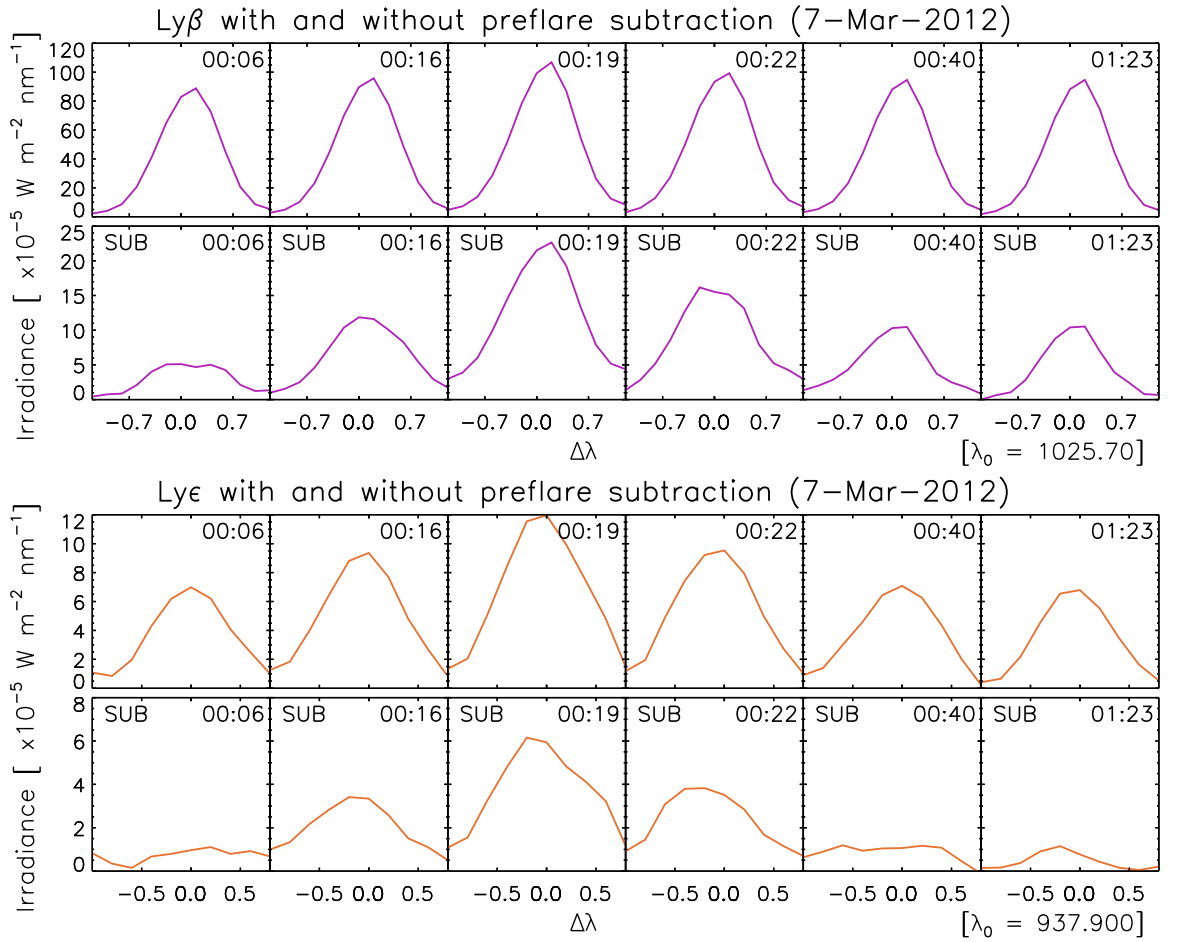


**Figure 2.2:** Running comparisons between unsubtracted and preflare-subtracted Ly- $\beta$  (purple) and Ly- $\epsilon$  (orange) profiles during the X<sub>5.4</sub> flare observed on 07th March 2012. The upper panels show the full-disk “Sun as a star profiles”, which exhibit a good signal. The lower panels show the flare-excess profiles, which at late times are subject to increasing noise as the flare signal decays.

### 2.1.2 The Atmospheric Imaging Assembly

Since the EVE data do not contain spatial information, images are required to provide context to our spectral observations. AIA is an assembly of four telescopes that observe simultaneously, providing high-resolution full-disk images of the Sun at a cadence of 12 s and a spatial resolution of 1.5 arcsec (Lemen et al. 2012). A filter wheel is used to alternate the wavelength coverage of the observing channel in three of the telescopes, with a wavelength selector on the fourth. In total, AIA observes

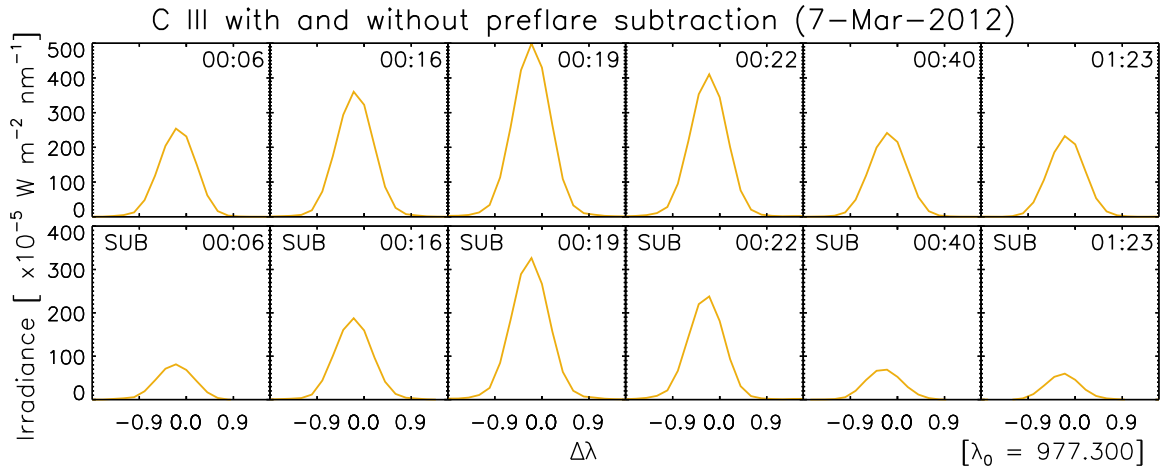


**Figure 2.3:** A running comparison between the “Sun as a star” and flare-excess C III line during the 07th March 2012 flare. In stark contrast to the Ly- $\epsilon$  line, C III maintains a very strong flare signature even after preflare subtraction over the entire duration of the flare.

ten passbands: seven EUV, two UV and one optical.

AIA’s regular and detailed images of solar emission comprise a wide range of characteristic ion formation temperatures and thus span a variety of atmospheric regions. The response functions for the 193 and 94 Å filters have components covering the Fe xxiv ( $\log(T)=7.3$ ) and Fe xviii ( $\log(T)=6.8$ ) ions, allowing the hottest regions of the corona to be observed during flares, while the relatively cool chromosphere is well represented by the He II line, observed by the 304 Å filter. In addition, the photosphere and temperature minimum region are imaged by the 1600 and 1700 Å filters.

In chapter 3, we use AIA images to aid interpretation of the Doppler shifts that we observe, in order to evaluate possible contributions to the line shifts from high-speed ejecta.

## 2.2 Radiative Transfer in a One-Dimensional Atmosphere

While observations are an essential part of studying aspects of the chromosphere, certain aspects of their interpretation can be challenging. Our ability to understand

observations is enriched by modelling. By simulating aspects of flares and synthesising model spectra, we can identify similarities in the behaviour between the observed and modelled data, and use the model data to help further our understanding of the observations.

To complement our observations in chapter 3, we will utilise two numerical codes to synthesise model line profiles from simulations of a dynamic, impulsively-heated atmosphere. In order to understand these models, we first need to visit the concepts related to the propagation of light in an atmospheric slab.

The majority of astrophysical information available to us is provided in the form of photons, which can be scattered, absorbed, re-emitted or have their wavelength altered on their journey to our detectors. Once there, the information they carry is further affected by the dispersive properties and resolution of the instrument. Disentangling all of these factors and retrieving meaningful knowledge about the state of the plasma the light was emitted from is challenging, but the theory of radiative transfer can guide us.

We consider a ray of light of frequency  $\nu$ , with a specific intensity  $I_\nu$ , emitted from a downwards atomic transition from level  $j \rightarrow i$ . As it passes through a distance  $ds$  of atmosphere, atomic processes can both contribute to and diminish the intensity of the ray. Spontaneous and stimulated downwards  $j \rightarrow i$  transitions can add photons to the ray, where level  $j$  may be populated either due to the prior absorption of a photon, or via collisional excitation. Conversely, a photon may be removed from the ray via an upwards excitation followed by a downwards collisional de-excitation, which heats the plasma. Additionally, photons may be given to or removed from the ray via the presence of a shared upper atomic level, whereby an electron may transition downwards to a different level from that which it was originally excited from (Raman scattering).

The continual population and depopulation of these atomic levels can be described in terms of a transition rate ( $P_{ij}$ ), described by:

$$P_{ij} = R_{ij} + C_{ij}, \quad (2.1)$$

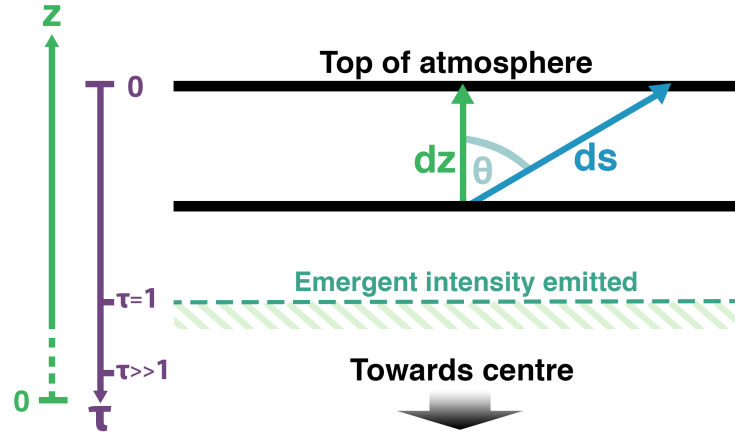


**Figure 2.4:** Diagram showing the relevant vector quantities used to describe the propagation of radiation within a plane-parallel semi-infinite atmosphere. Here,  $ds$  is the distance travelled by a ray, observed at angle  $\theta$  with respect to the height travelled  $dz$ .  $\tau$  increases in the opposite direction to  $z$ .

where  $R_{ij}$  and  $C_{ij}$  are the transition rates due to radiative and collisional influences respectively. Because the overall rate is influenced by the hydrodynamical aspects of the atmosphere, we restrict further discussion of the level populations until §2.3.2.

Multiple formalisms exist for describing the process of radiative transfer. For example, one may wish to describe terms as a function of unit path length, or of the material properties of the gas. Here, we follow that adopted by [Carlsson & Stein \(1997\)](#), with additional guidance provided by [Rutten \(1993\)](#) and [Pradhan & Nahar \(2011\)](#). For a slab of gas of mass density  $\rho$ , the change in the specific intensity of a ray of light propagating a distance  $ds$  (as shown in Figure 2.4) through the slab can be expressed as:

$$\frac{dI_\nu}{ds} = j_\nu \rho - \kappa_\nu \rho I_\nu, \quad (2.2)$$

Where  $j_\nu$  and  $\kappa_\nu$  are the emission and absorption coefficients respectively. We define  $\mu$  to be equal to the cosine of the angle between the ray-propagation direction and the normal to the atmosphere, such that  $ds = dz/\mu$ . Additionally, we redefine

$j_\nu\rho$  as the *emissivity* ( $\eta_\nu$ ) and  $\kappa_\nu\rho$  as the *opacity* ( $\chi_\nu$ ). From [Uitenbroek \(2001\)](#) and [Hubeny & Mihalas \(2014\)](#), these can be expressed (for a bound-bound transition) as:

$$\eta_{ji}(\nu) = \frac{h\nu}{4\pi} n_j A_{ji} \psi_{ji}(\nu), \quad (2.3)$$

$$\chi_{ij}(\nu) = \frac{h\nu}{4\pi} [n_i B_{ij} \phi_{ij}(\nu) - n_j B_{ji} \psi_{ji}(\nu)]. \quad (2.4)$$

Here,  $A_{ji}$ ,  $B_{ij}$  and  $B_{ji}$  are the Einstein coefficients for spontaneous emission, absorption and stimulated emission respectively. We define  $\psi_{ji}(\nu)$  and  $\phi_{ij}(\nu)$  as the line emission and absorption profiles.

It is often desirable to instead describe the process as a function of the *optical depth* ( $\tau$ ) of the atmosphere. This is given by

$$d\tau_\nu = - \int_{z_0}^{z_1} \chi_\nu dz. \quad (2.5)$$

The negative term arises as  $\tau_\nu$  increases with increasing depth in the atmosphere, in the opposite direction to the  $z$  co-ordinate which increases with altitude. We also define the *source function* to be the ratio of the emissivity to the opacity, given by

$$S_\nu = \frac{\eta_\nu}{\chi_\nu}. \quad (2.6)$$

By accounting for the geometry, and dividing through by  $\chi_\nu$ , we can then substitute [2.5](#) and [2.6](#) into equation [2.2](#) and rearrange to obtain the equation of radiative transfer for a semi-infinite, one-dimensional, plane-parallel atmosphere:

$$\mu \frac{dI_\nu}{d\tau_\nu} = I_\nu - S_\nu. \quad (2.7)$$

The formal solution for this equation is given in [Carlsson & Stein \(1997\)](#), where the emergent intensity  $I_\nu$  can be written as:

$$I_\nu = \int_{z_0}^{z_1} S_\nu \tau_\nu e^{-\tau_\nu} \frac{\chi_\nu}{\tau_\nu} dz \quad (2.8)$$

It is important to note that both  $\eta_\nu$  and  $\chi_\nu$  for a transition between levels  $i$  and  $j$  are functions of the level population numbers  $(n_i, n_j)$ , and that  $\chi_\nu$  has both a positive and negative term as the incident photon may stimulate either an absorption or an emission (Uitenbroek 2001). As  $\chi_\nu$  and  $\eta_\nu$  are both dependent on the level populations, it becomes clear that an accurate calculation of  $S_\nu$ , and thus the emergent intensity, requires a correct solution for the population numbers, which themselves are influenced both by the radiation field and collisions in the plasma.

## 2.3 RADYN

### 2.3.1 Development Of RADYN

RADYN is a numerical code that was developed in FORTRAN by Carlsson & Stein in order to model the observed appearance of bright points in the Ca II H and K lines (Carlsson & Stein 1992, 1997). This was done by the upwards propagation of acoustic waves from a sub-photospheric piston into a one-dimensional atmosphere. The code provided the first non-equilibrium (time-dependent) solution to the plane-parallel equations of radiation hydrodynamics, coupled to the radiative transfer equation, for a one-dimensional atmosphere not in local thermodynamic equilibrium (non-LTE) conditions.

Abbett & Hawley (1999) modified the code to calculate the heating rate in response to a flux of non-thermal electrons injected at the top of the grid, simulating the propagation of an electron beam downwards along the half-length of a symmetric flare loop. Allred et al. (2005) further extended RADYN's capabilities by the addition of a double-power law beam description, and improvements to the heating resulting from inward-directed SXR and EUV photons. Recently, Kerr et al. (2016) used a version of RADYN modified to include a heating term resulting from the dissipation of Alfvén waves in the chromosphere to explore the formation of the Mg II and Ca II lines.

The strengths of RADYN have been outlined in many other studies. Carlsson & Stein (1997) first replicated aspects of observed bright grains in the Ca II H<sub>2V</sub>

line using it, which allowed them to constrain the frequency range of the waves producing the grains, and later used it to compare the dynamic timescales in the atmosphere with those of ionisation and recombination for hydrogen (Carlsson & Stein 2002). Abbett & Hawley (1999) found that the impulsive phase in RADYN was differentiated into a gradual and explosive evolution when they applied a constant beam flux, and that the  $H\alpha$  and  $\text{Ca II K}$  profiles were asymmetric as a result of the flows generated during the latter phase. Allred et al. (2005) used RADYN to model an atmosphere heated by a double-power law beam, and found that a bubble was generated during the impulsive phase as a result of the plasma being unable to radiate away the injected energy fast enough, producing an explosive wave. They were also able to examine enhancements in the optical and ultraviolet lines and continua.

Using RADYN, Kuridze et al. (2015) found that, rather counter-intuitively, the frequently-observed red asymmetries in  $H\alpha$  need not be associated with redshifted emission due to downflows in the flaring atmosphere, and may be caused by upflows in absorbing material. Simões et al. (2016) found an association between the beam spectral index in RADYN and the intensity of the calculated  $\text{He II } 304 \text{ \AA}$  line. Kerr et al. (2016) successfully used RADYN to demonstrate the ability of Alfvén waves to heat the chromosphere, and found that features in the  $\text{Mg II}$  lines may be able to discriminate between a beam-heated and a wave-heated atmosphere. While it remains much more challenging to simulate any specific flare in detail, Rubio da Costa et al. (2016) managed to achieve a good match between the intensities in observed and synthetic chromospheric line profiles using a multithreaded approach.

### 2.3.2 RADYN Code Description

The radiative hydrodynamic equations are solved on a spatially adaptive grid (Dorfi & Drury 1987), capable of dynamically altering the distribution of grid points. This is essential to allow the equations to converge, as rapidly-propagating, highly-localised features in the flaring atmosphere are often produced as a result of the beam injection. By using an adaptive grid, the heating, density changes and radiative contributions from features such as shocks can still be resolved without the computational expense

of a sizeable uniformly-spaced grid.

Following [Allred et al. \(2015\)](#), these equations account for the conservation of mass (2.9), momentum (2.10) and internal energy (2.11) and are coupled to the non-equilibrium population equation (2.12) and radiative transfer equation (2.7).

$$\frac{\partial \rho}{\partial t} + \frac{\partial \rho v}{\partial z} = 0 \quad (2.9)$$

$$\frac{\partial \rho v}{\partial t} + \frac{\partial \rho v^2}{\partial z} + \frac{\partial (p + q_v)}{\partial z} + \rho g - A = 0 \quad (2.10)$$

$$\frac{\partial \rho e}{\partial t} + \frac{\partial \rho v e}{\partial z} + (p + q_v) \frac{\partial v}{\partial z} + \frac{\partial}{\partial z} (F_r + F_c) - Q = 0 \quad (2.11)$$

$$\frac{\partial n_i}{\partial t} + \frac{\partial n_i v}{\partial z} - \left( \sum_{j \neq i}^N n_j P_{ji} - n_i \sum_{j \neq i}^N P_{ij} \right) = 0 \quad (2.12)$$

Where the hydrodynamic quantities of  $\rho$ ,  $t$ ,  $v$ ,  $z$ ,  $p$ ,  $e$ , and  $g$  have their usual meanings of density, time, velocity, height, pressure, internal energy density and gravitational acceleration. Respectively, the terms  $A$  and  $Q$  refer to the momentum contribution and heating provided by the beam electrons.  $q_v$  is a viscous stress term proportional to the velocity gradient, required to aid numerical stability during the iteration process.  $F_r$  and  $F_c$  are the radiative and conductive fluxes. Spitzer conductivity is assumed for  $F_c$ , but is limited in cases of high flux so as not to exceed the saturation limit described in [Smith & Auer \(1980\)](#) and [Fisher et al. \(1985b\)](#).

Additionally,  $n_i$  and  $n_j$  denote the lower and upper level atomic population densities. The transition rates between these two levels,  $P_{ji}$  and  $P_{ij}$  are a sum of the collisional and radiative rates. The non-equilibrium solution for the level populations allows for the total number of populated states to change with time, and includes time-derivative terms.

The non-LTE formalism is important because generally the atomic level and ion populations cannot be described correctly by the Boltzmann and Saha equations, where the populations are influenced solely by the plasma temperature and thus collisional rates. In reality, the populations are influenced significantly by the

radiative rates (which may not be a function of the plasma temperature) in addition to collisions in the plasma, and so the LTE formalism does not hold (Pradhan & Nahar 2011; Hubeny & Mihalas 2014).

RADYN is able to solve these equations for 4 atomic species: a six-level with continuum hydrogen atom, a nine-level with continuum helium atom, a six-level with continuum Ca II ion, and a four-level with continuum Mg II ion. In our simulations, the Mg II ion is omitted. Transitions are computed with a total of 201 frequency points, and emergent intensities are obtained for a range of 5 different viewing angles on a grid with 300 spatial points. In addition to these explicitly-solved transitions, a background source of opacity is included which treats remaining continua in LTE as described by the Uppsala package (Gustafsson 1973). The time-step sizes are not enforced by the Courant condition, but are a function of the rate of change of the variables, and the solution is obtained using a Newton-Raphson iterative scheme.

An aspect of line formation in the chromosphere that is not fully encompassed by RADYN is how a photon gets redistributed in frequency throughout the line profile during an absorption and re-emission event. RADYN assumes that there is no coherence between the frequencies of a photon before an absorption and after it is re-emitted, a formalism known as *complete frequency redistribution (CRD)*. This assumption is not entirely correct, as the coherence is rarely fully eliminated. The more accurate alternative to CRD is known as *partial frequency redistribution (PRD)*. In the version of RADYN used here, the effects of PRD are approximated by assuming the Lyman lines have Doppler profiles, as in Leenaarts et al. (2012). In previous versions of RADYN, this was done by truncating the Lyman lines at a certain number of Doppler widths.

## 2.4 RH

### 2.4.1 The Frequency Redistribution of Line Photons

RADYN assumes CRD, whereas in fact there is some level of frequency coherence between an absorption and re-emission event. As mentioned before, accurate com-

putation of the line source function requires correct expressions for the emissivity ( $\eta_\nu$ ) and the opacity ( $\chi_\nu$ ). The general assumption made in CRD is that the emission profile ( $\psi_{ji}$ ) is equal to the absorption profile ( $\phi_{ij}$ ), facilitated by collisions in the plasma. However, for strong resonance lines, or for regions in the atmosphere where excitation of the line by radiation becomes more frequent than that by collisions (i.e. due to a low plasma density), the emission profile  $\psi_{ji}(\nu)$  then has a dependence on the radiation field.

The emission profile is then related to the absorption profile by the *redistribution function* ( $R_{kji}$ ), which describes the conditional probability of a photon being absorbed at a frequency  $\nu'$  from a direction  $n'$  in a transition  $k \rightarrow j$ , and being re-emitted with a frequency  $\nu$  in direction  $n$  in a transition  $j \rightarrow i$ . As in [Uitenbroek \(2001\)](#), the redistribution function can be written as:

$$R_{kji} = \gamma R_{kji}^{II} + (1 - \gamma) \phi_{kj} \phi_{ij}. \quad (2.13)$$

Where  $R_{kji}^{II}$  is the angle-averaged, generalised redistribution function, which describes CRD-like behaviour for absorptions in the line core, but also has a narrow peak for photons absorbed in the line wings. For a detailed discussion of  $R_{kji}^{II}$ , the reader is encouraged to consult [Adams et al. \(1971\)](#) and [Hubeny & Mihalas \(2014\)](#).  $\gamma$  is the *coherency fraction*, and essentially describes how important PRD-effects are for the line. It is given by:

$$\gamma = \frac{P_j}{P_j + Q_j}. \quad (2.14)$$

$P_j$  is the combined radiative and collisional depopulation rate of level  $j$ , and  $Q_j$  is the rate of elastic collisions affecting the upper level.  $\gamma$  therefore provides a measure of the rate of level depopulation with respect to the frequency of collisions in the plasma, and encompasses how much the frequency of the transition is redistributed before it de-excites.

With the emission profile dependent on the radiation field, the source function can be rewritten as in [Uitenbroek \(2001\)](#):

$$S(\nu) = \frac{n_j A_{ji} \rho_{ij}(\nu)}{n_i B_{ij} - n_j B_{ji} \rho_{ij}(\nu)}. \quad (2.15)$$

Here,  $\rho_{ij}(\nu)$  is simply the ratio of the emission and absorption profiles ( $\psi_{ji}/\phi_{ij}$ ). In CRD, the expression for the redistribution function results in  $\psi$  trivially reducing to  $\phi$ , leading to  $\rho = 1$  and a relatively simple expression for  $S_\nu$ . In PRD,  $\psi$  crucially does not reduce to  $\phi$ , and the form of  $S_\nu$  then depends on the coherency fraction.

The physical consequence of assuming CRD is that, given the absorption of a photon (even in the far wings), it will be re-emitted with a frequency very close to that of the line core as the sublevels of  $j$  are “reshuffled” by collisions with particles in the plasma. Realistically, the density of the chromospheric plasma may not be high enough to provide a sufficient number of collisions before the atom de-excites, especially if the line is particularly strong and can be easily de-excited radiatively. In this case (PRD), a wing photon does not get reshuffled into the core, but instead is re-emitted coherently. This therefore has consequences for the emergent core and wing intensities of a given line.

### 2.4.2 The RH Code

Developed by [Uitenbroek \(2001\)](#), the numerical code RH allows for the radiative transfer equation to be solved including the effects of PRD in a multi-level atom. A previous approach to computing PRD in a transition was implemented by [Paletou \(1995\)](#), who used the Multilevel Accelerated Lambda Iteration (MALI) iterative scheme ([Rybicki & Hummer 1991](#)). This earlier scheme involved direct perturbation of the source function but this can lead to problems in obtaining a linear solution for the populations as non-linearities can arise in the stimulated emission term.

To overcome this issue, RH is based on a later MALI formalism that operates on the emissivity and not the source function ([Rybicki & Hummer 1992](#)), and accounts for overlapping transitions. Written in C, the independence of geometry in the solution process has allowed for four variants of the code to be established; one-dimensional plane-parallel, two and three-dimensional Cartesian grids, and a spherically-symmetric grid.

RH solves the radiative transfer equation for a given set of “active” atoms, which are treated in non-LTE conditions. A supplementary number of background “passive” species are also included to the radiation field, but with their populations given either by the LTE solution or from a specified populations file. The initial solution for the populations of a given species can either be specified as the values given from the statistical equilibrium equation with the radiation field set to zero, the values as obtained from LTE conditions, or from a specified input file.

The list of included atoms references a number of “atom files”, usually stored in another directory. These files, which now cover an extensive range of species, contain the energy levels, the line oscillator strengths ( $f$ ), the atomic parameters (i.e, damping and collisional rate coefficients), and continuum intensities for a given atom or molecule. Bound-bound transitions also have their profiles specified in these files (i.e, Voigt, PRD).

Once the wavelength list and initial populations are established, RH solves the statistical equilibrium and radiative transfer equations, iterating until the changes in the population numbers and the angle-averaged mean intensities are smaller than the pre-defined convergence criterion. To decrease the computational time required, the acceleration method of Ng (1974) is used to accelerate the iterative process. In our case, these equations are solved on a specified one-dimensional atmospheric grid.

We use the results from our RADYN simulations as the starting atmosphere for which RH is run. For a given solution output from RADYN, we decompose its time-dependent grid of atmospheric variables into a series of “snapshots”. These atmosphere files list the temperature, electron density, atmospheric velocity, and microturbulent velocity on a column mass grid scale. A shell script is used to run RH sequentially through each atmosphere, eventually returning solutions for each time-step. This provides us with synthetic Lyman line profiles, with the effects of PRD included.

As RH does not account for temporal variation, the level populations are re-solved in statistical equilibrium for each snapshot, whereas in RADYN there is an additional  $\frac{\partial n}{\partial t}$  term to account for non-equilibrium effects. Effectively this means that RH does

---

not account for the “history” of the atmosphere, although the inclusion of the electron densities from RADYN should at least partially mitigate some of this problem.

In chapter 4, we use RADYN to simulate three flare variants which are differentiated by their chosen beam parameters. This allows us to examine the conditions of formation for the Lyman lines. In chapter 5, the output from these simulations are then input to RH to obtain a secondary set of model line profiles.

## Chapter 3

# EVE Observations of Doppler Shifted Emission in the Lyman Lines During Flares

*The work presented in this chapter was published in [Brown et al. \(2016\)](#).*

This chapter will detail both the spectral and imaging observations of 6 solar flares during solar cycle 24, obtained from SDO data. For these flares, we measured variations in the positions of the line centroids for the Lyman lines (from Ly- $\beta$  to Ly- $\epsilon$ ) and the C III 97.7 nm line, and use these to calculate the Doppler shifts and determine the associated plasma velocities.

### 3.1 Selection of Flare Data

Limited by the 3-hour MEGS-B exposure window, we are confined to a relatively narrow list of appropriate flare events with an appreciable strength (either GOES M or X class). An initial survey of all M and X class flares observed between 2011 and 2015 by EVE was performed, with only those exhibiting a discernible enhancement in the Ly- $\beta$  lightcurve retained for further analysis.

This left us with a sample of 17 flares that had both preflare-data and a notable flare enhancement above the pre-flare background, important for ensuring reason-

SOL Identifier	GOES Classification	Location
SOL2011-02-15T01:45	X2.2	S20, W10
SOL2011-03-07T19:46	M3.7	N30, W48
SOL2011-11-03T20:20	X1.9	N22, E63
SOL2012-03-07T00:07	X5.4	N18, E31
SOL2014-01-01T18:44	M9.9	S16, W45
SOL2014-01-07T18:06	X1.2	S12, W08

**Table 3.1:** Dates and start-times for each flare, listed in the format of a SOL (Solar Object Locator) identifier. The GOES classification and heliographic co-ordinates of each event are also listed.

able flare-excess signals. While the Ly- $\beta$  line was fitted in all 17 events, systematic line shifts could generally only be observed in the stronger events. This was to be expected, as a reliable measurement of a flow in the flare-excess spectra requires a robust enhancement of the Lyman line intensities above their pre-flare levels.

The work that was published in this chapter was performed using Version 5 of the *Level2* EVE spectral data for a final selection of 6 solar flares. These flares are listed in Table 3.1, and details of each event are given in the subsections of §3.3. For this chapter, we present results obtained using the newer Version 6 data. The version 6 data incorporates an updated degradation correction for both MEGS-A and MEGS-B detectors, and applies an adjusted dark correction. However, using the updated data has not altered the results from those published in Brown et al. (2016), indicating that the changes applied in version 6 are minor.

## 3.2 Methods for Doppler Shift Detection

For a given observation, the FITS file containing the spectra is read into IDL using the `eve_read_whole_fits.pro` procedure<sup>1</sup>, and formed into arrays containing the

<sup>1</sup>[ftp://sohoftp.nascom.nasa.gov/solarsoft/sdo/eve/doc/eve\\_read\\_whole\\_fits-code.html](ftp://sohoftp.nascom.nasa.gov/solarsoft/sdo/eve/doc/eve_read_whole_fits-code.html)

wavelength, irradiance, errors and time information. For flares spanning more than one MEGS-B FITS file (one hour of data), the arrays are concatenated so that the full extent of the flare is included.

The lightcurve of the Ly- $\beta$  line is then inspected, to define two time ranges: one corresponding to preflare conditions, and the other bounding the duration of the flare. The preflare spectrum is time-averaged and the flare-excess irradiance array is obtained by subtracting this mean preflare spectrum from each of the flaring spectra. The wavelength values that bound the extent of each spectral line are also established by eye. These arrays are then analysed using three different approaches to calculate Doppler shifts and corresponding plasma velocities as a function of time during the flare; single Gaussian fitting, cross-correlation, and intensity-weighted mean wavelengths.

In the Gaussian and intensity-weighted methods, preflare line centroids ( $\lambda_{pf}$ ) are first calculated, and are subtracted from each of the subsequent flaring line centroids ( $\lambda_f$ ) to obtain the Doppler shift ( $\Delta\lambda$ ) at any given time. In the cross-correlation method,  $\Delta\lambda$  is calculated directly. The plasma velocity corresponding to a given shift is calculated by:

$$v_d = \frac{\Delta\lambda}{\lambda_{pf}} c. \quad (3.1)$$

It is worth clarifying at this point that the convention used in this thesis is that the Doppler shift is the subtraction of the preflare centroid from the flaring centroid. This means that a velocity directed away from the observer, with a redshifted line profile is positive, and a blueshifted profile will have a negative velocity directed towards the observer.

### 3.2.1 Single Gaussian Fitting

This first method models each line profile as a simple 4-parameter Gaussian, parameterised by the spectral line's height, centroid, width, and the background upon which it sits. The background is assumed to be constant over the small range in wavelength occupied by the line. The irradiance of a line profile can then be expressed as:

$$I(\lambda) = I_0 e^{-\frac{(\lambda-\lambda_0)^2}{2\sigma^2}} + I_b. \quad (3.2)$$

The height of the Gaussian is given by  $I_0$  and the line centroid is denoted by  $\lambda_0$ . The FWHM of the Gaussian is given by  $2\sqrt{2\ln 2}\sigma$ , where  $\sigma$  is the standard deviation of the Gaussian function. The background intensity is given by  $I_b$ .

For a given line, the preflare centroid is first determined. This is crucial, as the Doppler shifts should be determined with respect to a rest wavelength derived from the data, and not some absolute reference. It has been established that the daily orbital motion of the SDO spacecraft introduces a small wavelength variation of the order  $\sim 3 \text{ km s}^{-1}$  (Hudson et al. 2011). Similarly, thermal variations within the instrument could also cause slight wavelength variations. Therefore, it is important to determine Doppler shifts self-consistently, with respect to the measured pre-flare line centroids. We impose two rather liberal constraints on the parameters before fitting the preflare line profiles. These are:

- The height of the gaussian cannot be lower than the minimum irradiance value present across the line profile ( $I_0 > I_{min}$ )
- The centroid of the gaussian cannot be more than 0.06 nm from the central (median) wavelength bin. For the Lyman lines, the bin size (0.02 nm) corresponds to a Doppler shift of around  $60 \text{ km s}^{-1}$ . This constraint therefore forbids a preflare velocity of  $\sim 170 \text{ km s}^{-1}$ . This is only a constraint, and it is not expected that preflare velocities are as high as this.

These constraints are permissive, but this is not a problem for the preflare profiles which have an excellent signal and are therefore very clear. The wavelength, irradiance and error arrays are input to the **mpfitfun.pro** procedure<sup>2</sup>, which performs a least-squares Gaussian fit to the data while constraining the parameters. Fitting of the preflare profiles is performed for each of the Lyman lines and the C III line, and the parameters returned by **mpfitfun** provide robust estimates for the preflare line centroids ( $\lambda_{pf}$ ).

<sup>2</sup><https://hesperia.gsfc.nasa.gov/ssw/gen/idl/fitting/mpfit/mpfitfun.pro>

For each of the timesteps during the flare, **mpfitfun** is again used to fit the flaring line profiles. This is done both for the Sun-as-a-star and flare-excess profiles. Because the flare produces a greater number of Doppler-shifted photons, and because the flare-excess profiles are often noisy upon subtraction of the preflare, the line shapes during the flare can be irregular. Because of this, a more rigid set of constraints is enforced in order to achieve a sensible fit. The constraint on the height parameter is as in the preflare case, while the others are:

- The centroid of the gaussian is further limited. Its variation is now limited to 2.25 wavelength bins, excluding Doppler velocities that exceed  $\sim 130 \text{ km s}^{-1}$ . This still permits measurements of speeds within the range of that expected for these low-temperature lines, and reduces the chance of fitting over emission from potential blends.
- The standard deviation of the Gaussian is now limited. From visually inspecting the line profiles it was found that their FWHM values were generally close to 0.1 nm, with variations rarely exceeding more than 10% of this. The standard deviation is therefore constrained to values corresponding to a maximal FWHM variation of 15% from the baseline of 0.1 nm.

Using the stricter constraints, the line profiles are fitted for both Sun-as-a-star and flare-excess arrays, and the flaring line centroids ( $\lambda_f$ ) are obtained at each timestep. In Figure 3.1, Gaussian fits returned by this method are shown for each of the preflare-subtracted lines for a number of timesteps during the SOL2012-03-07 flare. For Ly- $\beta$ , Ly- $\gamma$  and C III, a Gaussian fit remains a suitable choice for the majority of the flare. When the excess signal in Ly- $\delta$  and Ly- $\epsilon$  weakens, the SNR in the line profiles decreases and achieving an acceptable Gaussian fit proves more challenging.

### 3.2.2 Cross Correlation

While a Gaussian manages to reasonably describe the shape of each line at most of the times throughout a flare, there are times when it fails. A second method to measure the Doppler shifts in each line is used, which does not make any assumption

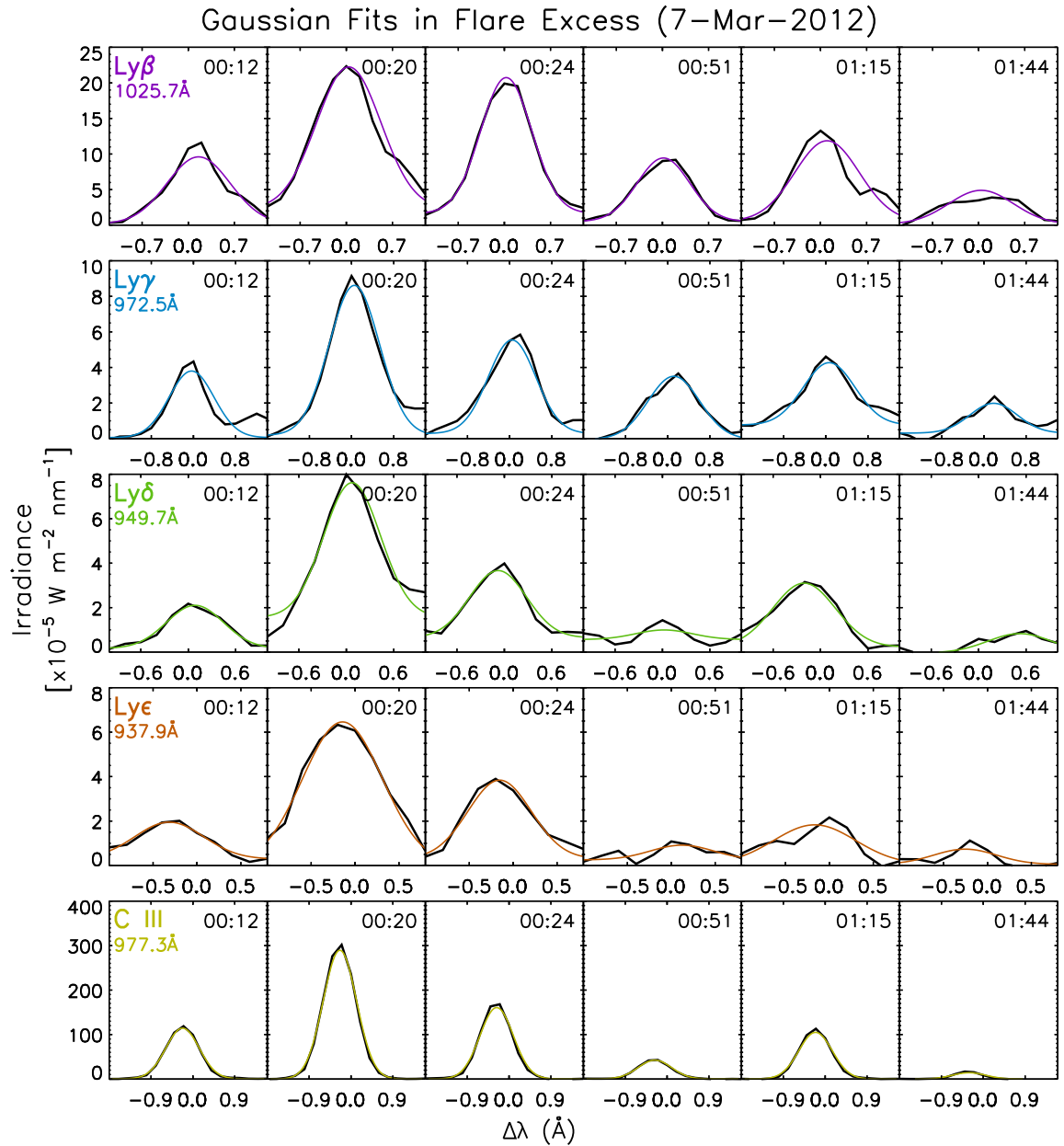


**Figure 3.1:** Gaussian fits to each of the considered line profiles at a series of timesteps spanning the 07th March 2012 flare. The black lines show the EVE data, while the coloured lines represent the Gaussian fit obtained from `mpfitfun`. Each of the profiles shown are preflare-subtracted.

about the shape of a given line. The process of cross correlating two signals allows for their similarity to be quantified as a function of the distance between them. Often

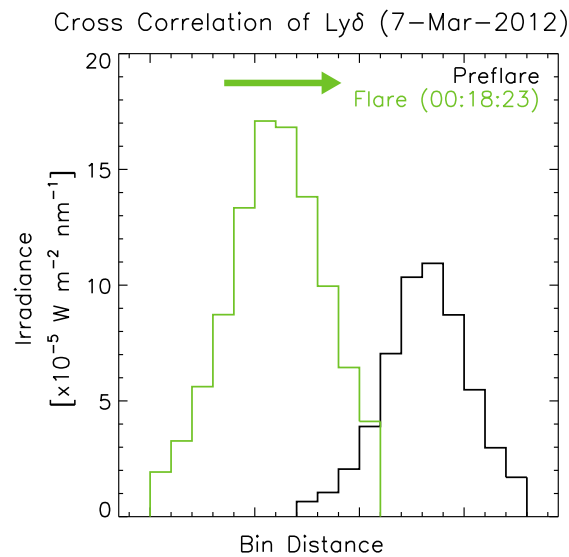


**Figure 3.2:** Visualisation of the Cross Correlation between the flaring (in green) and preflare (in black) Ly- $\delta$  profiles during a timestep on the 07th March 2012 flare. The flaring profile is not preflare-subtracted. The flaring line profile is offset such that its red wing is sampled initially (here with a lag of  $-7$ ), before it is slid across the preflare profile.

this distance is in the time or frequency domain, but we consider the distance in wavelength. By cross correlating in wavelength space, the similarity of two line profiles can be probed as a function of the wavelength separation between them.

For each time, the cross correlation function (CCF) between a flaring line profile and its preflare counterpart is computed for a range of lags, which is permitted to vary between  $-7$  and  $+7$  wavelength bins, and is done for both the Sun-as-a-star profiles and the flare-excess profiles. This is evaluated using the IDL `c_correlate.pro`<sup>3</sup> procedure. The CCF is computed for each amount of shift, providing an array of CCF values as a function of the lag. The Doppler shift between the two line profiles should then be given by the lag value at which the CCF array peaks. Figure 3.2 illustrates the cross-correlation process.

However, because the typical Doppler shifts are generally less than a single

<sup>3</sup>[http://www.lancesimms.com/programs/IDL/lib/c\\_correlate.pro](http://www.lancesimms.com/programs/IDL/lib/c_correlate.pro)

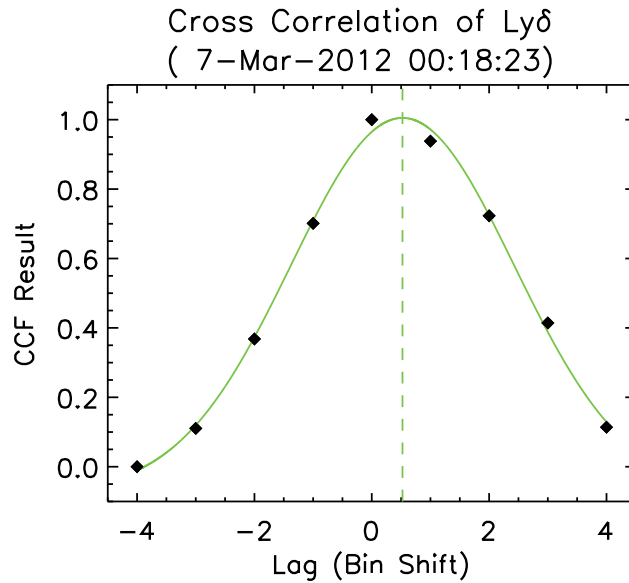


**Figure 3.3:** The results from cross-correlating a preflare-subtracted flaring Ly- $\delta$  profile (close to the flare peak) with its preflare counterpart during the 07th March 2012 flare. Overplotted in green is the Gaussian fit to these results. The dashed line indicates the derived sub-pixel lag value, showing that at this time the flaring profile is offset from the preflare profile by around one half of a wavelength bin.

wavelength bin ( $\sim 60 \text{ km s}^{-1}$ ), we need to derive the lag with sub-pixel accuracy. This can be achieved by utilising the distribution of CCF values about the peak value. The 4 CCF values and their corresponding lags either side of the peak value are extracted, and `mpfitfun` is again used to fit a 4-parameter Gaussian to the CCF results. This process is illustrated in Figure 3.3, and the “centroid” parameter returned is the true sub-pixel lag value corresponding to the peak in the CCF, which gives the Doppler shift.

Equation 3.1 is then used to convert the Doppler shift into a plasma velocity. As this method does not provide us with an estimate of the preflare line centroid, the median of the wavelength array constituting the line profile is used as the rest wavelength.

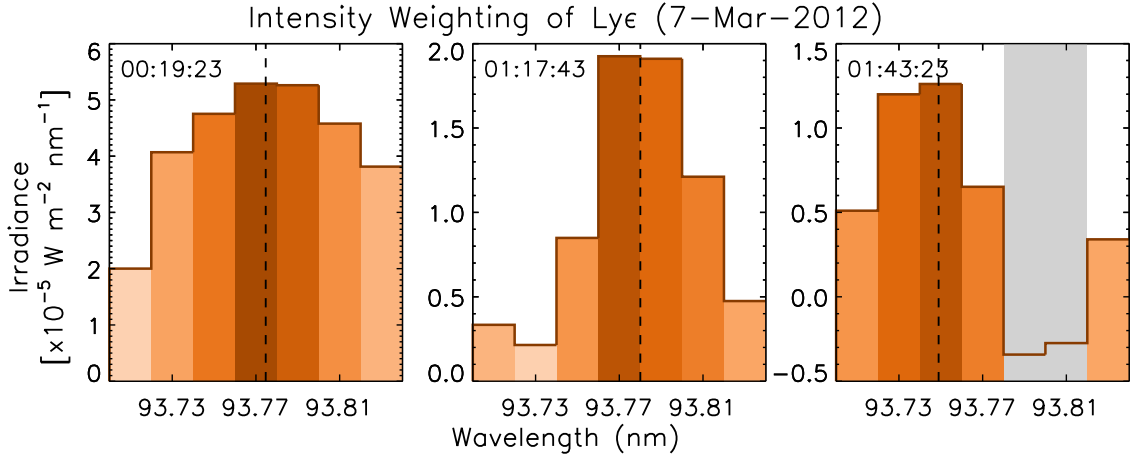


**Figure 3.4:** Visualisation of the calculation of the intensity-weighted mean wavelength for flare-excess Ly- $\epsilon$  profiles. Each panel indicates a different time during the SOL2012-03-07 flare. The bins shaded with fainter colours contribute less to the mean wavelength. Bins that are shaded in grey contain negative irradiance values as a result of the preflare-subtraction, and are excluded from the calculation.

### 3.2.3 Intensity-Weighted Calculation of the Mean Wavelength

The final method by which a Doppler shift is estimated is by calculating a spectral line's mean wavelength weighted by intensity. This simple approach essentially calculates the "centre-of-mass" of the line profile. This method benefits from not requiring an assumption about the shape of the line. The "intensity-weighted mean wavelength" can be calculated by:

$$\bar{\lambda} = \frac{\sum_{i=1}^n I_i \lambda_i}{\sum_{i=1}^n I_i}, \quad (3.3)$$

where  $n$  denotes the total number of bins included. For each spectral line, a calculation of  $\bar{\lambda}$  is first performed for the preflare arrays, returning  $\bar{\lambda}_{pf}$ . The summation is done over a total of 7 points, symmetric about the bin containing the theoretical rest wavelength. This process is visualised in Figure 3.4. The wavelength bins that contain a larger irradiance measurement contribute more to the weighted sum, influencing the mean towards the more intense regions of the line profile. The preflare-subtracted profiles may contain a negative irradiance in a given bin during

the decay phase of a flare, in which case the bin is excluded from the calculation.

Once the mean wavelengths are obtained for the preflare, the calculation is then done again for each line at each subsequent time in the flare. The mean wavelengths are calculated for both the Sun as a star profiles and those in flare-excess. With  $\bar{\lambda}_f$  now evaluated, the  $\bar{\lambda}_{pf}$  values can be subtracted and the Doppler shift can again be calculated. This gives us a third, independent route for evaluating the plasma velocities.

### 3.2.4 Error Estimation

#### 3.2.4.1 Error Analysis Using EVE "Precision" Data

The EVE data structures contain a "precision" array, containing uncertainties for each wavelength bin at each observation time. These precision errors attempt to quantify the noise in a given wavelength bin, by taking into account the overall count rate after each 10 s integration and the summation of the 2D image of the spectrum across its height (D. Woodraska, R. Milligan, private communication). The EVE documentation states that a precision value of 0 implies a perfect measurement, and a value of 1 means that the signal equals the noise.<sup>4</sup> Values greater than 1 indicate a noise-dominated bin. Throughout the Lyman series, these precision values are generally between 0 and 1. It also indicates that multiplication of the irradiance by the corresponding precision values results in the irradiance error for any given wavelength bin at any given time, which can be propagated through the calculations described in §3.2.1 - §3.2.3.

However, the observed irradiance variations in a given bin over a span of time are generally much smaller than those expected from the EVE "precision" values. Figure 3.5 shows each of the Lyman lines close to the peak of the 07th March 2012 flare with two series of error bars: those averaged from the "precision" values quoted in the EVE data, and those given by the standard deviation of the irradiance values in a given bin throughout the course of a flare (this encompasses both noise and flare-

---

<sup>4</sup>[http://lasp.colorado.edu/eve/data\\_access/evewebdata/products/level2/EVE\\_L2\\_V6\\_README.pdf](http://lasp.colorado.edu/eve/data_access/evewebdata/products/level2/EVE_L2_V6_README.pdf)

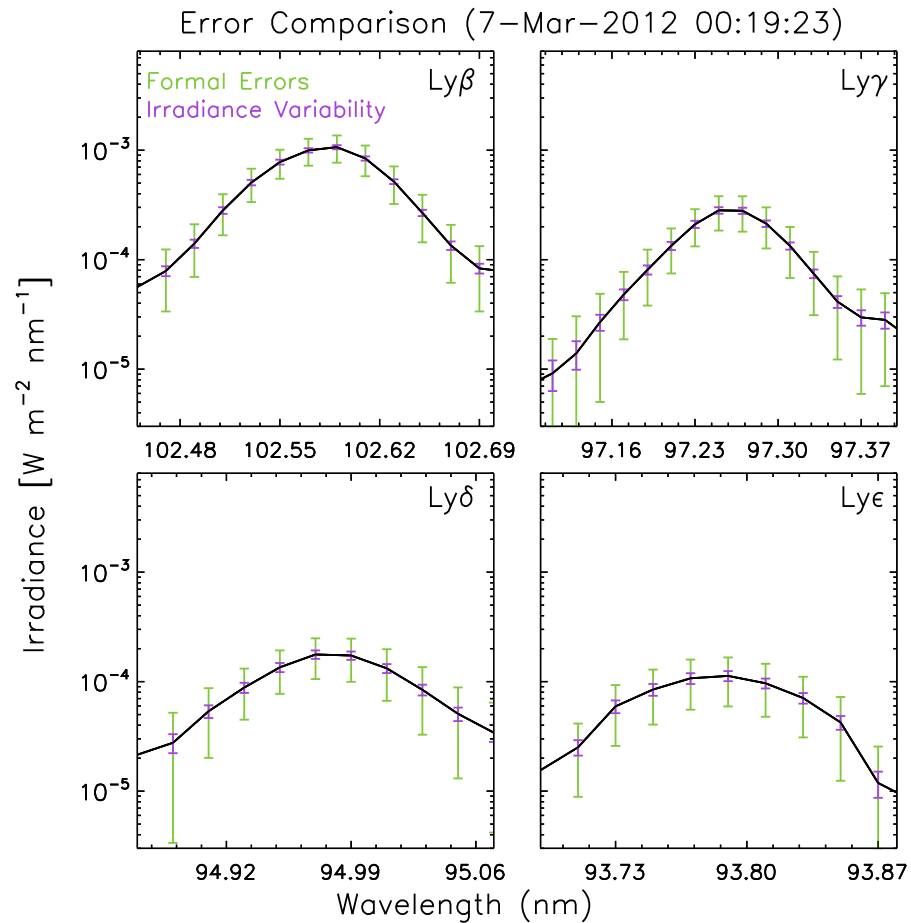


**Figure 3.5:** Lyman line profiles (with no preflare-subtraction) close to the peak of the 07th March 2012 flare. Overplotted are the errors given by the EVE “precision” data (in green), and the standard deviation of the irradiance values for each bin over the entire duration of the flare (in purple). The former clearly overestimate the actual observed variations in the line irradiance.

related variation). It is clear that the quoted irradiance errors overestimate the actual variation seen in any of the Lyman lines. Using these as the basis for further error propagation leads to unrealistically large values for errors in the centroid variations and subsequent velocity shifts.

Using the errors given by the EVE “precision” values results in several problems for calculating the associated errors on the line centroid positions and velocities. When subtracting the preflare to obtain the flare excess profiles, the relative error

on the irradiance values becomes severe as the errors combine from the preflare timerange and the current timestep, while the excess irradiance diminishes as the flare signal is isolated. When these errors are input to the Gaussian fitting process, they affect the calculation of the line centroid and result in relatively large errors in the Doppler velocity of around  $20 \text{ km s}^{-1}$ .

Propagating irradiance errors through the cross correlation method is also not straightforward. Because it is not trivial to propagate the irradiance errors into an error on the lag values used to perform the cross correlation, an alternative approach must be taken to account for variations in the irradiance. We can obtain a spread in the lag value where the CCF peaks via a process similar to that of [Peterson et al. \(1998\)](#). This is done using a Monte-Carlo approach, generating a large number of synthetic profiles, each based on the original profile but with the irradiance in each bin altered by a random deviate derived from the irradiance error.

Cross correlating a large number of these synthetic profiles across the preflare profile allows for a distribution of peak lag values to be found, which can be translated into an error estimate on the line centroid. However, this approach cannot be taken for the line profiles if the EVE “precision” values are used, as the errors can seed irradiance deviates so large that when added to the initial profile result in the general shape of the profile being destroyed. This means that the CCF may peak at any of the wavelength bins, as it is computed between the preflare profile and what is now essentially noise.

#### 3.2.4.2 An Empirical Approach

In reality, the noise on a single EVE measurement is a combination of instrumental effects, photon counting and intrinsic solar variability. We want to understand how the derived velocities vary as a result of all of these. To do this, we will use an overall measure of the error based on the observed fluctuations. We selected a MEGS-B spectrum file obtained on the 25th February 2011. The hour spanned in this observation (19:00 - 20:00) did not contain any flare-related activity, and there were no sunspots visible on the disk. The selection of this particular observation ensures that any measurements characterise the quiet Sun, and not any flaring phenomena.

The spectrum is time-averaged over the first 20 minutes, and the methods in §3.2.1 - §3.2.3 are used to calculate the average line centroids in several lines over this time period. These initial measurements provide the baseline rest wavelengths for each line profile. For the remaining 40 minutes, the line centroids are calculated at each time using all methods, and the Doppler shifts are calculated with respect to the rest wavelengths. This provides us with a time-resolved array of Doppler velocities for any given line profile for a particular method. Taking the standard deviation of this array provides us with an empirical velocity error for a given line and method, and represents how the intrinsic variability of the data results in a spread in velocity values.

By definition, there is no preflare for such an observation of the quiet Sun, and so we assume that these errors apply both to velocities obtained with and without preflare subtraction. These may be a naive choice for the errors in flare-excess velocities, but it is likely that these better represent the variability in velocity as opposed to the EVE precision-based errors.

## 3.3 Flows Observed with the EVE Instrument

### 3.3.1 The 15th February 2011 Flare - Predominant Redshifts

The 15th February 2011 flare (SOL2011-02-15) was one of the first significant eruptions of solar cycle 24, peaking with a GOES classification of X2.2. It occurred in active region (AR) 11158, located in the southern hemisphere (S20, W10), following several days of small B and C class flares. We find clear redshifted signatures in all lines in this flare, indicating downflows of between 30 – 50 km s<sup>-1</sup>.

The lightcurve for this flare in the core of the Ly- $\beta$  line is shown in Figure 3.6, which shows that the Ly- $\beta$  emission rises for 5 minutes, until peaking at ~01:56, after which it decays much more gradually over the following hour. The initial 35 minutes are chosen to define the preflare, as the lightcurve remains generally flat over this period.

Using the defined time range for the preflare, the rest wavelengths were calculated

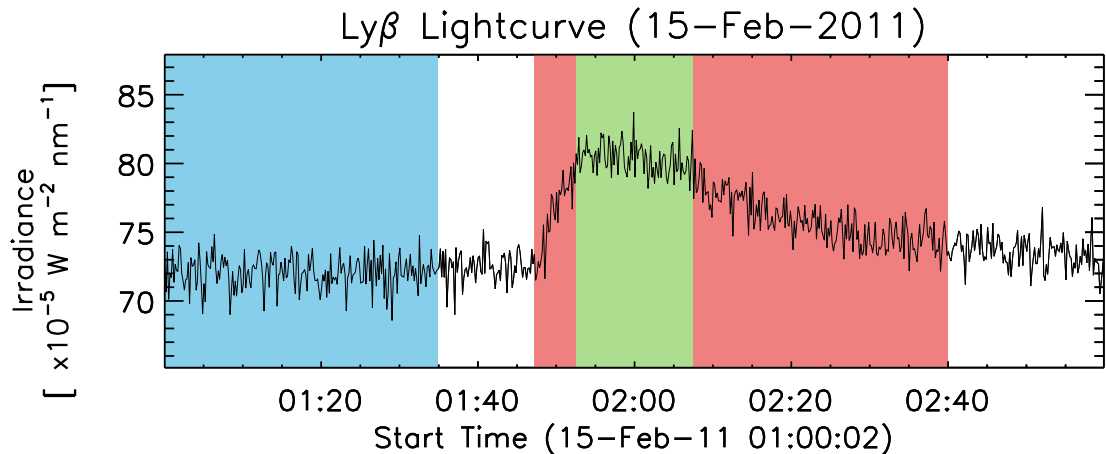


**Figure 3.6:** Lightcurve of the core of the  $\text{Ly-}\beta$  line during the 15th February 2011 X2.2 flare. The time range highlighted in blue is designated as the preflare, and that in red encompasses the duration of the flare. The subrange highlighted in green represents the time where the lightcurve is mainly  $2\sigma$  above its average value throughout the whole time interval.

for the Gaussian and intensity-weighted methods. The preflare was also subtracted from the full flaring spectrum to isolate the flare-excess. Using both the Sun-as-a-star and the preflare-subtracted spectra, two sets of velocity results were obtained using the aforementioned methods.

Velocities derived from the non-subtracted spectra are shown in Figure 3.7. Also overplotted are the velocity profiles smoothed with a boxcar of 9 data points, which are shown to aid visibility of flows. Immediately noticeable is a well-defined downflow in the  $\text{C III}$  line, which increases in magnitude over several minutes before peaking at around 01:56 with a velocity of  $\sim 30 \text{ km s}^{-1}$ . The downflow signature then slowly diminishes, eventually disappearing at 02:25. This feature is apparent in the results across each of the three methods.

To a lesser extent, the Lyman lines are also redshifted. Downflows initiate in all of the Lyman lines at 01:45, and also reach their maximum speed at 01:56. There appears to be an ordering in the series with respect to the maximum speed, as the  $\text{Ly-}\beta$  line does not exhibit a flow faster than  $5 \text{ km s}^{-1}$  while the higher order lines reach successively higher speeds.  $\text{Ly-}\gamma$  and  $\text{Ly-}\delta$  reach slightly higher speeds of  $\sim 6-7$

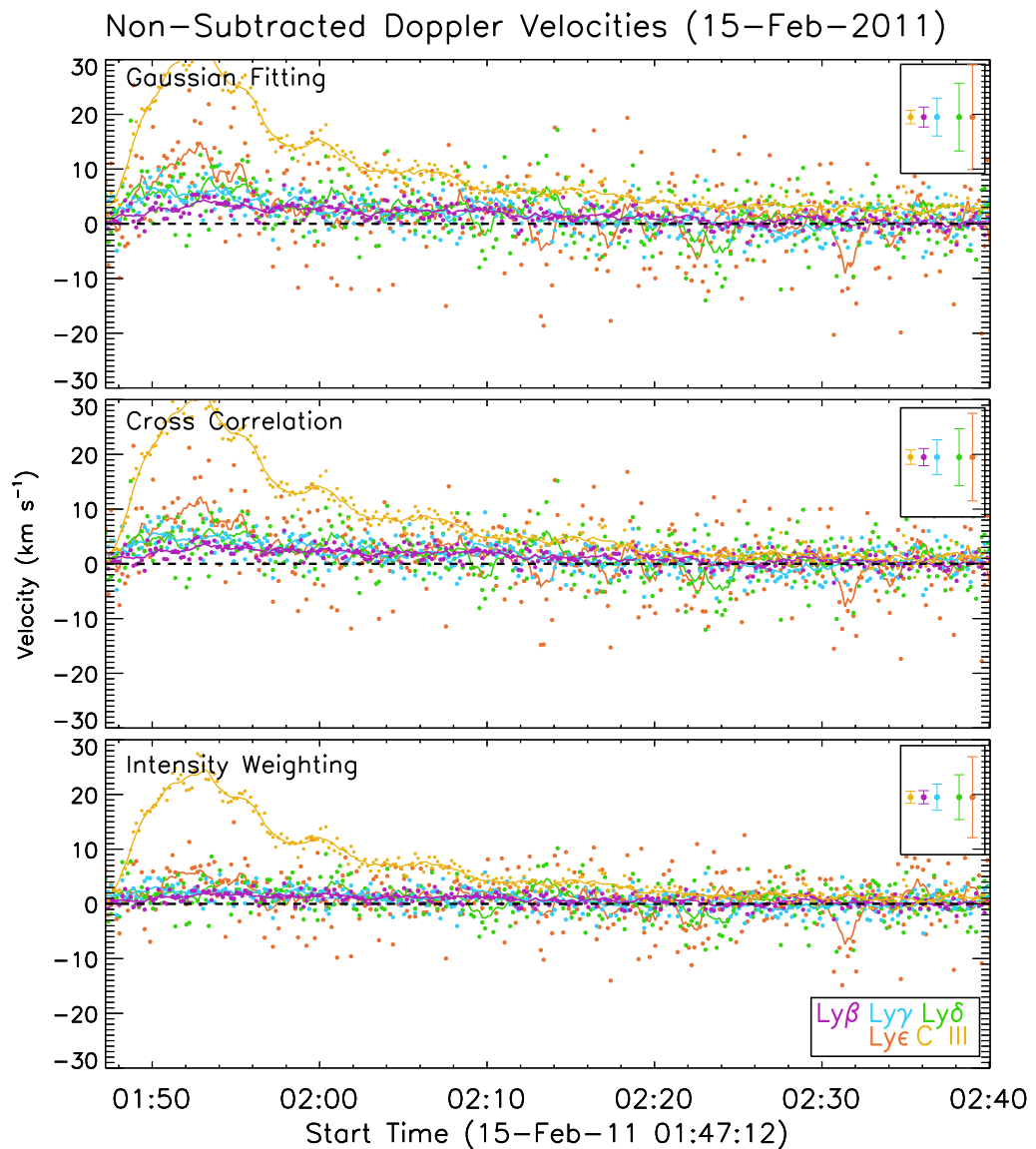


**Figure 3.7:** Doppler velocities obtained for each of the Lyman lines and the C III line for non-subtracted Sun-as-a-star spectra during the 15th February 2011 flare. Velocities are shown for each of the methods used, with positive values indicating downflows. Velocities are smoothed (solid lines) with a boxcar of 9 to help identify systematic patterns. The representative size of the velocity errors are plotted in the upper right, and are obtained empirically as described in §3.2.4.2.

$\text{km s}^{-1}$ , while the highest order line,  $\text{Ly}\epsilon$  plateaus at  $10 - 12 \text{ km s}^{-1}$ . However, this may not be a genuine property of the velocities, as the higher order lines also have

larger errors.

Despite the lightcurve remaining enhanced until around 02:40, all signatures of downflowing material cease around 20 minutes before this time. It is also apparent that the intensity-weighted method finds lower flows in the Lyman lines, while the Gaussian and CCF methods are consistent to a greater degree. This can be seen clearly in the velocity results in the C III line, where the intensity-weighted method does find a downflow, but with a slightly weaker peak velocity of  $25 \text{ km s}^{-1}$  as opposed to  $30 \text{ km s}^{-1}$  in the other methods.

It is not immediately clear why the intensity-weighted method underestimates the flow speed with respect to the other two methods. It could be that the selection of wavelength bins symmetric about the theoretical rest wavelength results in an inherent biasing of the mean wavelength towards the rest wavelength, but it may also be that the processes of Gaussian fitting and cross-correlation simply allow for a greater accuracy in determining the centroid positions as they both involve fitting the data.

While it is clear from Figure 3.7 that the Lyman and C III lines appear to be redshifted during this flare, there remains the issue of the velocity signals being diminished by the contributions from the rest of the disk. In order to account for this, and to provide further evidence that the flows observed in Figure 3.7 are genuine, we consider the velocities obtained after the flare spectra undergo preflare-subtraction. However, It should be noted that this does not necessarily isolate individual flows, and that there is still likely an integration over potentially numerous flows of differing speeds and direction. This is explored further in §3.4 -3.5.

The flare-excess velocities for this flare are plotted in Figure 3.8, and the challenges that accompany use of the preflare-subtracted spectra immediately become apparent. All Lyman lines now have an increased amount of noise in their velocity profiles, although the C III line does retain excellent stability. Also apparent is that initially, and towards late times, the velocity profiles “fan-out” and essentially become noise-dominated. These noise-dominated regions occur when the flare-excess profiles return towards (or have not appreciably surpassed) their preflare levels, resulting in a very low SNR when the preflare is subtracted. This makes it challenging

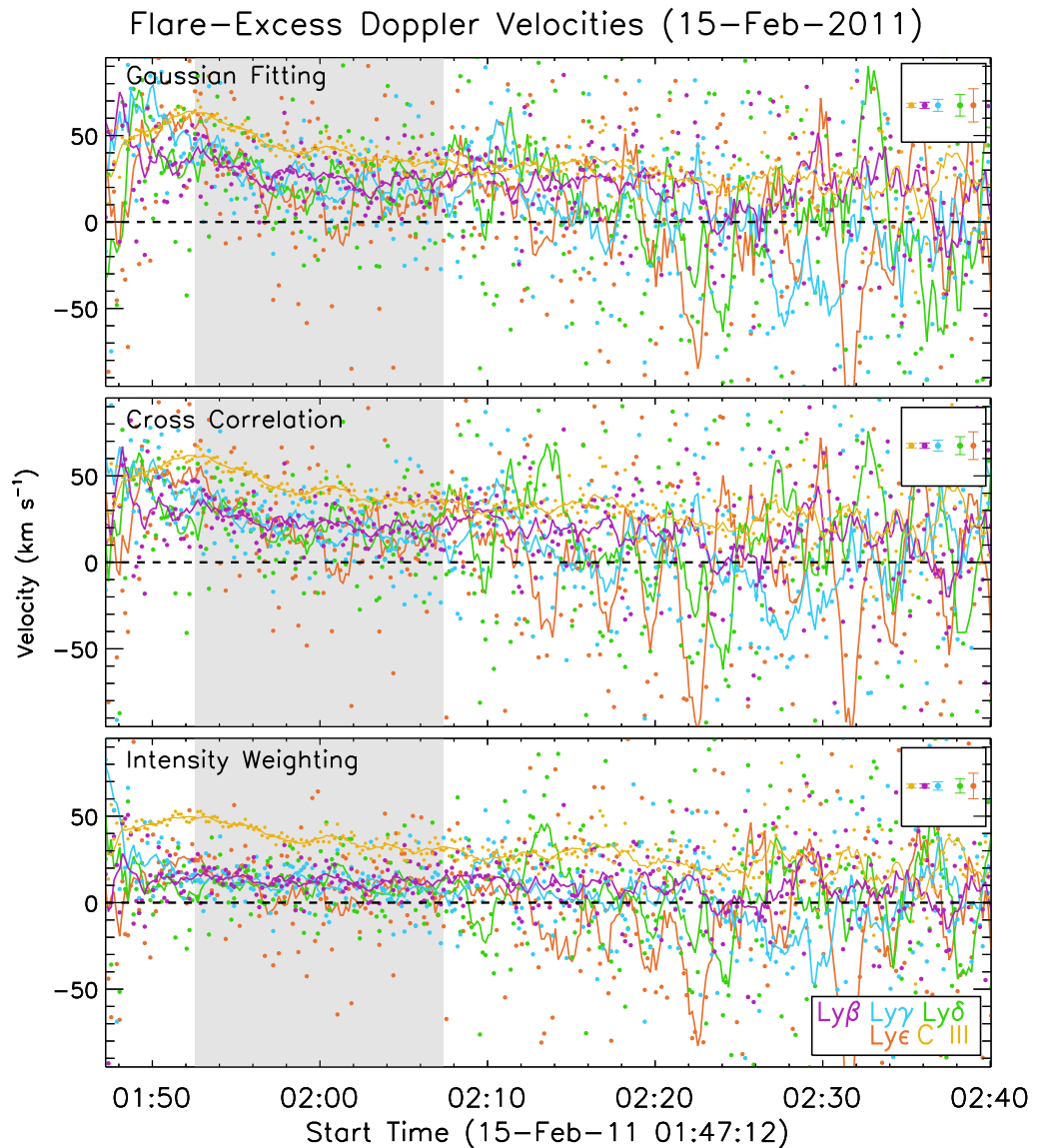


**Figure 3.8:** Doppler velocities as in Figure 3.7, using preflare-subtracted spectra. As in Figure 3.7, the velocities are smoothed to accentuate the patterns, and positive values correspond to downflows. The region highlighted in grey corresponds to when the  $\text{Ly}\beta$  lightcurve is predominantly  $2\sigma$  above its average value.

for any of the methods to reliably determine a Doppler shift.

However, it is still possible to discern the presence of downflows around the peak of the flare ( $\sim 01:56$ ). We focus on the time-range bounded by the first and final instances of the  $\text{Ly}\beta$  lightcurve being  $2\sigma$  above its preflare value, which ensures that

the flare-excess signal is strong. Between 01:52 - 02:00, the variability in the velocity profiles is less severe, and the downflows become apparent. The sustained downflow in C III is again observed, but with a higher maximum velocity of around  $50 \text{ km s}^{-1}$  as a result of isolating the flare emission. The Gaussian and CCF methods find the Lyman lines to exhibit a relatively uniform downflow signature, with velocities tightly-clustered around  $30 \text{ km s}^{-1}$ . The ordering of the speeds that was found in the non-subtracted velocity results is not found here. Again, the intensity-weighted method somewhat underestimates the speeds obtained with the other two methods. The intensity-weighted method suggests downflow speeds of  $10 - 20 \text{ km s}^{-1}$  for the Lyman lines.

Beyond 02:00, the velocity profiles for Ly- $\beta$ , Ly- $\gamma$  and C III all point to a slow diminishing of the flow speed, with the velocities from the higher order Lyman lines beginning to suffer from increased noise. After 02:10, it becomes increasingly difficult to establish systematic trends in the velocity profiles in any of the lines beyond Ly- $\beta$  and C III. From Figures 3.7 and 3.8, there are clear signatures of downflowing plasma in the Lyman lines and C III, with the flare-excess velocities suggesting maximum speeds of around  $30 \text{ km s}^{-1}$  for the Lyman lines and  $50 \text{ km s}^{-1}$  for C III.

### 3.3.2 The 07th March 2011 Flare - Predominant Blueshifts

Located close to the western limb (N30, W48), AR 11164 emitted an M3.7 class flare on the 07th March 2011 (SOL2011-03-07). Strongly blueshifted profiles are observed in each of the lines during this flare, indicating upflows of between  $50 - 100 \text{ km s}^{-1}$ . This event ejected a considerable amount of plasma from the Sun's surface, which is discussed further in §3.4.

The Ly- $\beta$  lightcurve for the event is shown in Figure 3.9, indicating the onset of the flare at 19:45, with the peak at around 20:00. The Ly- $\beta$  enhancement then gradually diminishes over the following hour. The first 25 minutes of spectra are used to establish the preflare, and the Sun-as-a-star and flare-excess velocities are calculated as before.

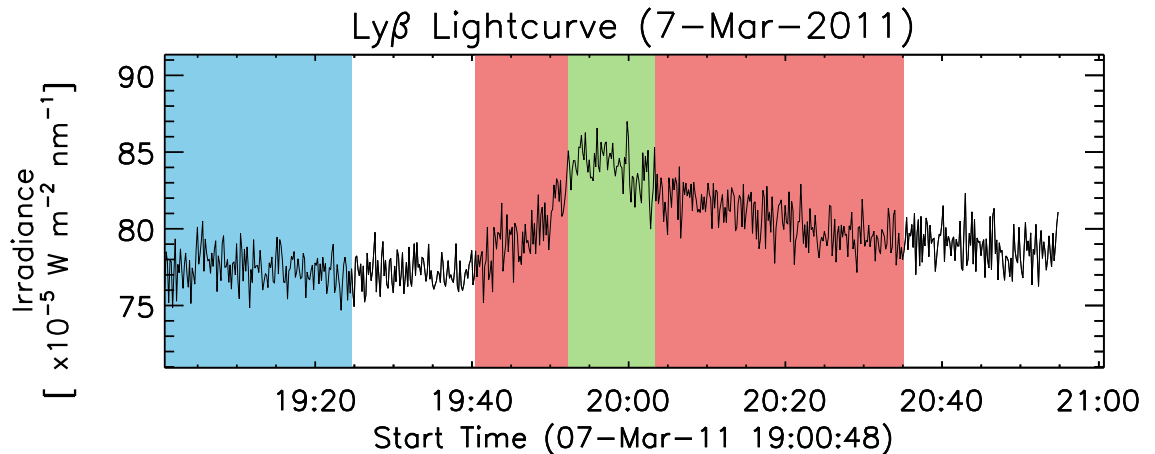


**Figure 3.9:** Lightcurve of the core of the Ly- $\beta$  line during the 07th March 2011 M3.7 flare. As before, the region shaded in blue indicates the preflare, with the flare highlighted in red. Again, the region shaded in green is bounded by the first and last instances of the Ly- $\beta$  irradiance being  $2\sigma$  above its average value throughout the whole time interval. There is an absence of MEGS-B spectral data from 20:55 in this observation.

The velocities obtained from the non-subtracted Sun-as-a-star spectra are shown in Figure 3.10. Across all methods, the flow speeds peak at 19:56. As with SOL2011-02-15, the flow signature of C III is the clearest. From 19:46 - 19:56, the velocity profiles for C III show a steady rise in the flow speed, from rest to around  $10 \text{ km s}^{-1}$ . The scatter in the C III data is also very small. However, in contrast to SOL2011-02-15, the Doppler velocities are negative, signifying blueshifts in the line profile and upflows in the flaring plasma. Observable upflows in C III cease between 20:05 - 20:10

The Lyman lines also display a net blueshifted signal in the Sun-as-a-star data. The velocity data-points for Ly- $\beta$ , with the smallest amount of scatter, show an upflow of  $4 - 5 \text{ km s}^{-1}$  peaking at 19:53, slightly earlier than the C III line. As before, the velocities derived from intensity-weighting find weaker flows of around  $3 \text{ km s}^{-1}$ . The velocity profile of Ly- $\gamma$  is very similar to that of Ly- $\beta$ , but with a slightly higher peak velocity of  $5 - 7 \text{ km s}^{-1}$ . The flow signature of Ly- $\delta$  is slightly noisier,

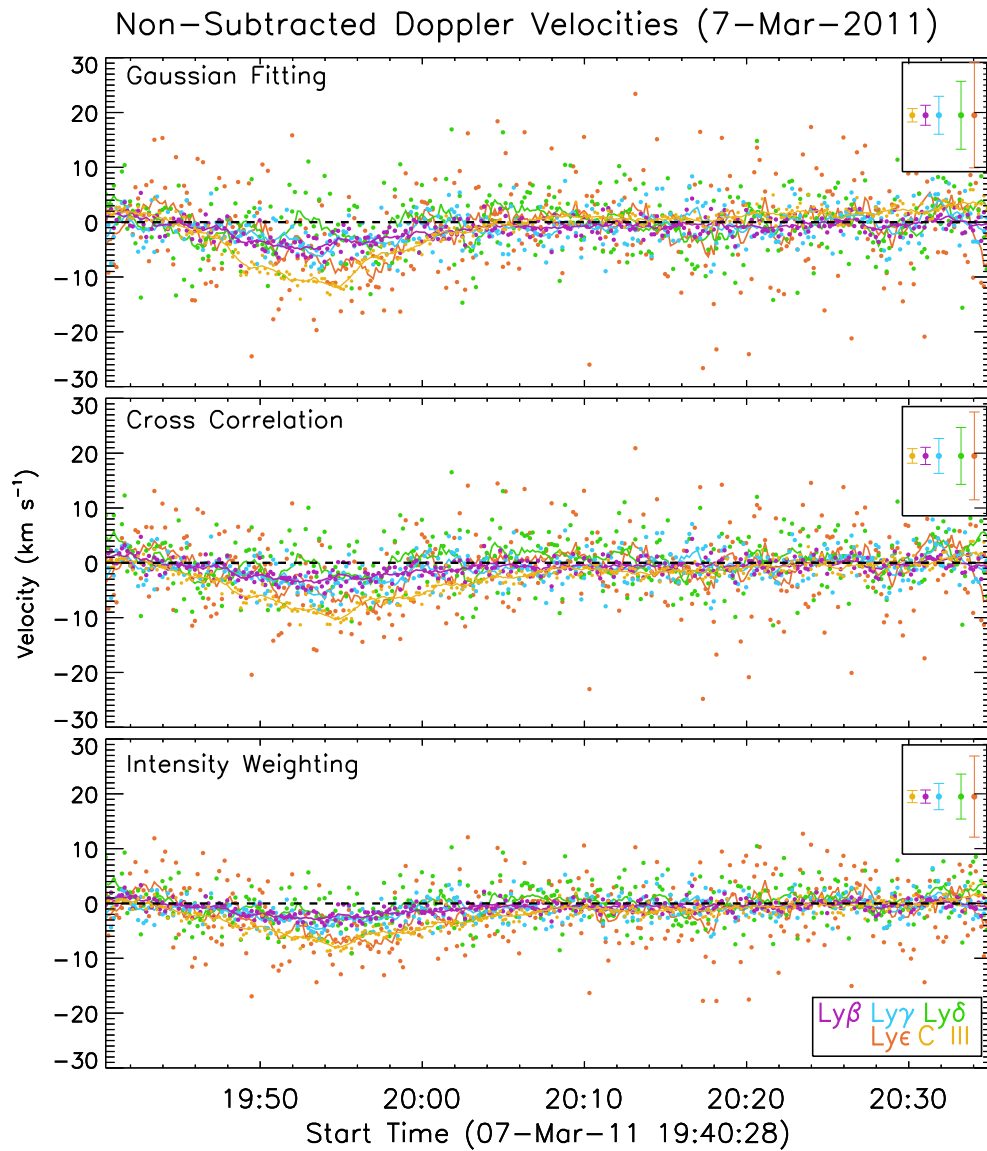


**Figure 3.10:** Doppler velocities obtained for each of the Lyman lines and the C III line for non-subtracted Sun-as-a-star spectra during the 07th March 2011 flare. As before, smoothed and unsmoothed velocities are plotted for each of the methods. Negative velocities correspond to upflows. As before, the representative errors are those discussed in §3.2.4.2.

particularly in the Gaussian and cross-correlation methods, but matches that of  $\text{Ly}\beta$  and  $\text{Ly}\gamma$  in the intensity-weighted velocities.  $\text{Ly}\epsilon$  has the highest flow speed of the Lyman lines, reaching  $7 - 9 \text{ km s}^{-1}$ , and peaks in synchronisation with the C III line.

As before, there is an ordering in the derived flow velocities with respect to the order of the Lyman lines, with the lowest order line (Ly- $\beta$ ) displaying the weakest flow, with the higher order lines peaking at increasingly fast speeds. All of the spectral lines exhibit an upflowing signature, but in order to obtain a more accurate estimate of their speeds the flare-excess velocities are required.

The flare-excess velocities for this flare are displayed in Figure 3.11. Again, the variability in the velocity profiles is severe for much of the flare due to subtraction of the preflare, but is reduced while the Ly- $\beta$  lightcurve is enhanced by  $2\sigma$  above its mean (highlighted in grey). During this relatively short period of time, only Ly- $\delta$  and Ly- $\epsilon$  appear to suffer from a significant amount of noise.

The C III line again retains excellent stability during both the time highlighted in grey, and outwith this time. The peak flare-excess velocity of C III has a rather large variation in magnitude with the method used, but ranges between  $25 - 50 \text{ km s}^{-1}$ , with the intensity-weighted method again returning the weakest flow speeds. The cross-correlation and intensity-weighted methods give a peak time of 19:56, but the Gaussian method finds the flow to peak earlier, at 19:50.

Ly- $\beta$  and Ly- $\gamma$  exhibit similar upflow signatures between 19:52 – 20:00, with a flow speed that decreases with time from the initial peak close to 19:50. As with the C III line, there is a significant variation in the derived peak velocity with the method used. The Gaussian fitting method returns surprisingly fast velocities in excess of  $100 \text{ km s}^{-1}$  for Ly- $\beta$  and  $70 \text{ km s}^{-1}$  for Ly- $\gamma$ , but it is challenging to see a consistent signature in the Ly- $\delta$  line. Ly- $\epsilon$  displays more variation, but appears to have a peak velocity of  $70 - 80 \text{ km s}^{-1}$ .

Both Ly- $\beta$  and Ly- $\gamma$  peak between  $70 - 100 \text{ km s}^{-1}$  when examined using cross-correlation, with Ly- $\delta$  again failing to produce a clear signal. Ly- $\epsilon$  again has a peak flow speed of around  $70 \text{ km s}^{-1}$  after cross-correlation. The velocity profiles obtained from the intensity-weighted method remain the most tightly-constrained. The intensity-weighted velocity profiles show the least amount of scatter, and give peak velocities of  $40 - 50 \text{ km s}^{-1}$  for Ly- $\beta$  and Ly- $\gamma$ ,  $20 - 30 \text{ km s}^{-1}$  for Ly- $\delta$ , and around  $50 \text{ km s}^{-1}$  for Ly- $\epsilon$ .

The upflow signatures in SOL2011-03-07 are interesting for several reasons: the

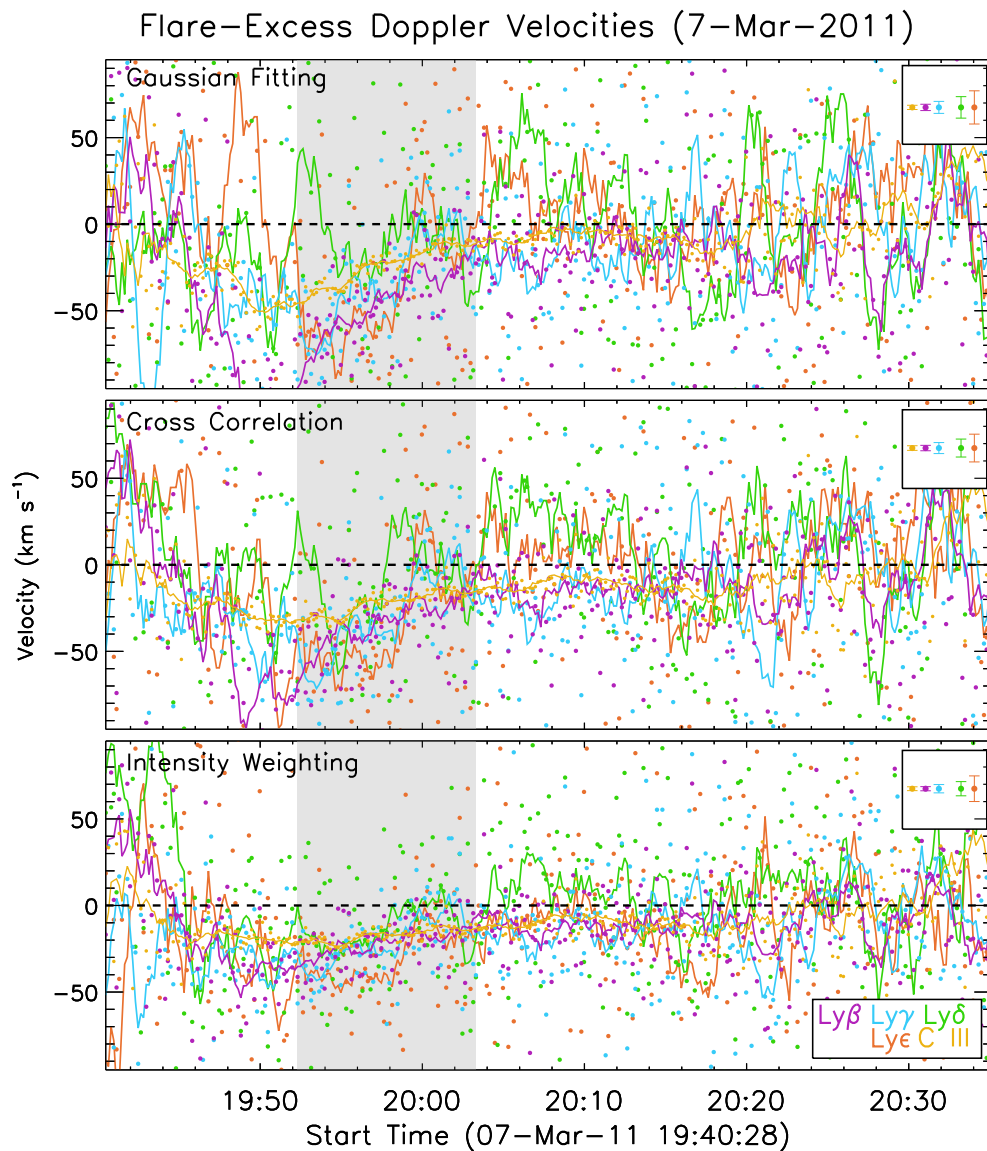


**Figure 3.11:** Doppler velocities as in Figure 3.10, but measured after preflare-subtraction in the line profiles. All other aspects retain their previous meanings, and the duration of the  $2\sigma$  enhancement in the  $\text{Ly}\beta$  lightcurve is again highlighted in grey.

first being that the initial assumption was that downflows were to be expected in the cool, chromospheric Lyman lines. The second is that the noise in the velocity profiles after preflare-subtraction is noticeably worse during this flare compared to SOL2011-02-15, which may be due to the relatively moderate strength of the flare

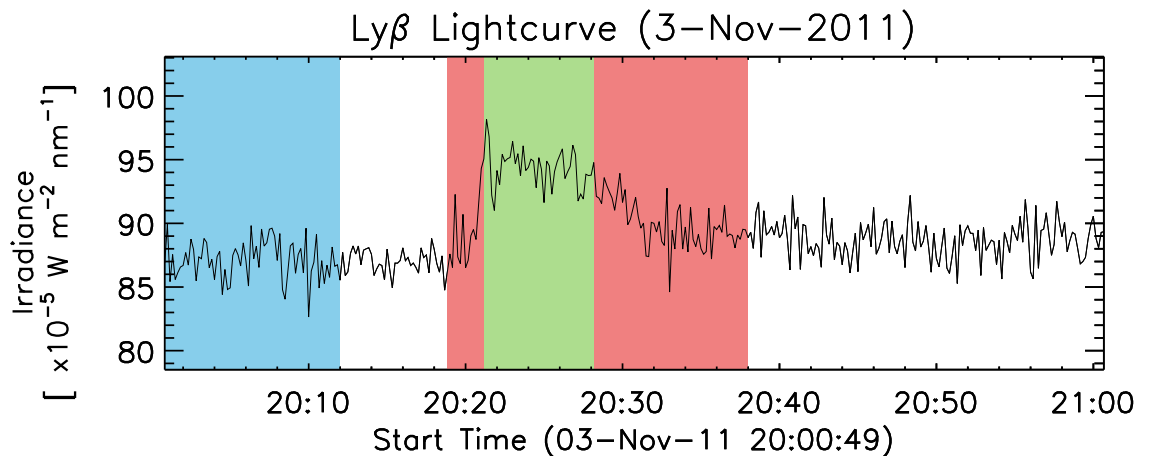


**Figure 3.12:** Lightcurve of the core of the Ly- $\beta$  line during the 03rd November 2011 X1.9 flare, where the highlighted regions retain their previous meanings.

(M3.7). The third is that, for at least two of the methods, the derived velocities are particularly fast. Ly- $\beta$  retains a relatively stable velocity profile between 19:50–20:00, but achieves peak velocities between 100–150 km s<sup>-1</sup>. It may be that the upflows are caused by a case of gentle evaporation, but then this would predict relatively slow upflows, not those observed. AIA observations of this event are used to aid further interpretation of this event, discussed in §3.4.

### 3.3.3 The 03rd November 2011 Flare - Predominant Blueshifts

The X1.9 flare observed on the 03rd November 2011 (SOL2011-11-03) was emitted from AR 11339, located close to the eastern limb (N22, E63). Despite being a particularly strong flare, it was a confined event and did not result in any major eruptions (Liu et al. 2014). Blueshifts are again observed throughout the duration of this flare, suggesting upflow speeds between 20 – 60 km s<sup>-1</sup>.

The lightcurve for the flare (Figure 3.12) shows a rise in the Ly- $\beta$  irradiance from 20:18, peaking at 20:21 and decaying over the following 10 – 15 minutes. The initial 12 minutes are used to establish the preflare, from which the flare-excess spectra are obtained.

As with the previous flares, Doppler velocities for SOL2011-11-03 are plotted in Figure 3.13 for spectra that have not undergone preflare subtraction. An upflow is readily noticeable in C III, peaking at 20:22 with a velocity around  $25 \text{ km s}^{-1}$  in the Gaussian and cross-correlation methods, and  $15 \text{ km s}^{-1}$  using the intensity-weighted method. The C III velocity slows slightly after 20:22, briefly exhibiting a smaller peak at 20:25, before decaying steadily and returning to rest at 20:32.

While of a weaker extent, slight upflows in the Lyman lines are visible concurrent with the peak in the C III flow. As with the Sun-as-a-star velocity profiles for previous flares, the Ly- $\epsilon$  line has the fastest flow speed, peaking at  $10 \text{ km s}^{-1}$  in all three methods. Ly- $\delta$  attains a peak upflow speed of  $5 - 6 \text{ km s}^{-1}$  at 20:22, with Ly- $\beta$  and Ly- $\gamma$  peaking at  $3 - 4 \text{ km s}^{-1}$ . While the overall upflow signal in the lower-order Lyman lines is rather weak, it is bolstered by the presence of more prominent upflow signatures in Ly- $\epsilon$  and C III.

As with the previous flares, the Doppler velocities for the preflare-subtracted line profiles are calculated, and are shown in Figure 3.14.

The C III velocity profiles in 3.14 generally have little scatter before 20:30. Throughout the duration of the peak of the Ly- $\beta$  lightcurve (in grey), the C III line appears to exhibit an upflow of a slight oscillatory nature. The Gaussian and cross-correlation methods find the C III upflows to vary semi-periodically about  $35 - 45 \text{ km s}^{-1}$ . The intensity-weighted method again arrives at a slightly lower flow speed, closer to  $25 \text{ km s}^{-1}$ .

As the flare-excess signal becomes significant (20:21), the Ly- $\beta$  line reveals upflows of between  $50 - 60 \text{ km s}^{-1}$  (around  $35 \text{ km s}^{-1}$  after intensity-weighting). Two minutes later, the flow speed drops somewhat before plateauing at  $\sim 20 - 30 \text{ km s}^{-1}$ . The upflows in Ly- $\gamma$  contain more scatter, but tend to suggest a gradual increase in flow speed from around  $25 \text{ km s}^{-1}$  at 20:21 to  $45 \text{ km s}^{-1}$  at 20:26. Both Ly- $\delta$  and Ly- $\epsilon$  show a greater amount of scatter (although this is not as severe in the intensity-weighted method), but tend to average out at around  $30 \text{ km s}^{-1}$ . Beyond 20:30, the flare-excess signals in the Lyman lines begin to degrade, after which it becomes difficult to discern any further flow signatures.

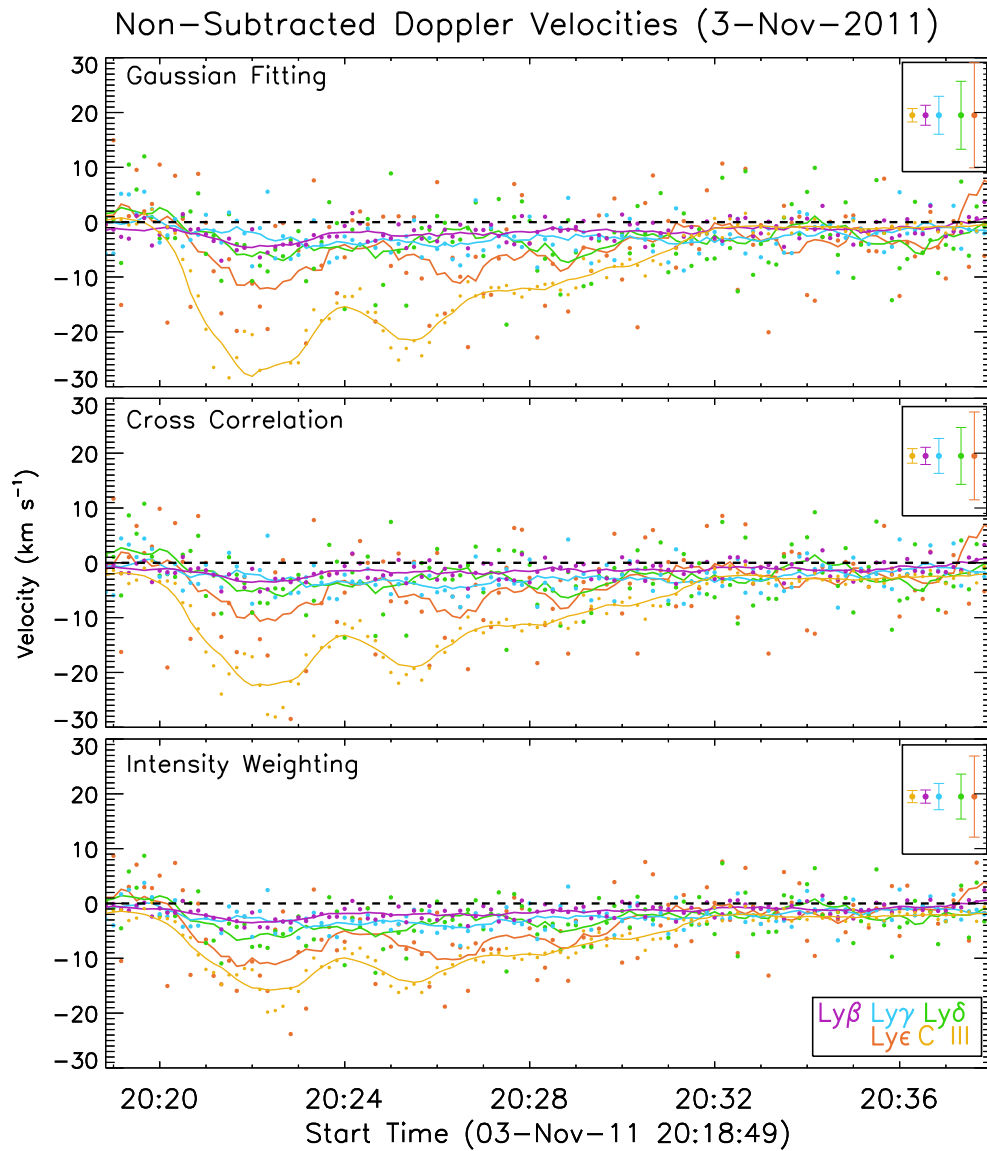


**Figure 3.13:** Doppler velocities obtained for each of the Lyman lines and the C III line for non-subtracted Sun-as-a-star spectra during the 03rd November 2011 flare. All aspects and conventions retain their previous definitions.

### 3.3.4 The 07th March 2012 Flares - Predominant Blueshifts

Originating from a particularly eruptive active region, AR 11429, the X5.4 flare emitted on the 07th March 2012 (SOL2012-03-07) constituted the most intense of several major eruptions from this region. Located at heliographic co-ordinates

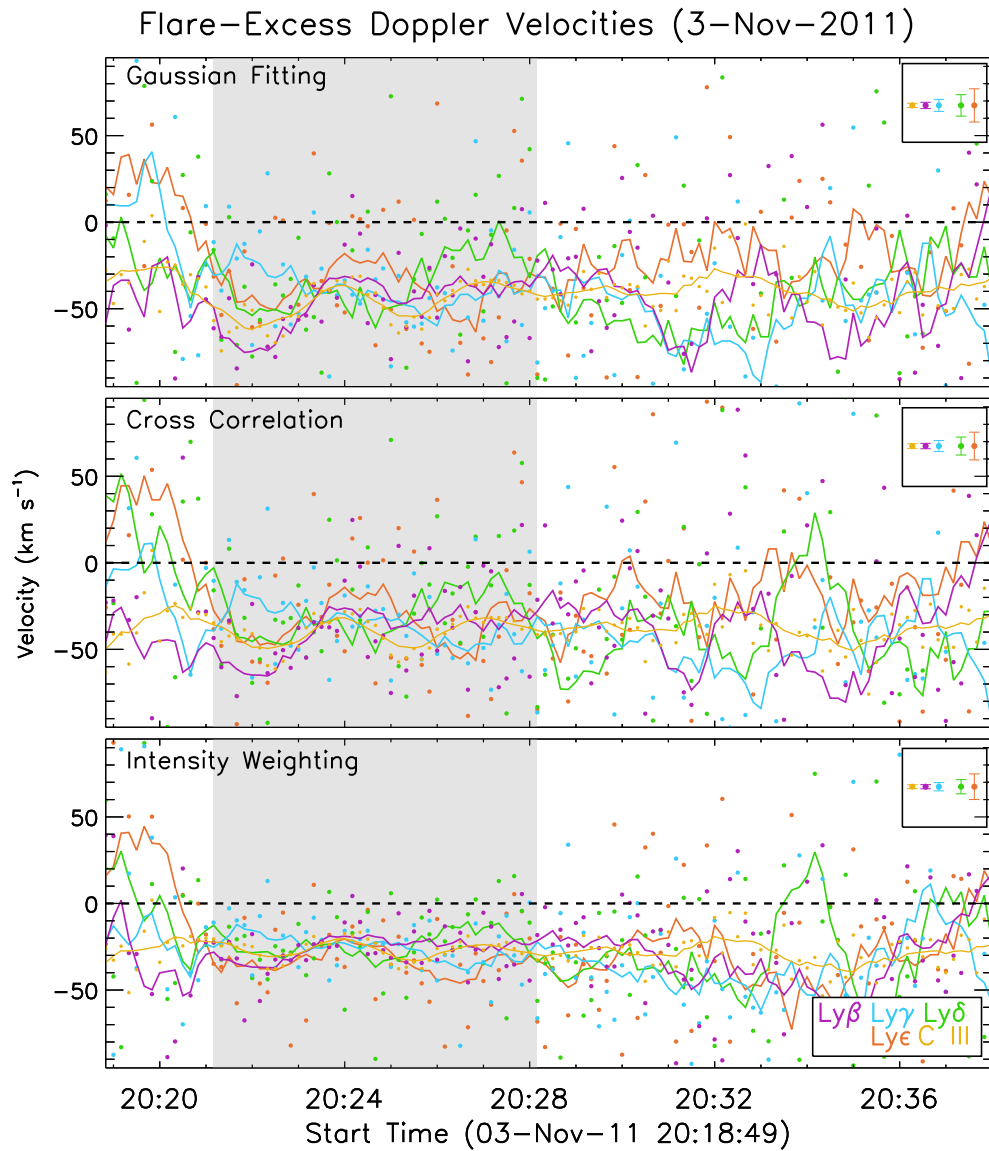


**Figure 3.14:** Doppler velocities as in Figure 3.13, but measured after preflare-subtraction in the line profiles. All other aspects retain their previous meanings, and the duration of the  $2\sigma$  enhancement in the Ly- $\beta$  lightcurve is again highlighted in grey.

(N18, E31), this event was responsible for the triggering of a fast CME. This flare was followed by an additional X1.3 event roughly an hour afterwards, which itself produced a secondary CME (Patsourakos et al. 2016).

The X5.4 event has been a focus of several other studies. Del Zanna & Woods

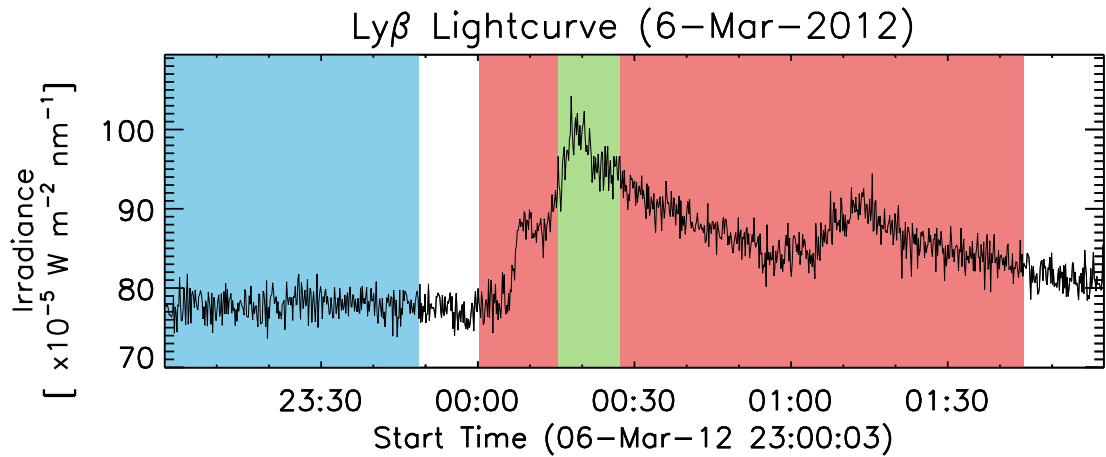


**Figure 3.15:** Lightcurve of the core of the Ly- $\beta$  line during the X5.4 and X1.3 07th March 2012 flares, where the highlighted regions retain their previous meanings.

(2013) found the spectral lines from EVE in this event to be useful for diagnostic purposes. At higher energies, the  $\gamma$ -ray flux during the event was studied by Ajello et al. (2014). The eruption and propagation of the two resulting CMEs was detailed by Patsourakos et al. (2016), while Dzifčáková et al. (2018) investigated departures from Maxwellian particle distributions during the event.

Very clear blueshifted signatures were observed in this flare, with all lines indicating upflows of between  $20 - 30 \text{ km s}^{-1}$ . The Ly- $\beta$  lightcurve during the two flares is shown in Figure 3.15. The time bounded between 23:00-23:48 is used to define the preflare, with the flaring time spanning between 00:00-01:45. The first flare peaks at around 00:20, with the following flare peaking close to 01:15. The velocity profiles for the two flares are not divided into separate events, as the lightcurve (Figure 3.15) does not return to preflare levels in the intermediate time.

Sun-as-a-star velocity profiles for the 07th March 2012 event are displayed in Figure 3.16. Owing to the intensity of the X5.4 flare, a ubiquitous upflow signature is observed in all lines despite the lack of preflare-subtraction. As before, the C III line exhibits the strongest signal in the Sun-as-a-star data, and suggests a long-lived upflow in the plasma. Peaking with a velocity of  $15 - 20 \text{ km s}^{-1}$  at 00:20, the flow speed gradually diminishes for 45 minutes until rest, before again transitioning into

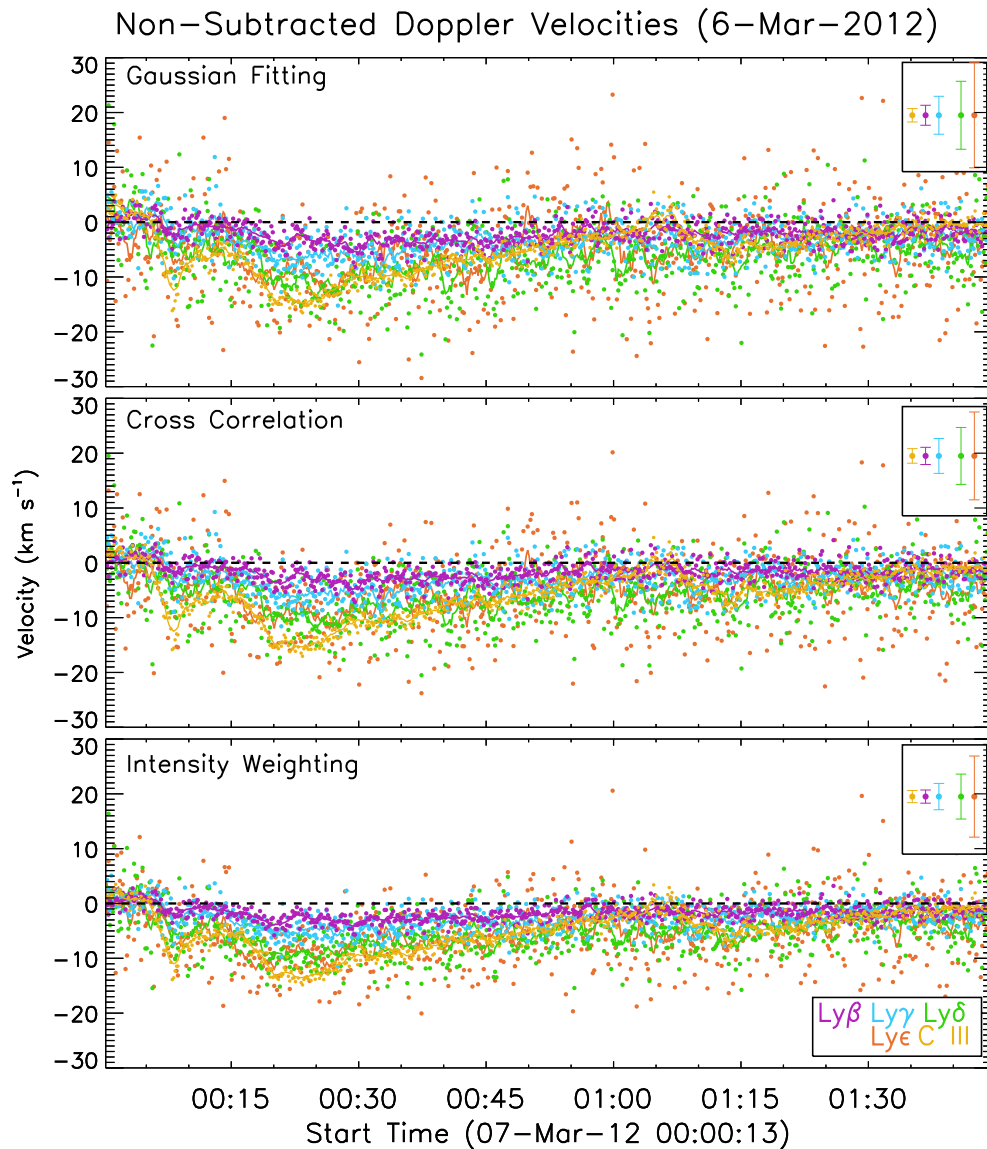


**Figure 3.16:** Doppler velocities obtained for each of the Lyman lines and the  $\text{C III}$  line for non-subtracted Sun-as-a-star spectra during the 07th March 2012 flares. All aspects and conventions retain their previous definitions.

upflow with the initiation of the X1.3 flare. The secondary peak in the  $\text{C III}$  velocity profile reaches a speed of  $10 \text{ km s}^{-1}$  at 01 : 15, after which the flow slowly dissipates.

While not as prominent as in  $\text{C III}$ , upflows are also observed in all of the Lyman lines. Again, the lower order lines reach smaller peak velocities than the higher order lines.  $\text{Ly}-\beta$  has a similar temporal profile to  $\text{C III}$ , with an upflow increasing in

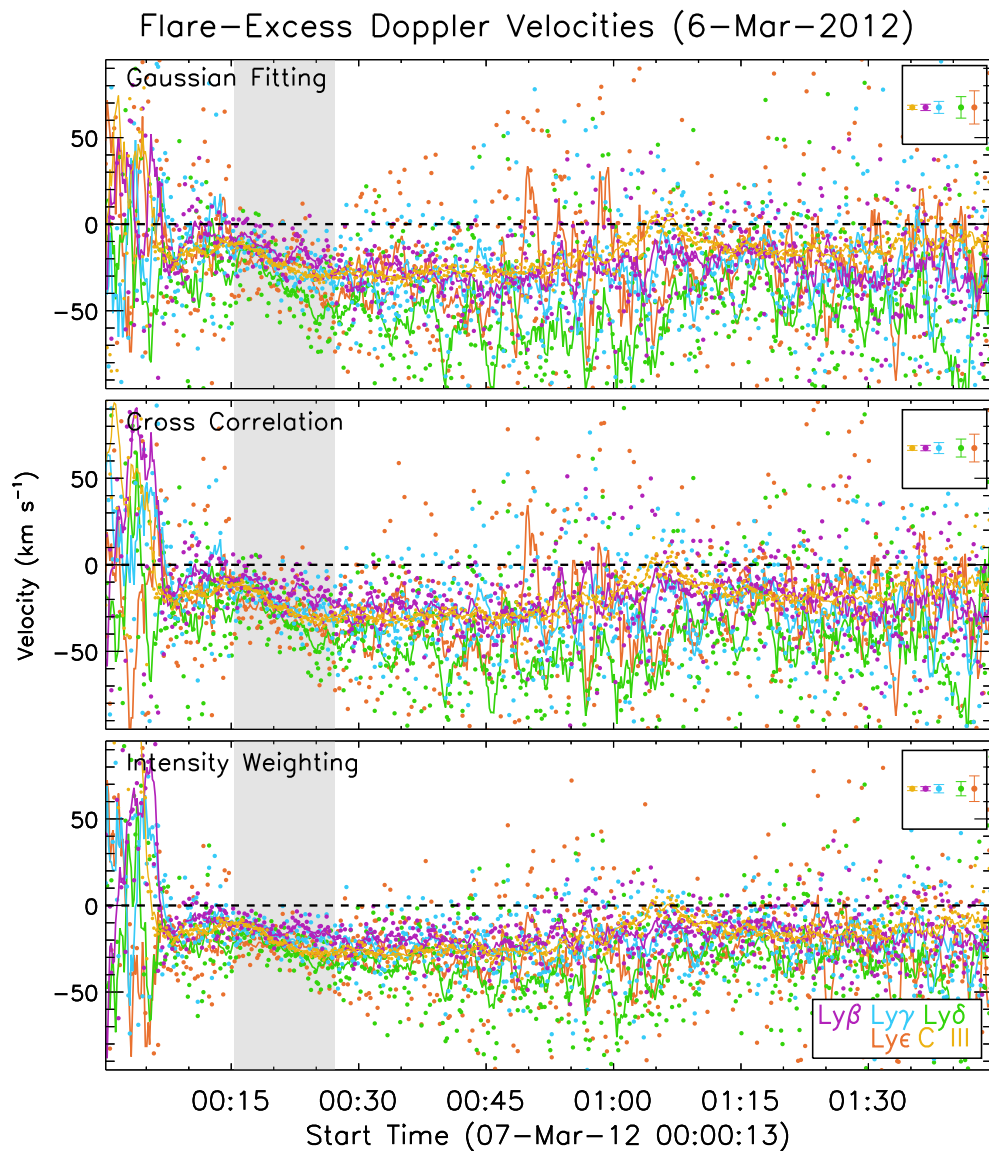


**Figure 3.17:** Doppler velocities as in Figure 3.16, but measured after preflare-subtraction in the line profiles. All other aspects retain their previous meanings, and the duration of the  $2\sigma$  enhancement in the  $\text{Ly}\beta$  lightcurve is again highlighted in grey.

velocity for 20 minutes, peaking with a speed of around  $5 \text{ km s}^{-1}$  before gradually diminishing over the following 45 minutes.  $\text{Ly}\gamma$  attains higher Sun-as-a-star velocities than  $\text{Ly}\beta$ , following a similar temporal profile but with a peak speed of  $8 - 9 \text{ km s}^{-1}$ .  $\text{Ly}\delta$  and  $\text{Ly}\epsilon$  exhibit a greater amount of variability (a now familiar property of the

higher order lines), but reach speeds between  $10 - 15 \text{ km s}^{-1}$ . A prominent initiation of upflows in synchronisation with the X1.3 flare is not visible in the Lyman lines in the Sun-as-a-star data, however it should also be noted that none of the lines fully return to rest in the intermediate time.

To probe the true upflow velocity during these events, the velocities after preflare-subtraction are again calculated and are shown in Figure 3.17. As expected, scatter in the velocity data points becomes problematic for the higher order Lyman lines when the excess signal is low. The excess is particularly weak in the late decay phase of the first (X5.4) flare. C III maintains an excellent excess signal throughout, with Ly- $\beta$  representing the most stable signal in the Lyman lines.

Between 00:16-00:25, the preflare-subtracted line profiles retain an appreciable amount of irradiance, as evidenced by the tighter clustering of the velocity profiles around the time highlighted in Figure 3.17. Throughout this time, the spread in the C III data points is remarkably small across all three methods. The C III velocity profile indicates a plasma upflow, the speed of which increases until 00:25, at which point it plateaus at a speed of  $30 - 35 \text{ km s}^{-1}$ . The upflows remain at this speed for a further 40 minutes, before quickly returning to rest between 01:00 – 01:05, before a second upflow initiates as a result of the X1.3 flare and reaches a velocity of  $25 - 30 \text{ km s}^{-1}$ .

Ly- $\beta$  exhibits a long-lived upflow of  $20 - 30 \text{ km s}^{-1}$  for the majority of the duration of both flares. While the excess signal is strong, (00:16-00:25), upflows in Ly- $\beta$  accelerate from  $10 \text{ km s}^{-1}$  to  $25 \text{ km s}^{-1}$ . Ly- $\gamma$  behaves similarly, but reaches velocities between  $30 - 40 \text{ km s}^{-1}$ . Ly- $\epsilon$  exhibits similar flow velocities to Ly- $\gamma$  throughout, but suffers from an increased amount of noise after 00:45 due to the weak excess signal. Ly- $\delta$  also suffers from an increased amount of variability due to its weak excess signal, but shows the fastest upflows while the signal is strong, reaching between  $40 - 60 \text{ km s}^{-1}$ .

While Ly- $\delta$  and Ly- $\epsilon$  fail to indicate stable flow signatures during the second flare, Ly- $\beta$ , Ly- $\gamma$  and C III suggest further upflows of around  $25 \text{ km s}^{-1}$  throughout the second event. As before, the intensity-weighted method obtains relatively slow flows, but with less scatter and variability. Regardless of the method used, a clear picture

can be seen: upflows of  $30 - 50 \text{ km s}^{-1}$  are initiated by the X5.4 flare, which persist for 40 minutes. The flows diminish at 01:05, after which they resume to a weaker extent with the onset of the X1.3 flare. The combination of the flare-excess speeds (Figure 3.17) with the clear velocity profiles in the Sun-as-a-star data (Figure 3.16) provide convincing evidence for strong plasma upflows during these flares.

### 3.3.5 The 01st January 2014 Flare - Predominant Redshifts

The beginning of 2014 was accompanied by a moderate M9.9 flare from AR 11936 (SOL2014-01-01). Clear redshifts are observed in the C III line during this flare, but these signatures are very faint in the Lyman lines. A conspicuous ejection can be seen during this event, which is discussed further in §3.4.2.

Located at (S16, W45), the lightcurve for the event (Figure 3.18) shows a prominent enhancement in the Ly- $\beta$  line initiating at around 18:45, and ending roughly 30 minutes later. Two spikes appear in the lightcurve, at 18:25 and 19:44, but due to their transient nature they are not considered to be authentic flare signatures. Inspection of the full spectrum was performed at the times corresponding to these spikes, but no large-scale enhancements could be found. Additionally, the EVE data flags around these times did not indicate any expected problems with the data. It may be the case that these spikes could have been caused by particle strikes. The rise-time for the lightcurve during the flare is rather rapid, increasing from preflare to peak level in 2 minutes.

Doppler velocities with no preflare-subtraction are shown in Figure 3.19. A very prominent redshift is seen in the C III line, corresponding to a downflow which peaks at 18:46 in the cross-correlation and intensity-weighted methods with a velocity of  $12 - 18 \text{ km s}^{-1}$ . The Gaussian method does obtain a peak in the velocity profile at this time, but suggests higher velocities afterwards. The downflow persists with a near-constant velocity of  $10 - 15 \text{ km s}^{-1}$  until 19:05, after which it gradually begins to decrease in speed.

Despite a clear downflow in the C III and a prominent enhancement in the Ly- $\beta$  line, there appears to be little signature of flows in the Lyman lines. Until 18:55, the

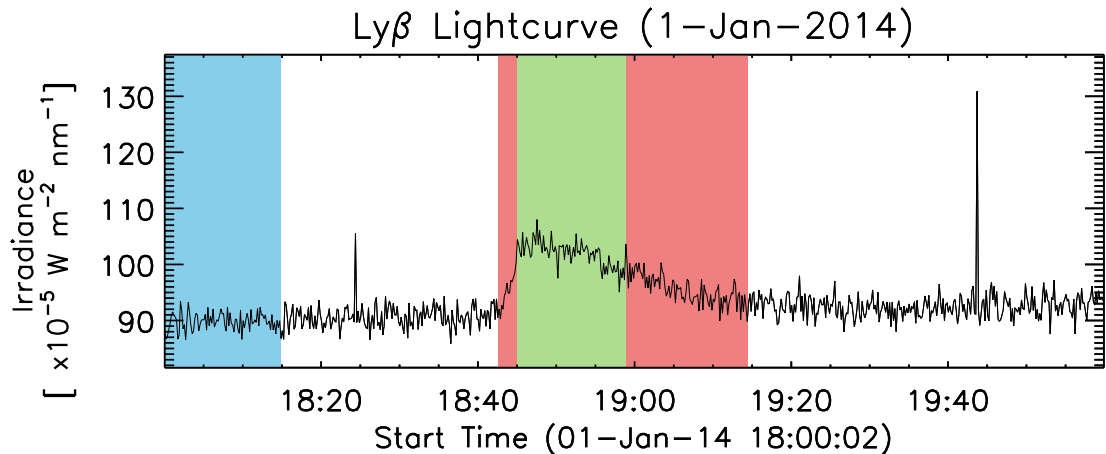


**Figure 3.18:** Lightcurve of the core of the Ly- $\beta$  line during the M9.9 01st January 2014 flare, where the highlighted regions retain their previous meanings.

Doppler velocities for the Lyman lines tend to average out towards zero. However, after 18:55, there are faint suggestions of downflow in their velocity profiles. A weak but sustained downflow of around  $2 \text{ km s}^{-1}$  can be seen in the Ly- $\beta$  line in the Gaussian and cross-correlation methods. A similar weak signature is also seen in the higher order lines after 18:55, with the majority of the smoothed velocity curves lying above the  $v_d = 0$  line. This is not true of the intensity-weighted results, but this is unsurprising as this method has frequently recovered velocities of a lower magnitude than the other methods.

The flare-excess Doppler velocities, displayed in Figure 3.20, paint a rather ambiguous picture of the plasma flows during this flare. Despite the Sun-as-a-star velocity profiles showing a clear peak in the C III downflow speed at 18:47, the flare-excess profiles suggest that the C III downflow continues to increase in speed until around 19:00, when it plateaus at around  $50 \text{ km s}^{-1}$ .

Curiously, the Lyman lines do not appear to exhibit any significant flows while the excess signal is strong. However, as with the Sun-as-a-star results, the situation changes at 18:55. After this time, all three methods reveal strong signatures of downflow in the Ly- $\beta$  line, with a low amount of scatter in the velocity data. This corresponds in time to the duration of the plateau in the C III velocity. Ly- $\beta$  reaches

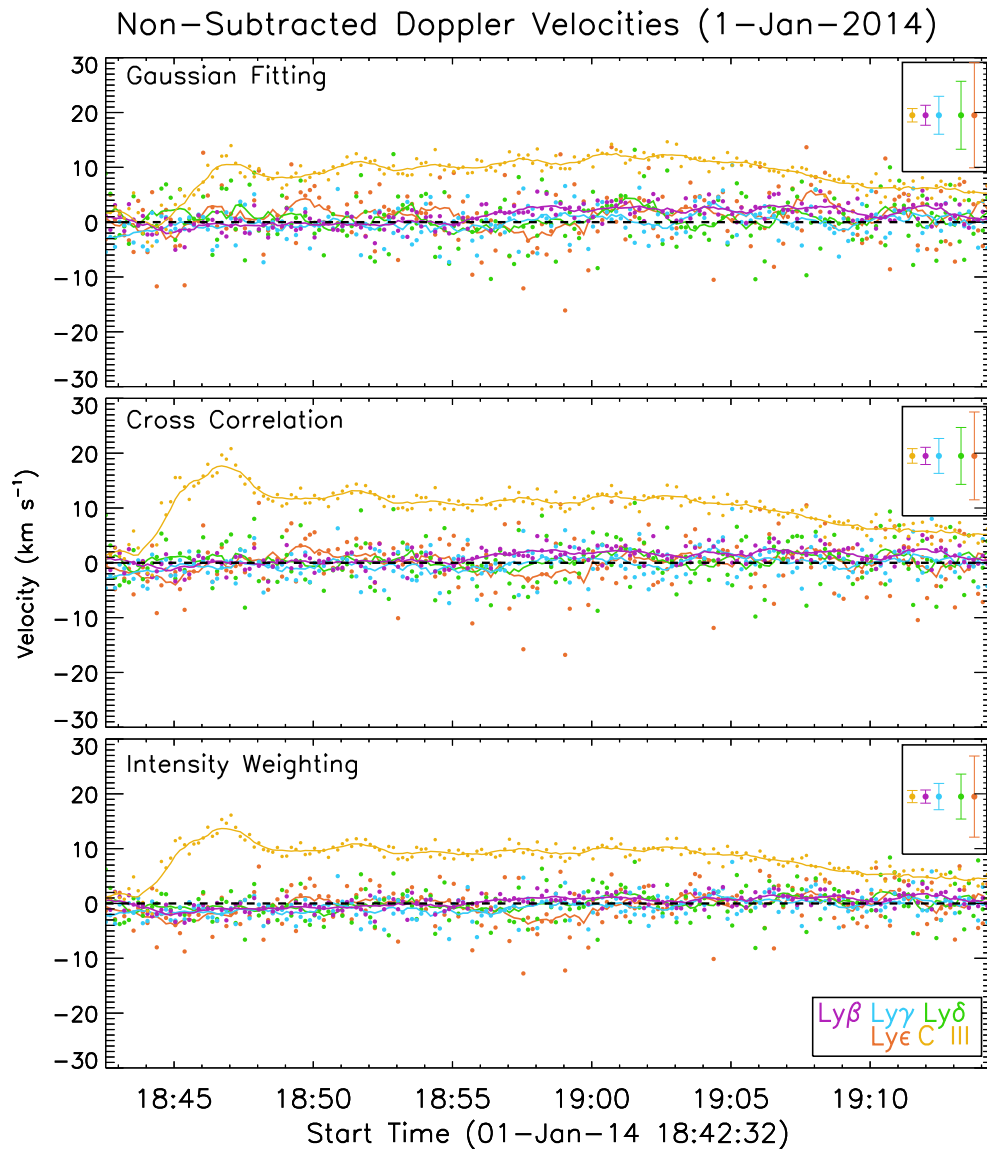


**Figure 3.19:** Doppler velocities obtained for each of the Lyman lines and the C III line for non-subtracted Sun-as-a-star spectra during the 01st January 2014 flare. All aspects and conventions retain their previous definitions.

a peak downflow velocity of around  $40 \text{ km s}^{-1}$  in the Gaussian and cross-correlation methods at 19:09, with a lesser peak speed of  $\sim 20 \text{ km s}^{-1}$  in the intensity-weighted method. All Lyman lines of higher order than  $\text{Ly}\beta$  exhibit a large of variability after 18:55, but generally appear to indicate downflows.

Intepreting the results from Figures 3.19 and 3.20 proves challenging. While the

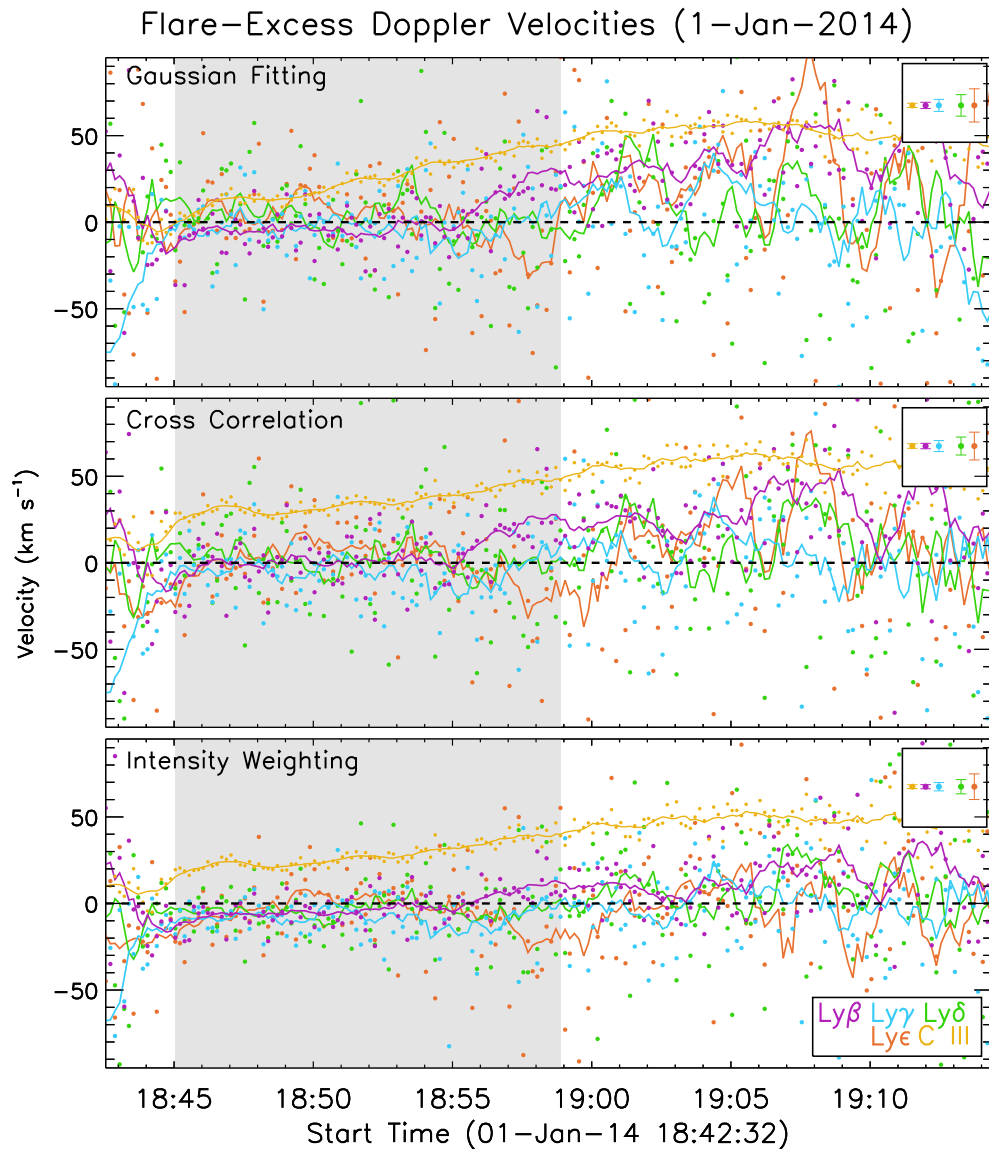


**Figure 3.20:** Doppler velocities as in Figure 3.19, but measured after preflare-subtraction in the line profiles. All other aspects retain their previous meanings, and the duration of the  $2\sigma$  enhancement in the  $\text{Ly}\beta$  lightcurve is again highlighted in grey.

Lyman lines display next to no flow signatures while the excess irradiance is strong, they exhibit a tendency to show weak downflows in the Sun-as-a-star data after 18:55. A clear downflow signature can be also seen in the  $\text{Ly}\beta$  line in the flare-excess data after 18:55. While variable, the flare-excess velocities after 18:55 for the higher-order

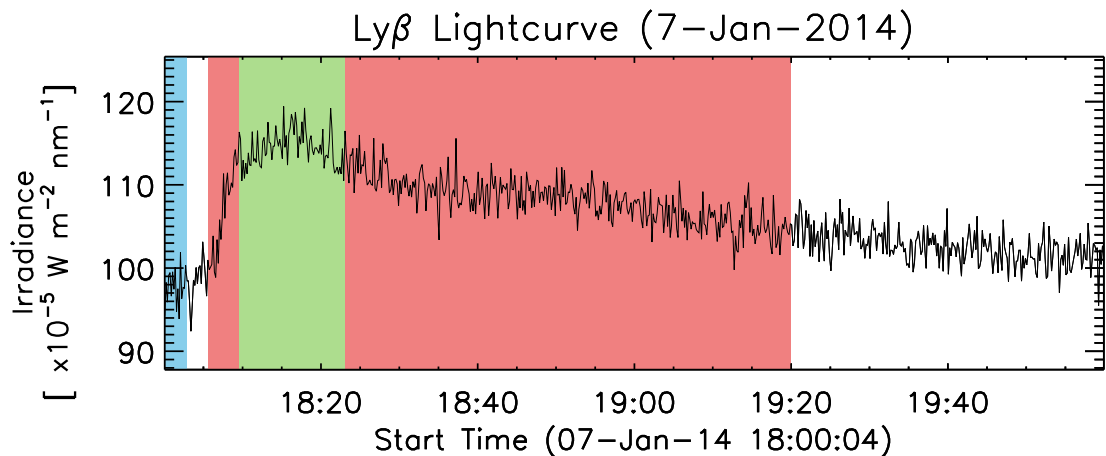


**Figure 3.21:** Lightcurve of the core of the Ly- $\beta$  line during the X1.2 07th January 2014 flare, where the highlighted regions retain their previous meanings.

Lyman lines also appear to predominantly imply downflows. All velocity profiles for the C III line unambiguously indicate downflows.

It is worth noting at this point that in all of the prior flares, the Lyman lines consistently exhibit an atmospheric flow in the same direction as that of the C III line. It is curious that despite such an obvious downflow in the C III line, and a prominent enhancement in the Ly- $\beta$  lightcurve, the downflow signatures in the Lyman lines are so weak. This flare is revisited in §3.4, where AIA images are used to further our understanding of the situation.

### 3.3.6 The 07th January 2014 Flare - Predominant Redshifts

Close to disk centre, AR 11944 emitted an X1.2 flare on the 07th January 2014 at heliographic co-ordinates (S12, W08). Prominent downflow signatures were observed in all of the lines during this flare (SOL2014-01-07), with speeds between 15 – 40 km s<sup>-1</sup>.

From the Ly- $\beta$  lightcurve (Figure 3.21), it can be seen that a rapid enhancement in the Ly- $\beta$  line core is followed by an extremely gradual ( $\geq 2$  hours) decay in the line irradiance. The flare initiates soon after MEGS-B began exposing, meaning that there

are only a few minutes available to define the preflare. As with the previous events, we first examine the Doppler velocities obtained from non-subtracted spectra, and then those obtained in flare-excess.

The Doppler velocities for the Sun-as-a-star data are shown in Figure 3.22. As with all previous flares, a well-defined excursion is seen in the velocities for the C III line. Initially at rest at 18:05, a downflow develops in the line which peaks with a velocity of  $20 - 30 \text{ km s}^{-1}$  at 18:10. Both the Gaussian and intensity-weighted methods find slightly lower velocities than the cross-correlation method in this case. The C III downflow begins to diminish from 18:17, and from 18:30 decays very slowly, only approaching rest at 19:15.

A downflow is also visible in the Lyman lines between 18:05-18:25, although is less obvious in the results obtained using intensity-weighting. There does not seem to be a large amount of differentiation in the downflow velocity between differing Lyman lines, with flow speeds reaching  $3 - 6 \text{ km s}^{-1}$ . Again, Ly- $\beta$  exhibits the least amount of variation, with data points in the higher order lines subject to increased scatter. The downflows in the Lyman lines peak at around the same time as that in C III (18:10), before gradually decaying. Beyond 18:30, it is difficult to observe any flows persisting in the Lyman lines.

The preflare-subtracted velocities are shown in Figure 3.23, and as before, the time corresponding to a strong flare-excess signal is highlighted, ranging from 18:10-18:23. The C III velocity still peaks at 18:10, but now with a maximum speed of  $\sim 40 \text{ km s}^{-1}$  (the Gaussian method obtains a lower velocity of around  $30 \text{ km s}^{-1}$ ). The C III velocity again decays very slowly, and in flare-excess does not return to zero by 19:20.

Between 18:10-18:23, the velocities in Ly- $\beta$  exhibit little variation. Both Gaussian and cross-correlation methods obtain relatively constant downflow speeds of  $20 \text{ km s}^{-1}$  in the line during this time, with the intensity-weighted showing speeds of  $10 \text{ km s}^{-1}$ . The Ly- $\gamma$  line shares a similar peak velocity with Ly- $\beta$ , but by 18:23 has already decayed to zero. Ly- $\delta$  and Ly- $\epsilon$  also share peak velocities at 18:10 of  $\sim 20 \text{ km s}^{-1}$  ( $10 \text{ km s}^{-1}$  after intensity-weighting), but display a large amount of scatter. After 18:30, it is not possible to discern any convincing flows in the Lyman lines beyond Ly- $\beta$ .

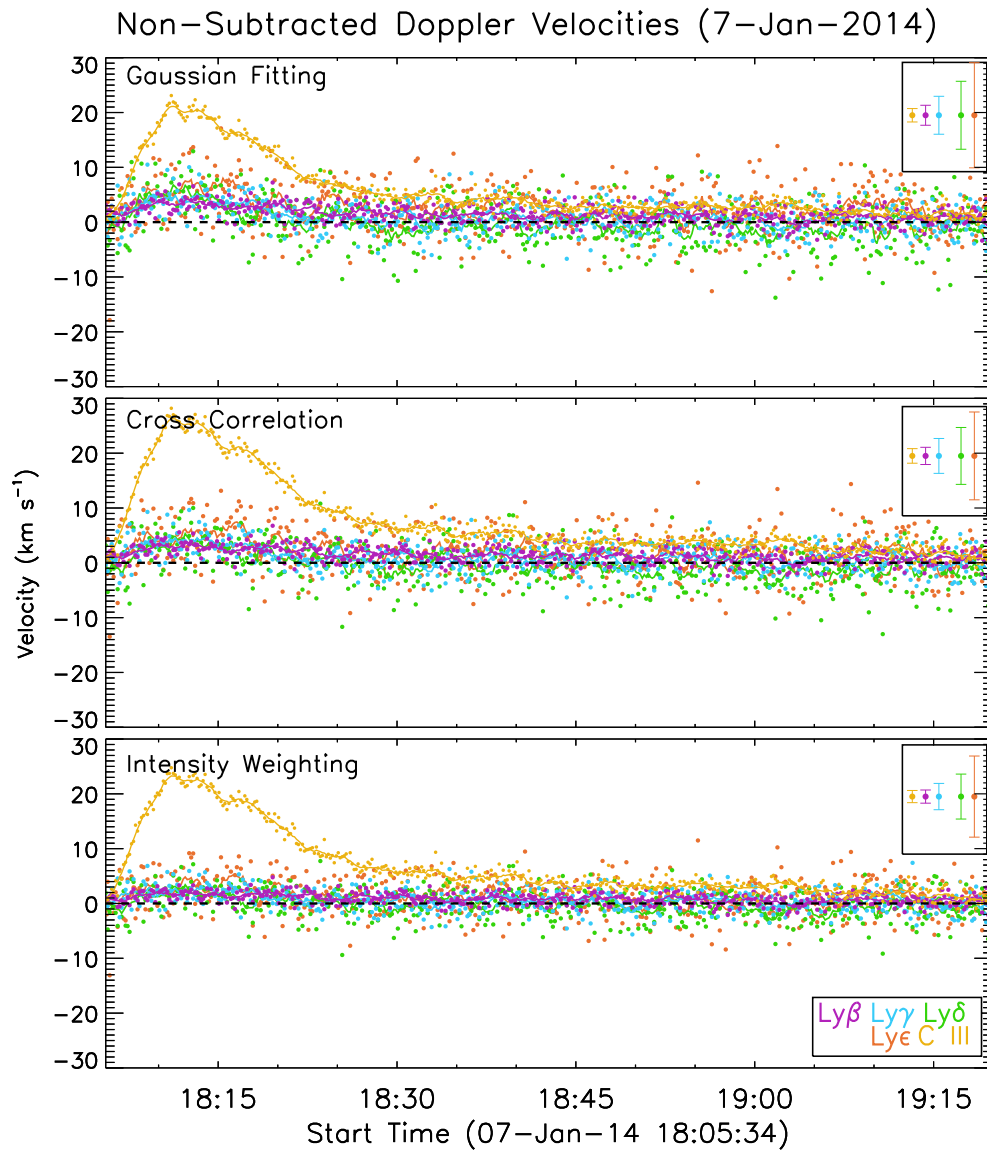


**Figure 3.22:** Doppler velocities obtained for each of the Lyman lines and the C III line for non-subtracted Sun-as-a-star spectra during the 07th January 2014 flare. All aspects and conventions retain their previous definitions.

Both the Sun-as-a-star and flare-excess results for this flare indicate downflows in all of the lines, with apparent peak velocities in C III of  $\sim 40 \text{ km s}^{-1}$  and  $\sim 20 \text{ km s}^{-1}$  in the Lyman lines.

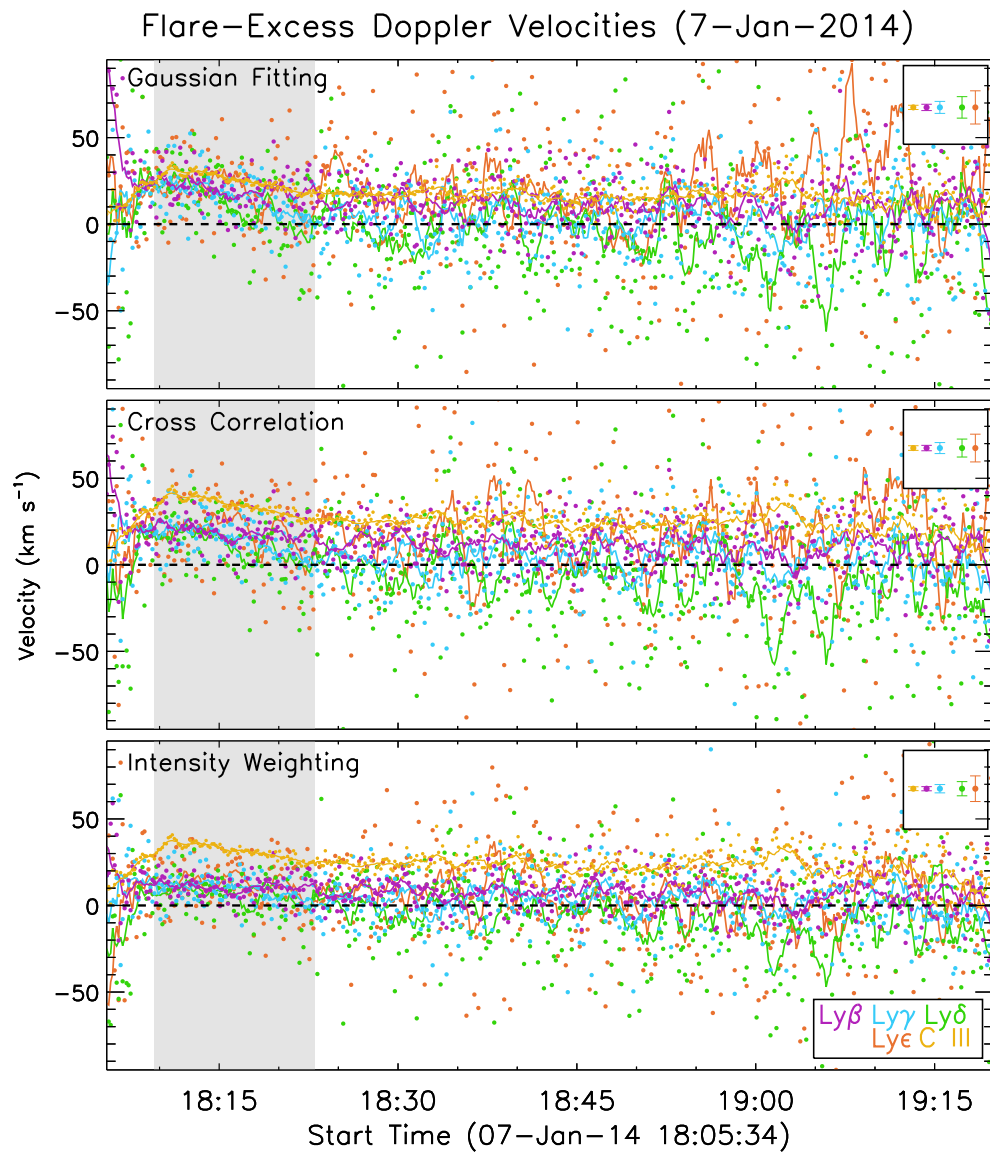


**Figure 3.23:** Doppler velocities as in Figure 3.22, but measured after preflare-subtraction in the line profiles. All other aspects retain their previous meanings, and the duration of the  $2\sigma$  enhancement in the  $\text{Ly}\beta$  lightcurve is again highlighted in grey.

## 3.4 Imaging of Ejection Events with AIA

The velocity results from the six flares considered in §3.3 share several commonalities, which we discuss further in §3.6. However, it is interesting that upflows have been observed in three of the flares: SOL2011-03-07, SOL2011-11-03 and SOL2012-03-07 all exhibit prominent blueshifts in the Lyman and C III lines. It is well-documented that H $\alpha$  displays a redshift in the flaring chromosphere (Ichimoto & Kurokawa 1984; Wülser et al. 1994; Kuridze et al. 2015), and that generally the low-temperature chromospheric lines (including the Lyman lines) are redshifted (Lemaire et al. 1984; Kamio et al. 2005; Milligan & Dennis 2009; Taroyan & Bradshaw 2014). Therefore, it is slightly surprising that upflow signatures of several tens of km s<sup>-1</sup> have been observed in the Lyman lines. These could be cases of gentle evaporation, but it is difficult to reconcile this scenario with some of the high flow speeds observed and particularly with the strengths of the 07th March 2012 (X5.4) and 03rd November 2011 (X1.9) flares.

In this section, we discuss two events in which notable ejections can be observed in AIA data, which may explain the strong blueshifts observed in the 07th March 2011 flare, and the weak redshifts in the Lyman lines during the 01st January 2014 flare. Interpretation of the other events that exhibit upflows is covered in §3.5.

### 3.4.1 An Eruption During the 7th March 2011 Flare

The 7th March 2011 flare exhibited a clear upflow signature in the non-subtracted velocity results for all lines considered (Figure 3.10), initiating at roughly 19:45 and ceasing close to 20:10. The flare-excess velocities (Figure 3.11) revealed strong upflow velocities (50-100 km s<sup>-1</sup>) in the Lyman lines, although with a large amount of variability.

Inspection of the 304 and 171 Å channels in AIA (Figure 3.24) unveil a conspicuous ejection of material between 19:44 - 20:10, directed normal to the surface. The event occurred at W48, so it is reasonable to assume that a non-negligible component of the ejecta's velocity is directed along the line of sight.

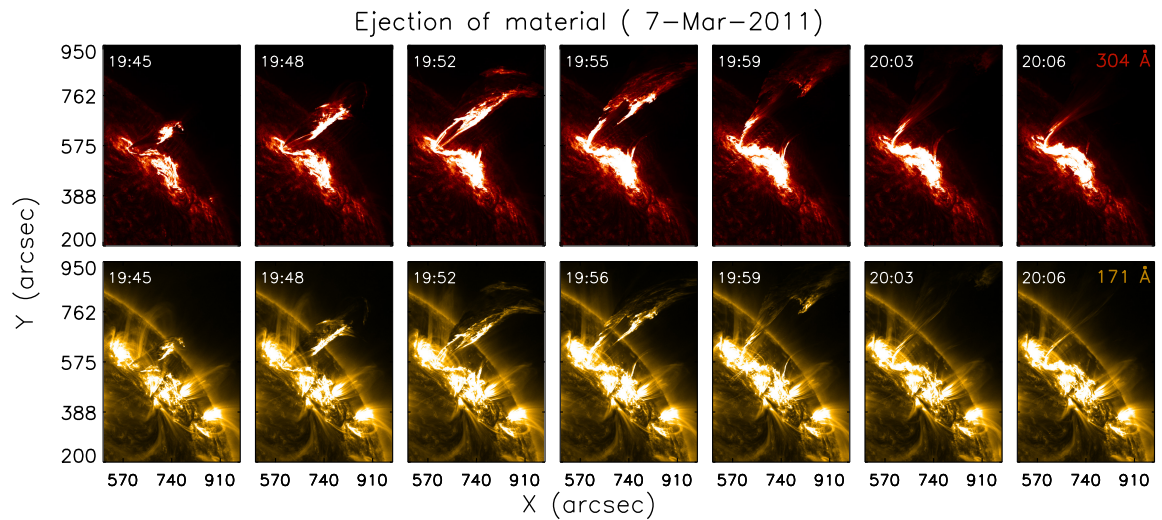


**Figure 3.24:** Images of AR 11164 during SOL2011-03-07 in 304 and 171 Å showing a prominent outward eruption of material. The eruption is concurrent with the observed upflows in the Lyman lines (Figures 3.10 and 3.11) during this flare.

By visually monitoring the leading edge of the ejected material, the pixel distance in the plane of the sky is divided by the duration in time to obtain a rough estimate of the speed of the eruption. For this ejection, the projected velocity in both filters is roughly around  $150 \text{ km s}^{-1}$ . The true radial velocity will be larger than the projected speed calculated this way. Given that the eruption appears to be moving radially, it should have a component towards the observer. If this plasma is emitting in the Lyman lines, then this eruption will result in them being blueshifted, which can conceivably explain the high upflow velocities observed during the flare.

### 3.4.2 An Eruption During the 1st January 2014 Flare

The 1st January 2014 flare displayed a conspicuous downflow signature in the C III line, with flare excess velocities reaching as high as  $50 \text{ km s}^{-1}$ . While the flare-excess velocities in the Ly- $\beta$  line do also suggest downflows of a similar peak speed, the general signature from the Lyman lines is more ambiguous. During the peak of the flare, indicated in green in Figure 3.18, the Lyman lines do not appear to be affected by downflows, which only become apparent after 18:55 with a large amount

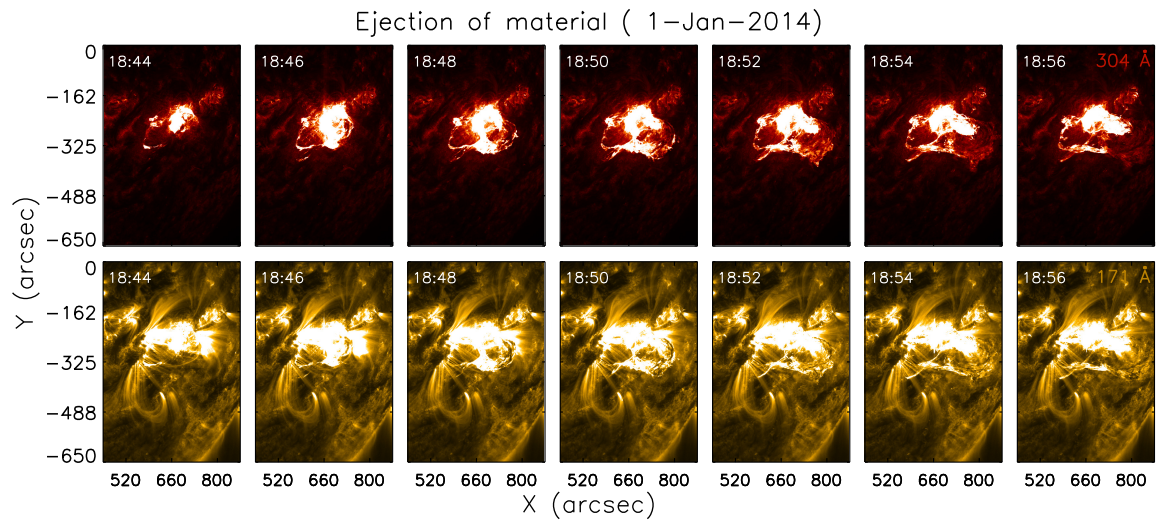


**Figure 3.25:** Images of AR 11936 during SOL2014-01-01 in 304 and 171 Å showing an ejection of material in the southern hemisphere. The eruption takes place during the time range in which C III exhibits clear downflows but no flows are visible in the Lyman lines (Figures 3.19 and 3.20).

of variability. Given the strong enhancement in the  $Ly-\beta$  lightcurve, and the clear downflow observed in C III, it is curious that the Lyman lines do not exhibit a clear flow signature at early times.

As with SOL2011-03-07, AIA images in the 304 and 171 Å passbands were examined in order to determine if any ejections of material could be obfuscating the chromospheric velocity signatures. Figure 3.25 shows that this flare was accompanied by a notable ejection, which corresponds well in time to the absence of flows in the Lyman lines (18:44-18:56).

As with SOL2011-03-07, the leading edge of the eruption was monitored and the pixel distance travelled was used to estimate a projected ejection speed. The projected speed is roughly  $65 \text{ km s}^{-1}$ , which will be an underestimate of the true outward velocity. Given that the active region is located at (S16, W45), there should be a line-of-sight component of the ejecta's velocity which will lead to blueshifted emission in any of the lines emitted by the plasma.

It may be the case that hydrogen embedded in the eruption, emitting in the

Lyman lines, contributes a blueshifted component to the line profiles. The eruption may not be rich in C III, due to a combination of the ion's abundance relative to hydrogen, and also its atomic weight. If this is the case, then it could be that the downflow observed in C III (and at later times in Ly- $\beta$ ) is representative of the true chromospheric motion. This downward motion is then temporarily obscured in the velocity signatures of the Lyman lines by the ejection of an outwardly-directed, hydrogen-rich parcel of plasma, which counteracts any redshifted signal.

### 3.5 More Interpretation of Upflow Signatures

With AIA images (in both 171 and 304 Å) providing possible explanations for both the upflow signatures in the SOL2011-03-07 flare and the absence of flows at flare peak during SOL2014-01-01, there remain two flares which demonstrate upflows from EVE lineshifts.

The SOL2011-11-03 event shows unambiguous evidence of blueshifts in all of the Lyman and C III lines (Figures 3.13 and 3.14). This flare was studied by [Chen et al. \(2013\)](#) in AIA and *STEREO*, who identified the event as a failed filament eruption. The authors showed that several segments of the filament were ejected upwards between 20:20-20:25, with speeds of up to 400 km s<sup>-1</sup>. It is conceivable that a line-of-sight component of this fast-moving filament material is responsible for shifting the Lyman and C III lines blueward, resulting in upflows being measured. However, it should be noted that the flows observed in this flare do appear to continue beyond the dynamic timescale of the filament eruption, and that it is also surprising that such a small feature could contribute heavily to the observed flow signatures. [Liu et al. \(2014\)](#) also identified upward loop motion of several tens of km s<sup>-1</sup> during this event.

The final event exhibiting upflow signatures is the X5.4 and X1.3 dual-flare event on the 07th March 2012. These flares initiated long-lived and clear upflow signatures in all of the lines considered (Figures 3.16 and 3.17), with the flare-excess velocities suggesting upflows of between 20-40 km s<sup>-1</sup>. Both of the flares in this two-hour period were associated with the emission of a CME, with the first (00:20) being

directed to the north-east and the second (01:14) emitted in the south-west direction [Schmidt et al. \(2014\)](#); [Patsourakos et al. \(2016\)](#).

AIA images in the 171 Å channel indicate an appreciable amount of motion of the active region loops during the first flare, both to the north-east and to the south-west of the active region. It is possible that the combination of the ejected coronal material and upwards motion of the active region loops introduce blueshifted features along the line of sight. If so, then these may be able to explain the upflows observed during this majorly eruptive event, although the temporal extent of the upflow signatures do hint at a more sustained source of motion as opposed to something of a more transient nature.

### 3.6 Summary of Flows Observed by the EVE Instrument

Six flares in solar cycle 24 were observed by the MEGS-B detector to have enhancements in the Lyman lines with associated Doppler shifts. Three independent methods were used to detect and quantify the extent of the Doppler shifts in 4 low-order Lyman lines and the C III line. Gaussian fitting remains a robust approach as long as the line profiles do not have irregular, noise-dominated shapes or blends with other lines. Cross-correlation makes no assumptions about the shapes of the line, but can also lead to spurious results if the flaring profiles have irregular shapes. Intensity weighting consistently returns velocities of a lower magnitude than the other two methods, but tends to lead to velocity profiles with less scatter.

In principle, subtracting the preflare from the flaring spectra gives a more realistic estimate of the plasma velocities associated with the flare, as the contributions from the remainder of the disk are removed. In practice, this presents an additional problem as there exists only a narrow window of time during which the SNR of the flare-excess Lyman lines is sufficient for fitting purposes. This makes it more challenging for the methods to obtain the correct plasma velocity, and all flare-excess velocity profiles generally suffer from a large amount of scatter. To aid a quantitative discussion of the Doppler shifts observed, the flare-excess velocities are time-averaged for 5 time bins around the peak of each flare and are listed in Table

		Ly- $\beta$	Ly- $\gamma$	Ly- $\delta$	Ly- $\epsilon$	C III
<b>15th February</b> 2011 - 01:56	G	$23 \pm 10$	$30 \pm 7$	$35 \pm 11$	$21 \pm 12$	$50 \pm 2$
	C	$22 \pm 8$	$28 \pm 5$	$28 \pm 10$	$20 \pm 11$	$50 \pm 2$
	W	$12 \pm 7$	$16 \pm 5$	$10 \pm 7$	$14 \pm 8$	$43 \pm 2$
<b>07th March</b> 2011 - 19:53	G	$-71 \pm 8$	$-75 \pm 9$	$-14 \pm 58$	$-30 \pm 39$	$-35 \pm 3$
	C	$-53 \pm 10$	$-69 \pm 9$	$-8 \pm 57$	$-23 \pm 38$	$-28 \pm 3$
	W	$-33 \pm 6$	$-42 \pm 4$	$-27 \pm 20$	$-34 \pm 27$	$-20 \pm 2$
<b>03rd</b> <b>November</b> 2011 - 20:22	G	$-59 \pm 7$	$-46 \pm 9$	$-36 \pm 11$	$-50 \pm 27$	$-57 \pm 6$
	C	$-51 \pm 5$	$-40 \pm 9$	$-33 \pm 8$	$-47 \pm 27$	$-50 \pm 6$
	W	$-30 \pm 3$	$-28 \pm 6$	$-27 \pm 6$	$-40 \pm 18$	$-32 \pm 4$
<b>07th March</b> 2012 - 00:19	G	$-15 \pm 4$	$-15 \pm 4$	$-31 \pm 10$	$-16 \pm 5$	$-18 \pm 2$
	C	$-16 \pm 4$	$-15 \pm 4$	$-29 \pm 9$	$-19 \pm 6$	$-18 \pm 2$
	W	$-16 \pm 3$	$-14 \pm 4$	$-23 \pm 6$	$-20 \pm 3$	$-16 \pm 2$
<b>01st January</b> 2014 - 18:46	G	$0 \pm 5$	$-6 \pm 10$	$-1 \pm 10$	$19 \pm 12$	$8 \pm 3$
	C	$6 \pm 4$	$-5 \pm 7$	$3 \pm 9$	$4 \pm 12$	$29 \pm 2$
	W	$-4 \pm 2$	$-8 \pm 4$	$-5 \pm 7$	$-7 \pm 7$	$21 \pm 2$
<b>07th January</b> 2014 - 18:15	G	$19 \pm 6$	$15 \pm 5$	$25 \pm 7$	$35 \pm 12$	$29 \pm 2$
	C	$18 \pm 6$	$15 \pm 4$	$23 \pm 8$	$36 \pm 10$	$37 \pm 2$
	W	$10 \pm 4$	$8 \pm 4$	$13 \pm 4$	$19 \pm 7$	$34 \pm 2$

**Table 3.2:** Summary of velocity results observed in the 6 flares by EVE using preflare-subtracted spectra. The three methods are denoted by “G” (Gaussian), “C” (cross correlation), and “W” (intensity weighted). The quoted velocity values are obtained by time-averaging the Doppler velocities for 5 time bins about the quoted peak of each flare. Standard errors obtained from averaging the velocities throughout the 5 time bins are also listed.

3.2. The observed flows are briefly summarised in the remainder of this chapter, using a combination of the Sun-as-a-star and flare-excess results.

The X2.2 flare on 15th February 2011 led to pronounced redshifts in all of the Lyman and the C III lines studied, corresponding to downflows in the plasma. These

downflows persisted for roughly 30 minutes (Figure 3.7). Around the peak of the flare (01:56), the Lyman lines exhibited downflow velocities of  $20 - 30 \text{ km s}^{-1}$ , with lower speeds ( $\sim 10 - 15 \text{ km s}^{-1}$ ) when intensity-weighting was used. The C III line suggested a slightly faster downflow in the atmosphere, peaking at  $50 \text{ km s}^{-1}$ .

The weakest flare in the sample (M3.7) surprisingly resulted in some of the fastest flows observed. The 7th March 2011 event exhibited conspicuous upflows in both Sun-as-a-star and flare-excess velocity profiles, initiating at 19:44 and lasting for around 25 minutes. The flare-excess velocities around the peak of the flare (19:53) show highly-variable velocity profiles in the higher order lines, but suggest rapid upflows with maxima of  $50-70 \text{ km s}^{-1}$  for the lower order Lyman lines. The C III line maintains a much more stable velocity profile, which appears to indicate upflows of  $20 - 30 \text{ km s}^{-1}$ . This flare was associated with a notably large ejection of material, simultaneous with the upflows observed. It is likely that the ejected material carries a component towards the observer that introduces a significant amount of blueshift in the line profiles, leading to the observed upflows.

The X1.9 flare on 3rd November 2011 also exhibited prominent upflows in both the Sun-as-a-star and flare-excess data. These upflows initiate at 20:24 and persist for roughly 13 minutes. The Sun-as-a-star velocity profiles show two peaks: one at 20:22 and a secondary maximum at 20:26. All Lyman lines have similar flare-excess upflow velocities around the flare peak (20:22), ranging between  $30 - 50 \text{ km s}^{-1}$ . The C III line suggests upflows of around  $30 - 60 \text{ km s}^{-1}$  in flare-excess, and appears to have a slight periodicity in its velocity profiles. This event was associated with a failed filament eruption (Chen et al. 2013; Liu et al. 2014), which ejected a small amount of plasma upwards. This ejection could potentially contribute a blueshifted component to the line profiles, although given its size this would be rather surprising.

The most intense events studied in this work were the combined X5.4 and X1.3 flares during 7th March 2012. Initiating shortly after midnight, the lightcurve for the initial X5.4 flare peaked at 00:19, decaying over the following hour until a secondary peak was registered with the X1.3 flare at 01:15. This event produced long-lived and clearly-detectable blueshifted signatures in all lines considered. While the flare intensities were high, the flare-excess velocities were rather moderate. Around the

peak (00:19), upflows in the Lyman lines were observed to be of the order  $15 - 30 \text{ km s}^{-1}$ , with C III ranging between  $15 - 20 \text{ km s}^{-1}$ . This event was associated with two CME ejections and outward expansion of the flare loops, both of which could contribute toward a blueshifted component in the Lyman lines.

The M9.9 1st January 2014 flare displayed prominent redshifts in the C III line, but the dynamics of the atmosphere remained ambiguous in the velocity profiles for the Lyman lines. A downflow is observed in the C III line from 18:43, and persists after the Ly- $\beta$  lightcurve has returned to quiet-Sun levels. During the peak of the flare (18:46), C III unambiguously exhibits flare-excess downflow velocities of around  $20 \text{ km s}^{-1}$ , although the temporal behaviour of the downflow is different to that observed in the Sun-as-a-star velocity profile, peaking at a much later time with a velocity close to  $50 \text{ km s}^{-1}$ . During the peak, the Lyman lines do not exhibit flows, but after 18:55 they appear to predominantly reflect the downflow observed in the C III line. For the time associated with no flows in the Lyman lines, an outwards ejection of material is observed in AIA data. It could be the case that the chromospheric velocity signatures are temporarily obscured by this eruption, which introduces blueshifted components in the Lyman lines.

The 7th January 2014 X1.2 flare revealed downflows in the chromosphere, initiating at 18:05 and persisting significantly for a further 45 minutes. The Lyman lines suggest plasma downflows of  $20 \text{ km s}^{-1}$  around the flare peak (18:15), with C III achieving faster speeds of  $25 - 35 \text{ km s}^{-1}$ .

Throughout the course of these flares, Doppler shifted emission has been observed in all of the Lyman and the C III lines. While three flares (SOL2011-02-15, SOL2014-01-01 and SOL2014-01-07) do suggest downflows in the chromosphere as expected (although with additional complications in the 01st January event, as explained above), the remaining three flares in the sample (SOL2011-03-07, SOL2011-11-03 and SOL2012-03-07) exhibit strong signatures of plasma upflows.

A convincing explanation for the upflows in the 07th March 2011 event is given by a large, outwards ejection of material observed at the same time as the flow signatures. The 07th March 2012 event was associated with two CME emissions, and a moderate amount of loop motion, but it is difficult to reconcile the long-lived

upflows observed with a transient event such as a CME emission. While the ejection of a small segment of filament material may be responsible for the upflows observed in the 03rd November 2011 flare, given its size it is surprising that it could lead to such a pronounced upflow signature in the velocity profiles. While the blueshifted emission in the Lyman and C III lines can be traced back to events involving material ejection, understanding the extent of the influence these ejecta have on the line profiles observed by EVE remains challenging.

While many of the flare-excess velocity profiles show an increased (and at times large) amount of scatter in the data points, the observations achieved in this chapter are reinforced by several aspects of the methodology. The first is simply that the results are obtained using three, completely-independent methods. The fact that the velocity profiles retain common general shapes and features across each of the three methods verifies that the observed Doppler velocities are robust. The intensity-weighted method, however, does appear to obtain consistently lower velocities than the other two methods. This method may suffer from a lack of a fitting mechanism.

Additionally, flows can be observed in the Sun-as-a-star data for all flare considered (albeit with a lower magnitude). While the flare-excess profiles give velocities more representative of the flare, the fact that there are flow signatures even before subtraction of the preflare indicates that there are genuine Doppler shifts in the line profiles.

Another consideration is that for the flare-excess velocity results, we generally restrict our focus to the times at which the Ly- $\beta$  lightcurve has an appreciable enhancement, ensuring that the line profiles at a given time are not completely noise-dominated. It would be naive to give weight to the flare-excess results throughout the entirety of a flare's duration, and so a more selective approach that focusses on the peak of the flare provides more robust measurements when preflare-subtracted spectra are used.

A sensible approach to understanding these results combines a consideration of both the Sun-as-a-star and the flare-excess velocities. The Sun-as-a-star velocity profiles demonstrate the general direction and duration of the flows, while the flare-excess results provide a better estimate of the flow speeds. Generally, flows of the

order  $20 - 30 \text{ km s}^{-1}$  are observed in the Lyman lines, with the C III line occasionally attaining higher velocities ( $50 \text{ km s}^{-1}$  during SOL2011-02-15). It seems to be the case that the C III line is involved in similar dynamics to the Lyman lines, as it exhibits the same flow direction as the Lyman lines in all flares considered.

For the flares exhibiting downflows, the velocities are roughly in line with expectations and may indicate condensations in the cool chromospheric lines of several tens of  $\text{km s}^{-1}$ . While upflow signatures could be explained by ejection features, it is still unclear how much of a contribution to the observed velocity profiles should be expected. Additionally, it is unlikely that the upflow signatures observed in these flares are related to gentle evaporation, as even the weakest event is still a moderately strong M3.7 flare.

To achieve a better understanding of whether the upflow signatures in the Lyman lines can be attributed to chromospheric motions, the concept must be approached from a different perspective. In Chapter 4, numerical modelling and simulations are used to investigate how the Lyman lines are formed in the chromosphere, and how they respond when the atmosphere is perturbed by a flare.

## Chapter 4

# Flare Simulations and the Formation of the Lyman Lines

*The work presented in this chapter was published in [Brown et al. \(2018\)](#)*

With the observations in Chapter 3, a relatively consistent picture of the speed of flowing chromospheric plasma during flares has been obtained. While the Doppler shifts observed by EVE frequently suggest flow velocities of  $20 - 30 \text{ km s}^{-1}$  in the Lyman lines, the preferred flow direction is less clear. Given that three flares exhibit signatures of upflowing plasma, it becomes necessary to investigate circumstances in which red- or blue-shifted lines are produced, and how the shifts are related to the chromospheric flows.

This question can be addressed by flare simulation. In this chapter, the RADYN code is used to simulate four variants of flares, with the resulting motions and emission properties of the flaring atmosphere calculated by the hydrodynamic and radiative transfer equations. The hydrodynamics of the atmosphere are then assessed simultaneously with the model line profiles output by RADYN. This allows the formation of the Lyman lines to be explored, and the influence of atmospheric flows on the line shapes to be understood.

This chapter will first describe the structure of the preflare atmosphere, before outlining the four flare models used to perturb it. These flare models were obtained from the solar flare model database, which was prepared by the F-CHROMA

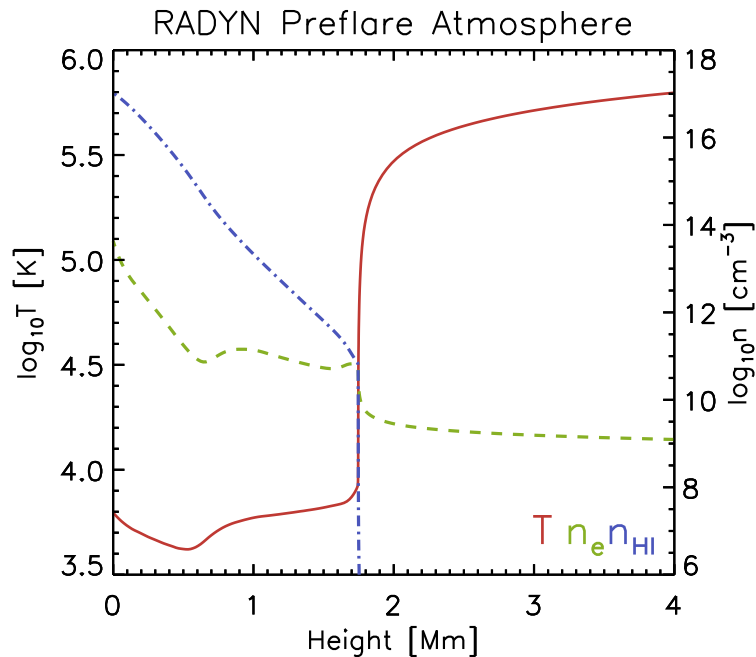


**Figure 4.1:** The temperature and density structure of the preflare atmosphere used as basis for the RADYN simulations, with the height axis originating in the photosphere. The solid red line describes the atmospheric temperature, while the electron and neutral hydrogen population densities are overplotted in the green (dashed) and blue (broken) lines, respectively.

consortium and contains a number of flare simulations spanning a range of beam descriptions <sup>1</sup>. The formation of the Lyman lines is then investigated for each of the flare simulations. Finally, an incentive for the use of an additional radiative transfer code (RH) is provided.

## 4.1 The Preflare Atmosphere

The simulations conducted in this chapter require an initial equilibrium solution for the solar atmosphere, from which a perturbation is introduced via the injection of a beam of electrons.

<sup>1</sup><https://star.pst.qub.ac.uk/wiki/doku.php/public/solarmodels/start>

The prescription for the preflare atmosphere is based on that outlined by the Quiet-Sun description in [Vernazza et al. \(1981\)](#), commonly referred to as the VAL3C model. This model is semi-empirical, constrained by Ly- $\alpha$  and UV continuum observations, and constructed using hydrostatic and non-LTE statistical equilibrium ([Vernazza et al. 1981](#); [Carlsson 2007](#)). The starting atmosphere used in the models in this chapter differs slightly from the VAL3C model in that the temperature structure is used to calculate the required heating function in order to keep the corona hot, and the atmosphere plus heating function is then allowed to relax to a state of equilibrium by which the heating function is balanced by the radiative and conductive losses ([Allred et al. 2015](#)).

Figure 4.1 shows the preflare atmosphere model used in the simulations. The atmospheric grid has an altitude of zero at photospheric heights, with a temperature minimum of  $\sim 4000$  K at  $z = 500$  km. The transition region is marked by a sharp rise in temperature at 1.7 Mm, with the corona extending upwards beyond this. Both the electron and neutral hydrogen density are high in the photosphere, dropping with altitude throughout the lower atmosphere, before dropping again at the transition region.

The neutral hydrogen density drops to zero as coronal conditions are reached and hydrogen becomes fully ionised. The electron density has a maximum of  $10^{13}$  cm $^{-3}$  close to the photosphere, with the transition region boundary marking a decrease from  $10^{11}$ - $10^{9.5}$  cm $^{-3}$ .

## 4.2 Flare Models

The modifications to RADYN introduced by [Abbett & Hawley \(1999\)](#) allow the preflare atmosphere described in §4.1 to be perturbed by the injection of a beam of electrons. This essentially simulates a flare, and the evolution and dynamics of the flaring atmosphere can then be examined. The energy loss rate of a beam of charged particles impinging on a “cold target” (velocity of the beam particles is much greater than the thermal velocity of the ambient plasma) of neutral charge, described in [Emslie \(1978\)](#), can be expressed as in [Allred et al. \(2015\)](#) as:

$$\frac{dE_n}{dt} = \frac{-2\pi e^4}{E} \frac{m}{m_e} Z^2 Z_n n_n \lambda_n v, \quad (4.1)$$

where  $dE_n/dt$  is the collisional energy loss rate.  $E$ ,  $m$ ,  $Z$  and  $v$  are the energy, mass, charge (in units of  $e$ ) and velocity of the bombarding particles.  $Z_n$  and  $n_n$  are the charge and number density of the ambient target atom, and  $\lambda_n$  is the effective Coulomb logarithm for the interaction. RADYN calculates the total energy losses due to collisions by summing equation 4.1 over all neutral species. Energy losses from collisions with ambient charged particles are also summed over, expressions for which can be found in [Allred et al. \(2015\)](#).

The above quantities, along with rates for pitch angle diffusion and scattering due to synchrotron radiation, are used to solve the Fokker-Planck equation for the particle distribution function,  $f(E, \mu, z)$ . This treatment has long been acknowledged as a more correct description of beam particles, accounting for pitch angle diffusion of the particles ([MacKinnon & Craig 1991](#); [Mauas & Gómez 1997](#)), and also accounts for losses due to synchrotron radiation. The total heating rate due to the electron beam ( $Q_{beam}$ ) is obtained, as in [Allred et al. \(2015\)](#):

$$Q_{beam} = \frac{d}{dz} \left( \int_{\mu} \int_E \mu v E f \, dE d\mu \right), \quad (4.2)$$

where  $\mu$  describes the pitch angle of the particles,  $E$  their energy and  $v$  their velocity. While the chromospheric heating need not arise solely due to Coulomb collisions between beam electrons and the ambient plasma, the process is still an important aspect of flare energy transport. Additional heating is provided to the chromosphere through radiative backwarming, and by conduction from the corona.

The primary specifications for a given flare model are detailed in a number of input files. The properties of the electron beam used to heat the preflare atmosphere are listed in the **ftab.dat** file. Here, the spectral index ( $\delta$ ), low-energy cutoff ( $E_c$ ) and beam flux (in  $\text{erg cm}^{-2} \text{s}^{-1}$ ) are tabulated for an array of time values (in s). The distribution of beam electrons injected at the top of the loop varies as  $(E/E_c)^{-\delta}$  ([Abbett & Hawley 1999](#)). The effects of varying  $E_c$  and  $\delta$  on the resulting penetration depth of the beam can be seen in Figure 6 of [Allred et al. \(2015\)](#), with the deepest depositions

of energy occurring for low- $\delta$ , high- $E_c$  beams. The pitch-angle distribution of the beam is also specified here, and in these models is set to be Gaussian-shaped in the forward hemisphere, with a width ( $\sigma$ ) of 0.1 (M. Carlsson, private communication).

The **param.dat** input file enables the injection of the electron beam specified in **ftab.dat**, and is used to toggle additional parameters such as the boundary conditions of the loop and the prescription for combined thermal soft X-ray, extreme ultraviolet and ultraviolet (XEUV) backwarming. In these simulations, a reflecting upper coronal boundary is used, which mimics the propagation of waves from the secondary footpoint.

The structure of the preflare atmosphere (§4.1) is described in the **atmdyn.dat** input file. Additional inputs are used to quantify the atomic parameters for each of the included species, and opacity contributions from background elements that do not receive a detailed treatment. Once the relevant input files are correctly modified, the RADYN code can be compiled and run. For the flare simulations outlined in this chapter, the electron beam is injected downwards through a loop of half-length 10 Mm, with a spatial extent of 300 grid points.

Four flare simulations are considered in this chapter, and are publically available to download courtesy of the F-CHROMA consortium on the solar flare model database <sup>2</sup>. The first simulation describes a moderate amount of energy injection, with a broad range of deposition altitudes. The second simulation has the same overall injected flux as the first simulation, but deposits a larger fraction of its energy at higher altitudes because the beam distribution is weighted more heavily to low-energy electrons (high  $\delta$ ). The third simulation has a slightly higher peak flux than the first two simulations, and continues to primarily deposit energy at higher altitudes due to a high beam  $\delta$ . The final simulation features a high-flux beam, deposited over a broader range of altitudes, using the same value of  $\delta$  as in the first simulation.

---

<sup>2</sup><https://star.pst.qub.ac.uk/wiki/doku.php/public/solarmodels/start>

### 4.2.1 The F10D3 Simulation

The first simulation (#55 in the model database) is characterised by the injection of an electron beam over an initial 20 s period, after which the beam ceases and the atmosphere evolves for a further 30 s. The beam flux increases linearly over the first 10 s, rising from near zero ( $1.7 \times 10^{-1}$ ) to  $1 \times 10^{10}$  erg cm<sup>-2</sup> s<sup>-1</sup> at peak. The factor and exponent of the peak flux value is used to label the beam (hence 1F10, or simply F10). The flux then decreases linearly to near zero ( $1 \times 10^{-1}$ ) over the following 10 s, after which it remains at this level for a further 30 s.

The electron beam has a spectral index of  $\delta=3$  and a low-energy cutoff of  $E_c=25$  keV. This means that there are no electrons injected with energies lower than 25 keV, and that above energies of 25 keV the distribution of electron energies has a power law variation, proportional to  $E^{-3}$ . The rather “hard” spectral index of 3 means that the number of electrons as a function of energy drops off relatively slowly compared to a higher value of  $\delta$ , permitting a relatively large number of high-energy electrons to penetrate the deeper regions of the atmosphere. To aid identification of the simulations, the  $\delta$  value is also used to label the beam (therefore F10D3).

The evolution of the flaring atmosphere in this simulation is shown in Figure 4.2, where the atmospheric temperature, velocity, electron density, and ionisation fraction are plotted at time-steps (indicated by varying colours) incremented by 1.0 s. The atmosphere’s thermal response to the beam injection is quick, with an overall increase in the temperatures below and above the transition region, and temperatures of 50,000 K at the base of the transition region within 10 s. The transition region itself moves upwards throughout the duration of the simulation, indicated by the upwards progression of the sharp temperature boundary, while the lower atmosphere gradually cools after the beam shuts off.

The upwards drift of the transition region is further shown in the atmospheric velocity, which indicates an upflow initiated by the injection of the beam, a result of evaporation due to heating the chromosphere. This upflow attains velocities of almost 80 km s<sup>-1</sup> in the lower atmosphere and transition region while the beam is switched on, but continually decreases once the energy deposition stops. At  $t=50$  s,

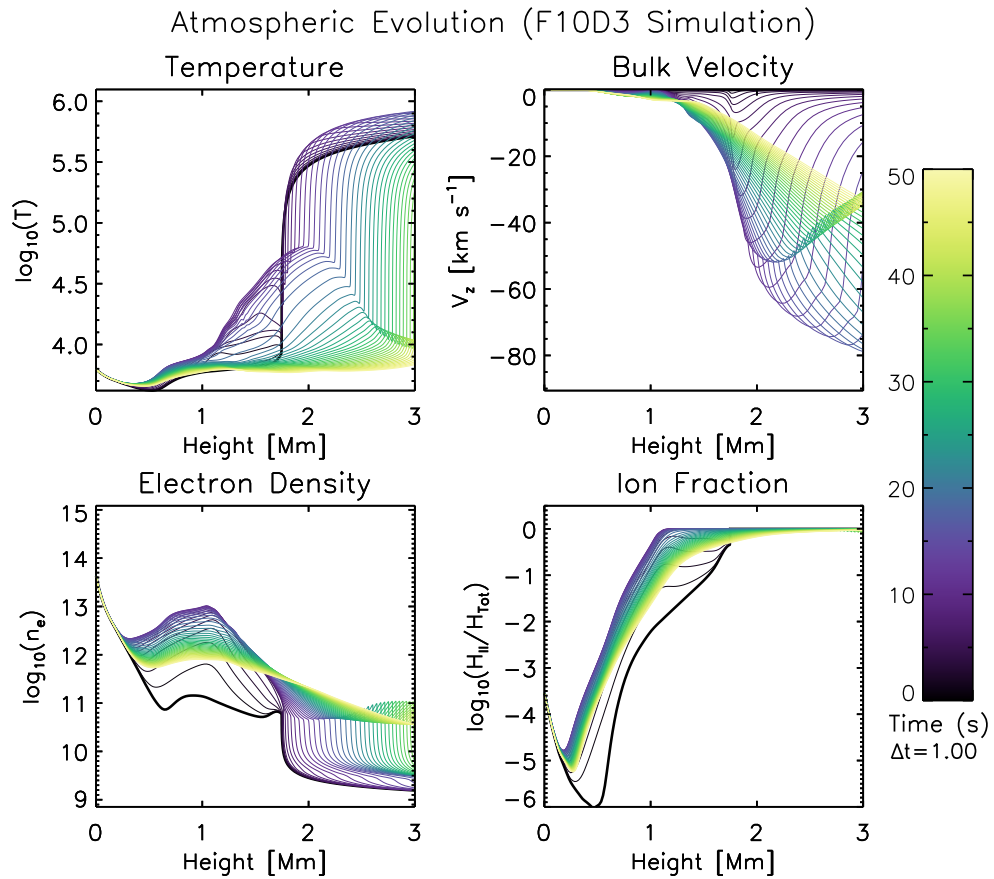


**Figure 4.2:** Evolution of the lower atmosphere in the F10D3 simulation. Variables are plotted with a line colour corresponding to a distinct time, incremented by 1.0 s. The preflare conditions are indicated by the thick, black line. As before, negative velocities correspond to upwards motion.

the upflows are more gentle, with velocities below  $40 \text{ km s}^{-1}$ .

The electron density is enhanced overall, and increases by a factor of 100 in the chromosphere during the initial stages of the beam heating. This increase is due to both the addition of non-thermal beam electrons and an increase in ionisation (which can also be seen in the lower-right panel of Figure 4.2), facilitated by the increased temperature and corresponding rise in collisional excitation.

### 4.2.2 The F1oD8 Simulation

The second simulation (model #60) maintains the same peak and integrated energy fluxes as the previous model, but is characterised by a higher value of  $\delta$ , which is now equal to 8.  $E_c$  remains fixed at 25 keV.

The distribution of electrons in a  $\delta = 8$  beam will be heavily-weighted to provide a large number of electrons with low energies, as the fraction of electrons drops off sharply with increasing energy. For a beam with a given value of  $E_c$ , a high  $\delta$  will deposit a larger fraction of its energy at higher altitudes than a beam with a low  $\delta$ , as the electrons lose the majority of their energy before reaching the deeper regions of the atmosphere.

The evolution of the atmosphere is shown in Figure 4.3. Relative to the F1oD3 simulation, the temperature increase produced by the collisional heating has more structure. The temperature at the base of the transition region again increases to around 50,000 K, but contains a sharp gradient at its upper edge, while no such feature is observed in the  $\delta = 3$  case. As before, the transition region moves upwards as the simulation progresses.

As with the previous simulation, an upflow is initiated by the injection of the beam, although has a slightly lower speed between  $z=1-3$  Mm ( $\sim 60$  km s<sup>-1</sup>) than in the  $\delta = 3$  case. The upflow has a steep velocity gradient at its leading edge, and similar sharp gradients can be seen in both the electron density and neutral hydrogen population throughout the beam-heating stage, suggesting that there is a dense material upflow and not just a front of increased ionisation.

### 4.2.3 The 3F1oD8 Simulation

The third simulation (model #66) continues to inject a greater portion of its energy at high altitudes, but has a moderately higher peak flux than the first two simulations. The injection timescale of the beam follows a triangular profile, rising from a flux of  $3 \times 10^8$  to  $3 \times 10^{10}$  erg cm<sup>-2</sup> s<sup>-1</sup> over the first 10 s. The beam's flux then decreases linearly to  $1 \times 10^{-1}$  erg cm<sup>-2</sup> s<sup>-1</sup> over the following 10 seconds, after which it remains

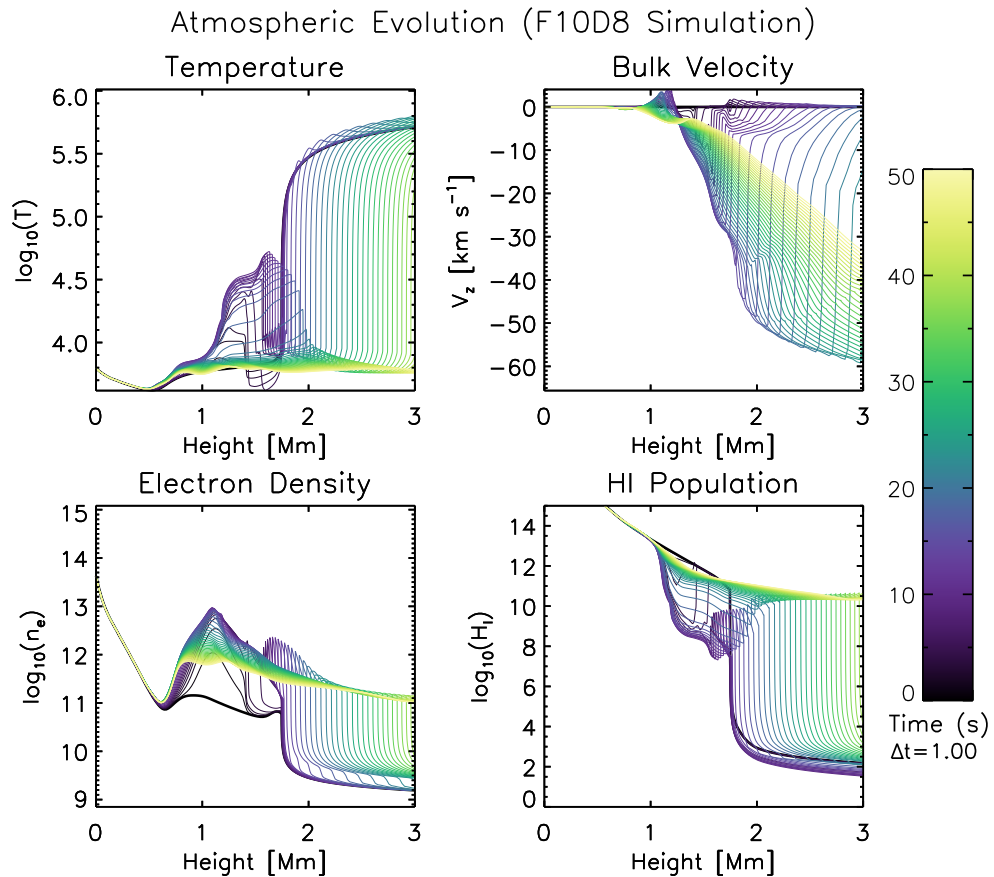


**Figure 4.3:** Evolution of the lower atmosphere in the F10D8 simulation. Variables are plotted with a line colour corresponding to a distinct time, incremented by 1 s. The preflare conditions are indicated by the thick, black line. As before, negative velocities correspond to upwards motion.

constant for the final 30 s of the simulation. As before,  $E_c$  has a value of 25 keV. The beam  $\delta$  has a relatively high value of 8 compared to the F10D3 simulation, which corresponds to a “soft” beam.

The evolution of the atmosphere is detailed in Figure 4.4, with the relevant variables plotted at 1 s intervals. At early times, during the beam injection, the temperature structure of the lower atmosphere and transition region is particularly complex. The thermal response to the beam is almost instantaneous, with temperatures at the top of the transition region reaching 1 MK. As the beam continues to heat the atmosphere, a narrow trough in the temperature profile can be seen. This

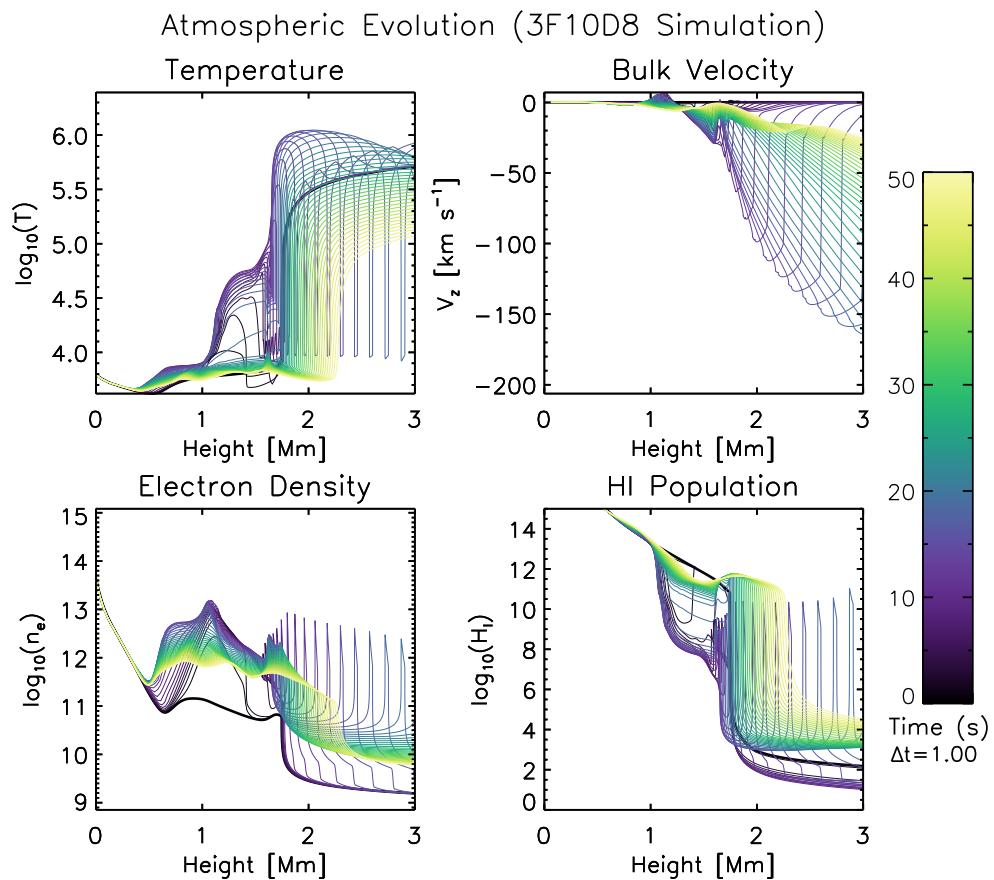


**Figure 4.4:** Evolution of the lower atmosphere in the 3F10D8 simulation. Variables are plotted with a line colour corresponding to a distinct time, incremented by 1 s. The preflare conditions are indicated by the thick, black line. As before, negative velocities correspond to upwards motion.

trough has a minimum temperature of roughly 10,000 K, and appears to be swept upwards throughout the atmosphere. At late times, the transition region settles at an altitude of 2.25 Mm.

This deep well in the atmospheric temperature is accompanied by a simultaneous high-speed upflow in the bulk velocity profile, which reaches in excess of 150 km s<sup>-1</sup>.

Coincident and cospatial with the troughs in the temperature profile are narrow spikes in the local electron density, which indicate electron densities roughly 100 times that of the underlying material, and over 1000 times higher than that of the

plasma above. These spikes in the electron density profiles are matched by similar localised enhancements in the overall neutral hydrogen population, which indicates that there is a propagation of plasma in the atmosphere and not just a front of enhanced ionisation.

All atmospheric parameters during the beam-heating stage of this simulation point to the initiation of a high-velocity ( $> 100 \text{ km s}^{-1}$ ) upflow, which carries a front of cool, dense, hydrogen-rich plasma.

#### 4.2.4 The F11D3 Simulation

The final simulation in this chapter (model #67) returns to the initial prescription of a low- $\delta$  beam, but deposits a large amount of energy. As with the previous simulations, the injection of the electron beam follows a triangular profile. The flux increments linearly in factors of  $1 \times 10^9$  until a peak flux of  $1 \times 10^{11} \text{ erg cm}^{-2} \text{ s}^{-1}$  is reached at  $t = 10 \text{ s}$ . The flux then decreases in the same manner, and beyond  $t = 20 \text{ s}$  it remains at a constant value of  $1 \times 10^{-1} \text{ erg cm}^{-2} \text{ s}^{-1}$ . Aside from the beam flux, the simulation is identical to the F10D3 model, with  $\delta = 3$  and  $E_c = 25 \text{ keV}$ .

The progression of the atmosphere is shown in Figure 4.5. As observed in the previous simulations, a rapid thermal response to the beam injection is exhibited, with a low-altitude enhancement accompanied by temperatures in excess of 1 MK in the corona. The transition region, initially at an altitude of  $\sim 1.7 \text{ Mm}$ , moves downwards as a result of the beam injection and does not return to its initial altitude, indicating a compression of the atmospheric layers.

An upflow is again initiated by the deposition of the beam, but this time it reaches a much higher velocity than the other simulations. The upflow speed reaches  $350 \text{ km s}^{-1}$  at 3 Mm. Between  $t = 45 - 50 \text{ s}$ , a highly-structured feature in the velocity profile can be seen at around above 1.5 Mm, containing both an upflowing and a downflowing component, the latter of which has a peak velocity of  $100 \text{ km s}^{-1}$ . Close to this time, a spike in the electron density is also observed at around 1.5 Mm.

The reversal of the velocity direction and the enhancement in the electron densities between  $t = 45 - 50 \text{ s}$  occur at an altitude close to the transition region, which by

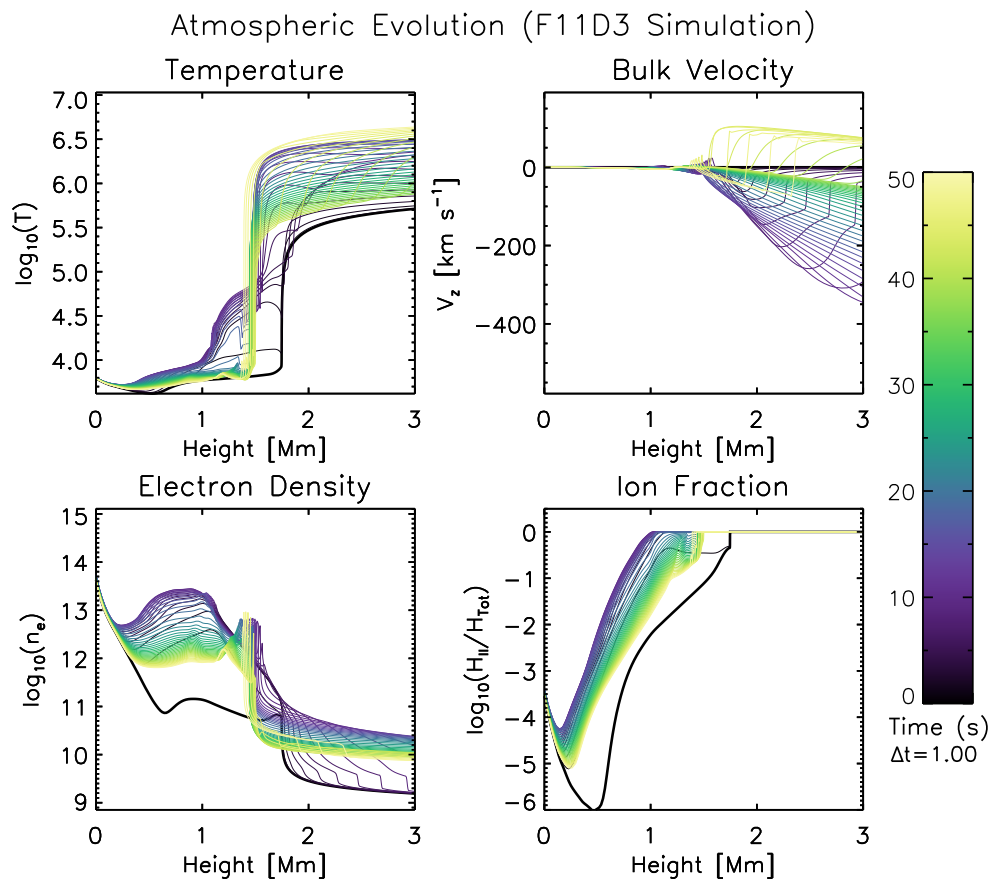


**Figure 4.5:** Evolution of the lower atmosphere in the F11D3 simulation. Variables are plotted with a line colour corresponding to a distinct time, incremented by 1.0 s. All aspects and conventions retain their previous meanings.

this time has a low altitude. This indicates the possibility of a downwards propagation of plasma parcel at late times in the simulation.

While each of the simulations are distinct in how the atmosphere responds to the beam injection, some commonalities are found. Typically, the beam induces an atmospheric upflow at early times, the speed of which scales with the amount of flux deposited. Motion of the transition region is also common, which exhibits gradual upwards drift in all simulations except the F11D3 model. The deposition of the beam, and the heating resulting from it, lead to a net increase in the overall electron density throughout the chromosphere. With the hydrodynamics described in the variables output by RADYN, it is now possible to investigate how the properties of

the atmosphere influence and affect the formation of the Lyman lines.

### 4.3 Formation of the Lyman Lines in RADYN

It has long been known that the Lyman lines, which are optically-thick, form over a range of heights in the chromosphere (Vernazza et al. 1981; Fontenla et al. 1990). As previously mentioned, the formation of a spectral line is largely dependent on  $S_\nu$ , the line source function. In RADYN, this does not vary as a function of frequency across a line profile, but does vary as a function of altitude.

We have already established that this region of the atmosphere can be highly disturbed by the injection of an electron beam (§4.2). The electron beam causes heating, but also initiates upflows. These upflows carry plasma, which may also be hot enough to produce emission in the Lyman lines. The motion of the material itself should lead to Doppler shifts in the emitted photons, but similarly will have consequences for the absorption of underlying material by the the moving plasma. This therefore alters the opacity structure of the chromosphere. Redistribution of the chromosphere and the transition region will alter the locality where LTE can be assumed. This will have consequences for the line source function.

There are clearly numerous factors that must be considered when assessing the origins of a spectral line in this complex, dynamic region of the Sun's atmosphere. In this section, each of the earlier simulations are analysed with the addition of the radiative output from RADYN. The formation of the Lyman lines is explained, with the hydrodynamic properties of the atmosphere used to provide context.

While it is initially daunting to approach the multi-faceted aspect of line formation, the problem can be made less arduous by decomposition into several key aspects. We revisit the equation of radiative transfer as in §2.2, and reiterate the formalism of Carlsson & Stein (1997), whereby the emergent intensity of radiation can be written as the integral over altitude of the *line contribution function* ( $C_I$ ):

$$I_\nu = \int_{z_0}^{z_1} C_I dz, \quad (4.3)$$

where  $C_I$  is given by:

$$C_I = S_\nu \tau_\nu e^{-\tau_\nu} \frac{\chi_\nu}{\tau_\nu}, \quad (4.4)$$

where  $S_\nu$ ,  $\tau_\nu$  and  $\chi_\nu$  describe the source function, optical depth, and opacity respectively. Essentially,  $C_I$  permits understanding of which regions in the atmosphere contribute most appreciably to the line emission. This deconstruction of the emergent intensity allows the formation of a given line to be probed in detail, using the height-dependent quantities embedded in  $C_I$ .  $S_\nu$  is large when emission processes are dominant over absorption. High temperatures in regions where the source function has not yet diverged from the Planck function ( $\sim T^4$ ) can result in large values for  $S_\nu$ , as there exists an appreciable amount of hot material to radiate.

The attenuation of radiation is described by the  $\tau_\nu e^{-\tau_\nu}$  term. This term has a maximum when  $\tau_\nu = 1$ , and allows us to determine the height in the atmosphere at which it is no longer optically thick to a photon of frequency  $\nu$ . As core photons are more readily absorbed than wing photons, the core formation height can be defined as the highest point in the atmosphere at which the atmosphere transitions from optically thick to thin.

The  $\frac{\chi_\nu}{\tau_\nu}$  term, where  $\chi_\nu$  is the monochromatic linear opacity, highlights regions in the atmosphere where there are many emitting particles, but where the optical depth is low. This emphasises velocity gradients, as material motion shifts the frequency at which the plasma radiates appreciably, and causes it to emit at frequencies where the overall optical depth is low. This allows flows in the atmosphere to be tracked.

In this chapter, the individual components of the contribution function are visualised for the Ly- $\alpha$  and Ly- $\beta$  lines as a function of the atmospheric height, and wavelength across the line profile.

### 4.3.1 Line Formation in the F10D3 simulation

The F10D3 model describes a moderate amount of energy being deposited into the lower chromosphere. In §4.2.1, an increase in the chromospheric temperature was accompanied by an atmospheric upflow of several tens of  $\text{km s}^{-1}$  in the lower

chromosphere. To investigate the interplay between the hydrodynamics of the atmosphere and the emission and absorption of radiation, the line contribution functions for Ly- $\alpha$  and Ly- $\beta$  are examined in Figures 4.6 through 4.9.

As a general rule, line formation proceeds similarly for the Lyman lines considered (Ly- $\alpha$  through Ly- $\delta$ ), and so only Ly- $\alpha$  and Ly- $\beta$  are shown in Figures 4.6 through 4.9. For the final simulations, we further restrict the detailed examination to Ly- $\alpha$ , in order to prioritise the description of a greater number of time-steps and make the explanations more manageable.

Images of the contribution function, and its constituent components, are shown as grayscale maps in Figure 4.6 for the Ly- $\alpha$  line at  $t = 20$  s.  $\frac{\chi_\nu}{\tau_\nu}$  is in the upper-left panel,  $S_\nu$  in the upper-right, and  $\tau_\nu e^{-\tau_\nu}$  in the lower-left. The contribution function,  $C_I$ , is the product of these constituents, and is shown in the lower-right panels. To improve clarity,  $\frac{\chi_\nu}{\tau_\nu}$  maps are plotted with logarithmic scaling, and  $C_I$  is scaled via normalisation.

Overplotted in the  $S_\nu$  panel are the source (in yellow) and planck (in blue) functions expressed as a function of height and the plasma temperature, such that the quantities increase towards the left. All panels additionally show the atmospheric velocity (in red) and  $\tau_\nu = 1$  surface (in green) as a function of height. For a given frequency, contributions from altitudes above the green line indicate optically thin emission, while contributions from altitudes at and below the line are optically thick. Finally, the  $C_I$  panel also shows the emergent intensity of the Ly- $\alpha$  line. The quantities are expressed as a function of wavelength (expressed as a Doppler shift) and altitude, where we again use the convention that negative velocities correspond to blueshifts (and therefore upflows).

At  $t = 20$  s, the electron beam has just finished heating the atmosphere. Figure 4.6 shows that the surface at which  $\tau_\nu = 1$  across the Ly- $\alpha$  line is not symmetric around the theoretical line core. The  $\tau_\nu = 1$  surface has a distinct asymmetry, and indicates that core formation is concentrated in the blue wing. Following Rathore & Carlsson (2015), we define that the frequency of the line core is that at which the  $\tau_\nu = 1$  surface peaks in altitude, as the core of the line should form at a higher altitude than any other frequencies across the line. The line core forms in the presence of an upflow of

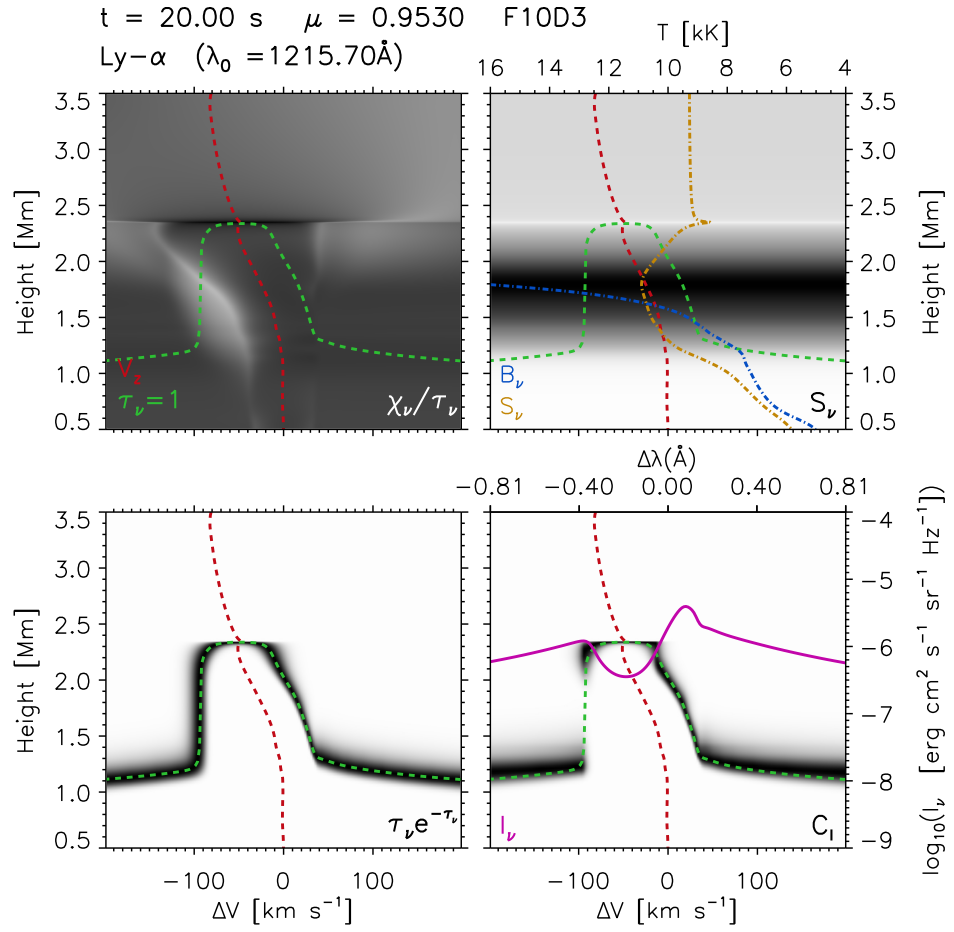


**Figure 4.6:** Components of the Ly- $\alpha$  contribution function at  $t = 20$  s during the F10D3 simulation. The quantities labelled in the bottom right-hand corners denote the variables shown in greyscale in each map, and are plotted as a function of increasing wavelength (expressed as a Doppler shift) and altitude. Dark colours correspond to large values. The dashed green and red lines indicate the  $\tau_\nu = 1$  surface and atmospheric velocity respectively. Overplotted as a function of the radiation temperature in the upper-right panels are the Planck ( $B_\nu$ ) and Source ( $S_\nu$ ) functions. The emergent intensity is indicated by the solid line in the lower-right panel.  $\frac{\chi_\nu}{\tau_\nu}$  is imaged with logarithmic scaling, while  $C_I$  is normalised. Negative velocities correspond to upflows.

$\sim 50 \text{ km s}^{-1}$ , which results in the core being blueshifted.

The  $\frac{\chi_\nu}{\tau_\nu}$  term has a maximum close to the core formation height, and is enhanced at the intersection between the  $\tau_\nu e^{-\tau_\nu}$  and  $V_z$  curves, as the flow results in emission being produced away from the theoretical line core.  $S_\nu$  is most pronounced at a height of 1.75 Mm, which is below the formation height of the line core ( $\sim 2.35$  Mm). The maximisation of the source function between the core and wing formation heights results in the line profile being centrally-reversed. The source and Planck functions are generally not coupled, but diverge strongly at  $z=1.6$  Mm, indicating a breakdown of LTE conditions.

The overall contribution function indicates that the core is optically-thick, with core photons produced very close to the  $\tau_\nu = 1$  surface. A small amount of optically-thin emission is produced in the wings, as indicated by contributions that lie above the  $\tau_\nu = 1$  surface. The emergent line profile exhibits a prominent central reversal at the line core. The core itself is also blueshifted, most likely a consequence of forming in the presence of an atmospheric upflow.

An equivalent breakdown of  $C_I$  for the Ly- $\beta$  line at this time ( $t = 20$  s) is shown in Figure 4.7, with many of the components echoing aspects of Ly- $\alpha$ 's formation. The core of the Ly- $\beta$  line forms around 0.1 Mm lower than that of the Ly- $\alpha$  line, but still does so in a region undergoing upflow ( $V_z = 50$  km s $^{-1}$ ). As with Ly- $\alpha$ , the upflow results in the opacity structure of the Ly- $\beta$  line being weighted to the blue, indicated by the asymmetric  $\tau_\nu = 1$  surface.

The source function for Ly- $\beta$  peaks in the low chromosphere ( $z = 1.45$  Mm).  $S_\nu$  then decreases with altitude over the line formation height, resulting in a centrally-reversed line core. The overall contribution function indicates that the majority of emission is optically-thick, originating from heights close to the  $\tau_\nu = 1$  surface. However, there is a greater amount of optically-thin emission in both the core and in the wings relative to Ly- $\alpha$ , as  $S_\nu$  undergoes less of a decrease above the core-formation height.

The emergent Ly- $\beta$  line is very similar in shape to the Ly- $\alpha$  line. It is primarily characterised by a centrally-reversed core, the frequency of which is blueshifted by the presence of an upflow. At  $t = 20$  s, the Ly- $\alpha$  and Ly- $\beta$  lines share some interesting properties: they are both centrally-reversed, and their cores are blueshifted. The

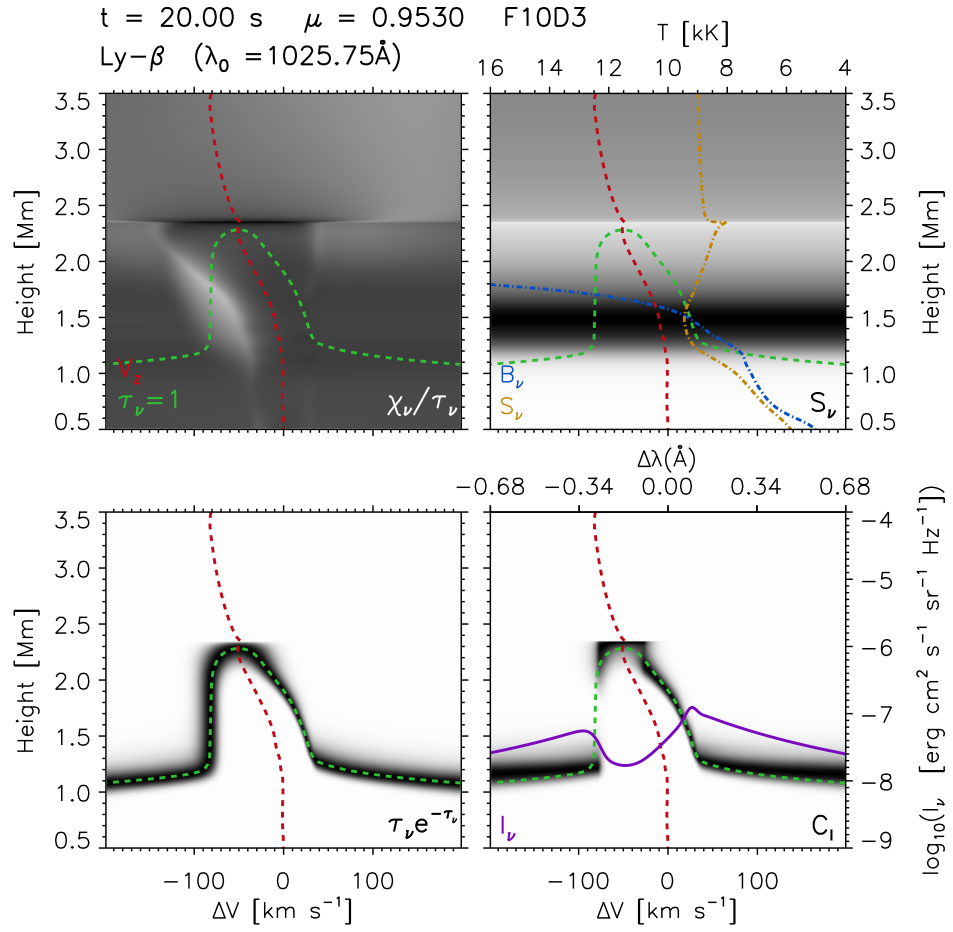


**Figure 4.7:** Components of the Ly- $\beta$  contribution function at  $t = 20$  s during the F10D3 simulation. Conventions and definitions retain their meanings from Figure 4.6. As before,  $\frac{\chi_\nu}{\tau_\nu}$  is scaled logarithmically, while  $C_I$  is normalised. Negative velocities correspond to upflows.

simultaneous presence of a central reversal and a blueshifted line core is not of little consequence. Because the core is blueshifted, its central reversal is also situated in the blue wing, and both lines show an excess of absorption in the blue wing relative to the red wing. In terms of emissivity, this means that both lines now have red wing asymmetries. The implications of this in the context of observations is discussed in Chapter 5.

After the cessation of the electron beam, the atmosphere undergoes relaxation for

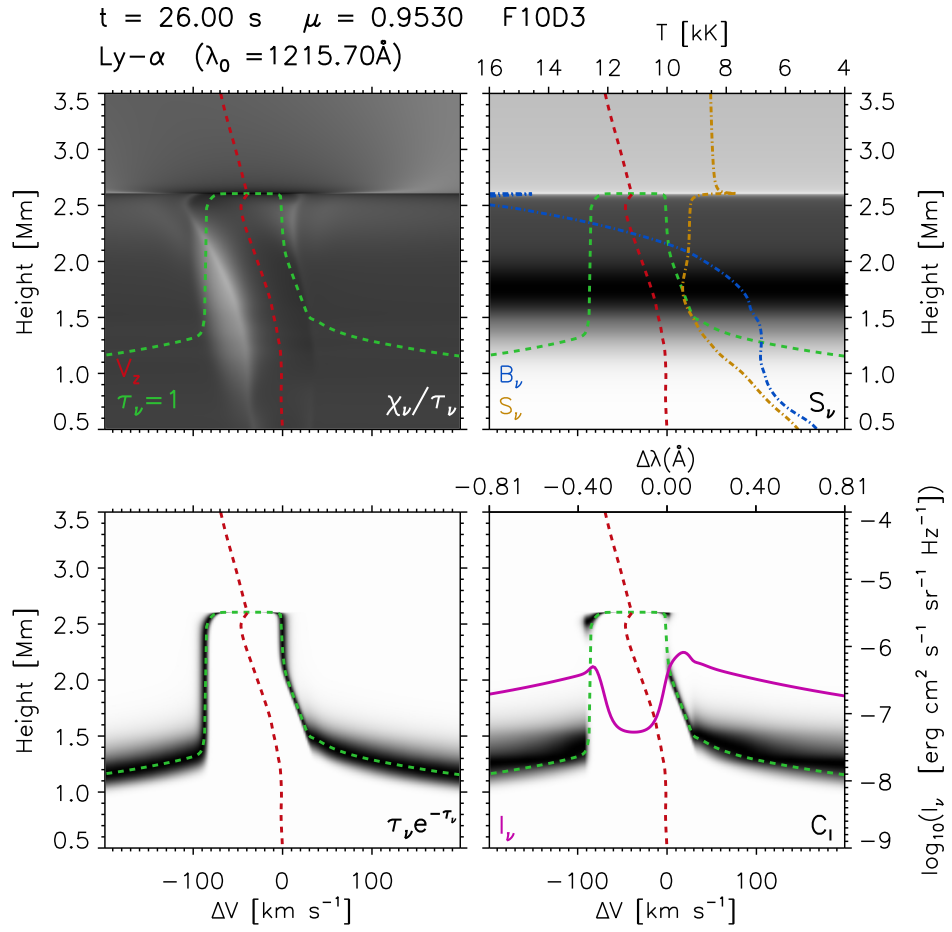


**Figure 4.8:** Components of the Ly- $\alpha$  contribution function at  $t = 26$  s during the F10D3 simulation. Conventions and definitions retain their meanings from Figure 4.6. As before,  $\frac{\chi_\nu}{\tau_\nu}$  is scaled logarithmically, while  $C_I$  is normalised. Negative velocities correspond to upflows.

a further 30 s. We revisit line formation at  $t = 26$  s, at which point the dynamics of the lower atmosphere are more gentle.

The contribution function for Ly- $\alpha$  is shown in Figure 4.8 for the later time of  $t = 26$  s. In contrast to Figure 4.6, the  $\tau_\nu = 1$  surface now appears largely symmetric, although is slightly shifted to the blue as a result of the entire line-formation region being subject to an upflow, which still maintains a peak velocity of  $\sim 50 \text{ km s}^{-1}$ .

The line core now forms at  $z = 2.6 \text{ Mm}$ , higher than at  $t = 20$  s. Figure 4.2

indicates that the transition region has also risen to a higher altitude, and at  $t = 26$  s appears to be co-spatial with the Ly- $\alpha$  core-formation height.  $S_\nu$  still peaks deep in the atmosphere ( $z = 1.6$  mm), meaning that the line is still centrally-reversed, and is largely decoupled from the Planck function throughout the lower atmosphere. The decoupling of  $S_\nu$  from  $B_\nu$  in the deep atmosphere indicates an increased influence of the radiation field on the level populations, arising from the atmosphere radiating away the energy that was provided by the electron beam.

The contribution function indicates that the core emission is formed in a very narrow zone close to the transition region. The far wings of the line are predominantly optically thick, but the near wings exhibit small optically thin components, with that blueward of the line core being more pronounced. The small, optically-thin blue-wing enhancement is a consequence of the  $\frac{\chi_\nu}{\tau_\nu}$  term being slightly amplified by the presence of the atmospheric upflow.

The equivalent  $t = 26$  s snapshot for Ly- $\beta$  is displayed in Figure 4.9. The opacity structure for the line is largely similar to that of Ly- $\alpha$ , with a slightly blueshifted but generally symmetric  $\tau_\nu = 1$  surface. The core of the line forms at the same height as Ly- $\alpha$ , at the top of the chromosphere ( $z = 2.6$  Mm).  $S_\nu$  has decreased throughout the line formation region, resulting in a line profile with a weaker intensity than at  $t = 20$  s. The source function still has a local maximum below the core-formation height and increases above the transition region, and so the line profile remains centrally reversed.

While Figures 4.6-4.9 are rather dense in information, there are general key points that can be extracted. All contribution functions for Ly- $\alpha$  and Ly- $\beta$  in this simulation confirm that the lines are predominantly optically-thick, with cores formed higher in the atmosphere than the line wings. The line formation is affected by the presence of a  $\sim 50$  km s $^{-1}$  upflow throughout the chromosphere, and as a result the cores are blueshifted with respect to the theoretical rest wavelength. The simulation suggests that the upflowing plasma can radiate appreciably in the Lyman lines.

Generally, the line source functions are not peaked at the region of core formation, instead having local maxima between the core and wing formation heights. This results in the Lyman lines being centrally reversed. During the beam-heating stage

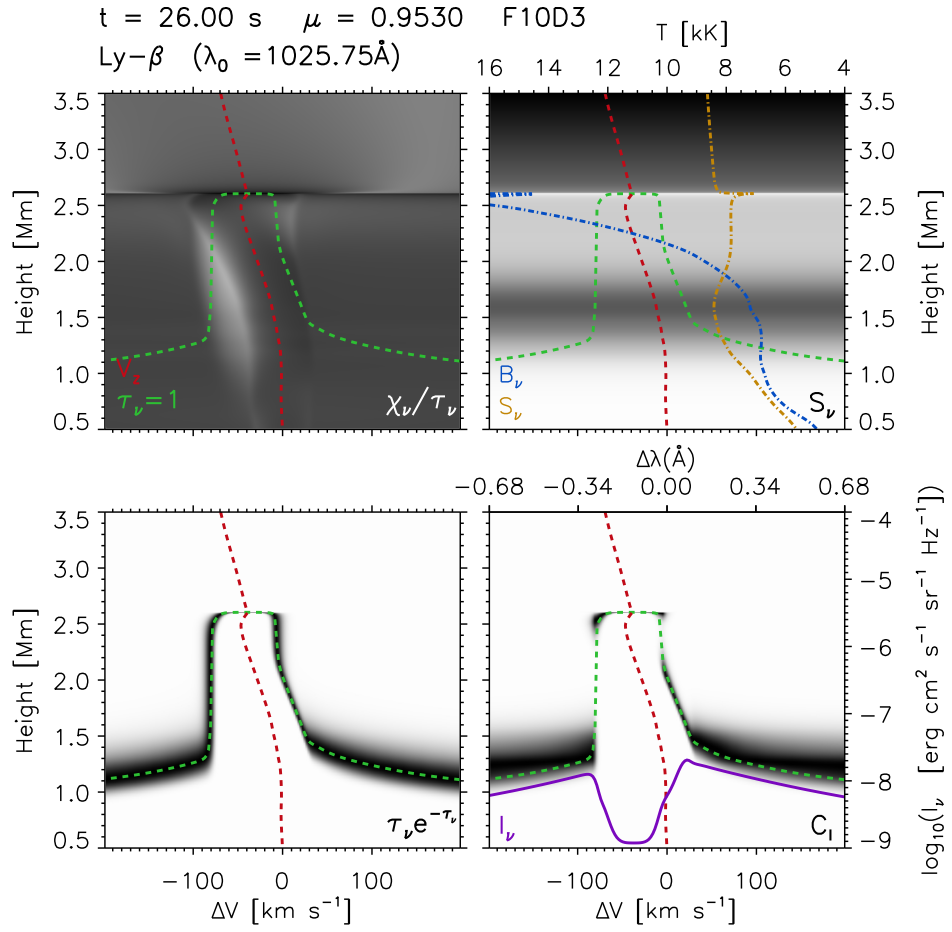


**Figure 4.9:** Components of the Ly- $\beta$  contribution function at  $t = 26$  s during the F10D3 simulation. Conventions and definitions retain their meanings from Figure 4.6. As before,  $\frac{\chi_v}{\tau_v}$  is scaled logarithmically, while  $C_I$  is normalised. Negative velocities correspond to upflows.

(Figures 4.6 and 4.7), the combination of blueshift and central reversal in the line cores results in an excess of emission in the red wing relative to the blue wing. These features persist until the end of the simulation, although the line profiles gradually diminish in intensity (Figures 4.8 and 4.9).

Beyond Ly- $\alpha$  and Ly- $\beta$ , the radiative transfer is solved for the higher-order lines, Ly- $\gamma$  and Ly- $\delta$ . While we do not present additional contribution function plots for these lines, we present their emergent intensities (along with those of the lower-order

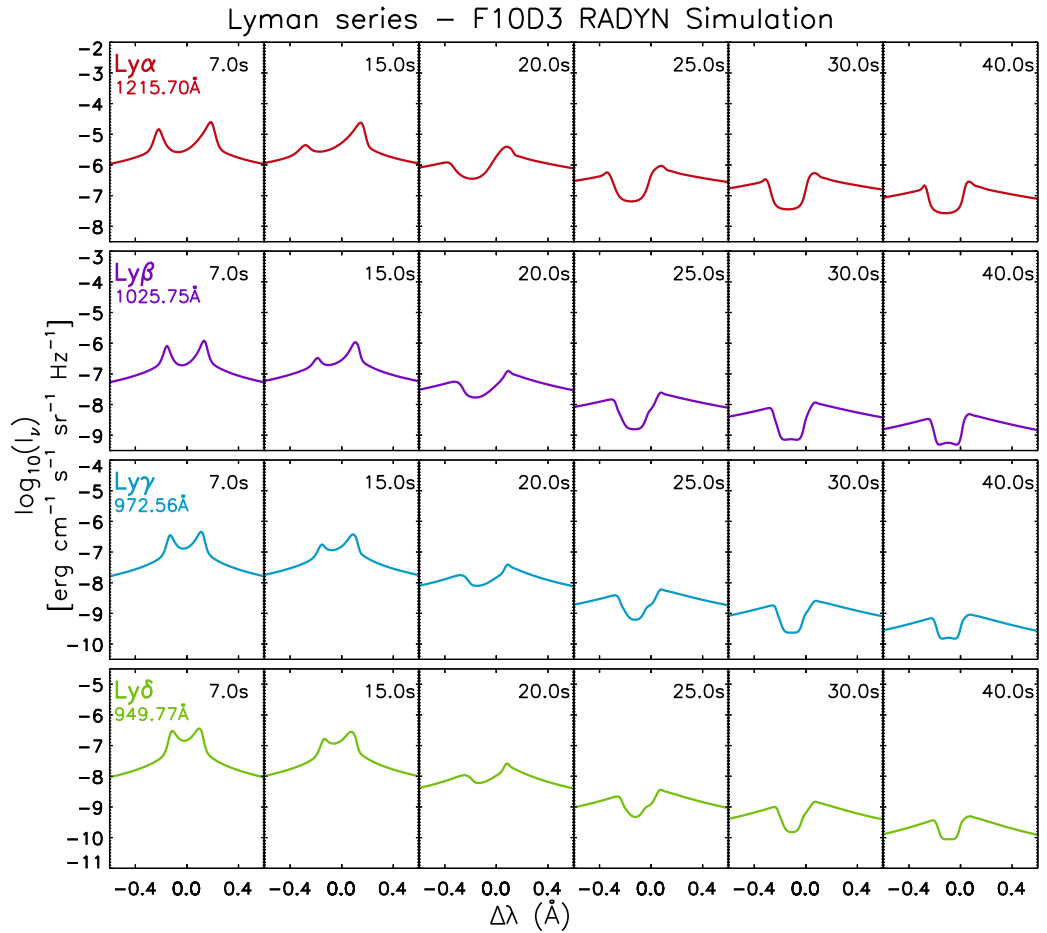


**Figure 4.10:** Snapshots of each of the Lyman lines at various time-steps (labelled in black) throughout the F10D3 simulation. All lines are plotted with a wavelength range of  $1.2 \text{ \AA}$ , symmetric about the theoretical rest wavelength.

lines) for a number of time-steps in Figure 4.10.

It is clear from Figure 4.10 that there is great similarity throughout the Lyman series with respect to the line shapes. The injection of the electron beam enhances the emergent intensities of all of the Lyman lines, with each of them exhibiting a centrally-reversed core. In all lines, the self-reversed cores encroach further into the blue wings at  $t = 15$  and  $t = 20$  s, indicating that all Lyman lines experience the effects of the upflow. The line shapes also exhibit a strong levels of consistency at  $t = 40$  s, at which point the central reversals continue to persist and remain blueshifted.

While some particularities exist for each line, it is convincing from Figure 4.10

that line formation generally proceeds the same way for each of the Lyman lines as they all exhibit similar shapes. The higher order lines have lower intensities, as should be expected for transitions that originate from higher atomic levels.

### 4.3.2 Line Formation in the F10D8 simulation

While the overall amount of energy injected into the atmosphere in the F10D8 simulation is unchanged from the F10D3 model, the altitude range of its deposition is different. Figure 4.3 reveals that the dynamics of the evolving atmosphere are slightly different from the  $\delta = 3$  case, with steep gradients present in both temperature and velocity. We therefore examine the formation of the Ly- $\alpha$  line to determine if there are any differences in its origin with respect to the F10D3 simulation.

Because we include a model that increases both the  $\delta$  and  $F$  values (3F10D8), we consider only two time-steps for analysis of the line contribution functions in this simulation as we only wish to examine the effects of increasing  $\delta$  while keeping  $F$  fixed. To facilitate comparison with the F10D3 model, we again examine the contribution function at  $t = 20$  s and  $t = 26$  s. Figure 4.11 shows the line contribution function for Ly- $\alpha$  at  $t = 20$  s, upon cessation of the electron beam. As in Figure 4.6, the presence of the atmospheric upflow shifts the opacity structure of the line and results in an asymmetric  $\tau_\nu = 1$  surface. The line core forms at  $z = 2.1$  Mm, where the upflow has a velocity of  $50 \text{ km s}^{-1}$ .

As in the F10D3 simulation,  $S_\nu$  is not peaked at the core-formation height, but does so close to  $z = 1.8$  Mm. The source function is largely decoupled from the Planck function above  $z = 1.6$  Mm, and  $B_\nu$  exhibits a prominent dip just below the core-formation height, likely as a result of the sharp temperature gradient seen below the transition region in Figure 4.3.

The contribution function confirms that the majority of the line is optically thick, with minor optically thin enhancements in the near blue and red wings ( $\Delta V = -80$  &  $10 \text{ km s}^{-1}$ ). The emergent Ly- $\alpha$  line is again centrally-reversed, but as the line core is formed in an upflowing region this feature (as in the F10D3 simulation) is again shifted to the blue. The central reversal is situated wholly in the blue, whereas in the

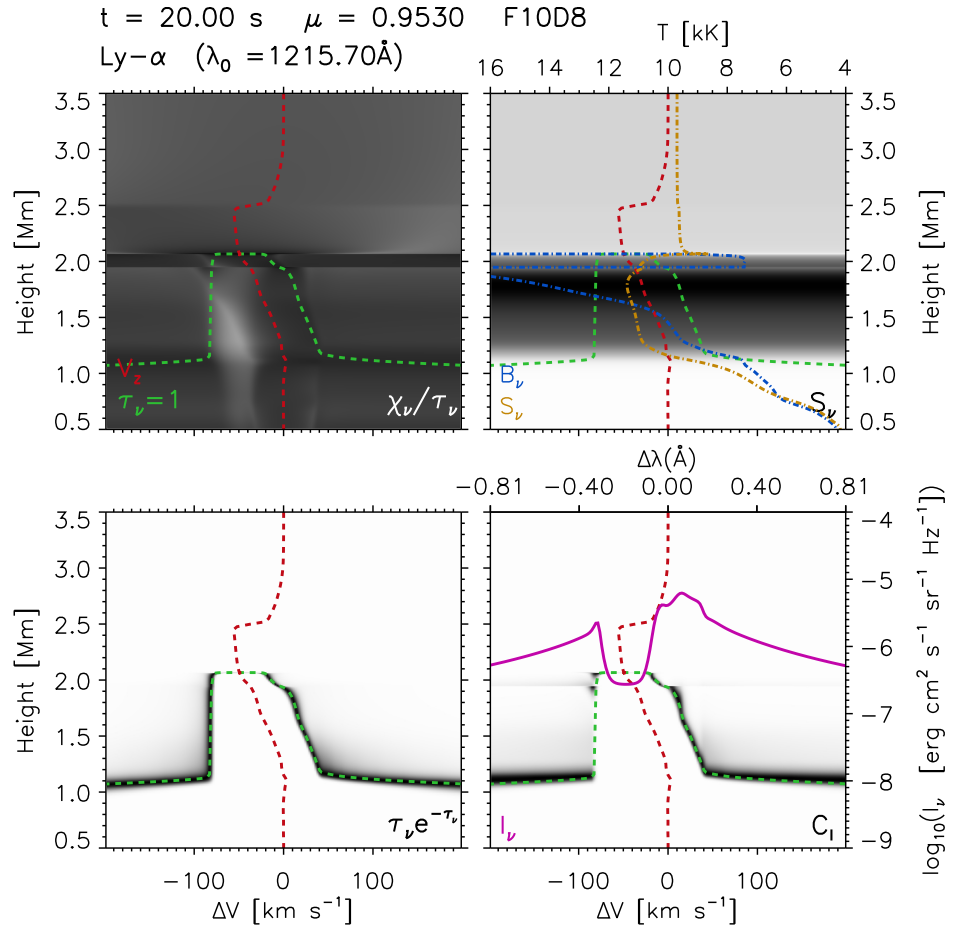


**Figure 4.11:** Components of the Ly- $\alpha$  contribution function at  $t = 20$  s during the F10D8 simulation. The quantities labelled in black are represented in grayscale, with  $V_z$  and the  $\tau_\nu = 1$  surface overplotted in red and green respectively. The broken blue and yellow lines indicate the Planck and source functions. As before,  $\frac{\chi_\nu}{\tau_\nu}$  is scaled logarithmically, while  $C_I$  is normalised. Negative velocities correspond to upflows.

F10D3 simulation there remains some absorption at the theoretical line core.

It is interesting that while Ly- $\alpha$  forms in the presence of  $\sim 50 \text{ km s}^{-1}$  at  $t = 20$  s in both F10 simulations, the blueshift in the line core is more pronounced in this model. By comparing Figures 4.6 and 4.11, it can be seen that in this simulation the region in which the line core forms is extremely narrow, whereas it has a greater vertical extent in the F10D3 simulation. As the core formation region becomes narrower, the

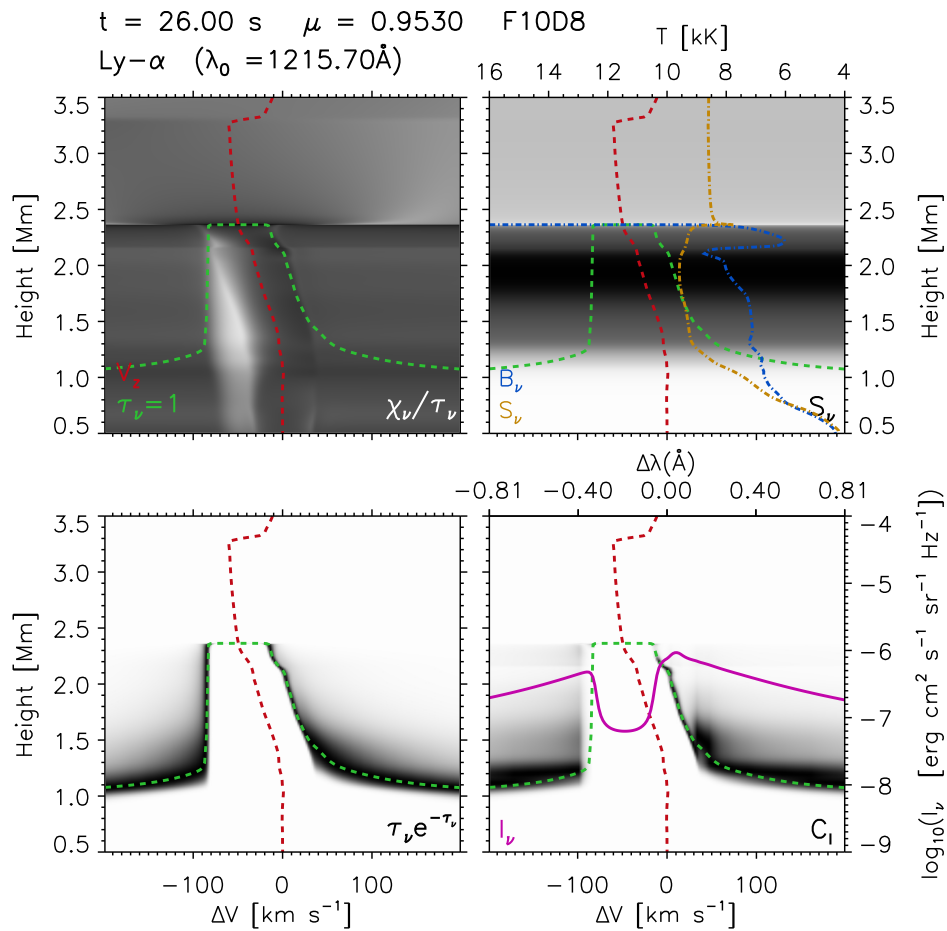


**Figure 4.12:** Components of the Ly- $\alpha$  contribution function at  $t = 26$  s during the F10D8 simulation. Conventions and definitions retain their meanings from Figure 4.11. As before,  $\frac{\chi_\nu}{\tau_\nu}$  is scaled logarithmically, while  $C_I$  is normalised. Negative velocities correspond to upflows.

emission produced there samples a smaller extent of the atmosphere. If the Ly- $\alpha$  line now forms in a thin layer, it should be expected that its shape should be more indicative of the atmospheric dynamics at that height, potentially explaining the more pronounced blueshift visible in Figure 4.11.

By  $t = 26$  s (Figure 4.12), the line-formation region has extended upwards as the atmospheric layers continue to move to greater heights as indicated by the motion of the transition region. The line core is now formed close to 2.4 Mm, and the line

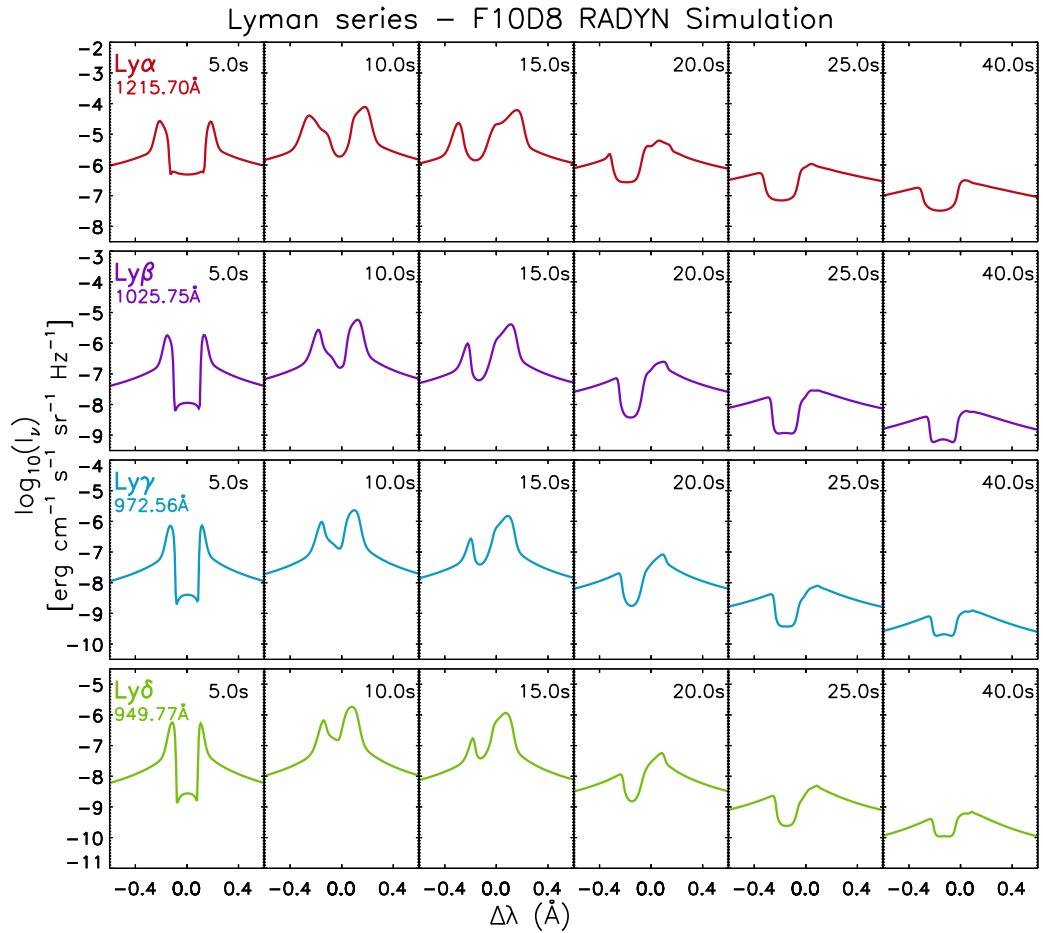


**Figure 4.13:** Snapshots of each of the Lyman lines at various time-steps (labelled in black) throughout the F10D8 simulation. All lines are plotted with a wavelength range of  $1.2 \text{ \AA}$ , symmetric about the theoretical rest wavelength.

source function has undergone an overall decrease since  $t = 20\text{s}$ , resulting in a less intense profile.  $S_\nu$  is still peaked at a height below where the core is formed, and so the line continues to be centrally reversed.

The line contribution function shows that the line core is formed in an extremely narrow region, and continues to be optically-thick. A greater amount of optically-thin emission contributes to the red wing as a result of  $S_\nu$  peaking higher than the  $\tau_\nu = 1$  surface height at these frequencies. The resulting Ly- $\alpha$  line still exhibits a central reversal, which continues to be concentrated primarily blueward of the theoretical line core.

While the Ly- $\alpha$  line forms in a region upflowing at a speed of  $50 \text{ km s}^{-1}$  in both the F10D3 and F10D8 simulations, the effects of the upflow appear to be more pronounced in the emergent line profiles in the F10D8 simulation. In this case, the central reversal is pushed entirely to the blue, while in the  $\delta = 3$  case there remains some absorption at the theoretical line core.

Snapshots of the Ly- $\alpha$  through  $\delta$  lines are shown in Figure 4.13, in which it can be seen that all lines evolve almost identically. All lines are affected by the upflow in the atmosphere, with each of them being centrally reversed. The reversals in the Ly- $\beta$  and higher order lines are narrower than that in the Ly- $\alpha$  line. The similarity throughout the Lyman series again indicates that all lines generally share the same formation process.

### 4.3.3 Line Formation in the 3F10D8 simulation

The most prominent characteristic of the 3F10D8 simulation is the generation of a dense, low-temperature front of material that sweeps rapidly upwards with speeds in excess of  $100 \text{ km s}^{-1}$  (Figure 4.4). The material in the upflow is hydrogen-rich, with a HI population around  $10^6$  greater than the surrounding plasma. It is therefore expected that the upwards propagation of the front of dense plasma should produce a prominent signature in the Lyman line profiles.

Due to similarity in the line profile shapes throughout the Lyman series, we provide a detailed examination of the line formation process for only the Ly- $\alpha$  line. The Ly- $\alpha$  contribution function at  $t = 8 \text{ s}$ , and its individual components, are displayed in Figure 4.14. At this time, the beam's flux is increasing.

At  $t = 8 \text{ s}$ , the Ly- $\alpha$  emission is primarily formed close to the base of the transition region, between  $z = 1.0 - 1.7 \text{ Mm}$ . An upflow with a peak velocity of  $30 \text{ km s}^{-1}$  persists between the core and wing formation heights. Above  $z = 1.7 \text{ Mm}$ , the velocity field abruptly falls to zero, indicating a strong velocity gradient at the base of the transition region. As a result of this, the opacity structure (indicated by the the  $\tau_\nu = 1$  surface) is irregular and asymmetric.

The line source function is peaked at an altitude close to the wing formation

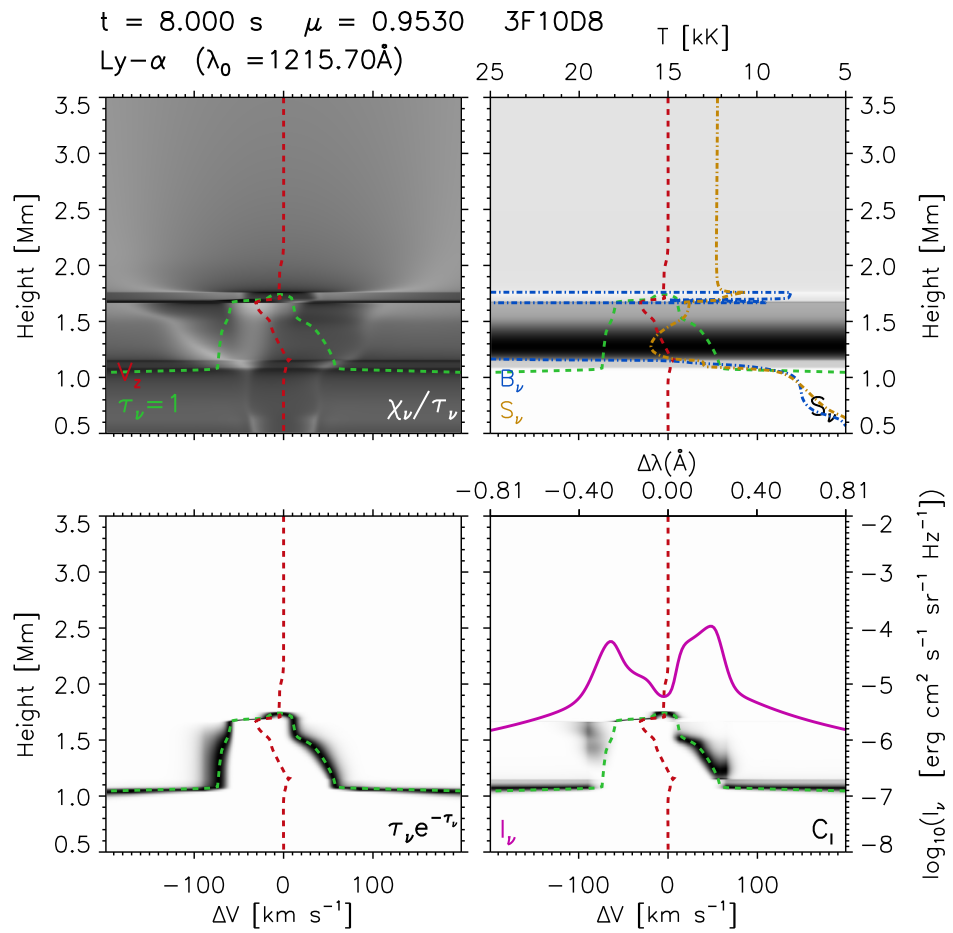


**Figure 4.14:** Components of the Ly- $\alpha$  contribution function at  $t = 8$  s during the 3F10D8 simulation. The quantities labelled in black are represented in grayscale, with  $V_z$  and the  $\tau_\nu = 1$  surface overplotted in red and green respectively. The broken blue and yellow lines indicate the Planck and source functions. As before,  $\frac{\chi_\nu}{\tau_\nu}$  is scaled logarithmically, while  $C_I$  is normalised. Negative velocities correspond to upflows.

height, resulting in an excess of wing emission relative to that in the line core. The line therefore has a central reversal. The Ly- $\alpha$  contribution function indicates that the emission in the core and red wing is predominantly optically-thick. Emission in the far side of the blue wing is largely optically-thin, potentially due to the presence of the upflow. The emergent line profile exhibits a complex shape about the central reversal, with the peaks at the wings supplemented by additional enhancements.

The deepest part of the reversal is still centred at the theoretical rest wavelength, suggesting that the core-formation height is as of yet unperturbed by the flow in the atmosphere.

By  $t = 16.5$  s the beam flux has begun to decrease, while the dynamics of the atmosphere have evolved considerably. Figure 4.4 associated this time with the high-speed upwards propagation of a cool, dense front of material. The Ly- $\alpha$  contribution is examined at this time in Figure 4.15, the components of which indicate particularly interesting consequences as a result of the atmospheric flow structure. Immediately noticeable is a bifurcation in the  $\tau_\nu = 1$  surface, which now has two distinct components.

The central component of the  $\tau_\nu = 1$  surface is largely symmetric, but is slightly shifted to the blue as a result of a weak ( $v_z = 20 \text{ km s}^{-1}$ ) upflow close to the core formation height. The secondary component is symmetric but significantly blueshifted, and indicates that emission in this region of the blue wing is optically thick over an extended range of altitudes. The blue wing photons only become optically-thin at the same height at which the velocity field in the atmosphere reaches its peak speed. This indicates that the rapidly upflowing front of material produces its own emission, which is strongly blueshifted. The  $\frac{\chi_\nu}{\tau_\nu}$  term can be seen to produce strong contributions to the intensity at both points where the velocity field has local maxima ( $z = 1.6$  and  $2.4$  Mm).

The source function throughout the formation region of the central “stationary”  $\tau_\nu = 1$  component is peaked between the core and wing formation heights, resulting in a central reversal. Above this,  $S_\nu$  has a secondary peak at  $2.4$  Mm, cospatial with where the upflowing front of material reaches its peak velocity. This confirms that the upflowing material acts a secondary source of emission, which itself can be clearly seen in the resulting line profile. The emergent Ly- $\alpha$  line has two distinct components, a slightly-blueshifted centrally-reversed core (formed in the low atmosphere), accompanied by an additional centrally-reversed source of emission in the blue wing.

The additional blue wing component is produced by the high-velocity upflow of material, and is formed at  $z = 2.4$  Mm.  $S_\nu$  sharply decreases above the local maximum at this height, resulting in the secondary line component also being self-reversed.

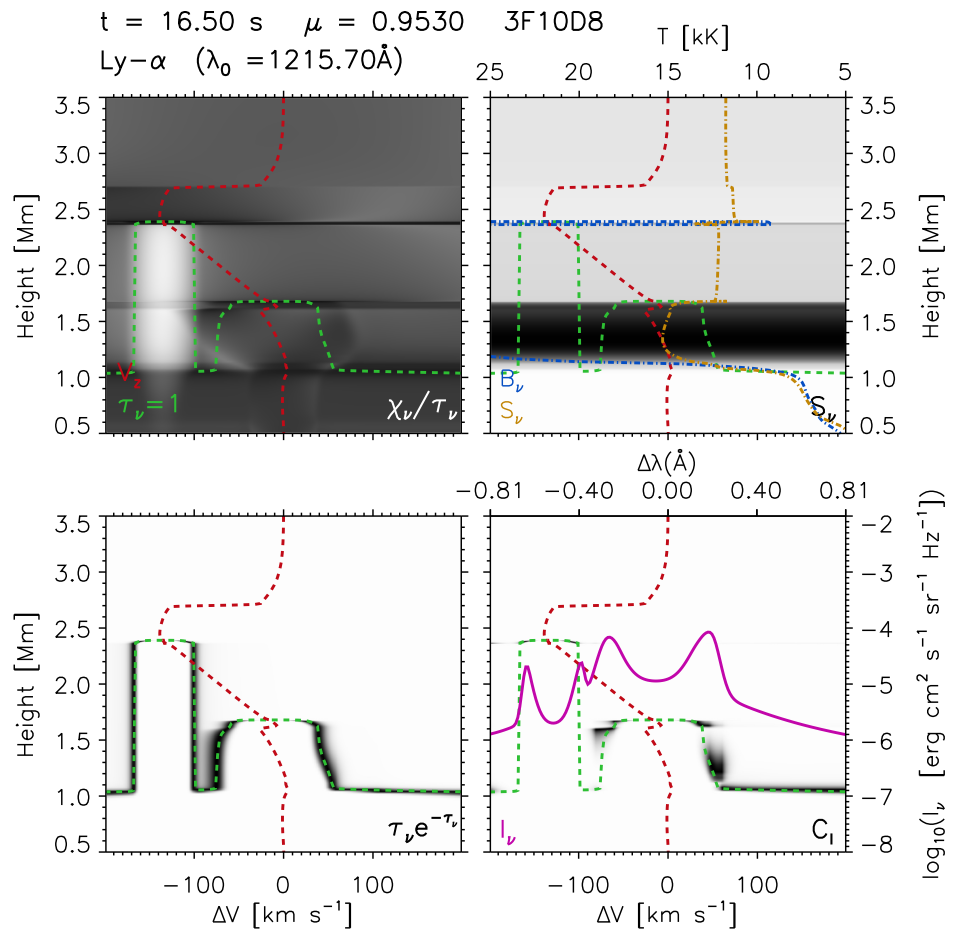


**Figure 4.15:** Components of the Ly- $\alpha$  contribution function at  $t = 16.5$  s during the 3F10D8 simulation. Definitions retain their meanings from Figure 4.14. As before,  $\frac{\chi_\nu}{\tau_\nu}$  is scaled logarithmically, while  $C_I$  is normalised. Negative velocities correspond to upflows.

The line contribution function indicates that the central and blueshifted “cores” are optically-thick, while the wings of the stationary component have optically-thin contributions. The blue wing of the stationary component is predominantly formed at  $z = 1.6$  Mm, indicating a strong contribution from the weakly-upflowing plasma in the low chromosphere.

The electron beam has just stopped heating at  $t = 21$  s, but the dynamics of the atmosphere have not yet had time to equilibrate. Figure 4.16 displays the

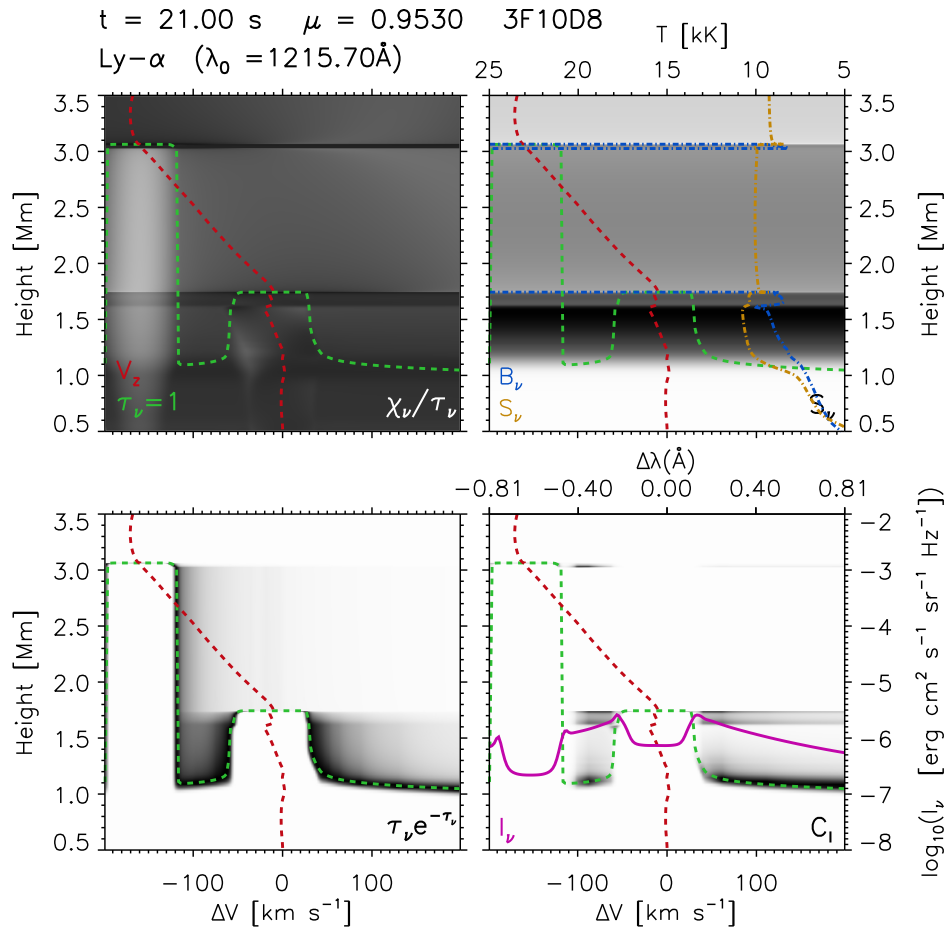


**Figure 4.16:** Components of the Ly- $\alpha$  contribution function at  $t = 21$  s during the  $3F10D8$  simulation. Definitions retain their meanings from Figure 4.14. As before,  $\frac{\chi_\nu}{\tau_\nu}$  is scaled logarithmically, while  $C_I$  is normalised. Negative velocities correspond to upflows.

contribution function for Ly- $\alpha$  at this time, and shows a clear progression of the conditions observed in Figure 4.15.

By  $t = 21$  s, the upwards propagation of the dense material has accelerated, so that the secondary peak in the  $\tau_\nu = 1$  surface moves further into the blue wing. The material itself has moved to a higher altitude, and now acts as a source of opacity at  $z = 3.0$  Mm. Despite the presence of the upflow enhancing the  $\frac{\chi_\nu}{\tau_\nu}$  term, the source function at this height does not have an appreciable enhancement, and the secondary

component is primarily in absorption.

The central “stationary” part of the line has not changed significantly since  $t = 16.5$  s. The primary line core is still formed at a height of 1.7 Mm, and the weak  $20 \text{ km s}^{-1}$  upflow is still present throughout the formation region. The source function peaks around 0.1 Mm lower than where the core is formed, resulting in a shallow central reversal. Due to the flow structure in the lower atmosphere, the  $\frac{\chi_\nu}{\tau_\nu}$  term is enhanced between  $z = 1.6 - 1.7$  Mm and results in an appreciable amount of optically-thin emission in the wings.

The general picture at  $t = 21$  s can be understood as a progression of the case at  $t = 16.5$  s. With the reduction of  $S_\nu$  at high altitudes, the contribution of the secondary line component to the emergent intensity is no longer emissive, and results in a deep excavation of the intensity in the blue wing. Owing to the weak upflows in the lower atmosphere, the centrally-reversed primary component still has a slight blueshift. Both the  $t = 16.5$  and 21 s snapshots indicate that the Ly- $\alpha$  profile is influenced by two distinct flow signatures that originate from different regions of the atmosphere.

Towards the end of the simulation, the secondary component of the  $\tau_\nu = 1$  surface is still a key feature in the opacity structure of the Ly- $\alpha$  line. At  $t = 49$  s (Figure 4.17), the blue wing is optically thick over a very extended region (almost 8 Mm). At  $z = 8$  Mm, the atmosphere is still upflowing with a velocity of around  $170 \text{ km s}^{-1}$ . At this time, the primary component of the  $\tau_\nu = 1$  surface is still blueshifted, due to the persistence of the  $\sim 20 \text{ km s}^{-1}$  upflow in the lower chromosphere.

The Ly- $\alpha$  source function now has a simple profile as a function of altitude, with an initial maximum deep in the chromosphere ( $z = 1.7$  Mm).  $S_\nu$  then decreases with altitude, and remains constant until a secondary peak is contributed at 7.6 Mm by the dense, upflowing front of material. It is again observed that both the stationary and moving components of the line are self-reversed as a result of  $S_\nu$  peaking at altitudes deeper than where the corresponding core photons can be emitted.

The emergent Ly- $\alpha$  line at  $t = 49$ s is composed of a stationary and the moving component, featuring an optically-thick line core with optically-thin wings. Owing to an overall decrease in  $S_\nu$  since  $t = 21$  s, the intensity of the line profile is now

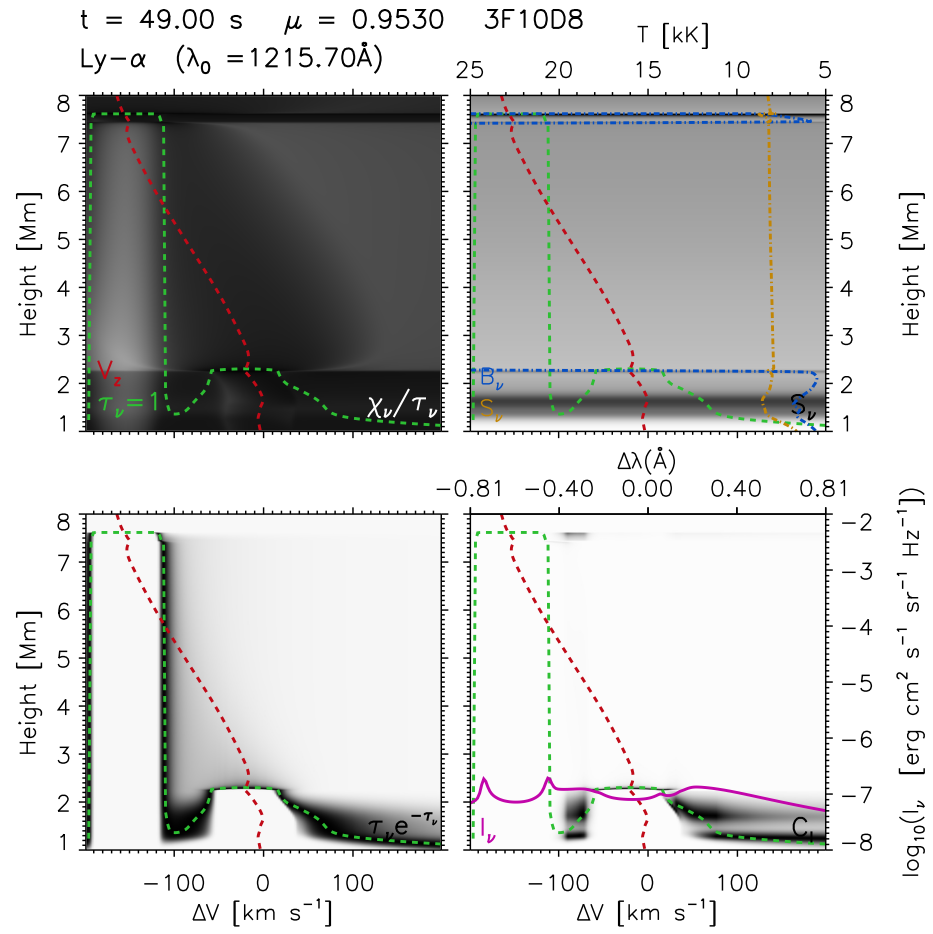


**Figure 4.17:** Components of the Ly- $\alpha$  contribution function at  $t = 49$  s during the  $3F10D8$  simulation. Definitions retain their meanings from Figure 4.14. As before,  $\frac{\chi_\nu}{\tau_\nu}$  is scaled logarithmically, while  $C_I$  is normalised. Negative velocities correspond to upflows.

weaker than before. Combined with the central reversal, this results in a rather flat line profile. The moving component of the line is highly blueshifted and is flanked by wing-like structures either side of its self-reversal, which contribute a high amount of emission relative to the rest of the profile.

The formation of the Ly- $\alpha$  line in this simulation strongly reflects the complex velocity field in the atmosphere. A clear bifurcation in the opacity structure of the line is formed as a result of a rapid ( $v_z = 150 \text{ km s}^{-1}$ ) upflow, which carries with it an

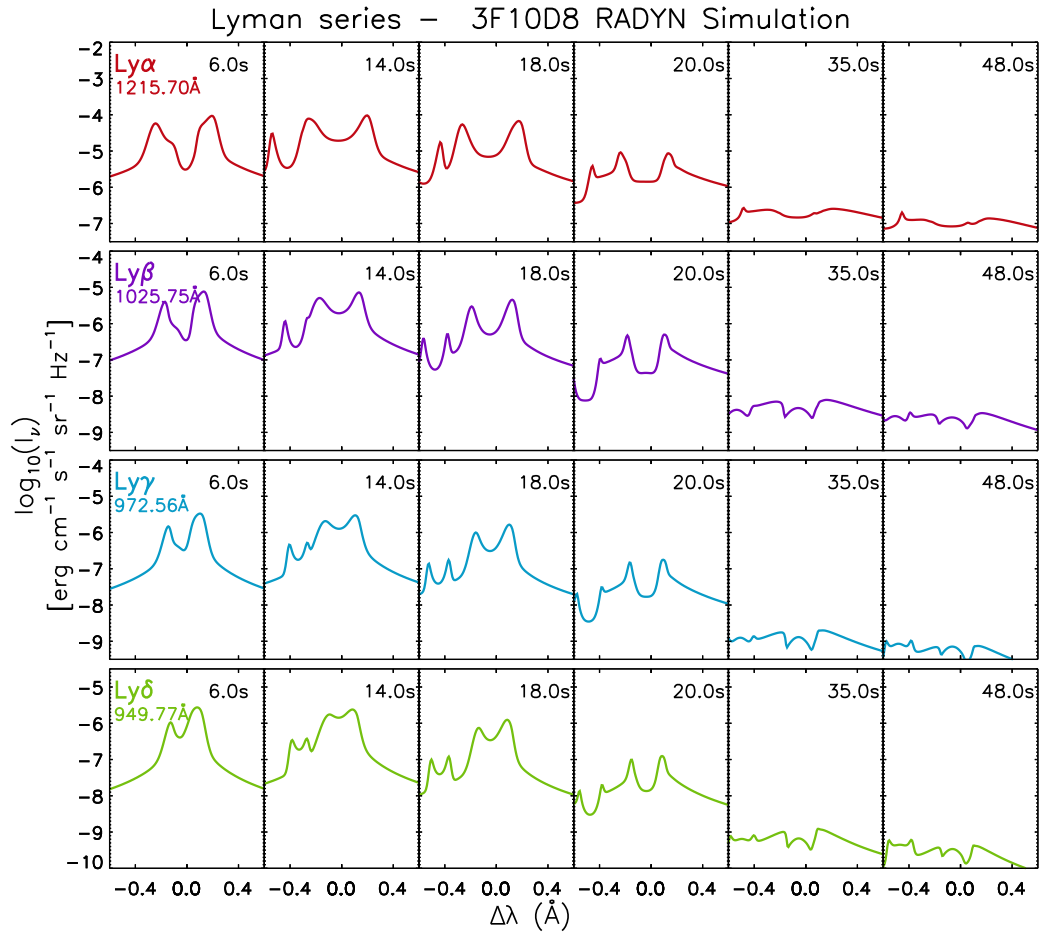


**Figure 4.18:** Snapshots of each of the Lyman lines at various time-steps (labelled in black) throughout the 3F10D8 simulation. All lines are plotted with a wavelength range of 1.2 Å, symmetric about the theoretical rest wavelength.

appreciable amount of plasma. This plasma acts as a secondary source of emission, as evidenced by an additional blueshifted line component which has a frequency extent equal to that of the secondary  $\tau_{\nu} = 1$  surface. The acceleration of this material leads to a secondary emission signature in the Ly- $\alpha$  line which propagates through the blue wing between  $t = 10 - 20$  s. The primary component of the line is also subject to a slight blueshift as a result of a weak ( $\sim 20$  km s $^{-1}$ ) upflow permeating the lower chromosphere.

As with the F10 simulations, maxima in the line source function are attained at intermediate altitudes between the core and wing formation heights for both the

stationary and moving line components. This results in both components of the line being self-reversed, and introduces a varying amount of both emission and absorption in the blue wing.

In Figure 4.18, it can clearly be seen that all Lyman lines in this simulation exhibit the secondary blueshifted component, indicating that the upflowing plasma emits in all of the Lyman series. Weak blueshifts are also observed in all cases in the central cores of these lines, which are all centrally-reversed. The combination of these factors assures us that, as with the F10D3 simulation, the line-formation process generally proceeds the same way for each of the lines.

#### 4.3.4 Line Formation in the F11D3 simulation

The final simulation considered is characterised by a high peak flux, with a beam injection profile and evolution timescale equal to that of the F10D3 model. As in §4.3.3, the detailed aspects of line formation throughout this simulation are outlined for only the Ly- $\alpha$  line as a result of the higher order lines displaying similar characteristics.

At  $t = 9$  s, the beam is close to reaching its peak flux ( $1.0 \times 10^{11}$  erg cm $^{-2}$  s $^{-1}$ ). The Ly- $\alpha$  contribution for this time is displayed in Figure 4.19. At this time, the majority of the chromosphere is subject to a very fast ( $v > 200$  km s $^{-1}$ ) upflow, which has a steep gradient at its upper edge ( $z = 2.9$  Mm). However, as indicated by the  $\tau_\nu = 1$  surface, the height at which the line core forms is actually flowing downwards with a speed of 20 km s $^{-1}$ . At this height, there exists a notable velocity gradient as the lower layers of the atmosphere are upflowing.

The  $\tau_\nu = 1$  surface is asymmetric, with a sharp red-wing boundary in altitude at  $\Delta V = 60$  km s $^{-1}$ . Conversely, the blue wing becomes optically thin at frequencies closer to the line core than in the red wing, which facilitates an enhancement in the  $\frac{\chi_\nu}{\tau_\nu}$  term blueward of the core. The height of the  $\tau_\nu = 1$  surface indicates that the line core is formed at  $z = 1.55$  Mm.

As observed in the previous simulations,  $S_\nu$  is again peaked deep in the chromosphere, below the core-formation height. The line contribution function indicates

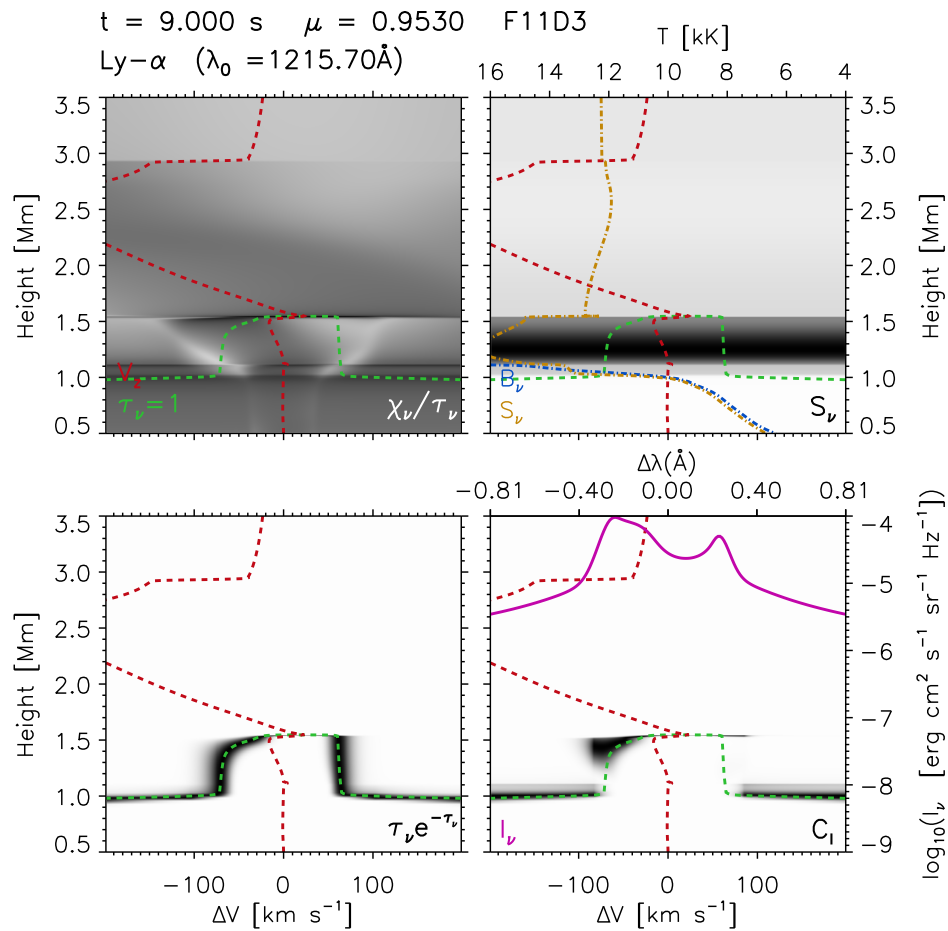


**Figure 4.19:** Components of the Ly- $\alpha$  contribution function at  $t = 9$  s during the F11D3 simulation. Quantities labelled in black are imaged in grayscale, with  $V_z$  and the  $\tau_\nu = 1$  surface overplotted in red and green respectively. The broken blue and yellow lines indicate the Planck and source functions. As before,  $\frac{\chi_\nu}{\tau_\nu}$  is scaled logarithmically, while  $C_I$  is normalised. Negative velocities correspond to upflows.

that while the line core is optically-thick, both wings contain appreciable amounts of optically-thin emission, with that in the blue wing being more pronounced. This is due to the high opacity at the core-formation height combined with the drop in  $\tau_\nu$  in the blue wing.

The emergent Ly- $\alpha$  line is again centrally-reversed, due to  $S_\nu$  reaching a maximum deep in the chromosphere where the line wings are formed. The core itself is slightly

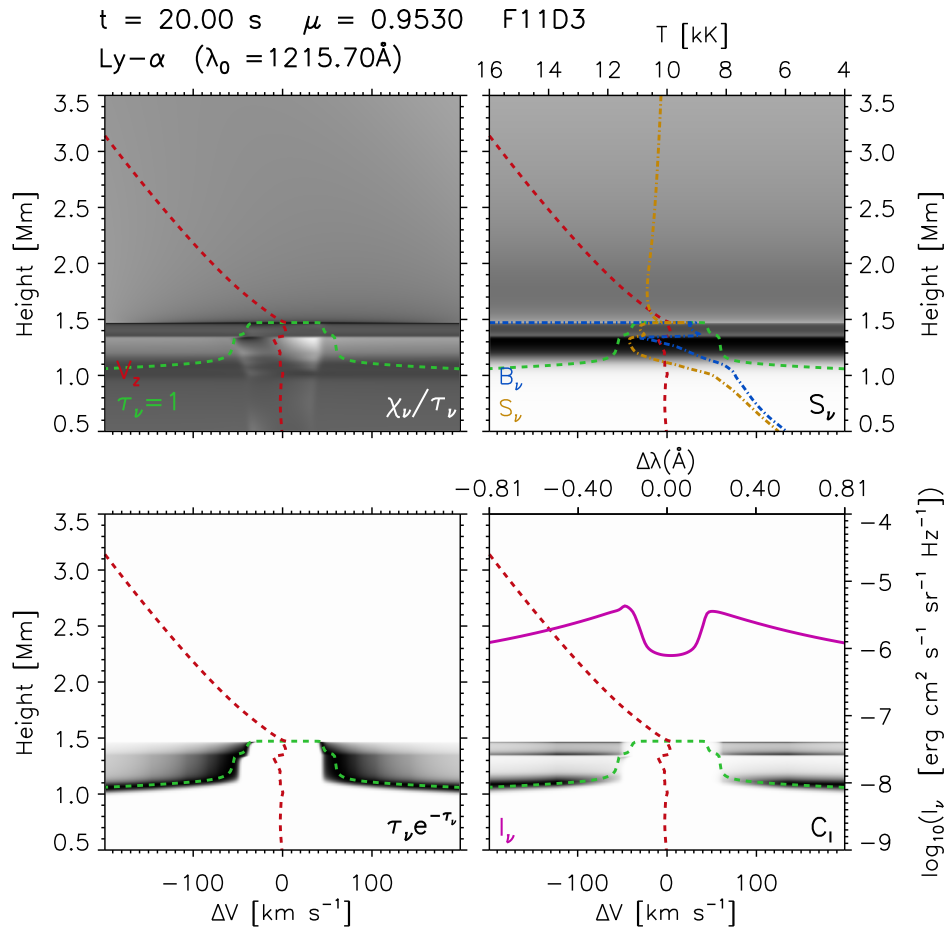


**Figure 4.20:** Components of the Ly- $\alpha$  contribution function at  $t = 20$  s during the F11D3 simulation. Definitions retain their meanings from Figure 4.19. As before,  $\frac{\chi_\nu}{\tau_\nu}$  is scaled logarithmically, while  $C_I$  is normalised. Negative velocities correspond to upflows.

redshifted, and is flanked by enhancements in both wings, with the blue wing being more intense.

At  $t = 20$  s (Figure 4.20), the electron beam has just stopped heating the atmosphere. The  $\tau_\nu = 1$  surface has become largely symmetric, and now peaks just below  $z = 1.5$  Mm, slightly deeper in the atmosphere than at  $t = 9$  s. The core-formation height is completely isolated from the effects of the fast upflow that permeates the majority of the upper atmosphere, and is cospatial with an extremely weak downflow.

A weak ( $\sim 10 \text{ km s}^{-1}$ ) upflow can be seen at  $z = 1.35 \text{ Mm}$ , which produces a slight enhancement in  $\frac{X_\nu}{\tau_\nu}$ .

$S_\nu$  has undergone an overall decrease throughout the line formation, and continues to peak at an intermediate altitude between where the far wings and line core are formed. As a result, the line is still centrally-reversed. The line contribution function suggests that the line core is optically-thick but the wings are predominantly optically-thin, and the resulting Ly- $\alpha$  line is largely symmetric as the region over which it forms is dynamically inert. While there are very fast upflow speeds within the atmosphere, they do not affect the deep chromosphere and the emergent Ly- $\alpha$  line reflects this.

While the dynamics of the beam-heating stage of the simulation do not greatly affect the formation of the Lyman lines, the later stages of this simulation present some interesting results. At  $t = 45 \text{ s}$  (Figure 4.21), the dynamics of the atmosphere have changed considerably. While the atmosphere in the upper chromosphere and transition region was previously upflowing, it now exhibits a strong downflow of around  $100 \text{ km s}^{-1}$ .

The  $\tau_\nu = 1$  surface indicates that the opacity structure of the Ly- $\alpha$  line now encompasses a narrow range of heights, with only  $0.25 \text{ Mm}$  spanned between where the core and wings become optically thick. The line core is formed at  $z = 1.5 \text{ Mm}$ , and does so at the base of the transition region. Directly above this height there exists a steep velocity gradient, linking the stationary core-formation height to the fast downflow propagating down from the corona.

At this time,  $S_\nu$  is now dominant above the  $\tau_\nu = 1$  surface of the Ly- $\alpha$  line, with only a minor enhancement at the core-formation height. It peaks just above this height, and diminishes gradually with altitude. As a result, the emergent line profile is much weaker in intensity than at  $t = 20 \text{ s}$ . It is predominantly emitting with weak far wings, but does have a shallow central-reversal, potentially a result of the production of optically-thin emission in the near wings.

The line formation process then evolves considerably as the downflowing material from the corona reaches the core formation height. At  $t = 47 \text{ s}$  (Figure 4.22), the velocity structure in the atmosphere is complex. 2 s prior to this time, the atmosphere

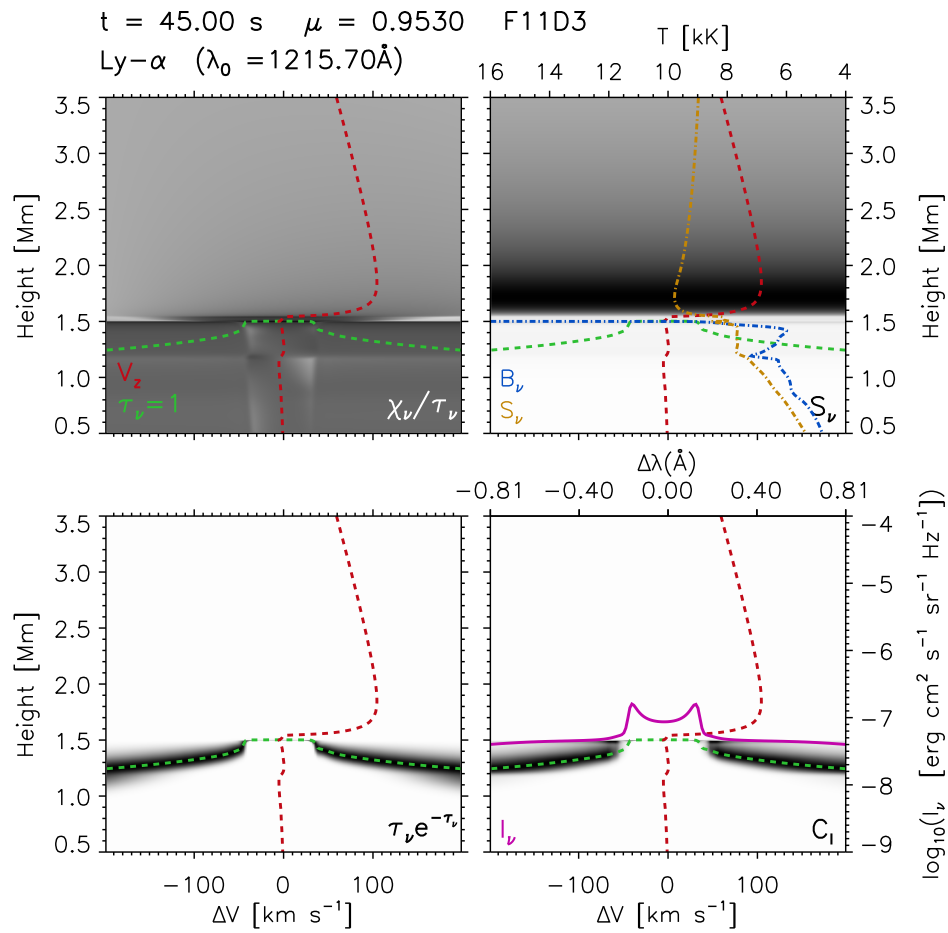


**Figure 4.21:** Components of the Ly- $\alpha$  contribution function at  $t = 45$  s during the F11D3 simulation. Definitions retain their meanings from Figure 4.19. As before,  $\frac{X_v}{T_v}$  is scaled logarithmically, while  $C_I$  is normalised. Negative velocities correspond to upflows.

above  $z = 1.5$  Mm was wholly downflowing. There now exists an upflow between  $z = 1.45 - 1.7$  Mm, above which there is a steep velocity gradient as the upflowing material runs into the continuous downflow from the corona.

It appears that upon reaching the core-formation height (close to the transition region), the downflowing material rebounds and begins to propagate upwards. The velocity field also indicates that the core-formation height moves downwards as a result, with a speed of  $\sim 25 \text{ km s}^{-1}$ . This, along with the visible motion of the

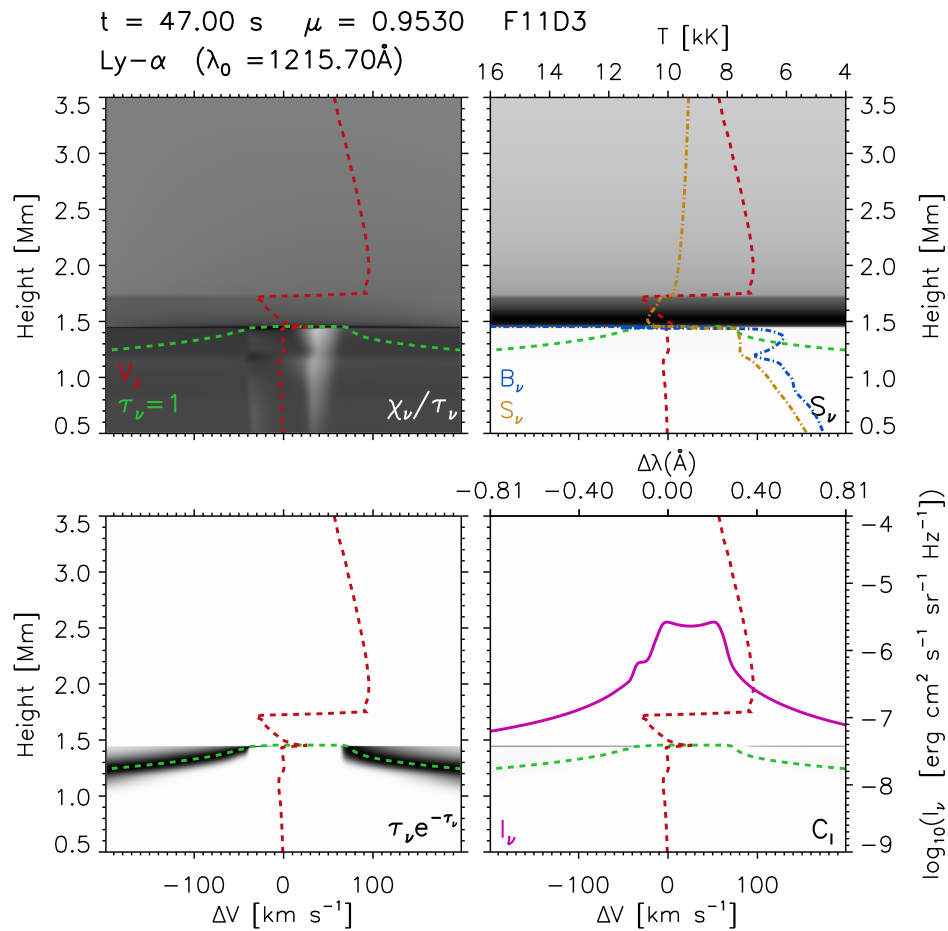


**Figure 4.22:** Components of the Ly- $\alpha$  contribution function at  $t = 47$  s during the F11D3 simulation. Definitions retain their meanings from Figure 4.19. As before,  $\frac{\chi_v}{\tau_v}$  is scaled logarithmically, while  $C_l$  is normalised. Negative velocities correspond to upflows.

transition region and enhancement in  $n_e$  in Figure 4.5 suggest that this region is compressed somewhat by the downflowing material and is also driven downwards as a result.

The line source function has increased since  $t = 45$  s and is primarily concentrated in the upflowing region of the atmosphere, above the core-formation height. The line contribution function indicates that emission is produced exclusively within an extremely thin region of the atmosphere, co-spatial with the height that the

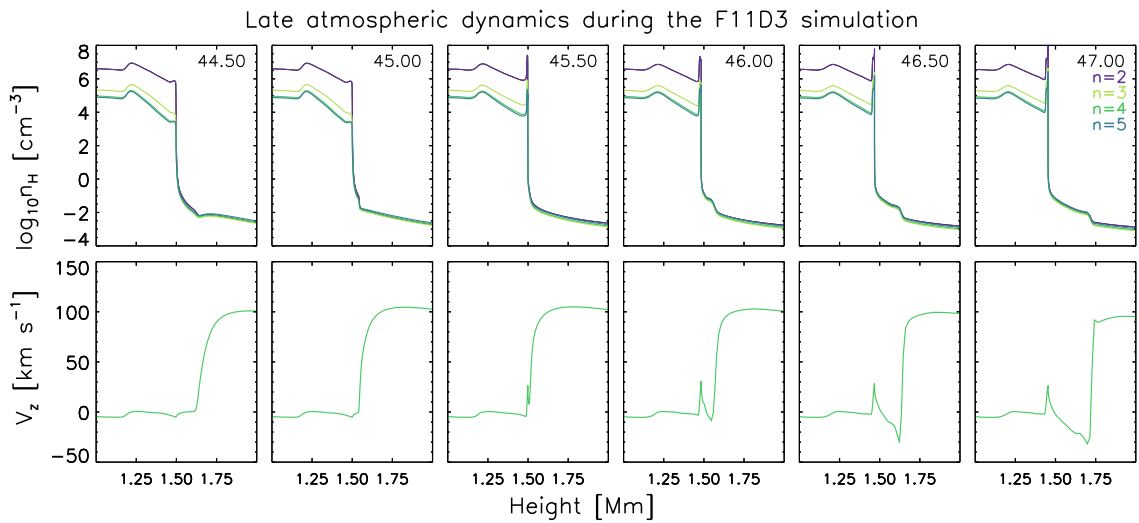


**Figure 4.23:** Population densities of the upper levels of hydrogen (upper panels) plotted for the labelled time steps. The atmospheric velocities at these times are plotted in the lower panels, with positive values indicating downflowing plasma.

atmospheric flow rebounds from.

The resulting line profile is visibly enhanced with respect to that of 2 s prior, with a notable redshift as a result of the downflow at the core-formation height. It is predominantly emissive, with a very shallow reversal at the line core. An additional, weakly-emitting component can be seen in the blue wing, produced by an enhancement in  $\frac{\chi_\nu}{\tau_\nu}$ .

The generation of the emission in Ly- $\alpha$  from  $t = 45$  s onwards can be explained as follows: downward flowing plasma from the corona (likely as a result of the reflecting upper boundary which is included to mimic waves incoming from the other footpoint) meets stationary plasma at the base of the transition region. The downward flow compresses the plasma in this region, facilitating the collisional population of the upper levels of hydrogen, which causes the line to radiate. The previously-downflowing plasma then abruptly changes direction, rebounding upwards. Figure 4.23 displays the population densities of the upper levels of hydrogen around this time, along with the atmospheric velocity structure. Prominent enhancements in the level populations can be seen at  $z = 1.5$  Mm, cospatial with the reversal in the

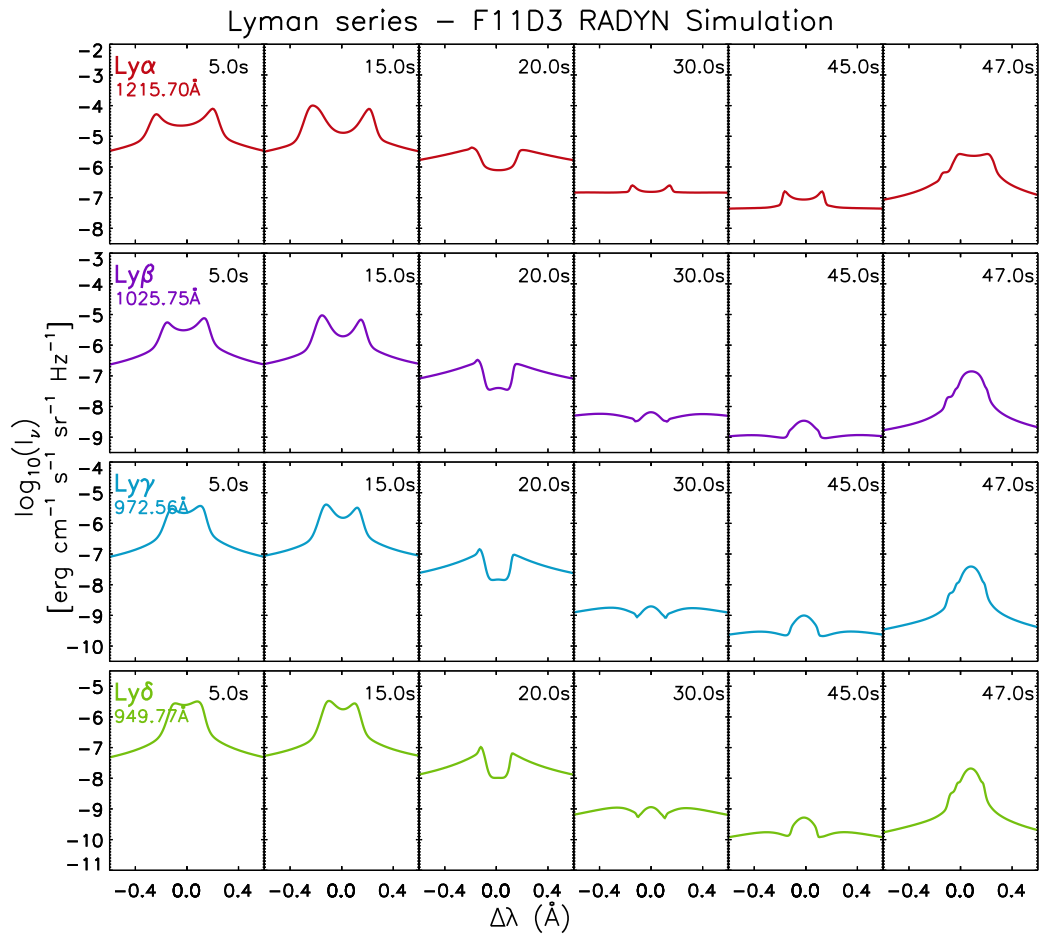


**Figure 4.24:** Snapshots of each of the Lyman lines at various time-steps (labelled in black) throughout the F11D3 simulation. All lines are plotted with a wavelength range of  $1.2 \text{ \AA}$ , symmetric about the theoretical rest wavelength.

atmospheric flow direction.

In Figure 4.24, additional snapshots of the higher order Lyman lines are shown for various time-steps throughout the F11D3 simulation. As in the previous models, all Lyman lines exhibit consistent shapes, indicating that they are formed under the same conditions. All lines respond to the compression of the atmosphere by the downflow between  $t = 45 - 50$  s by displaying heightened levels of emission.

## 4.4 Summary of Results from Flare Simulations

Across all of the simulations detailed in this chapter, the interplay between the atmospheric hydrodynamics and the radiation field has led to many intricacies being observed in the line formation process. While particularities remain with respect to the injected beam, there are some overarching concepts regarding the production of emission in the Lyman lines that can be briefly summarised:

- Line formation generally proceeds the same way for each of the Lyman lines, with the higher order lines displaying near-identical shapes to that of the Ly- $\alpha$  line.
- The cores of the Lyman lines are often centrally-reversed in these simulations, as a result of  $S_\nu$  peaking at heights below where the line cores are formed.
- The Lyman lines can be heavily influenced by the upflows initiated in these simulations. Both F10 simulations produce strongly blueshifted line cores, and the 3F10D8 simulation contains an additional blueshifted component produced by an emissive front of upflowing plasma.

It is important to note that the model line profiles from RADYN do not correctly account for PRD, and assume that there is no coherence between absorbed and re-emitted photons. While RADYN does not compute the Lyman lines with PRD, the formalism is approximated by using the method of [Leenaarts et al. \(2012\)](#). This approach models the Lyman lines as Gaussian profiles in CRD with Doppler broadening only, and was found to provide the best match in H $\alpha$  core-intensity to that of the same line in PRD.

In order to fully account for a partial level of frequency coherence in photons absorbed and re-emitted by the Lyman lines, the RH code ([Uitenbroek 2001](#)) is used (Chapter 5). Snapshots from each of the simulations described in this chapter are used as input to this additional code, with the radiative transfer re-solved for the Lyman lines with the effects of PRD included. The model line profiles from both RADYN and RH are then convolved with a synthetic instrumental profile, and

Doppler shifts in the lines are detected and quantified. This provides a basis from which a detailed comparison between simulations and observations can be assessed.

## Chapter 5

# Simulated Observations of Flows in the Flaring Chromosphere

*The work presented in this chapter was published in [Brown et al. \(2018\)](#)*

In Chapter 3, EVE observations of Doppler shifts in the Lyman lines were presented. The majority of the observed velocity profiles suggested flow speeds of around  $30 \text{ km s}^{-1}$ , but a consensus on flow direction was not found. In Chapter 4, flare simulations suggested that upflows are initiated in the chromosphere as a result of the beam injection, with the Lyman lines frequently exhibiting blueshifted line cores. However, these simulations did not correctly account for the effects of PRD.

The concept of PRD was established in §2.4.1, but it now becomes important to consider the relevance of this formalism for the treatment of the Lyman lines. It is worth reiterating that the effects of PRD should be considered for both strong and resonance lines, and in low-density media. Given that the resonance Ly- $\alpha$  line and the higher-order Lyman lines are strong emitters in the chromosphere, and that they are formed over a range of heights, a PRD treatment is recommended. We detail the key points in this section, but for more information the reader is encouraged to consult [Hubeny & Mihalas \(2014\)](#).

In computation of theoretical Ly- $\alpha$  profiles, [Vernazza et al. \(1973\)](#) found that the wing intensities obtained when using CRD were significantly larger than those observed. By adjusting the proportions of the scattering mechanism, greater agreement

was found with observed Ly- $\alpha$  profiles. To achieve this, the authors used coherent scattering 93 % of the time, with redistribution 7 % of the time in the line wings.

Hubeny & Lites (1995) incorporated PRD into the non-LTE code MULTI, and detailed the importance of these effects for the Ly- $\alpha$  and Ly- $\beta$  lines. They explain the importance of accounting for cross-redistribution (for example, Ly- $\beta$  shares the same upper level as H $\alpha$ ), and that a large amount of scattering in the wings of Ly- $\alpha$  can lead to a significant change in its flux. They showed that the choice of either CRD or PRD heavily influences the populations of the upper levels of hydrogen, and that while more important for the Ly- $\alpha$  line, the wing intensities in Ly- $\alpha$  and Ly- $\beta$  have a strong dependence on the scattering mechanism used.

Milkey & Mihalas (1973) note that the assumption of CRD can also lead to inaccuracies in the intensities in the Lyman continuum, and that the intensity ratio between Ly- $\alpha$  profiles computed with CRD and PRD can be as high as 6. Clearly, an inaccurate treatment of photon scattering in the Lyman lines is not of little consequence, particularly in Ly- $\alpha$ .

In this chapter, we consider a full treatment of PRD effects by using the RH code, and bridge the gap between observation and simulation. While we have connected features in the line profiles from RADYN to dynamical aspects of the simulated atmospheres, there remains the issue of how these line profiles would appear when observed by an instrument such as EVE.

In this chapter, the model line profiles from RADYN and RH are convolved with the EVE instrumental profile. The degraded profiles are then analysed using two of the methods described in Chapter 3, which allows Doppler shifts to be calculated in the synthetic Lyman lines. In effect, this allows us to simulate an observation. The Doppler velocity profiles are then compared to the flow signatures that were described in Chapter 4, and the differences between the RADYN (CRD) and RH (PRD) line profiles are assessed. Finally, a brief examination of the potential capabilities of the upcoming Solar Orbiter's Spectral Imaging of the Coronal Environment (SPICE) instrument is performed.

## 5.1 Model Line Profiles in RADYN and RH

For each of the simulations described in Chapter 4, their time-resolved atmospheric arrays were decomposed into a series of snapshots. These snapshots list the solutions for the atmospheric  $T$ ,  $n_e$ ,  $V_z$  arrays and a microturbulent parameter ( $V_{turb}$ ) on a depth scale described as a function of column mass. Each snapshot was then used as an input atmosphere to the 1-D RH code (**rhf1d**), which was run sequentially until all atmospheric grids for each simulation were used. The radiative transfer for each simulation was calculated in RH using an active 6-level hydrogen atom. Ca II and C I are included as active species and the remaining ions are treated as passive (LTE) elements.

Each of the Lyman line transitions in the hydrogen atom file were set to be calculated in PRD, and accounting for an upper continuum level this results in the calculation of model line profiles for Ly- $\alpha$  through Ly- $\delta$ . The initial solution for the hydrogen populations was obtained in statistical equilibrium by setting the radiation field to zero, as this was advised to be a more stable solution (J. de la Cruz Rodríguez, private communication). Each of the RADYN simulations had their time-dependent atmospheric arrays decomposed, producing snapshots at a 0.3 s cadence for each model. As a result of the steep velocity gradients induced in the  $\delta = 8$  simulations (F10D8 and 3F10D8 models), the RH code struggled to converge and many of the snapshots did not reach a solution in these models. Despite this, the RH code provides an additional set of model line profiles for each of the simulations.

The detailed examination of the Lyman lines in Chapter 4 was facilitated by the remarkable wavelength sampling of the model line profiles. In RADYN simulations, the wavelength sampling about the core of the computed Ly- $\alpha$  profiles is  $\sim 0.009$  Å. This resolution permits the examination of fine structure in the line. Similarly, when RH is used to obtain Ly- $\alpha$  profiles, the spacing of the wavelength bins around the core of the line is of the order  $\sim 0.002$  Å. In both RADYN and RH, the higher order lines are also resolved to the same order of magnitude as the Ly- $\alpha$  line.

We refrain from detailed visual comparisons between RADYN profiles and their RH counterparts until §5.2, in which similarities and differences are discussed for

each individual simulation. However, as a general overview, the emergent line profiles from RH are almost identical to those from RADYN at times corresponding to beam-heating in the RADYN simulations. After these times, the emergent wing intensities in the RH profiles sharply decrease relative to those in RADYN, dropping by more than an order of magnitude. Intensities in the cores of the RH lines also decrease, but by a less substantial amount. This leads to the RH lines having sharply-peaked cores after the beam-heating stage, in contrast to the RADYN profiles which remain dominated by central reversals. The reasons for this divergent evolution of the RH profiles relative to those from RADYN are discussed in §5.3.

## 5.2 Simulated EVE Observations of Flows

In contrast to the detailed model line profiles output by RADYN and RH, the EVE instrument does not have comparable levels of spectral resolution or temporal cadence. The spectral resolution of the EVE instrument is around  $1 \text{ \AA}$ , while the individual spacing of the wavelength bins is equal to  $0.2 \text{ \AA}$ . Additionally, a single data-point in the EVE spectrum requires an integration of 10 s, whereas the temporal capabilities in simulation allow for a cadence of below 1 s.

There must therefore be a loss of information in the spectral lines observed by EVE, as the lines are smeared out by the instrumental profile. It was found in Chapter 4 that there can be highly-localised and narrow features in the Lyman lines, and so it is important to consider how such details may be lost or misrepresented through the course of observation. According to [Crotser et al. \(2007\)](#), the resolution of the MEGS-B detector varies with wavelength, but throughout the Lyman series the resolution is maintained at  $\sim 0.85 \text{ \AA}$ .

In order to simulate an observation by an instrument such as EVE, the model line profiles from RADYN and RH must be altered. The RADYN line profiles have their range extended in wavelength in order to facilitate convolution. Both sets of line profiles are then convolved with a Gaussian of FWHM  $0.85 \text{ \AA}$  using the IDL

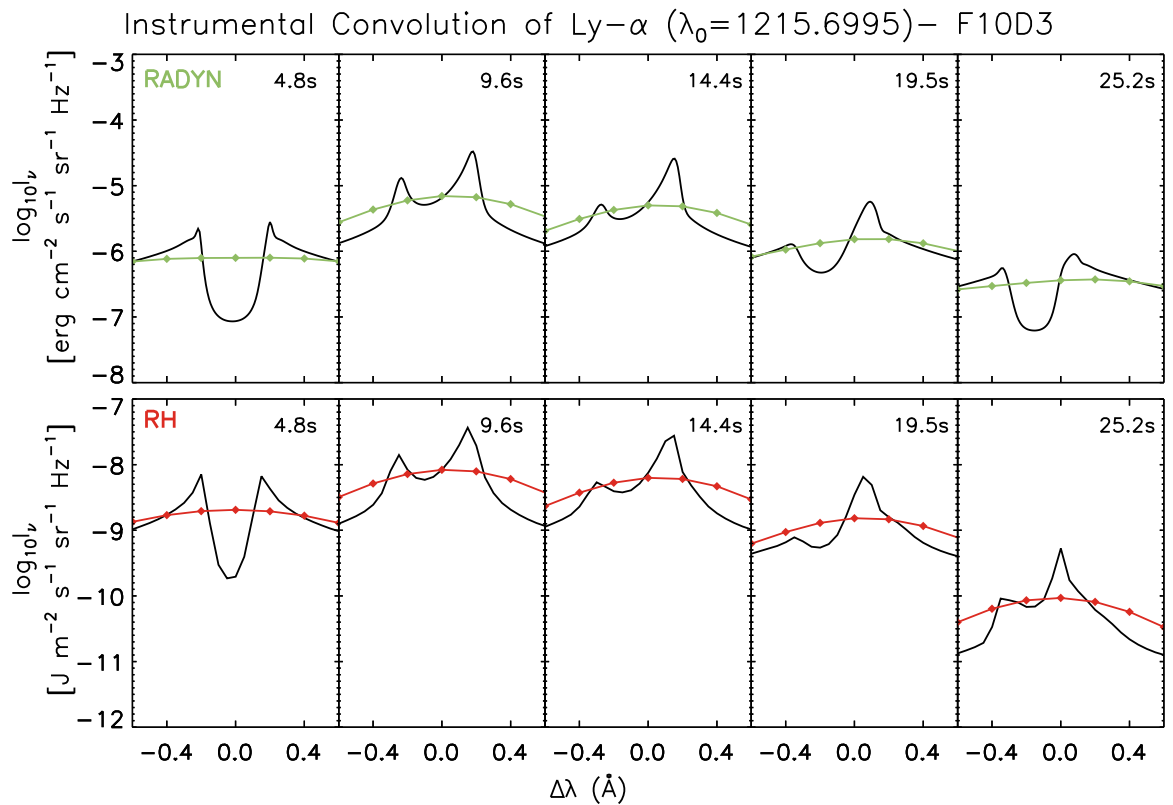


**Figure 5.1:** Ly- $\alpha$  profiles obtained from the F10D3 simulation, as calculated by RADYN (upper panels) and RH (using PRD, lower panels). Overplotted in the coloured lines are the resulting line profiles when they are convolved with EVE’s instrumental profile. The upper right of each panel lists the simulation time.

**gaussfold**<sup>1</sup> procedure. Given the instrumental parameters provided in [Crotser et al. \(2007\)](#), this should emulate the line spread function of MEGS-B with reasonable accuracy. Both sets of convolved arrays then undergo a final rebinning to the same wavelength spacing as the EVE instrument ( $0.2 \text{ \AA}$ ).

A comparison between the raw RADYN and RH line profiles before and after instrumental convolution is shown in Figure 5.1, which shows examples from the F10D3 simulation. The convolution process visibly degrades the line profiles, which exhibit a diminished amount of overall structure afterwards. Furthermore, all hints

<sup>1</sup>[https://github.com/emrahk/IDL\\_General/blob/master/third\\_party/aitlib/misc/gaussfold.pro](https://github.com/emrahk/IDL_General/blob/master/third_party/aitlib/misc/gaussfold.pro)

of a central reversal in a given line are generally erased, as the irradiance is smeared out by the instrumental profile.

The degraded profiles resulting from instrumental convolution are equivalent to those observed by the EVE instrument. In order to draw any conclusions regarding the observations made in Chapter 3 with respect to the simulated dynamics of the chromosphere in Chapter 4, the Doppler shifts in these degraded profiles must be calculated.

As in Chapter 3, measurements of the deviation of line centroid positions are performed using Gaussian fitting and intensity weighting. As the cross-correlation method requires a robust definition of a pre-flare line profile, this method is not performed as the electron beams in each simulation are initially injected at  $t = 0$  s. Gaussians are again assumed to consist of 4 parameters, allowing for a constant background intensity.

The parameters of the Gaussian fits are again constrained. The height of the Gaussian must lie between 0.5 and 1.05 times the maximum intensity in the convolved profile. The position of the line centroid is not constrained, but the width of the Gaussian must lie between 0.1 and 0.7 Å. Finally, the allowed value for the background intensity ranges from 0.1 to 1 times that of the minimum intensity in the line. These constraints are modified if the line is in absorption. Gaussian fits to model RADYN and RH Ly- $\alpha$  profiles after instrumental convolution are shown in Figure 5.2.

Measurements of the line centroids are obtained from these two methods at regular intervals (0.3 s) for each of the simulations. Doppler velocities are calculated with respect to the theoretical rest wavelength values in RADYN and RH. Additional velocities are obtained for lines that have been integrated for 10 second intervals in order to fully emulate the EVE observations. Integrating the line profiles for 10 s heavily reduces the number of data points, and so the velocity results from profiles that have not undergone time-integration are also presented.

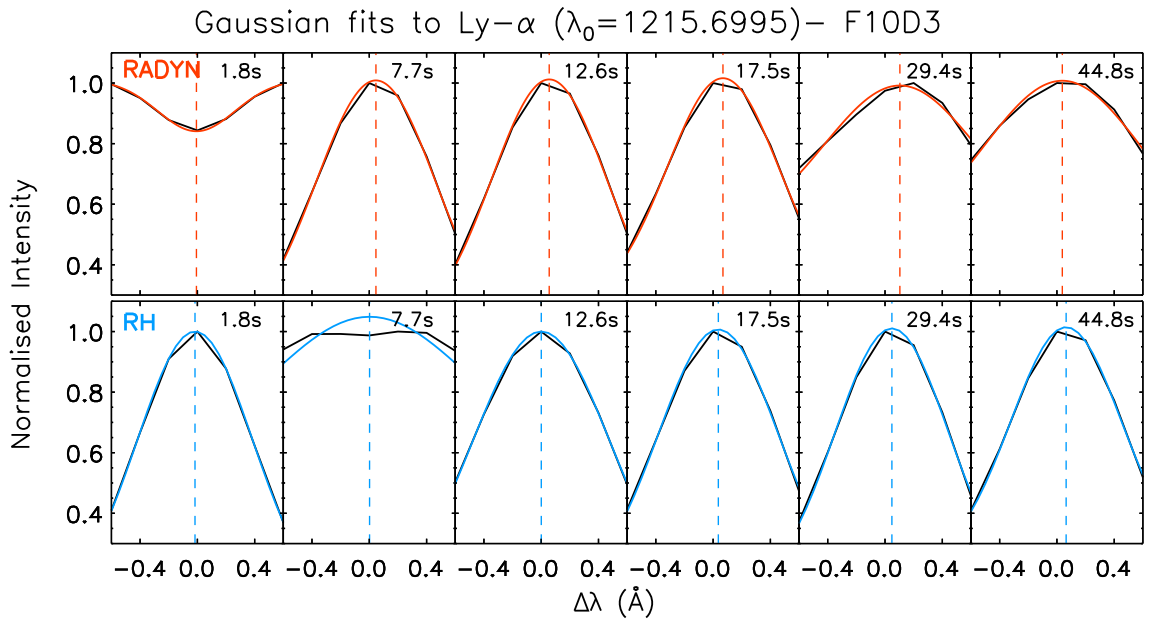


**Figure 5.2:** Ly- $\alpha$  profiles obtained from the F10D3 simulation post instrumental convolution, calculated from RADYN (upper panels) and RH (lower panels). Overplotted are the 4-parameter Gaussian fits to the line profiles, with the simulation time indicated in the upper right of each panel. The derived line centroids are indicated by the dashed vertical lines

### 5.2.1 Velocities from the F10 ( $\delta = 3$ ) simulation

The F10D3 simulation, introduced in §4.2.1, revealed upflows in the lower chromosphere as a result of the injection of the electron beam. Analysis of the line contribution functions (§4.3.1) revealed that the upflows in the atmosphere influenced the positions of the line cores. The cores, which exhibit central reversals, move into the blue wing due to plasma upflowing with a velocity of  $\sim 50 \text{ km s}^{-1}$ .

Doppler velocities are calculated for Ly- $\alpha$  through Ly- $\delta$  for both the instrumentally-convolved RADYN and RH profiles. Doppler velocity profiles for each of the Lyman lines are displayed in Figure 5.3, and are plotted for both the Gaussian and intensity-weighted methods. Velocities obtained from the time-integrated line profiles using the Gaussian method are plotted underneath the high-cadence velocity profiles.

Figure 5.3a displays the synthetic Doppler velocity profiles as obtained from

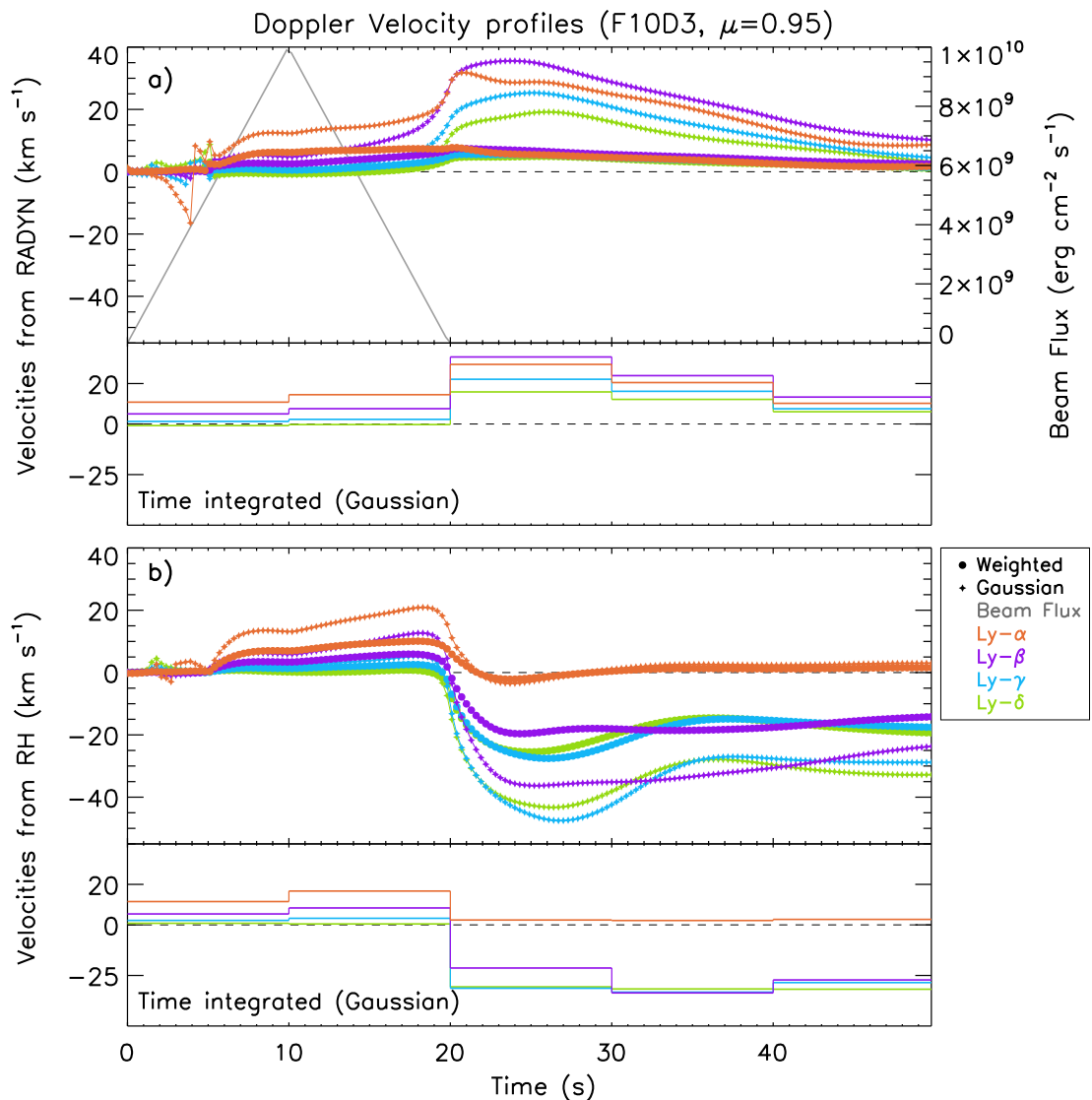


**Figure 5.3:** Doppler velocities during the F10D3 simulation, derived from the RADYN (a) and RH (b) profiles after they have undergone convolution with the EVE instrumental profile. Negative velocities indicate upflows.

the RADYN line profiles, in which sustained redshifted signatures are observed in all of the Lyman lines throughout both the initial 20 s (corresponding to the beam injection), and the remaining 30 s while the atmosphere relaxes. The derived velocities are temporarily affected at around  $t = 5$  s as a result of the post-convolution lines transitioning from absorption to emission.

Much like in Chapter 3, velocities obtained via the intensity-weighted method do not attain the same magnitude as those obtained from Gaussian fitting, but they do verify the direction of the line shift. By the Gaussian fitting approach, peak downflow velocities of  $\sim 25 - 35 \text{ km s}^{-1}$  are observed in Ly- $\alpha$  and Ly- $\beta$ , with Ly- $\alpha$  reaching its maximum speed first at  $t = 20.5 \text{ s}$ , and Ly- $\beta$  reaching a slightly higher peak velocity at  $t = 23 \text{ s}$ .

Ly- $\gamma$  also reaches its maximum speed slightly later, with velocities of  $25 \text{ km s}^{-1}$  at  $t = 25 \text{ s}$ . Ly- $\delta$  displays the weakest redshift, indicating downflows of  $15 \text{ km s}^{-1}$  at  $t = 26 \text{ s}$ . This ordering is in opposition to the ordering that was observed in Sun-as-a-star velocity profiles in Chapter 3, where the higher order lines exhibited greater flow speeds. Although it should be reiterated that this effect was not observed in the flare-excess profiles.

It is illuminating that these velocity profiles, obtained from instrumentally-convolved lines, exhibit redshifts. In §4.3.1, it was clear that all of the Lyman lines were subject to blueshifts as a result of an upflow permeating the core formation region of each line. Evidently, an aspect of the degradation caused by the instrumentation leads to the switching of the perceived sign of the Doppler shift.

The key to this problem lies in the presence of the central reversals in the line cores. From Figure 5.1, it is apparent that the smoothing of the Lyman lines by the instrumental profile erases any signature of a central reversal. Because the line cores are simultaneously blueshifted and centrally reversed, there exists a lack of emission in the blue wing relative to the red wing. When these lines are convolved with the instrumental profile, any semblance of a central reversal is lost while the only signature of the blueshifted core exists in the form of a strengthened red wing. This can easily be misinterpreted as a redshift in the line profile, resulting in perceived downflows at times when the line cores are actually blueshifted.

The source of the apparent redshifts in Figure 5.3a can be easily seen in Figures 4.6 through 4.9. Each of the line contribution functions shows that the line cores in Ly- $\alpha$  and Ly- $\beta$  are optically thick, and that they form at an altitude where the atmosphere is upflowing with a velocity of  $\sim 50 \text{ km s}^{-1}$ . Influenced by the velocity structure, and centrally-reversed due to the variation in altitude of  $S_{\nu}$ , the emergent

line profiles have notably blueshifted central reversals, which act to reduce the amount of emission produced in the blue wing. This is seen in all of the Lyman lines, as indicated by Figure 4.10. The removal of blue-wing irradiance, and the smearing of the profiles by the instrumentation, lead to degraded Lyman line profiles with red asymmetries.

The time-integrated velocities (Figure 5.3a, lower panel) are obtained using the Gaussian fitting method, and convey an additional loss of information about the nature of the observed flows. Although the general flow signatures are retained, it is clear that the dynamical effects of the atmosphere are not optimally represented.

The synthetic velocity profiles obtained from RH are shown in Figure 5.3b. While common features remain with respect to the RADYN velocities, other aspects of the velocity profiles are quite different. In a general sense, the observation of redshifts throughout the initial 20 s is retained. Similarly, the redshift signatures are stronger in the lower-order lines, with Ly- $\alpha$  and Ly- $\beta$  suggesting downflows of 20 and 10 km s<sup>-1</sup> respectively, with successively weaker velocities in the higher order lines.

The similarities between the velocity profiles from RADYN and RH end rather abruptly with the cessation of the electron beam. At  $t = 20$  s, Figure 5.3b shows a stark departure from the sustained redshifted signatures found in Figure 5.3a. The Doppler shift in Ly- $\alpha$  rapidly disappears, and for the remainder of the simulation this line does not indicate any flows when computed by RH. In contrast, each of the higher order lines abruptly transitions into exhibiting blueshifted signatures when the beam switches off, the magnitudes of which peak at around the same time as those found in Figure 5.3a.

When obtained from Gaussian fitting, the Ly- $\beta$  velocity profiles from RH indicate a maximum upflow speed of 35 km s<sup>-1</sup> at  $t = 23$  s. The flow suggested by Ly- $\gamma$  peaks at around  $t = 26$  s with a magnitude of around 45 km s<sup>-1</sup>, producing the strongest blueshifted signature in the simulation. Ly- $\delta$  indicates similar peak velocities and times to those found in Ly- $\gamma$ .

The starkest difference between the synthetic velocity profiles obtained using RADYN and RH line profiles is the abrupt switch in sign of the Doppler shift in RH. The flows reverse direction immediately upon the beam switching off in RH,

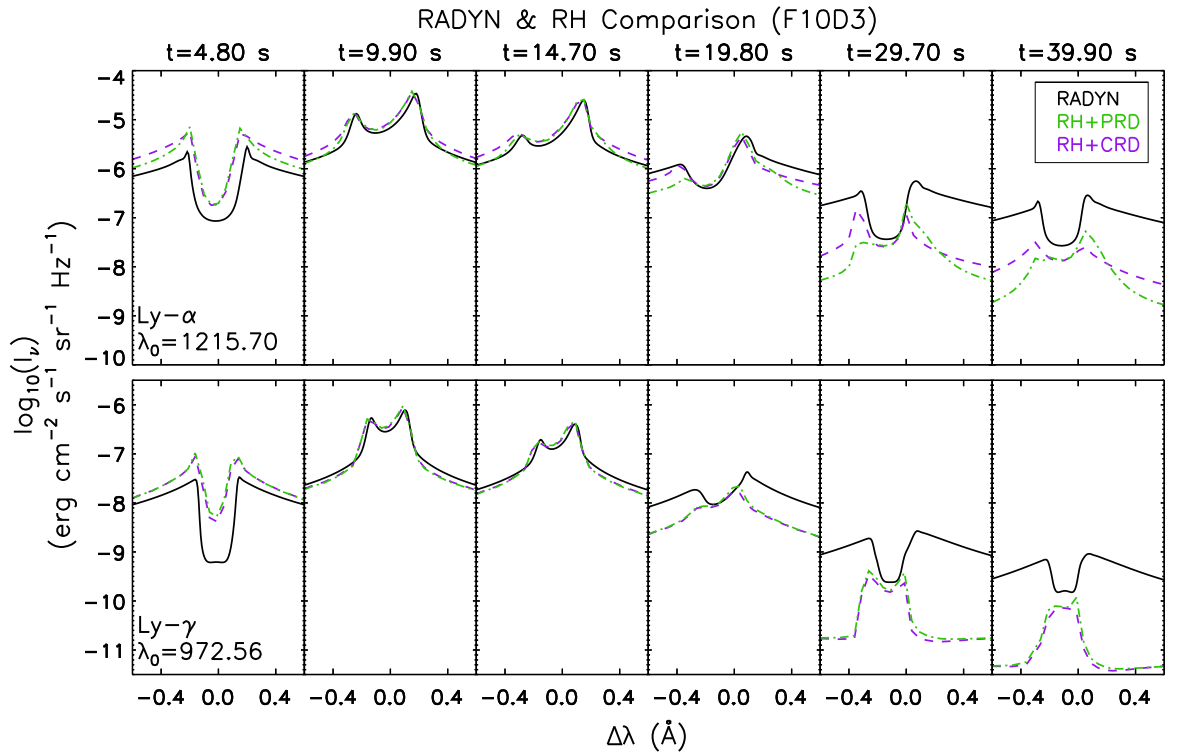


**Figure 5.4:** A running comparison between the Ly- $\alpha$  and Ly- $\gamma$  lines throughout the F10D3 simulation. Solutions from RH with assumptions of PRD (green) and CRD (purple) are included.

whereas in RADYN the same direction is sustained as the magnitude of the flow diminishes. To understand why the velocity results differ after the beam-heating stage, a comparison between the late-time behaviour of Ly- $\alpha$  and Ly- $\gamma$  in both RADYN and RH (with profiles computed both with PRD and CRD assumed) is shown in Figure 5.4

In Figure 5.4, it can be seen that as the beam heats the atmosphere ( $t = 0 - 20$  s), the Ly- $\alpha$  and Ly- $\gamma$  lines as computed from RH agree very well with those obtained from RADYN. In addition to this, there does not appear to be a large difference in the emergent RH profiles when CRD is assumed as opposed to PRD. This agreement visibly disappears upon the cessation of the electron beam ( $t > 20$  s). The Ly- $\alpha$  profiles as computed from RH (with PRD) indicate that while the core intensities remain comparable with those of the RADYN profiles, the wing intensities diverge

significantly. Furthermore, the intensities in the red and blue wings are also not comparable, with the red wing being strengthened relative to the blue wing. The overall blueshift in the Ly- $\alpha$  line competes with the intense red wing asymmetry to result in zero flows being detected in Figure 5.3b.

Ly- $\gamma$  indicates a similar effect, with RH verifying the RADYN solutions for the line while the electron beam is being applied, but opposing them after  $t = 20$  s. As with Ly- $\alpha$ , the wing intensities drop sharply after  $t = 20$  s, but in this case both the blue and red wings are diminished by a similar amount. Crucially, the core intensities continue to remain in line with those calculated by RADYN. This means that, as opposed to RADYN, the Ly- $\gamma$  line profile as obtained from RH is now strongly emitting and is no longer dominated by a central reversal. This means that the blueshift in the line core can now clearly be detected, whereas it remains masked in RADYN as a result of the line core being centrally reversed.

While differences were expected between the profiles obtained from RADYN and RH as a result of assuming PRD, Figure 5.4 shows that even the RH profiles computed with CRD can deviate from those obtained from RADYN. This indicates that there must be an additional factor that results in differences in line profiles calculated with the two codes. Further discussion on the factors contributing to these deviations is outlined in section 5.3.

While the evolution of the velocity profiles after the beam injection differs between the two codes, the general picture is clear. In both series of results in Figure 5.3, all Lyman lines exhibit an increasingly redshifted signature while the beam is being deposited. Smoothing of the lines by the instrumental profile erases the central reversals, which lie blueward of the theoretical line cores. The result of this is an accentuation of the red wing, which can be easily mistaken as a redshifted signature. After the beam switches off, the Lyman lines as computed from RADYN continue to suggest downflows, with increasingly diminished magnitudes. In RH, the wing intensities in the higher order Lyman lines drop significantly, which means that the lines are no longer dominated by a deep central reversal. This allows the blueshifts in the line cores to be clearly detected, producing the upflow signatures in Figure 5.3b.

It is also worth noting that the magnitudes of the peak velocities obtained from Gaussian fitting are typically between  $20 - 30 \text{ km s}^{-1}$ , depending on the line profile and the code used. This is largely in line with the typical flow speeds found in Chapter 3. As in Chapter 3, the intensity-weighted method finds weaker flows, but verifies the direction of those obtained from Gaussian fitting.

### 5.2.2 Velocities from the F10 ( $\delta = 8$ ) simulation

The F10D8 simulation did not inject any more energy than the F10D3 simulation, but instead altered the region of electron deposition. By changing to a high  $\delta$  value, the electron population contains fewer high-energy electrons, meaning a greater fraction of the electron population is stopped higher in the atmosphere than before. In §4.3.2, it was revealed that a similar upflow to the F10D3 simulation was produced, but with a sharp velocity gradient at its leading edge. Figures 4.11 and 4.12 show that, as in the F10D3 simulation, the upflowing plasma produces line profiles that are heavily blueshifted. The line cores are again centrally-reversed.

In Figure 5.5, a simulated EVE observation of the emergent line profiles is again performed on Ly- $\alpha$  through Ly- $\delta$ , with synthetic Doppler velocity profiles calculated. As a result of the more pronounced gradients produced in the atmosphere, some of the snapshots ( $t = 13 - 20 \text{ s}$ ) proved computationally challenging for RH and did not converge to a solution

While the beam heats the atmosphere, redshifted signatures are found in the line profiles obtained from RADYN (Figure 5.5a). It should be noted that the signatures produced between  $t = 0 - 5 \text{ s}$  are again influenced by the degraded profiles transitioning from absorption to emission. The redshifted signatures peak shortly after  $t = 20 \text{ s}$ , with Ly  $\alpha$  and Ly- $\beta$  both indicating maximum downflow velocities of almost  $30 \text{ km s}^{-1}$  when Gaussian fitting is used. Ly- $\gamma$  and Ly- $\delta$  again suggest incrementally weaker flow speeds, but both still peak at speeds upward of  $20 \text{ km s}^{-1}$ . Beyond  $t = 20 \text{ s}$ , the Doppler velocities obtained from RADYN continue to show redshifts, but with a very gradual decay in speed. At  $t = 50 \text{ s}$ , all Lyman lines show a sustained redshift.

The uniformity and persistence of these redshifted signatures in the lines obtained

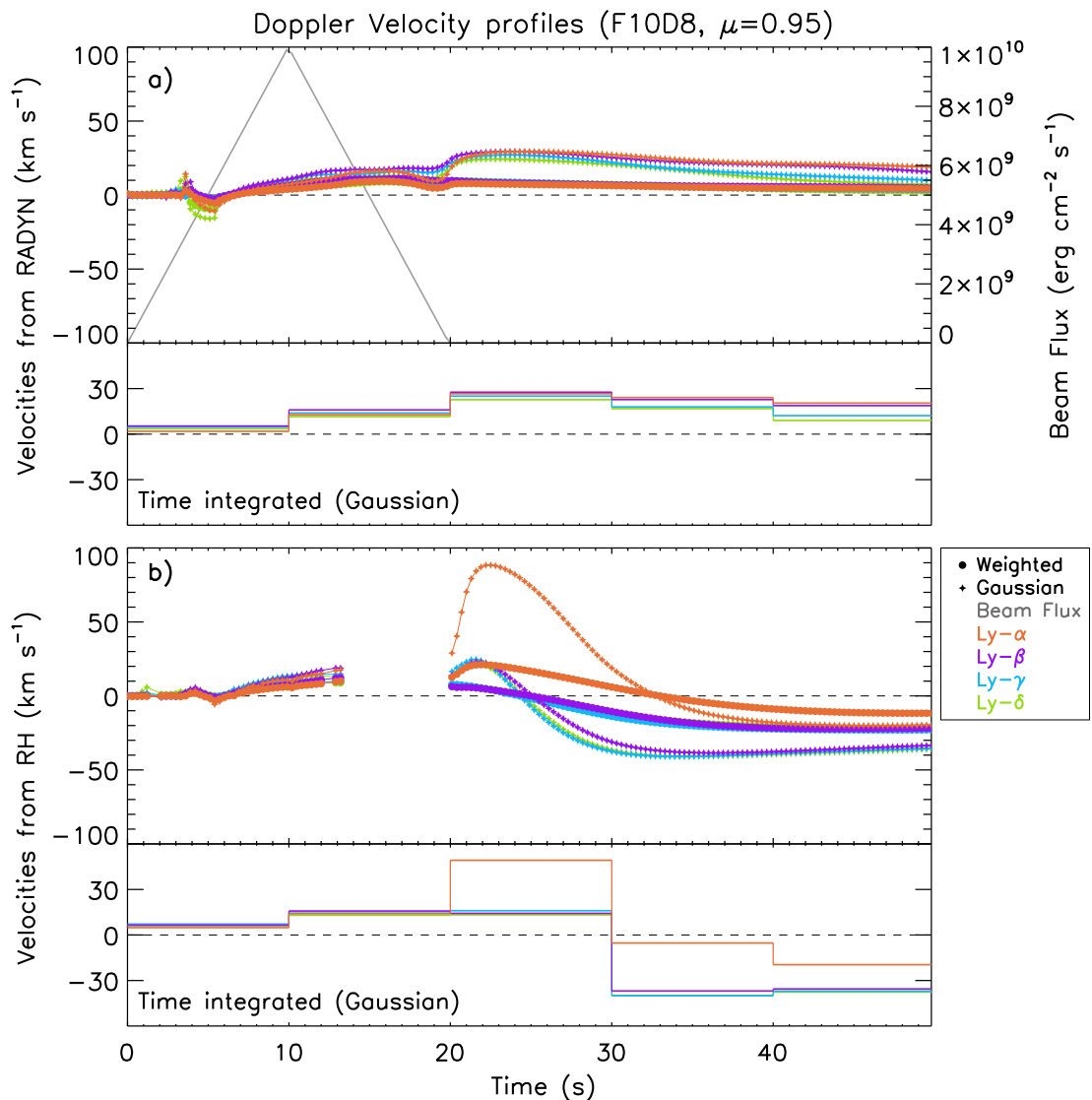


**Figure 5.5:** Doppler velocities during the F10D8 simulation, derived from the RADYN (a) and RH (b) profiles after they have undergone convolution with the EVE instrumental profile. Some of the atmospheric snapshots did not converge in RH. Negative velocities indicate upflows.

by RADYN can be understood by inspection of the line profiles and their formation (Figures 4.11 through 4.13). The line contribution functions indicate that the core of Ly- $\alpha$  forms in an extremely thin layer, which is in the process of upflowing with a velocity of 50 km s<sup>-1</sup>. Additionally, due to  $S_{\nu}$  peaking deeper in the atmosphere,

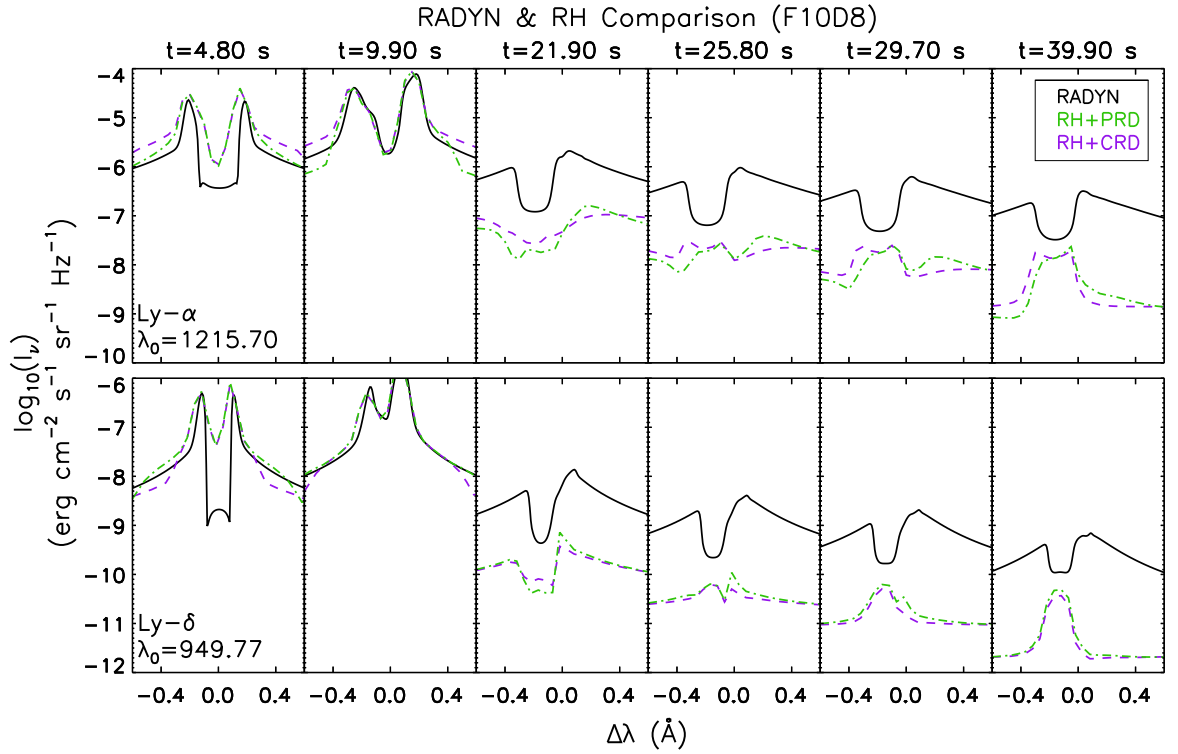
the core maintains a central reversal. As a result, the Ly- $\alpha$  and higher order lines have heavily blueshifted central reversals. Much like in the F10D3 simulation, this removes irradiance from the blue wing, and produces red asymmetries in each of the lines upon instrumental convolution. Because of this, the velocity profiles in Figure 5.5a largely echo those found in the F10D3 simulation (Figure 5.3a).

Figure 5.5b shows the equivalent Doppler velocity profiles from RH. As before, the velocity profiles as obtained from RH are consistent with those from RADYN while the beam is being applied, but depart significantly once the heating stops. Between  $t = 5 - 13$  s, the velocity profiles from RH match those found in RADYN. Aspects of the computation then become challenging for RH to perform, as there exists a strong velocity gradient in the atmospheric flow structure.

Beyond  $t = 20$  s, RH starts to converge again. Immediately noticeable is a very large redshift signature in the Ly- $\alpha$  line, peaking at  $t = 22$  s with a velocity of  $100 \text{ km s}^{-1}$ . The higher order lines also exhibit peak redshifted signatures at this time, but with much lower speeds ( $\sim 20 \text{ km s}^{-1}$ ). The redshifts then decay, eventually changing direction at  $t = 32$  s in Ly- $\alpha$ , and at an earlier time of  $t = 24$  s in the higher order lines. As in the F10D3 simulation, the blueshifts produced in Ly- $\alpha$  are weaker than in the higher order lines, with Ly- $\gamma$  and Ly- $\delta$  indicating maximum upflow speeds of  $40 \text{ km s}^{-1}$ .

The differences between Figures 5.5a and 5.5b are significant when the electron beam is switched off. This was also found in the F10D3 simulation. In Figure 5.6, a comparison between the RADYN and RH solutions for Ly- $\alpha$  and Ly- $\delta$  is shown for a number of times spanning the simulation. As before, consistency is found between the two codes while the beam is being applied, but this similarity departs as the beam switches off.

The source of the very fast downflow in Ly- $\alpha$  as obtained by RH can be seen in the upper panels, as the RH solution for Ly- $\alpha$  continues to exhibit a blueshifted central reversal at  $t = 21.90$  s, in addition to a comparably weak blue wing relative to the red wing in the PRD solutions. The combination of these factors produces a very strong red asymmetry, as evidenced in Figure 5.5b. As before, it is clear that while intensities in the line cores remain comparable between the two codes after



**Figure 5.6:** A running comparison between the Ly- $\alpha$  and Ly- $\delta$  lines throughout the F10D8 simulation. Solutions from RH with assumptions of PRD (green) and CRD (purple) are included.

$t = 20$  s (although the core intensities do differ by roughly an order of magnitude immediately after beam cessation), the wing intensities in the RH profiles noticeably drop. This allows the blueshifted line cores to be detected, as they are no longer centrally-reversed, explaining the change in direction of the velocity profiles at later times. As in the F10D3 simulation, the RH solutions for the higher order line (Ly- $\delta$ ) show comparable red and blue wing intensities after the beam heating stops, with the line core being enhanced above these.

The resulting velocity profiles for this simulation show a large degree of similarity with those found in the F10D3 simulation. By simulating an EVE observation, sustained redshifts are found in the Lyman lines when obtained from RADYN, as a strongly blueshifted central reversal persists in each of the lines until the end of the simulation. This remains true of the RH velocities while the beam is being applied,

but as before, it is found that the velocity profiles transition into producing blueshifts as the wing intensities in the RH profiles drop after  $t = 20$  s.

In both F10 simulations, the dynamics of the core formation region are dominated by upflows approaching  $50 \text{ km s}^{-1}$ . The only suggestion of this is found in late-time behaviour of the RH velocity profiles. As long as the line cores remain centrally-reversed, these observations cannot correctly determine the true velocity of the atmosphere.

### 5.2.3 Velocities from the 3F10 ( $\delta = 8$ ) simulation

The 3F10D8 simulation continued the injection of a soft beam, with a steep drop in electron number as a function of increasing energy. This again results in a greater amount of energy being deposited at higher atmospheric layers. In §4.3.3, it was found that the sweeping of a cool, dense front of plasma upwards through the atmosphere heavily influenced the shapes of the Lyman lines. This upflowing material acts as a secondary, distinct source of line emission, which propagates through the blue wing of each of the Lyman lines as it accelerates upwards.

In Figure 5.7, synthetic velocity profiles are shown for the Lyman lines post-degradation for both RADYN and RH outputs. This simulation was particularly challenging for the RH code to reach convergence with, likely as a result of the strong velocity and temperature gradients visible in Figure 4.4. As a result of this, many of the snapshots for this simulation did not converge in RH, and so Figure 5.7b does not reflect the full extent of the timescale spanned in Figure 5.7a.

Throughout the initial 10 s of the simulation, the synthetic Doppler velocity profiles obtained from the degraded RADYN profiles show an increasingly redshifted signal. At  $t = 10$  s, Ly- $\alpha$  and Ly- $\beta$  exhibit downflow velocities of  $15 \text{ km s}^{-1}$  when obtained by Gaussian fitting, with Ly- $\gamma$  and Ly- $\delta$  conveying downflows of  $10 \text{ km s}^{-1}$ . As in §5.2.1 and §5.2.2 these apparent downflows are due to the smoothing-over of centrally-reversed line cores which themselves are blueshifted. As before, the true direction of the flow is disguised by the Doppler shift occurring in an absorbing feature, the nature of which is lost when the profiles are convolved with

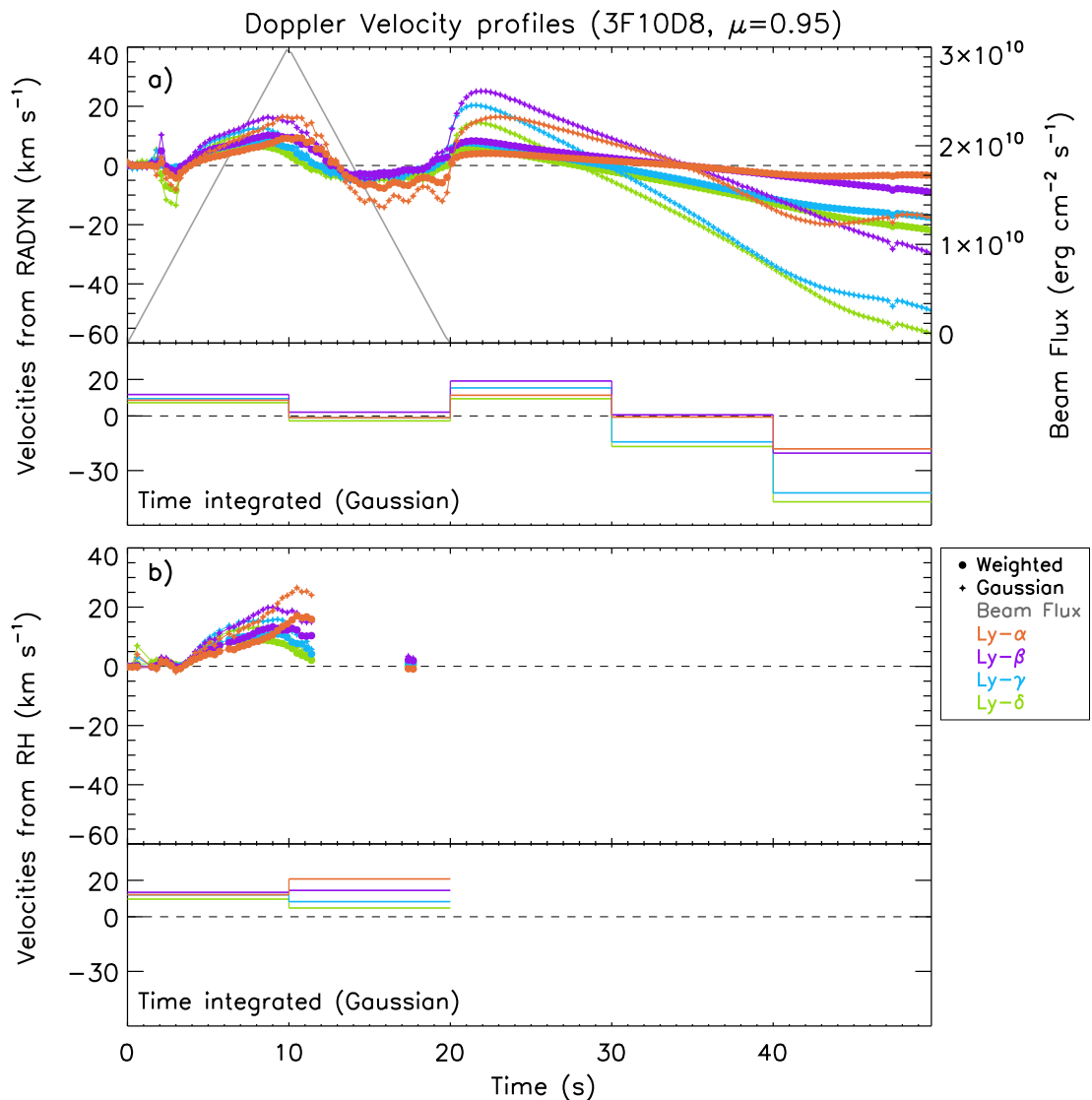


**Figure 5.7:** Doppler velocities during the 3F10D8 simulation, derived from the RADYN (a) and RH (b) profiles after they have undergone convolution with the EVE instrumental profile. The majority of snapshots did not converge successfully in RH. Negative velocities indicate upflows.

the instrumental profile.

Between  $t = 10\text{--}20$  s, these downflow signatures diminish, with all flows decaying to rest before transitioning into weak upflow. The reason for this is rather complex, as it is the result of the interplay between the Doppler shift in the primary core of

the line and the secondary line source produced by the upflowing plasma. While the central reversal in the primary line core is slightly blueshifted, which produces a slightly redshifted signature in the convolved profile, the secondary moving component of the line acts to enhance the overall emission in the blue wing. This can be seen in Figures 4.15 and Figure 4.18. As it propagates through the blue wing, the velocity profiles transition from redshifted to blueshifted as the blue wing becomes increasingly accentuated. An oscillation can be seen in the blueshifted signature produced by Ly- $\alpha$ , which is caused by a combination of the individual peaks of the secondary line component propagating through (and beyond) the range over which the line is fitted, and the deepening of the self-reversals in both line components.

Shortly after  $t = 20$  s, the moving component of the line develops a deeper self-reversal (Figure 4.16). This, combined with the slight blueshift in the centrally-reversed primary core of the line, acts to remove a considerable amount of blue-wing irradiance in each of the lines. This leads to an emphasis of the red wing once the profiles undergo instrumental convolution. As a result of this, the velocity profiles in Figure 5.7a transition back to exhibiting redshifted signals. Around  $t = 22$  s, all Lyman lines exhibit downflow velocities ranging between  $10 - 25 \text{ km s}^{-1}$ , with Ly- $\beta$  showing the strongest motion.

The perceived redshifts then diminish over the following 10 s, before again transitioning into blueshift. Close to the end of the simulation (Figure 4.17), it can be seen that the Ly- $\alpha$  profile is dominated by the secondary component, while the primary component of the line has decayed in intensity. This can be seen in all of the higher order lines (Figure 4.18), with the upflowing plasma strengthening the blue wings of the Lyman series. This heavily influences the derived centroids of the Gaussian fits, producing the strong blueshifted signatures at late times in Figure 5.7a.

Counterpart velocities obtained from smoothing the profiles computed by RH are shown in Figure 5.7b. While many of the snapshots failed to converge to a solution, a reasonable amount of time during the beam-heating stage is well sampled. Throughout the initial 10 s, the RH velocity profiles reasonably match those observed with the profiles from RADYN. Considering those obtained from Gaussian fitting,

Ly- $\alpha$  exhibits redshifts corresponding to a peak downflow speed of  $25 \text{ km s}^{-1}$ . Ly- $\beta$ , Ly- $\gamma$  and Ly- $\delta$  are also redshifted, suggesting speeds of 20, 15 and  $10 \text{ km s}^{-1}$  respectively.

As in Figure 5.7a, the redshifted signals begin to decay after the beam's peak flux is input at  $t = 10 \text{ s}$ . Shortly after this time, the RH code struggles to reach a solution as the atmospheric variables become computationally problematic. Regardless, around  $t = 17 \text{ s}$  two snapshots do converge, and indicate near-zero Doppler velocities in all of the Lyman lines, with a very minor amount of redshift. This is not dissimilar to what is observed in the RADYN velocity profiles at this time, where extremely weak blueshifts are seen. This indicates that the weakening of the initial redshifted signature throughout the first 10 s is again found when using RH profiles. This is a result of the secondary moving component of the line strengthening the blue wing, offsetting the redshift obtained when smoothing over the blueshifted central reversal.

After  $t = 17 \text{ s}$ , no further snapshots converge successfully using RH. Despite this, the velocity profiles shown in Figure 5.7 agree rather well throughout the beam-heating stage. This was also found in the previous F10 simulations (§5.2.1 and §5.2.2), with good agreement in the general flow direction and magnitude. Ly- $\alpha$  and Ly- $\beta$  exhibit the stronger redshifted signals during beam-heating, displaying peak speeds of  $20 - 25 \text{ km s}^{-1}$  when computed using RH. Ly- $\gamma$  and Ly- $\delta$  suggest weaker downflow speeds of  $10 - 15 \text{ km s}^{-1}$ .

Before the emergence of the moving component in these lines ( $t = 10 - 20 \text{ s}$ ), the general trend found in the velocity profiles is similar to the simulated observations found in the F10D3 model (Figure 5.3). Blueshifts in the central line cores are masked by the smoothing over of the lines by the instrumental profile, resulting in degraded line profiles with strengthened red wings. As material is swept upwards throughout the chromosphere, it accelerates and acts as an additional source of highly-blueshifted line emission. This leads to propagating features in the blue wings of each of the lines, which counteract the initial redshifted signal and cause the velocity profiles in Figure 5.7 to decay to near-zero between  $t = 10 - 20 \text{ s}$ .

The time-integrated velocities (Figure 5.7 lower panels) manage to reasonably

represent the magnitude of the flows, but clearly indicate a loss in temporal information. Time-averaging about the transition between redshift to blueshift at  $t = 35$  s leads to apparent velocities of zero, which does not correctly represent the non-zero velocities observed in the higher-cadence profiles.

#### 5.2.4 Velocities from the F11 ( $\delta = 3$ ) simulation

The final simulation considered is that of a high-flux, hard beam. This simulation is similar to the F10D3 model, albeit with a higher peak and integrated flux, and does not have a steep decay of electron number with energy as in the  $\delta = 8$  models. The late-time aspects of this simulation were particularly interesting (§4.3.4), in which a downwards propagating flow was found to rebound upwards after reaching the core formation height of the Lyman lines. This facilitated an increase in the upper level populations via collisions, producing enhancements in each of the Lyman lines, which in turn were affected by the flow structure.

As before, the line profiles from RADYN and RH are convolved with the EVE instrumental profile, and the apparent Doppler shifts in each of the Lyman lines are measured. The resulting Doppler velocity profiles are shown in Figure 5.8. The velocities obtained from the RADYN profiles (Figure 5.8a) during the first 8 s suggest very weak redshifts, with Ly- $\alpha$  conveying the strongest redshifted signature here, corresponding to  $3 \text{ km s}^{-1}$ . From the  $t = 5$  s snapshots shown in Figure 4.24, it can be seen that the Lyman lines are largely symmetric around this time, and so little Doppler shifted signatures are observed.

Between  $t = 8 - 20$  s, flows become apparent in Figure 5.8a, with all Lyman lines indicating blueshifts. These blueshifts peak between  $t = 9 - 10$  s, with Ly- $\alpha$  producing the strongest signal which suggests an upflow velocity of  $23 \text{ km s}^{-1}$  when Gaussian fitting is used. Ly- $\beta$  peaks shortly afterwards, with a speed of  $11 \text{ km s}^{-1}$ . Ly- $\gamma$  and Ly- $\delta$  indicate only weak upflows of below  $5 \text{ km s}^{-1}$ . Figure 4.19 shows that at  $t = 9$  s, Ly- $\alpha$  exhibits a strengthened blue wing, while the line core (which is centrally-reversed) is slightly redshifted by a downflow at the core formation height of  $20 \text{ km s}^{-1}$ . The combination of these factors leads to a strong blue asymmetry in

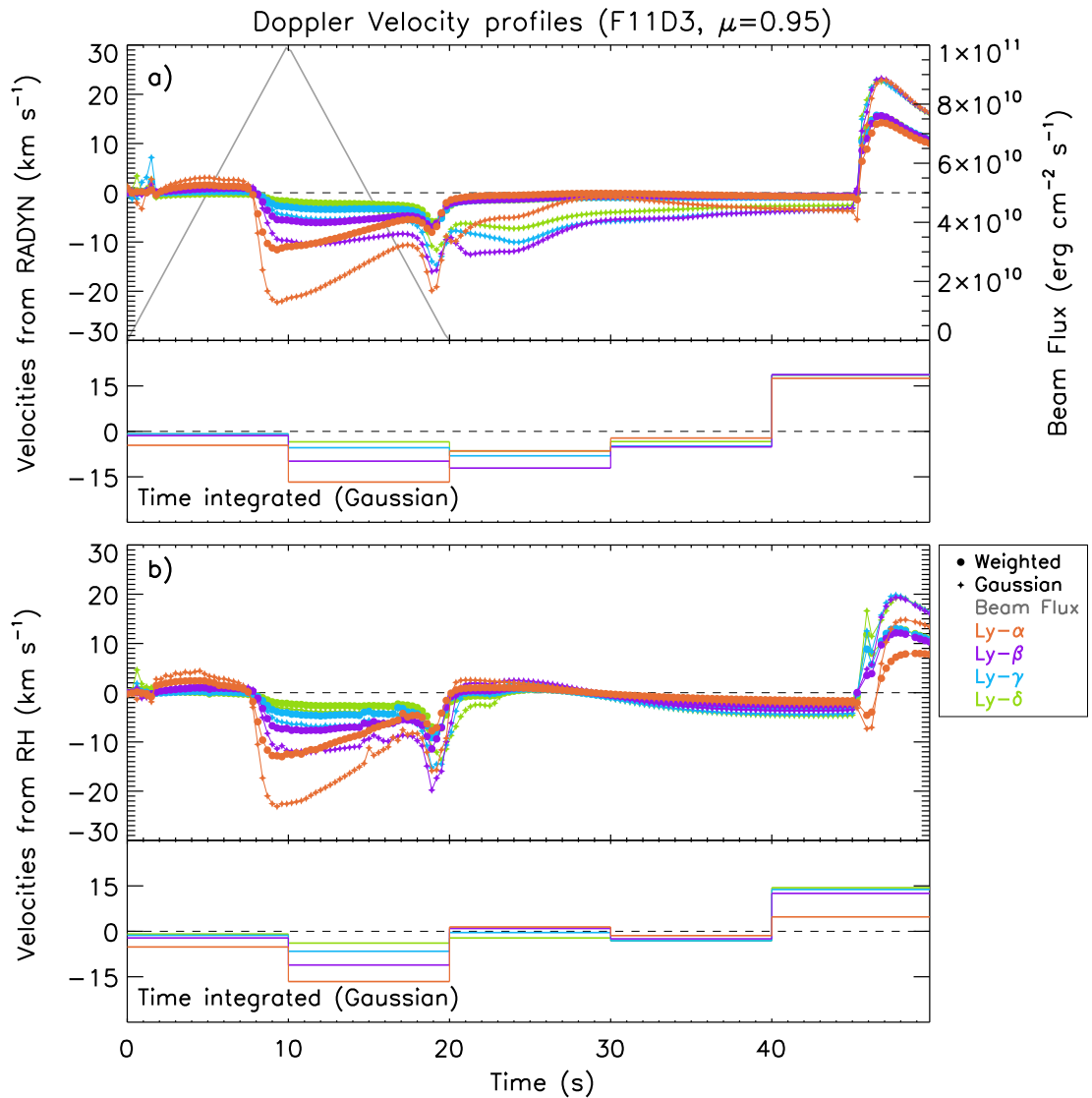


**Figure 5.8:** Doppler velocities during the F11D3 simulation, derived from the RADYN (a) and RH (b) profiles after they have undergone convolution with the EVE instrumental profile. Negative velocities indicate upflows.

the Ly- $\alpha$  line, which produces the upflow signatures at  $t = 9$  s.

The upflow signatures decay slightly as the blue wing component diminishes ( $t = 15$  s in Figure 4.24), before briefly peaking again at  $t = 20$  s as the redshifted central reversals deepen and remove more irradiance from the red wing. Beyond  $t = 20$  s, the blueshifted signatures decay as the Lyman lines become more symmetric,

and by  $t = 44$  s only weak blueshifts are obtained ( $\sim 5 \text{ km s}^{-1}$ ).

As the coronal downflow reaches the core-formation height at  $t = 45$  s, the velocity profiles abruptly transition from weak upflows to strong downflows. In Figure 5.8a, Ly- $\alpha$  indicates a downflow of  $20 \text{ km s}^{-1}$  at  $t = 46$  s, with similar velocities being found in the higher order lines. In Figures 4.22, it was observed that the Ly- $\alpha$  line produces heightened levels of emission as a result of the previously-downflowing plasma interacting with and compressing the core-formation region. As a result, the Ly- $\alpha$  line at  $t = 47$  s forms in an extremely thin layer, which is downflowing with a speed of  $\sim 20 \text{ km s}^{-1}$ , and is strongly redshifted. The same effect is seen in the higher order lines in Figure 4.24.

As the downflowing plasma from the corona rebounds from the core-formation height, the plasma in this region is compressed and is also driven downwards. Increased amounts of collisional excitation cause the Lyman lines to radiate heavily with respect to 2 s prior, and this radiation is strongly redshifted as a result of the downflow in the thin layer where the line cores are formed.

All Lyman lines lack a central reversal at this time, as emission is produced in a very thin region, above which  $S_{\nu}$  can be seen to decrease in Figure 4.22, and as a result the redshift in the line core is clearly detectable. As a result, downflows are obtained in Figure 5.8a which are consistent with the true speed and direction of the plasma at that height.

The counterpart velocities obtained from RH are displayed in Figure 5.8b, and show a strong degree of consistency with the velocities obtained from RADYN. While the beam heats the atmosphere, the Doppler velocities from RH are almost identical with those in RADYN.

As found in the previous simulations, the RH velocity profiles deviate from those in RADYN once the beam switches off, although the differences in Ly- $\alpha$  are not so pronounced. In Figure 5.8a, the upflow signatures decay gradually in each of the lines over the following 20 s. In RH, these blueshifts quickly disappear once the beam switches off, with each of the Lyman lines exhibiting very little Doppler shift until  $t = 45$  s, at which point the effects of the rebounding flow are again recovered in RH. As in Figure 5.8a, the Lyman lines quickly respond to this feature by exhibiting

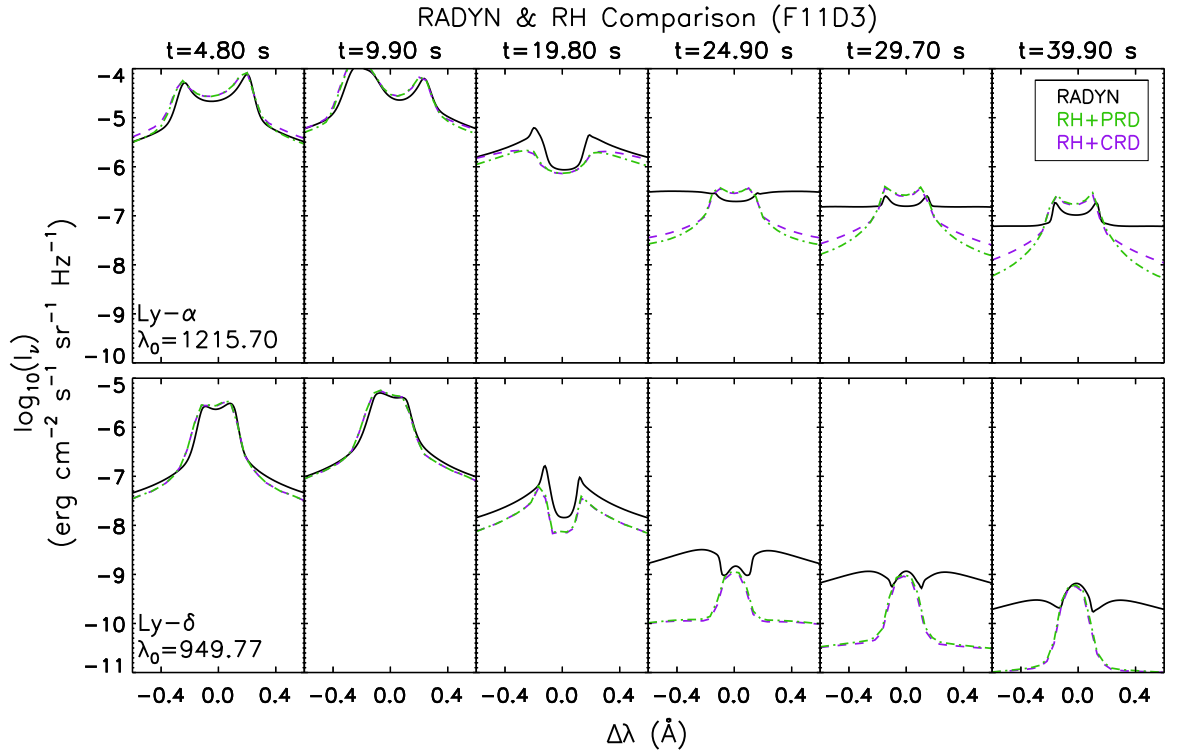


**Figure 5.9:** A running comparison between the Ly- $\alpha$  and Ly- $\delta$  lines throughout the F11D3 simulation. Solutions from RH with assumptions of PRD (green) and CRD (purple) are included.

redshifted signals, although in RH the effect on Ly- $\alpha$  is less pronounced.

A running comparison between the Ly- $\alpha$  and Ly- $\delta$  lines for this simulation, as computed from both RADYN and RH, is shown in Figure 5.9. As before, it can be seen that the solutions from RADYN and RH are very similar during the deposition of the electron beam, with differences arising afterwards.

As in Figures 5.4 and 5.6, the wing intensities as computed from RH drop after  $t = 20$  s, while the core intensities remain comparable with those from RADYN. This produces line profiles which are more prominently peaked relative to their RADYN counterparts, and in Ly- $\delta$  the central reversal vanishes entirely. In addition, the RH solutions computed with CRD are very similar to those obtained from PRD, again suggesting that the redistribution process is not the dominant factor responsible for the inconsistency between the RADYN and RH solutions.

Between  $t = 20 - 45$  s, the RH velocity profiles (Figure 5.8b) do not show appreciable Doppler shifts, while they do when Gaussian fitting is used on the profiles obtained from RADYN. Greater agreement is found in the intensity-weighted velocity profiles. Throughout this time, the RADYN profiles are particularly flat, with Ly- $\alpha$  showing a slight redshift in the centrally-reversed line core. This produces a slight blueshifted signal. Ly- $\delta$  does not appear to have a Doppler shifted core, but has a complex structure with a self-reversal in the near wings with an additional reversal at the line core. In RH, both the Ly- $\alpha$  and Ly- $\delta$  lines are more prominently peaked.

It is clear that the flattening of the Ly- $\alpha$  line and the complex structure of the Ly- $\delta$  line in RADYN produce line shapes that are distinctly non-Gaussian. Conversely, the drop in the wing intensities in the RH profiles lead to profiles that are notably more Gaussian in shape. The result of this is the velocities obtained from the RADYN profiles between  $t = 20 - 45$  s are likely affected as Gaussian fits become poor approximations to the line shapes, whereas in RH this is not the case.

The velocity profiles for this simulation are potentially more representative of the actual dynamics of the atmosphere, because they are less influenced by absorbing features in the line profiles. The blueshifted signatures observed throughout the first 20 s are predominantly caused by enhancements in the blue wings of the Lyman lines, which appear to be linked to the upflows seen in the atmosphere in Figure 4.19 (although the line core is not upflowing). At late times, the observed redshift signatures are also produced by emitting features, which can be linked to the downflow seen in Figure 4.22.

### 5.3 The Effects of Partial Redistribution on Model Lyman Line Profiles

The divergence of the Doppler velocity profiles as obtained from the RH solutions with respect to those from RADYN is a common feature throughout each of the simulations after the electron beam is switched off. As outlined in Chapter 2, one of the reasons why RH is particularly desirable for radiative transfer problems is its

ability to calculate line transitions with the assumption of PRD. This accounts for the likelihood that a photon absorbed within a transition will be re-emitted with some level of coherency, which is an important consideration when the plasma density is low or if the line is particularly strong and can easily be de-excited radiatively.

Because RH is capable of treating the Lyman lines with the assumption of PRD, differences between the emergent line profiles from RH and RADYN were expected. However, as evidenced in Figures 5.4, 5.6 and 5.9, even the line profiles computed by RH when CRD is assumed are notably different from their RADYN counterparts after the electron beam is switched off.

Furthermore, the RH solutions assuming CRD are often similar to those obtained assuming PRD, although the differences are more pronounced in the Ly- $\alpha$  and Ly- $\beta$  lines. While it was expected that the RH solutions assuming CRD would closely approximate the RADYN solutions, the resulting lines show a greater level of consistency with the RH profiles obtained assuming PRD. This not only indicates that the assumption of CRD may not be overly detrimental in some cases, but also that there exists a more dominant factor in RH that is responsible for the computed line profiles being different from those in RADYN.

This may be explained by the process by which RH computes the level populations for hydrogen. In RADYN, it is assumed that conditions are not in equilibrium, as indicated by the  $\frac{\partial n_i}{\partial t} + \frac{\partial n_i v}{\partial z}$  term in equation 2.12. This is an important consideration to take into account in an atmosphere in which the dynamics can change on timescales faster than the level populations. In RH, the level populations are calculated with the assumption of statistical equilibrium, by which it is assumed that the population of a level in a given atom or ion is constant ( $\frac{\partial n_i}{\partial t} = 0$ ).

By using this approach, RH re-solves each of the level populations with the assumptions of statistical equilibrium when each successive atmospheric snapshot is passed to it. This effectively neglects the “history” of the atmosphere, and also does not account for non-thermal collisions between the atmospheric plasma and the electron beam. Because the non-equilibrium electron densities are input to RH, it is hoped that at least some of this problem is mitigated, however RH will always try to return level populations to statistical equilibrium.

Greater agreement between the RADYN and RH solutions is found while the beam heats the atmosphere ( $t = 0 - 20$  s). Thereafter, the core intensities in a given line from RH reasonably match those obtained from RADYN, but the wing intensities noticeably decrease relative to the core, producing more prominently peaked profiles.

While the beam heats the atmosphere, the deposition of electrons increases both the amount of recombination in hydrogen and the amount of collisional excitation which leads to population of the upper levels. It may be the case that this allows the conditions in RADYN to approximate those of statistical equilibrium. Divergence between the RADYN and RH solutions is found after the beam switches off because the atmosphere continues to evolve on a rapid timescale, while there are no additional beam electrons available to influence the level populations. This leads to a departure from statistical equilibrium in RADYN.

This alternative process by which the level populations are calculated may explain why the RH profiles calculated assuming both CRD and PRD differ from those obtained using RADYN. A more desirable treatment would be to consider both non-equilibrium effects in tandem with PRD, as this would fully account for the rapid timescales at which the atmosphere evolves and how photons are redistributed within the radiation field. Figures 5.4, 5.6 and 5.9 do indicate the importance of assuming PRD, particularly when calculating intensities in the wings of Ly- $\alpha$ .

## 5.4 The Potential for Flow Measurements in Flares with Solar Orbiter's SPICE Instrument

In this chapter, the capabilities of an instrument such as EVE have been explored with respect to how successfully the features in a given line profile are retained during an observation. It has been shown that a correct interpretation of asymmetries in the Lyman lines requires knowledge of whether they are centrally reversed or not. While the EVE instrument is not capable of resolving these central reversals, there remains scope for such observations to be attempted with the Spectral Imaging of the Coronal Environment (SPICE) instrument (Fludra et al. 2013) on board the upcoming Solar

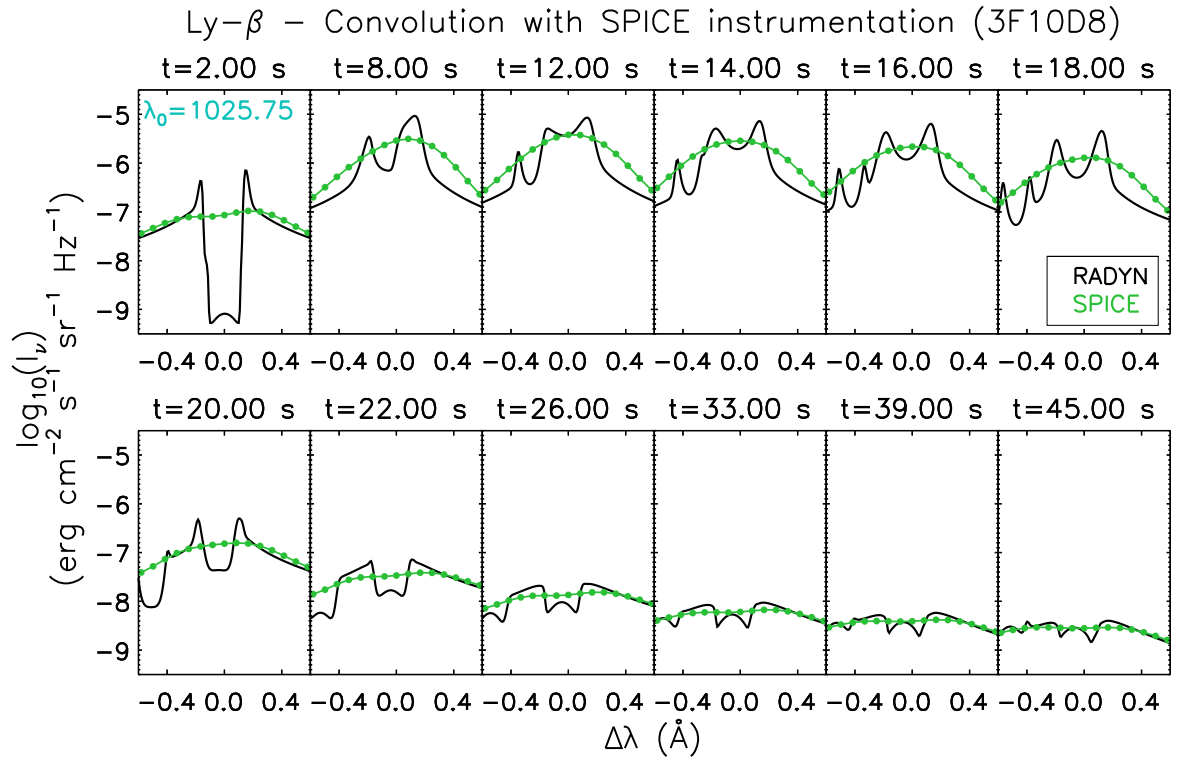


**Figure 5.10:** A series of snapshots of the Ly- $\beta$  line throughout the 3F10D8 simulation, before (black) and after (green) convolution with the SPICE instrumental profile.

Orbiter satellite. SPICE is an imaging spectrometer, and will make use of a slit to control the portion of the solar image that is passed to the grating and subsequent detector assembly.

The SPICE spectrometer includes a long wavelength band which will monitor the Sun in the region  $97.25 < \lambda < 104.93$  nm, allowing observation of the Ly- $\beta$  line. In this section, the potential capabilities of the SPICE instrument with regards to this line are briefly explored. Model Ly- $\beta$  line profiles from the 3F10D8 RADYN simulation are convolved with the SPICE instrumental profile, using a similar technique to that described in §5.1, and the resulting line profiles are assessed for detailed features and asymmetries. The 3F10D8 model is chosen as the Lyman lines calculated in this simulation were particularly feature-rich and complex, allowing us to better determine the capabilities of the SPICE spectrograph.

Fludra et al. (2013) details the optical parameters of SPICE's long wavelength

band. This band will have a spectral dispersion of  $0.083 \text{ \AA}$  per pixel at  $1010 \text{ \AA}$ , and the line spread function is expected to be approximately 4 pixels, leading to an overall FWHM of around  $0.4 \text{ \AA}$ . To approximate these instrumental effects, the Ly- $\beta$  line is again convolved with a Gaussian using the IDL **gaussfold**<sup>2</sup> procedure, this time with a FWHM of  $0.4 \text{ \AA}$ . The resulting profile is then rebinned to a wavelength spacing of  $0.083 \text{ \AA}$ , effectively accounting for the dispersion of the spectrometer. As the exposure time of the instrument may vary, the effects of time-integration are not considered here.

In Figure 5.10, multiple snapshots of the Ly- $\beta$  line are shown from the 3F10D8 simulation before and after the instrumental convolution is applied. At  $t = 2 \text{ s}$ , the Ly- $\beta$  profile post convolution shows a slight dip at the line core, which indicates that at certain times, SPICE may be capable of detecting the presence of a central reversal in the line. At  $t = 8 \text{ s}$ , the Ly- $\beta$  profiles after convolution also retain a clear signature of the strengthened red wing.

While the secondary blue-wing component remains a prominent feature in the Ly- $\beta$  line between  $t = 10 - 20 \text{ s}$ , no suggestions of its presence are found in the profiles once they undergo convolution with SPICE’s instrumental profile. At  $t = 16 \text{ s}$ , the near wings of the secondary component are particularly intense, but are still not retained after the convolution process. At  $t = 18 \text{ s}$ , it can be seen that the blueshift in the central reversal and the enhancements in the secondary blue-wing component effectively offset each other, producing a symmetric profile after convolution with SPICE. At later times, the secondary component contributes the majority of the line emission, which leads to strong blue asymmetries.

In Figure 5.11, Doppler velocity profiles are shown for the Ly- $\beta$  line (obtained from RADYN), having undergone the SPICE convolution process. As before, velocities are calculated using the Gaussian fitting and intensity weighted methods. The Ly- $\beta$  velocity profiles from SPICE are very similar to those obtained using the EVE parameters (shown in Figure 5.7a), with redshifts observed throughout the first 10 s and again after  $t = 20 \text{ s}$ . The diminishing of redshifts is again found between

---

<sup>2</sup>[https://github.com/emrahk/IDL\\_General/blob/master/third\\_party/aitlib/misc/gaussfold.pro](https://github.com/emrahk/IDL_General/blob/master/third_party/aitlib/misc/gaussfold.pro)

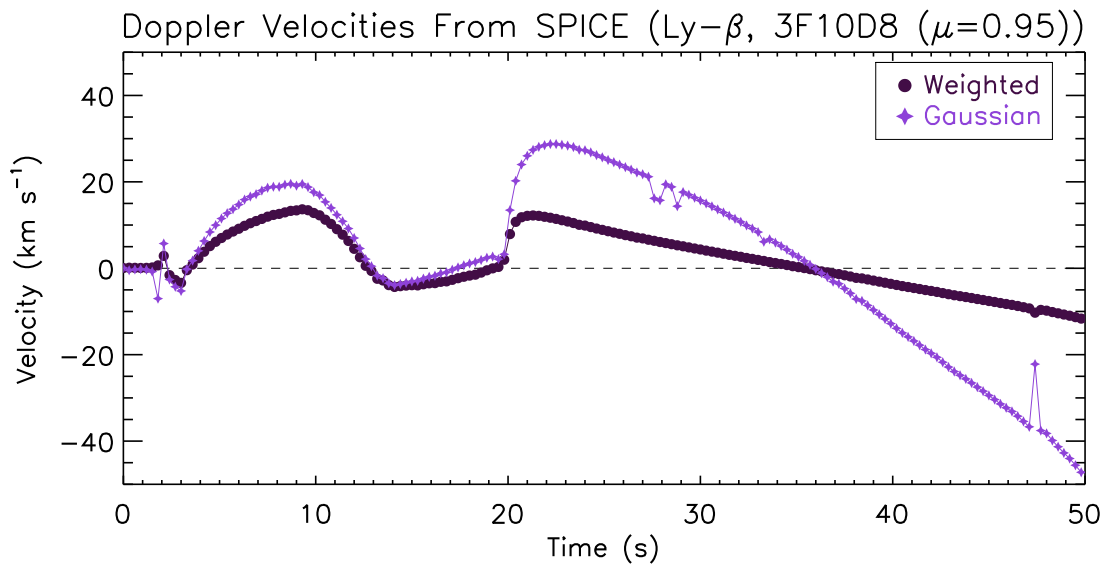


**Figure 5.11:** Doppler velocities measured in the Ly- $\beta$  line (3F10D8 simulation) after convolution with SPICE's instrumental profile. As before, negative velocities are upflows. Counterpart velocities using the EVE parameters are shown in Figure 5.7a.

$t = 10 - 20$  s as the secondary line component briefly acts to introduce a greater amount of emission in the blue wing, which counteracts the lack of emission within the blueshifted centrally-reversed line core.

While the peak downflow velocities obtained using the SPICE instrumental parameters (Figure 5.11) occur at the same times as those found using those from EVE (Figure 5.7a), the magnitudes of the peak velocities obtained from SPICE are greater. The velocities obtained from both the Gaussian and intensity-weighted methods are roughly  $5 \text{ km s}^{-1}$  higher than those found from EVE. This should be expected, as the line profiles as observed by SPICE contain a greater amount of detail than those from EVE, and should facilitate measurements of the line centroid variations to a greater degree of accuracy.

In Figure 5.12, the capability of SPICE to detect line asymmetries is explored. Defining  $A$ , the asymmetry in the Ly- $\beta$  line, as:

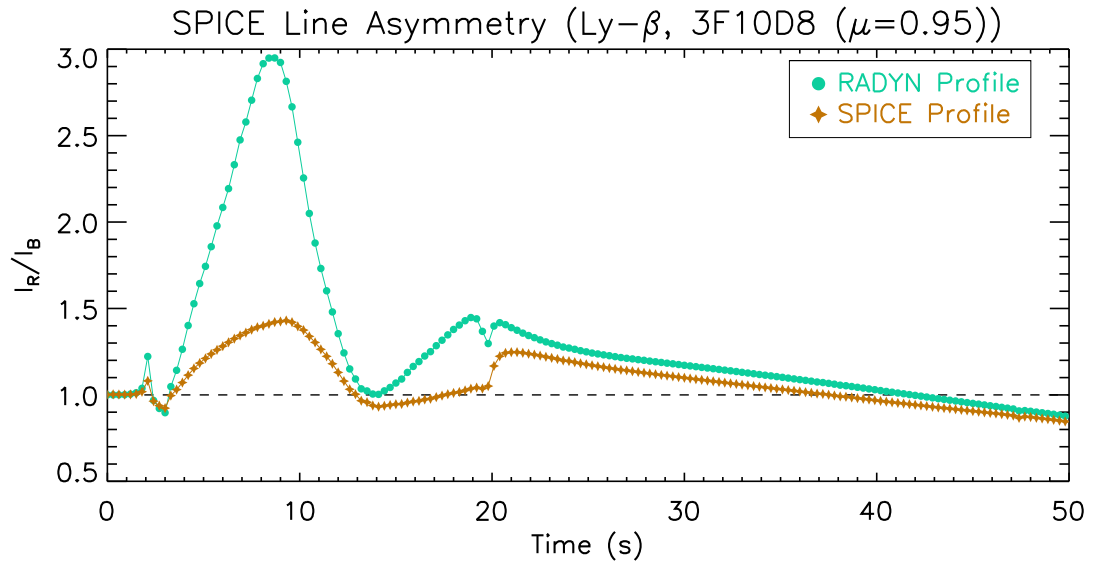


**Figure 5.12:** A running measurement of the asymmetry ( $A$ ) in the Ly- $\beta$  line after convolution with the SPICE instrumentation, relative to that in the profile output from RADYN.

$$A = \frac{I_R}{I_B} = \frac{\sum_{\lambda=\lambda_0}^{\lambda_0+\Delta\lambda} I_\lambda}{\sum_{\lambda=\lambda_0}^{\lambda_0-\Delta\lambda} I_\lambda}, \quad (5.1)$$

where  $\Delta\lambda = 0.58 \text{ \AA}$ , a running measurement of the asymmetry in the Ly- $\beta$  line is plotted for both the emergent profile from RADYN, and for the profile post-convolution with the SPICE instrumental parameters. A value of  $A = 1$  indicates no asymmetry. From Figure 5.12, it can be seen that even after convolution, the asymmetries in the line are clearly retained, indicating that SPICE should be well suited to detect line shifts in the Ly- $\beta$  line. However, it can be seen that between  $t = 8 - 9 \text{ s}$  the asymmetry measured by SPICE is notably less prominent than that in the unconvolved profile, indicating that the instrumentation still limits these measurements to an extent.

While the central reversal in Ly- $\beta$  is subtly hinted at in shallow dips at the line core at certain times after convolution, there are still many times at which there

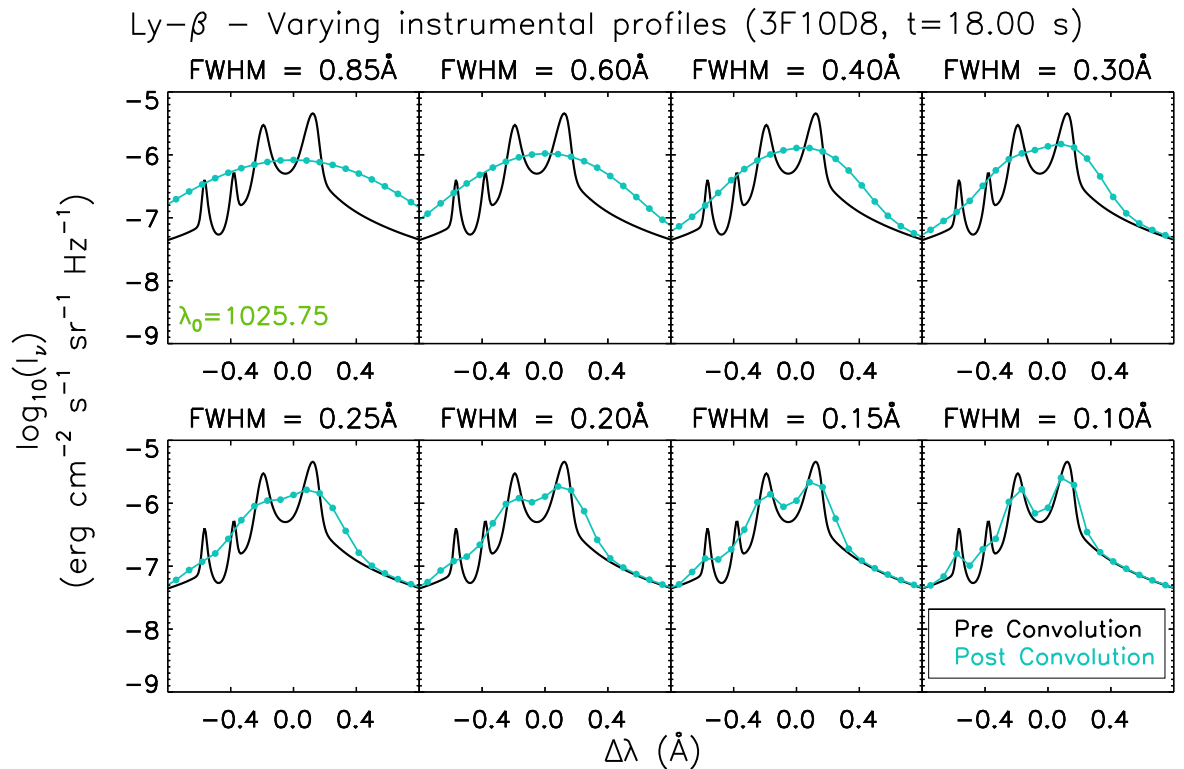


**Figure 5.13:** The Ly- $\beta$  line at  $t = 18$  s from the 3F10D8 simulation, before and after convolution with instrumental profiles of varying FWHM values. The FWHM is indicated above each individual panel. All profiles are rebinned to SPICE's wavelength spacing ( $0.083 \text{ \AA}$ ).

are no suggestions of such a feature in the SPICE profiles. To determine what sort of instrumental profile would be required to reliably retain such a feature, an incremental approach is shown in Figure 5.13. The Ly- $\beta$  profile at  $t = 18$  s is convolved with Gaussians with increasingly narrow FWHM values, with the resulting profile again rebinned to SPICE's wavelength spacing. From Figure 5.13, it can be seen that to reliably detect the central reversal, a FWHM value of around  $0.25 \text{ \AA}$  would be required, with the secondary blueshifted component becoming apparent from FWHM values narrower than  $0.20 \text{ \AA}$ .

## 5.5 Closing Remarks on Interpreting Lyman Line Asymmetries

The retention of central reversals in the cores of the Lyman lines has proved to be a very important factor in this chapter. From analysis of the F10 simulations, it can be seen that the Lyman lines after convolution with the EVE instrumentation do not correctly represent the direction of atmospheric flows. Because the lines are both centrally reversed and blueshifted, the profiles after convolution present red asymmetries as EVE cannot resolve the central reversal. If a line core is both centrally reversed and Doppler shifted towards a given wing, it will absorb more in that wing and the resulting profile after instrumentational effects will have an overall asymmetry in the opposite wing.

Correct interpretation of asymmetries in the Lyman lines, and therefore the direction of flows, clearly requires knowledge of whether or not the line is centrally-reversed or not. It is encouraging that SPICE may be able to detect these features at certain times (Figure 5.10), and it would be desirable to perform line shift analysis of the Ly- $\beta$  line during flares with this instrument. Because these features are not retained by EVE, there remains a challenge in interpreting flow directions from observations from this instrument. Therefore, in Chapter 6, a larger set of emission lines than those used in Chapter 3 are used to investigate line shifts in a recent EVE observation of an X9.3 flare, in order to test current assumptions of how flow direction is linked to line formation temperature.

## Chapter 6

# Comprehensive Dynamics of the X9.3 06th September 2017 Flare

While solar cycle 24 has generally been relatively quiet compared to other cycles, a period of activity during September 2017 could suitably be described as a finale. Following an X2.2 flare on the morning of the 06th September 2017 (SOL2017-09-06T09:10), active region 12673 emitted the strongest flare of the current solar cycle (SOL2017-09-06T12:02), peaking at 12:02 with a classification of X9.3. This was followed by an X8.2 event 4 days later (SOL2017-09-10T16:06).

In this chapter, additional EVE Observations are detailed for the X9.3 flare, with consideration of a more extensive series of lines available in the EVE data. As before, measurements of line shifts are performed in order to determine the magnitudes and directions of flows indicated by a number of ions spanning a wide range of formation temperatures. This should allow us to evaluate current assumptions about the relationship between the formation temperature of a given spectral line and the corresponding flow direction that will be exhibited by the line during a flare, as previously discussed in §1.3.4.

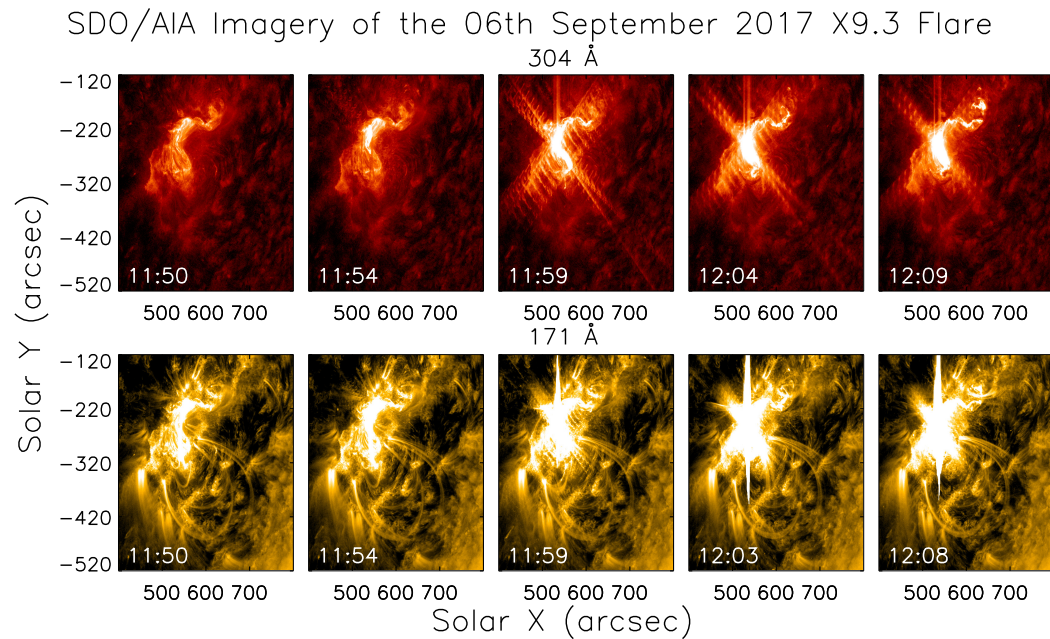


**Figure 6.1:** The progression of the 06th September 2017 X9.3 flare as observed in the 304 Å and 171 Å channels in AIA. The images in both channels have been scaled logarithmically to enhance the contrast. Observation times are indicated in the lower left of each panel.

## 6.1 The 06th September 2017 X9.3 Event

After emitting an X2.2 flare roughly three hours previously, AR 12673 again became the source of an increase in the GOES 1 – 8 Å flux starting at 11:53 UT on the 06th September 2017. Originating from heliographic co-ordinates (S09, W34), an X9.3 flare was emitted. The GOES Lightcurves for this event in the 1 – 8 Å and 0.5 – 4 Å bands are shown in Figure 1 of [Yan et al. \(2018\)](#), and indicate that the flare peaks at around 12:02 UT, with the SXR flux increasing by a factor of  $\sim 100$  relative to pre-flare levels. This flare, which constitutes the most powerful of the current solar cycle, has already been the subject of considerable study.

[Kolotkov et al. \(2018\)](#) note that the liberated energy was of the order  $10^{32}$  erg, and detected two quasi-periodic pulsations (QPPs) with both long (minutes) and short (seconds) periods in the thermal emission from this flare. [Romano et al. \(2018\)](#)

found evidence of shearing motions in the local photosphere both prior to and during the flare, and comment that this could be partially responsible for providing energy to the system. [Yan et al. \(2018\)](#) also acknowledge the role of shearing motions in providing energy during this event, and also investigate the role of sunspot rotation in this respect. The production of helioseismic waves ("sunquakes") in the pre-impulsive phase of this event, prior to the observation of HXR emission, is outlined by [Sharykin & Kosovichev \(2018\)](#).

In Figure 6.1, AIA images of the event are presented in the chromospheric 304 Å and coronal 171 Å channels. Brightenings in the 304 channel indicate that as the flare progresses, the affected area spreads towards the northwest, with the familiar two-ribbon structure becoming apparent from 12:09. The 171 Å channel also reveals that the northwestern part of the active region becomes increasingly affected as time progresses. Two coronal loops to the south of the active region also appear to move inwards during the course of the flare, which may indicate an implosion (see [Hudson 2000](#); [Wang et al. 2018](#)). In addition, a loop towards the east of the active region rapidly becomes bright and moves downwards between 11:58 and 12:02. [Yan et al. \(2018\)](#) detail the eruption of a flux rope during this flare, and present LASCO images showing a CME produced as a result of this.

This flare was also observed by EVE, and is currently the most intense event observed by the instrument. Given the strength of this event, the methods described in chapter 3 could again be used to study the dynamics of the flare through line shift analysis. However, given the clear ambiguities present in inferring flow directions from a restricted set of spectral lines from synthetic EVE observations outlined in chapter 5, we extended the set of lines to investigate, giving as complete a picture of the Doppler shifts as possible. Instead of focussing solely on the Lyman and C III lines as before, the full catalog of emission lines observable by the MEGS-B detector was taken into consideration. In this chapter, Doppler shifts are measured in a series of lines that span a wide range of formation temperatures. In chapter 1, it was outlined that the general paradigm for explosive evaporation predicts upflow signatures in high-temperature lines, and downflows in lines formed at low-temperatures. By measuring Doppler shifts in lines spanning a wide thermal range, the suitability of

this prediction can be tested for this flare.

## 6.2 Selection of Spectral Lines and Doppler Velocity Measurements

The MEGS-B detector on the EVE instrument provides wavelength coverage between 35 and 105 nm, which includes a wide range of emission lines beyond those of hydrogen. Particularly prevalent within this region are many lines produced by Fe and O at various stages of ionisation. In addition to these are a number of prominent lines from Mg, Si and Ne ions. Care must be taken, however, during selection of the emission lines used to measure Doppler shifts. Many lines within this region are plagued by “blends”, where two or more lines are closely spaced in wavelength. Lines that are affected by blends are unreliable candidates for diagnostic purposes, as the atomic transition responsible for a given observed feature (i.e, an asymmetry) will be ambiguous.

In addition to considering the emission lines listed in [Woods et al. \(2012\)](#), the flare spectra were analysed visually for the presence of prominent lines, and an initial sample of candidates was produced. Each line was then assessed for the presence of blends, by considering the relative intensities of nearby lines (closer than  $\sim 1 \text{ \AA}$ ) quoted in the line lists computed by version 7.0 of the widely-used CHIANTI package ([Dere et al. 1997](#); [Landi et al. 2012](#))<sup>1</sup>. Visual inspection of each spectral line was performed throughout all time-steps in the flare data, and the overall quality of each line was noted based on the amount of noise and the presence of any long-lived asymmetries (i.e, due to blends). Lines that had other strong lines present to within  $1 \text{ \AA}$  in the CHIANTI line lists, or those that appeared excessively noisy under visual inspection, were omitted from further investigation.

By checking the CHIANTI database for potential blends, and by qualitatively assessing each line, an initial sample of 33 emission lines in the MEGS-B data was reduced to 14. The final selection of emission lines span a temperature range between

---

<sup>1</sup><http://www.chiantidatabase.org/chiantilinelist.html>

Ion	Formation Temperature ( $\log_{10}(T)$ )	$\lambda_0$ (nm)	$\lambda_{min}$ (nm)	$\lambda_{max}$ (nm)
Si XII	6.30	52.07	51.95	52.20
Si XII	6.30	49.94	49.83	50.06
Ne VIII	5.80	77.04	76.93	77.16
Ne VII	5.70	46.52	46.42	46.65
O VI	5.50	103.19	103.08	103.34
O V	5.40	62.97	62.84	63.12
O III	5.05	52.58	52.46	52.71
O III	5.00	59.96	59.85	60.09
C III	4.95	97.70	97.55	97.90
He I	4.50	58.43	58.28	58.60
H I	4.25	102.57	102.45	102.70
H I	4.25	97.25	97.10	97.40
H I	4.25	94.97	94.87	95.07
H I	4.25	93.79	93.69	93.88

**Table 6.1:** Formation temperatures, and wavelength data for each of the emission lines observed during the 06th September 2017 X9.3 flare.  $\lambda_{min}$  and  $\lambda_{max}$  describe the range within which the spectral lines are fitted. Quoted rest wavelengths (excluding Ly- $\epsilon$ ) are obtained from the CHIANTI line lists.

$4.25 \leq \log_{10}(T) \leq 6.30$ , sampling both the chromospheric and coronal environments. A full MEGS-B spectrum observed around the peak of this flare is shown in Figure 6.2, with each of the emission lines in Table 6.1 highlighted. While the EUV spectrum is populated with many high-temperature Fe lines, none are suitable for line shift analysis. Table 1 of Del Zanna & Woods (2013) lists the observable Fe lines in the EVE data, and indicates that all of the Fe lines in the MEGS-B spectra suffer from the presence of blends, with only the MEGS-A lines being suitable for diagnostic purposes. As MEGS-A has remained switched off since 2014, no Fe lines are considered in this chapter.

The wavelengths and formation temperatures of the lines considered are listed

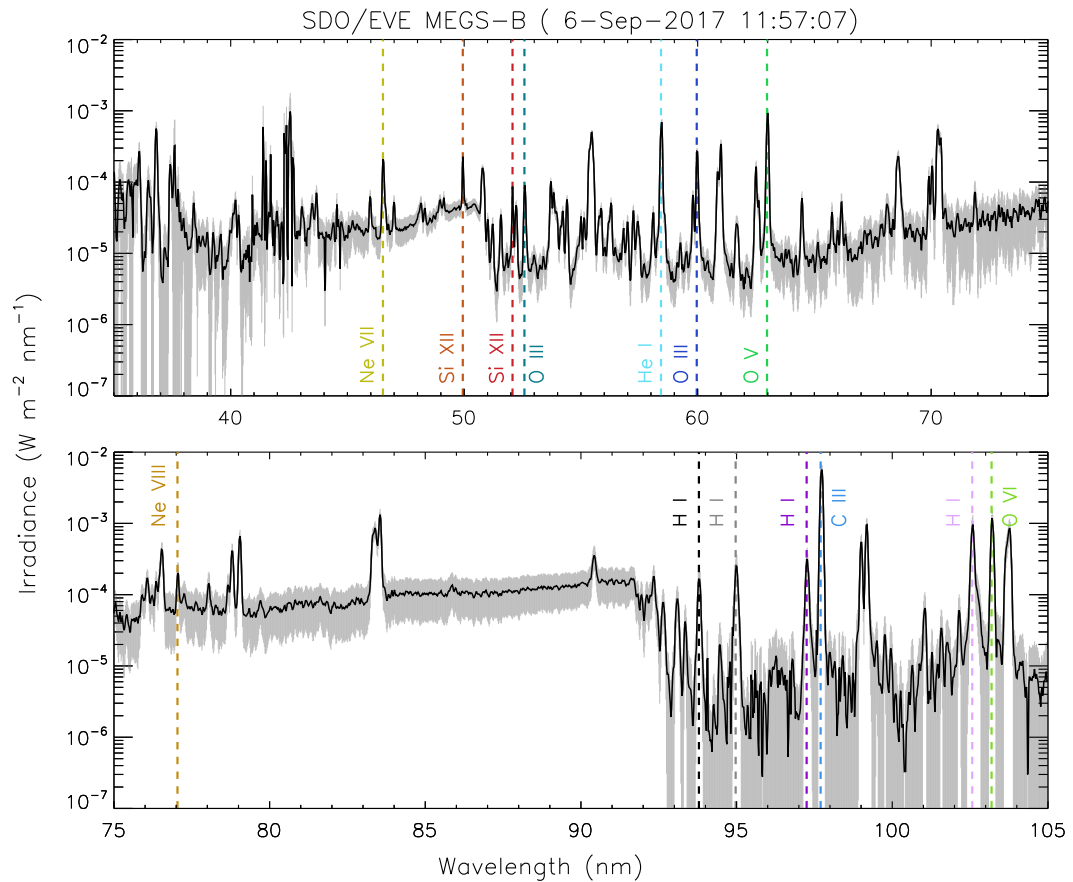


**Figure 6.2:** A complete MEGS-B spectrum observed during the first peak of the o6th September 2017 flare. No preflare subtraction has been performed. The formal “precision” errors are overplotted in light grey. The emission lines used to measure Doppler shifts in this chapter are highlighted by the dashed coloured lines.

in Table 6.1. The quoted formation temperatures were obtained by finding the temperature at which each line’s *contribution function* ( $G(n_e, T)$ ) reaches a peak value. This was done by using the IDL **gofnt** procedure, included as part of the **CHIANTI** package.<sup>2</sup> It is important to note that this definition of the contribution function is distinct from that in the previous chapters, and instead describes the overall contributions to emission in a given line as a function of the plasma parameters.

<sup>2</sup>[http://www.damtp.cam.ac.uk/user/astro/gd232/research/medoc\\_03/exercise/gofnt.pro](http://www.damtp.cam.ac.uk/user/astro/gd232/research/medoc_03/exercise/gofnt.pro)

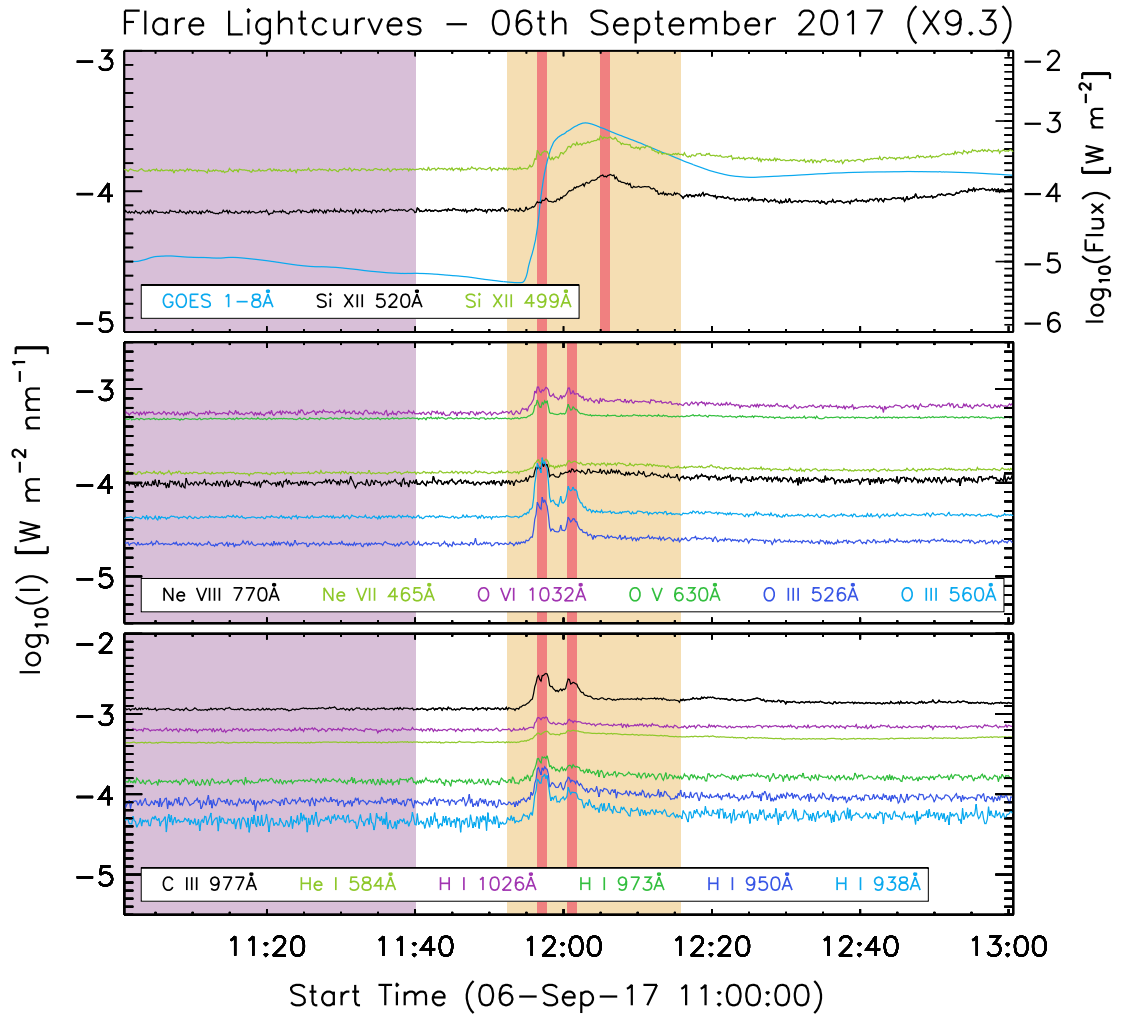


**Figure 6.3:** Lightcurves for each of the emission lines listed in Table 6.1 during the X9.3 flare, with the GOES 1-8 Å flux overplotted (right axis). The preflare and flaring time-ranges are highlighted in purple and gold respectively. Highlighted in red are three particular times, corresponding to peaks in the line emission.

For further discussion of this concept of the contribution function, the reader is encouraged to consult §2.8 of [Aschwanden \(2005\)](#).

The lightcurves in each of the emission lines are shown in Figure 6.3. Also plotted on the right axis is the observed GOES flux in the 1-8 Å channel. The majority of lines exhibit two peaks in their lightcurves, with an initial intense peak occurring at 11:57 UT, followed quickly by a secondary peak at 12:01 UT. It can be seen that the temporal

evolution of the Si XII lines is notably different from the lower temperature species. While these lines do show signatures of the first peak at 11:57, their lightcurves continue to intensify until indicating a “third” peak at 12:05 UT. This third peak, apparent only in the high temperature lines, occurs while the lower temperature lines are already undergoing their gradual phase. Emission in the high-temperature lines lags that of the low temperature species as the plasma requires time to be heated to sufficient temperatures.

In Figure 6.4, snapshots of each line before preflare subtraction are shown at several times throughout the flare’s duration. It can again be seen that the Si XII lines exhibit peak intensities at a later time than the lower-temperature species. Even the non-subtracted profiles exhibit notable enhancements. In chapter 3, it was found that while the velocity profiles obtained from profiles that had not been preflare-subtracted exhibited low noise, their magnitudes were notably diminished with respect to their flare-excess counterparts. It is therefore encouraging that the flare signal is visible even without subtraction of the preflare, as it should allow the velocity signatures to be clearly observed even without isolation of the flare emission.

Each of the lines listed in Table 6.1 was investigated for the presence of Doppler shifts using the three methods outlined in chapter 3. Preflare and flaring timescales were defined, and are indicated by the purple and gold shaded regions in Figure 6.3 respectively. Subtraction of the preflare again allows the flare signal to be isolated from emission across the rest of the disk, and measurements of the line centroid positions are performed in the data with and without preflare subtraction.

It should be emphasised that the Si XII line shapes are distinctly non-Gaussian (Figure 6.4), and so achieving an accurate measurement of the line centroid positions in these lines proves challenging when using the Gaussian fitting method. Both Si XII lines appear to have long-lived asymmetries in their red wings, likely indicative of the presence of blends with other spectral lines. However, the positions of these asymmetries are not consistent with the expected rest wavelengths of any of the lines quoted in the CHIANTI line lists. Searching the NIST atomic database<sup>3</sup> does indicate nearby spectral lines, but it remains challenging to determine which, if any, of these

---

<sup>3</sup><https://www.nist.gov/pml/atomic-spectra-database>

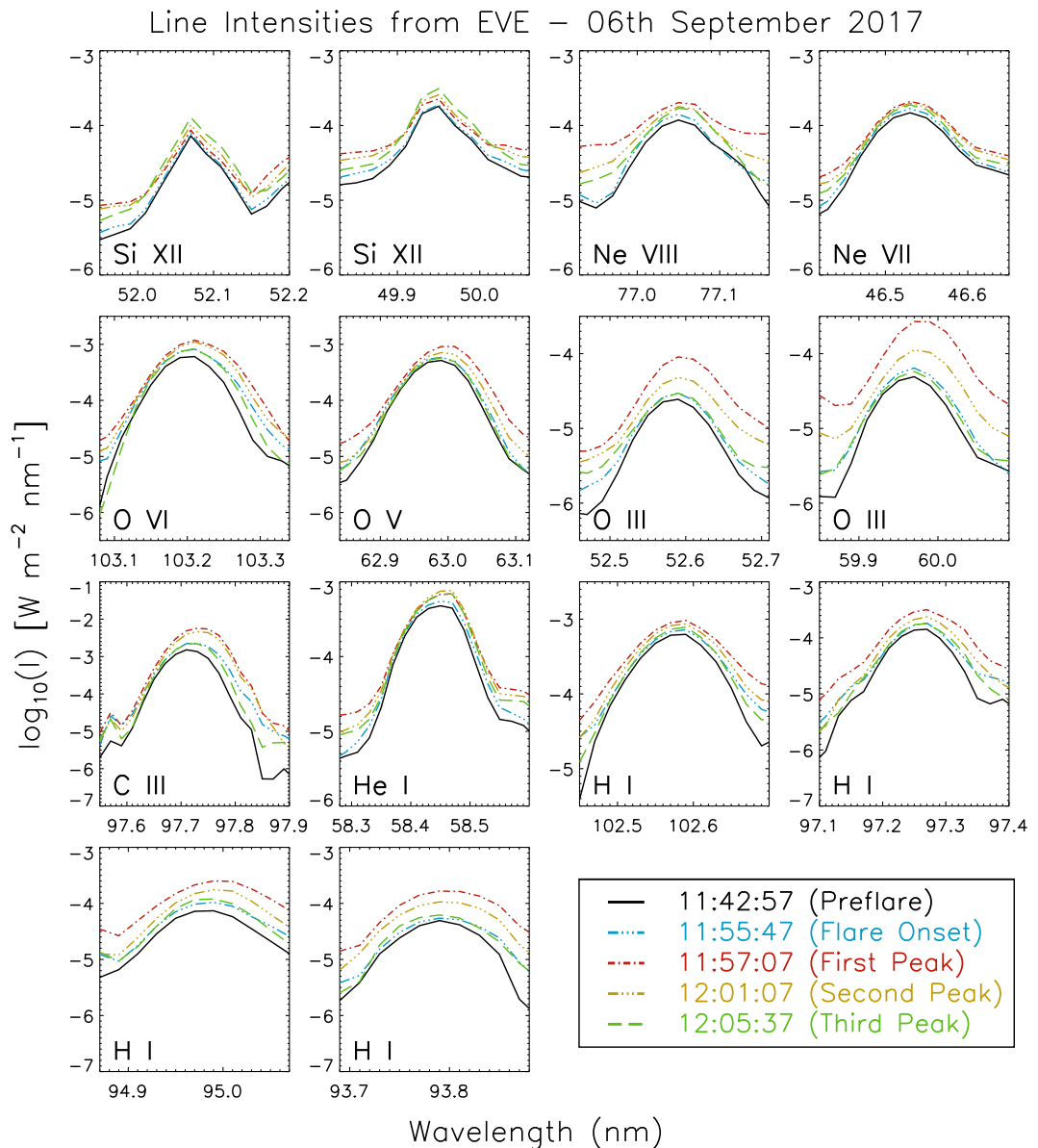


**Figure 6.4:** Snapshots of each of the emission lines throughout the flare’s progression. Times shown are the preflare (black), flare onset (blue), primary (red) and secondary (gold) flare peaks, and the gradual phase (green).

lines could be appreciably blended with the Si XII lines.

Removal of Si XII from the line list was considered, but this would critically restrict the range of sampled temperatures, lowering the upper temperature limit from around 2 MK to ~640 kK, and forbidding examination of any lines at formation

temperatures expected to be associated with upflows. Milligan & Dennis (2009) indicate that the transition between downflow and upflow in explosive evaporation lies somewhere between 1.5 and 2 MK. While the Si XII lines lie in an important region of parameter space, their line shapes are not ideal for analysis purposes. We stress that while the Si XII lines are included in our measurements, a greater deal of caution must be employed when interpreting their line shifts due to the presence of unidentified blends. To this end, the cross correlation and intensity-weighted methods are emphasised, as they do not rely on an assumption of the line's shape.

### 6.3 Doppler Velocity Profiles During The 06th September 2017 Flare

In Figure 6.5, Doppler velocities in each of the considered lines are shown throughout the course of this flare, and are measured without subtraction of the preflare profiles ("Sun as a star"). For conciseness, we only show results calculated using the cross-correlation method, but it should be noted that those obtained from Gaussian fitting and from Intensity weighting are overall very similar. We focus on this particular method because the Gaussian fits to the preflare Si XII lines are poor, and their derived line centroids are systematically skewed due to this, and because the intensity-weighted method again obtains slightly weaker flow speeds. To avoid overcrowding of the plots, the "heuristic" errors as in chapter 3 are not overplotted, but it is noted that the errors should be roughly the same size as those of the Lyman lines in chapter 3. Towards the end of this chapter, errors obtained from the variation in methods and time-averaging are shown.

In chapter 3, the lack of preflare subtraction led to very weak flow signatures; however, none of the flares in the previous study were as intense as this X9.3 event, and from Figure 6.4 it is clear that even without preflare subtraction the flare's presence can be ascertained in the evolving line shapes.

In Figure 6.5, the three flare "peaks" (indicated in red in Figure 6.3) are highlighted in lavender. Each line's Doppler velocities are overplotted for each of the

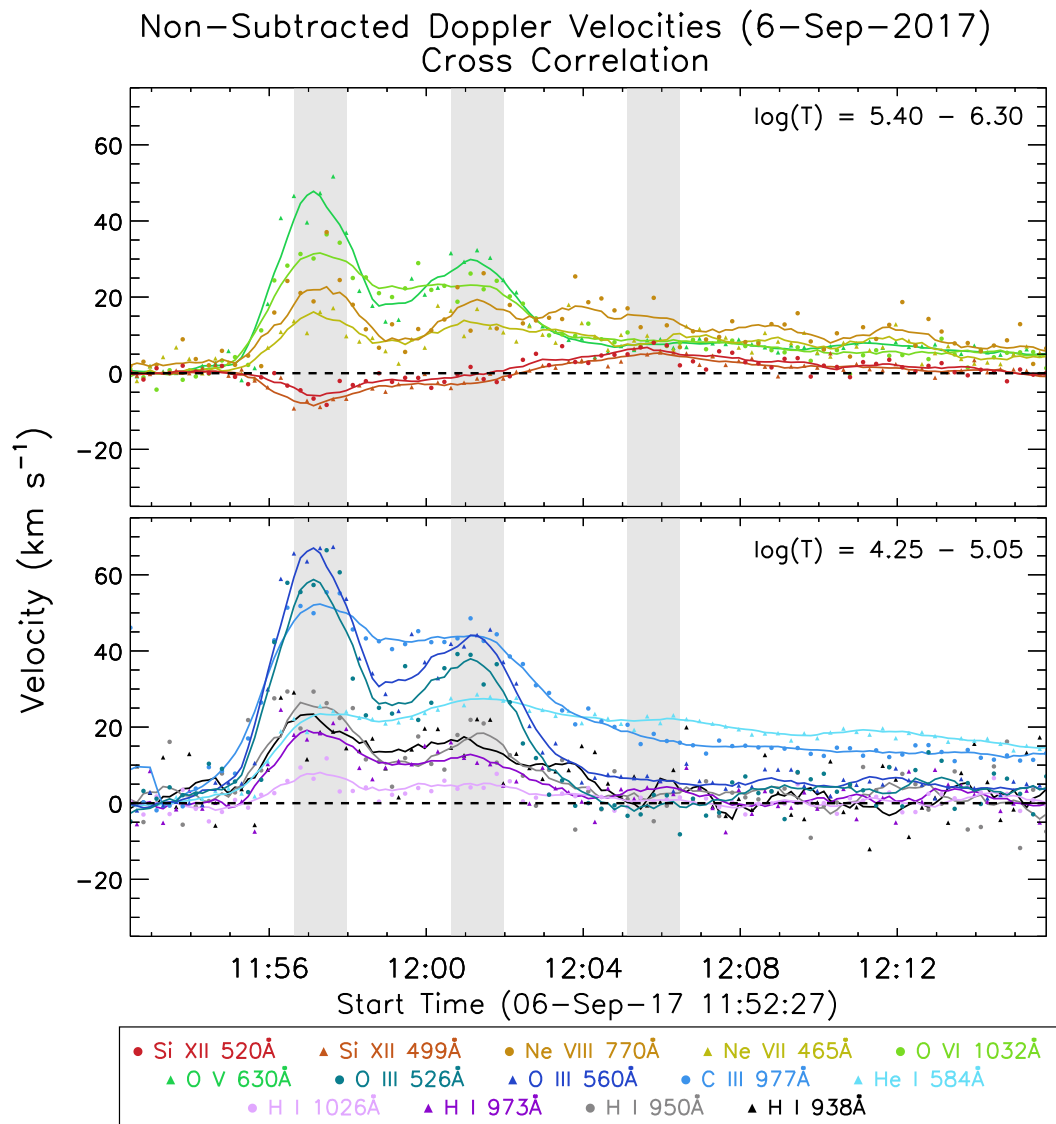


**Figure 6.5:** Doppler velocities obtained without preflare subtraction during the X9.3 06th September 2017 flare. Velocities are calculated using the cross correlation method. Positive velocities indicate downflows. The lines show the data smoothed with a boxcar of 9.

three methods. In order to reduce the amount of “crowding” in the plot area, every second data point is plotted. However, the smoothed velocities (indicated by the solid lines) are obtained by smoothing over all data points with a boxcar of 9.

Certain aspects of the velocity profiles are immediately noticeable. Nearly all of

the spectral lines begin to exhibit downflow signatures from 11:55, with the O III 560 Å line indicating the fastest speeds (40 – 60 km s<sup>-1</sup>). These downflow signatures peak concurrently with the first flare peak, at 11:57. The downflows then diminish slightly, before gradually increasing in speed, peaking again at 12:01. It should be noted that the observed velocity signatures in Sun-as-a-star should scale with the lightcurve intensity as the flare signal increases relative to the emission from the rest of the disk, so the double-peaked structure visible in the downflow signatures is most likely a result of the lightcurve, and may not be indicative of a dynamical effect.

The Lyman lines exhibit downflows in the Sun-as-a-star velocity profiles, with Ly- $\delta$  and Ly- $\epsilon$  suggesting flow speeds of 20 – 30 km s<sup>-1</sup>. The He I 584 Å line does not generally display a similar flow profile to the other lines, but does consistently suggest downflow speeds of 20 – 30 km s<sup>-1</sup>. The O III and C III lines show the strongest downflow response to the flare, with velocities generally ranging between 40 – 60 km s<sup>-1</sup>.

The observed velocity profiles in the Si XII lines are notably different from the cooler species. The velocity profiles indicate very slight blueshifts (5 – 10 km s<sup>-1</sup>) in these lines at the first flare peak (11:57), while the intensity-weighted method suggests greater upflow speeds in these lines at this time.

It was observed in Figure 6.3 that the temporal evolution of the Si XII lightcurves is qualitatively different from that of the low temperature lines, with an overall peak observed at 12:05. At this time, the velocity profiles indicate downflows in the Si XII lines, with speeds of ~5 km s<sup>-1</sup>.

As discussed in chapter 3, flare-excess velocity profiles more accurately quantify the flow speeds. Doppler velocity profiles, calculated after subtraction of the preflare irradiance, are shown in Figure 6.6, and represent line centroid variations solely as a result of the flare.

From Figure 6.6, it is clear to see that the flare-excess velocity profiles before ~11:56 are subject to a large amount of variation, with many of the velocities diverging strongly from rest. This is because the signal in flare-excess has not yet appreciably enhanced above preflare levels, resulting in noise-dominated profiles.

From 11:56 onward, a greater amount of structure is found in the derived velocity

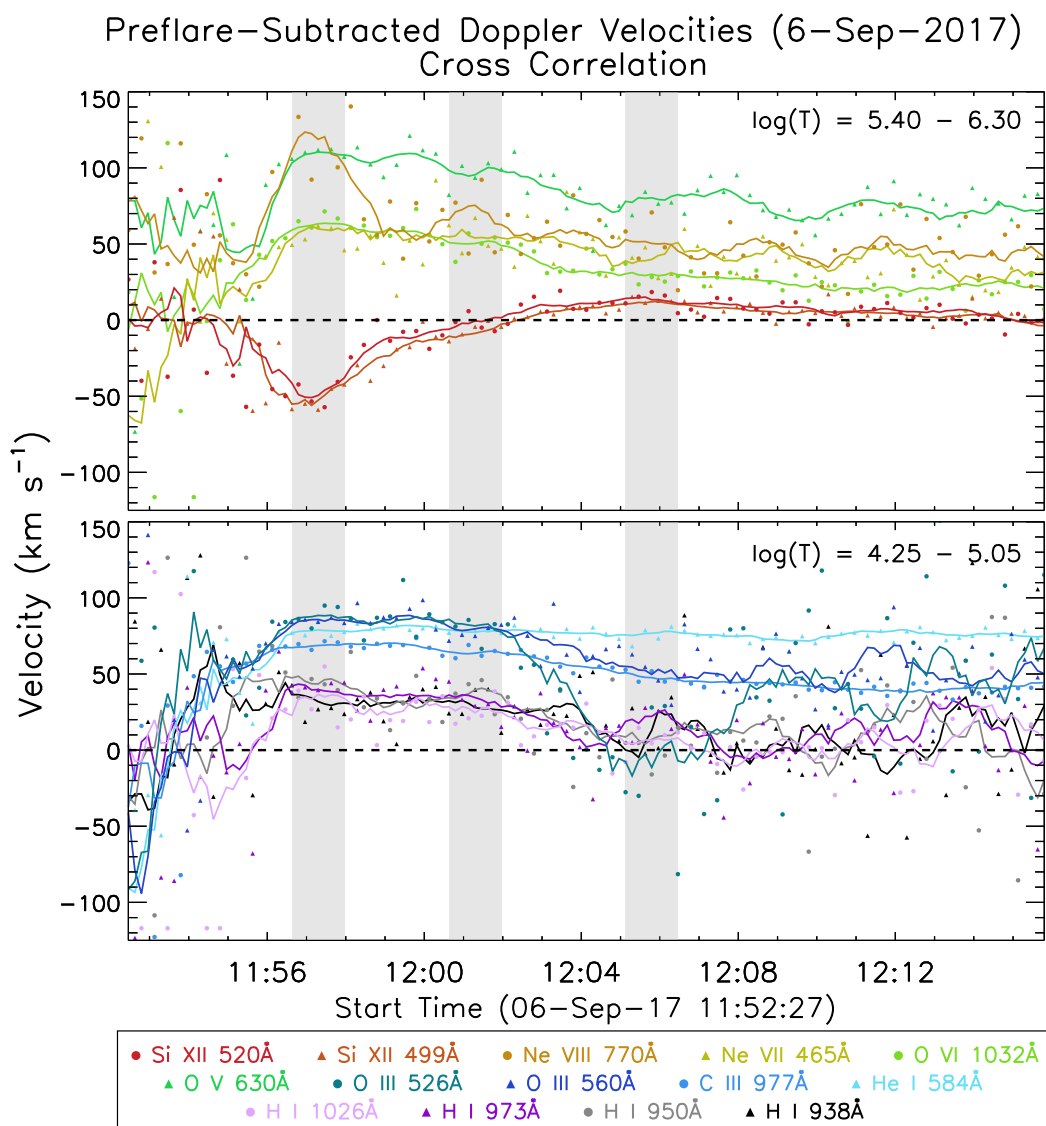


**Figure 6.6:** Flare excess Doppler velocities obtained after preflare subtraction during the X<sub>9.3</sub> 06th September 2017 flare. Positive velocities indicate downflows. Velocities are smoothed with a boxcar of 9.

profiles. Around the time of the first flare peak (11:57), the velocity profiles are relatively stable. Here, all lines with the exception of the Si XII lines exhibit downflows. Around this time, the Lyman lines suggest downflows of 30–50 km s<sup>-1</sup>. The Oxygen lines exhibit a stronger response; indicating downflow velocities ranging between 50–110 km s<sup>-1</sup>, with the latter velocity evidenced by the O V 630 Å line. The He I

and C III lines exhibit stable redshifted signals with a low amount of scatter, and indicate plasma downflows of  $60 - 80 \text{ km s}^{-1}$ .

The Ne VII  $465 \text{ \AA}$  line also maintains a near-constant downflow velocity of around  $50 \text{ km s}^{-1}$ . The flows indicated by the higher-temperature Ne VIII line are the fastest of all species, with downflows of  $120 \text{ km s}^{-1}$ . Both of the Si XII lines are consistently blueshifted around the time of the first flare peak, indicating upflows of  $50 \text{ km s}^{-1}$ .

Generally, the flow signatures described above persist with an almost-constant behaviour towards the time of the second flare peak (12:01). Most of the spectral lines do not exhibit a change in their velocity between the two flare peaks, with the only exceptions being the Ne VIII and Si XII lines. From Figure 6.3 it was apparent that the secondary flare peak is not visible in the Si XII lightcurves, and its presence is less prominent in the Ne VIII line. Around this time, the Si XII lines have diminished flow speeds relative to at 11:57.

The third flare peak, only apparent in the Si XII lightcurves, occurs between 12:05-12:06. At this time, the Si XII lines exhibit downflows, with speeds of  $20 \text{ km s}^{-1}$ . The evolution of the other lines at this time is less consistent. Some lines continue to indicate long-lived downflows. The hydrogen Lyman lines have begun to suffer from an increasing amount of noise, but also suggest weak downflows. The O III line  $526 \text{ \AA}$  line is particularly curious, as its downflows exhibit a rapid deceleration from around 12:02. The other O III line does not exhibit such a severe change in behaviour, and so it is not convincing that this sharp deceleration indicated by the  $526 \text{ \AA}$  line at 12:05 is genuine.

While the flare-excess velocity profiles in particular are complex and variable, some key points can be obtained by considering the dynamics at the three peak times indicated by the flare lightcurves. For the majority of lines that exhibit the first two peaks in their lightcurves (11:57 and 12:01), consistent downflows are observed between the two flare peaks. As in the Sun-as-a-star profiles, the downflow velocities are typically strongest in the Oxygen lines, although in flare-excess it is the O V line that suggests the maximum speed and not the O III line. The Si XII lines are the only lines that exhibit consistent upflow signatures, which are strongest around the time of the first flare peak. However, by the time of the third peak (12:05), these upflow

signatures have transitioned into weaker downflows.

## 6.4 The Variation of Flow Velocity with Line Formation Temperature

In this section, we investigate whether or not the formation temperature of a line has any bearing on the flows observed in this flare. In Figure 6.7, the quoted line formation temperatures from Table 6.1 are plotted against time-averaged Doppler velocities obtained from cross-correlation of the flare-excess spectra. This is done for each of the three flare peaks, corresponding to 11:57 (a), 12:01 (b) and 12:05 (c) respectively. Velocities are time averaged for 4 bins either side of the times quoted in each panel, sampling 9 bins in total.)

The cross-correlation method is chosen here, as we have discussed the problems encountered for Si XII when the Gaussian method is used, and because the intensity-weighting method frequently underestimates the speeds. Two sets of error bars are shown for each data point in Figure 6.7; the larger velocity errors are obtained by taking the standard deviation of the derived velocities across all three methods and the 9 time bins used to obtain the mean velocity. The errors with the narrower hats (which are typically smaller) do not consider alternate methods, and are derived solely from the time-averaging.

Throughout each of the times shown in Figure 6.7, the majority of lines within the  $\log_{10}(T)$ - $V$  space do not drastically change their position. In particular, Ne VII, O VI, O V, O III (560 Å), C III and He I exhibit remarkable stability in this respect. The hydrogen Lyman lines do show a weakening in the velocity field between 12:01 and 12:05 but consistently suggest downflows. The O III 526 Å line is harder to interpret, following the general downflow trend with formation temperature throughout the first two flare peaks, but exhibiting upflows afterwards. In Figures 6.7a and b there does appear to be a variation of the downflow velocity with formation temperature, peaking at  $\sim T = 250$  kK, indicated by the O V line.

As the formation temperature increases, the overall picture is less clear. While

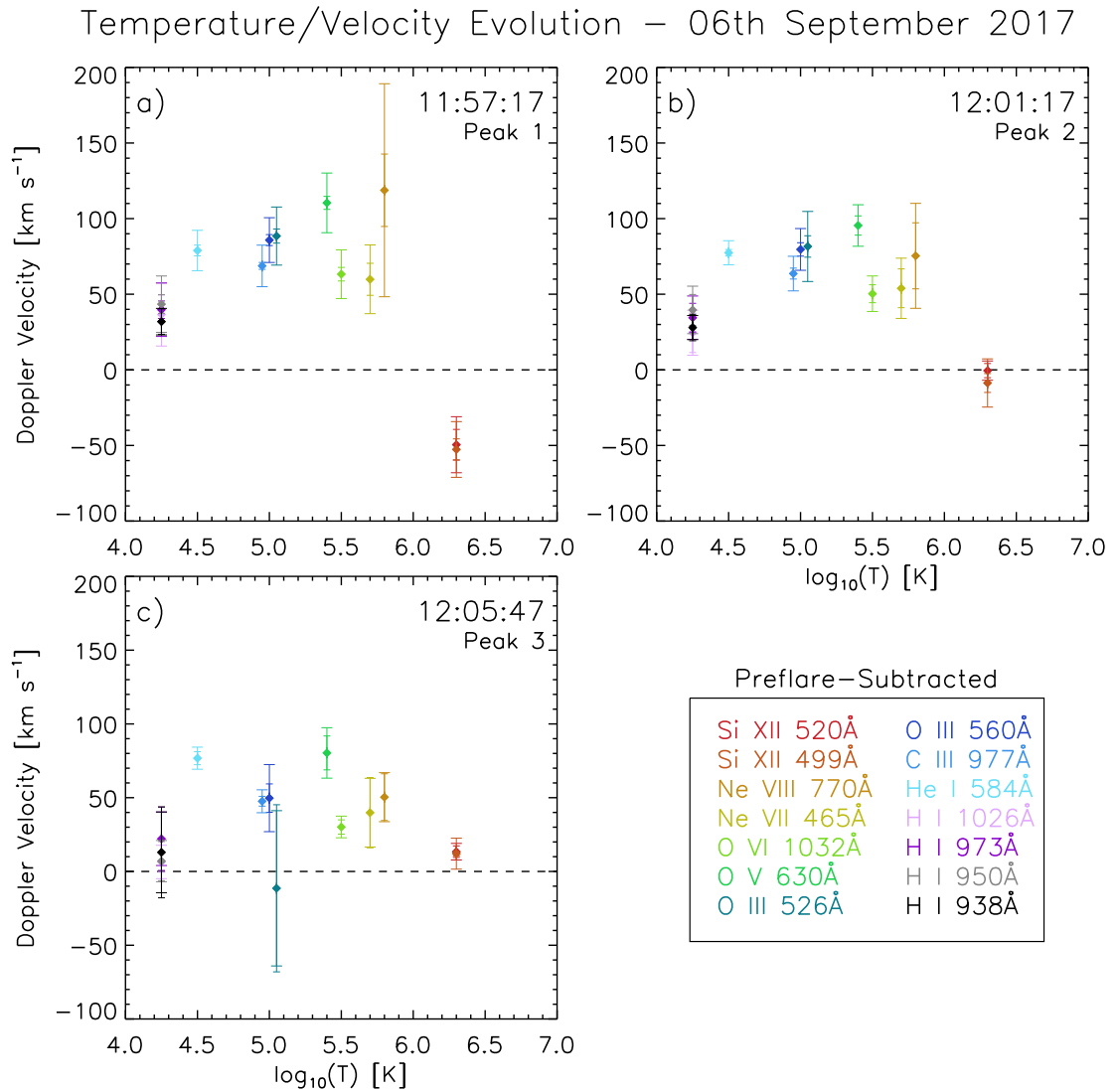


**Figure 6.7:** Flare-excess Doppler velocities obtained for the 06th September 2017 flare, plotted as a function of line formation temperature. Velocities have been time-averaged for a total of 9 data points about the times quoted in the upper right of each panel, and are obtained using the cross-correlation method. Velocity errors are obtained by taking the standard deviation of velocities across all three methods throughout the 9 time-points. The smaller error bars indicate averaging solely over time and not the method used.

Ne VIII does consistently indicate downflows, the intensity weighted method finds upflows in the line at 11:57, producing large error bars at this time. While the Si XII

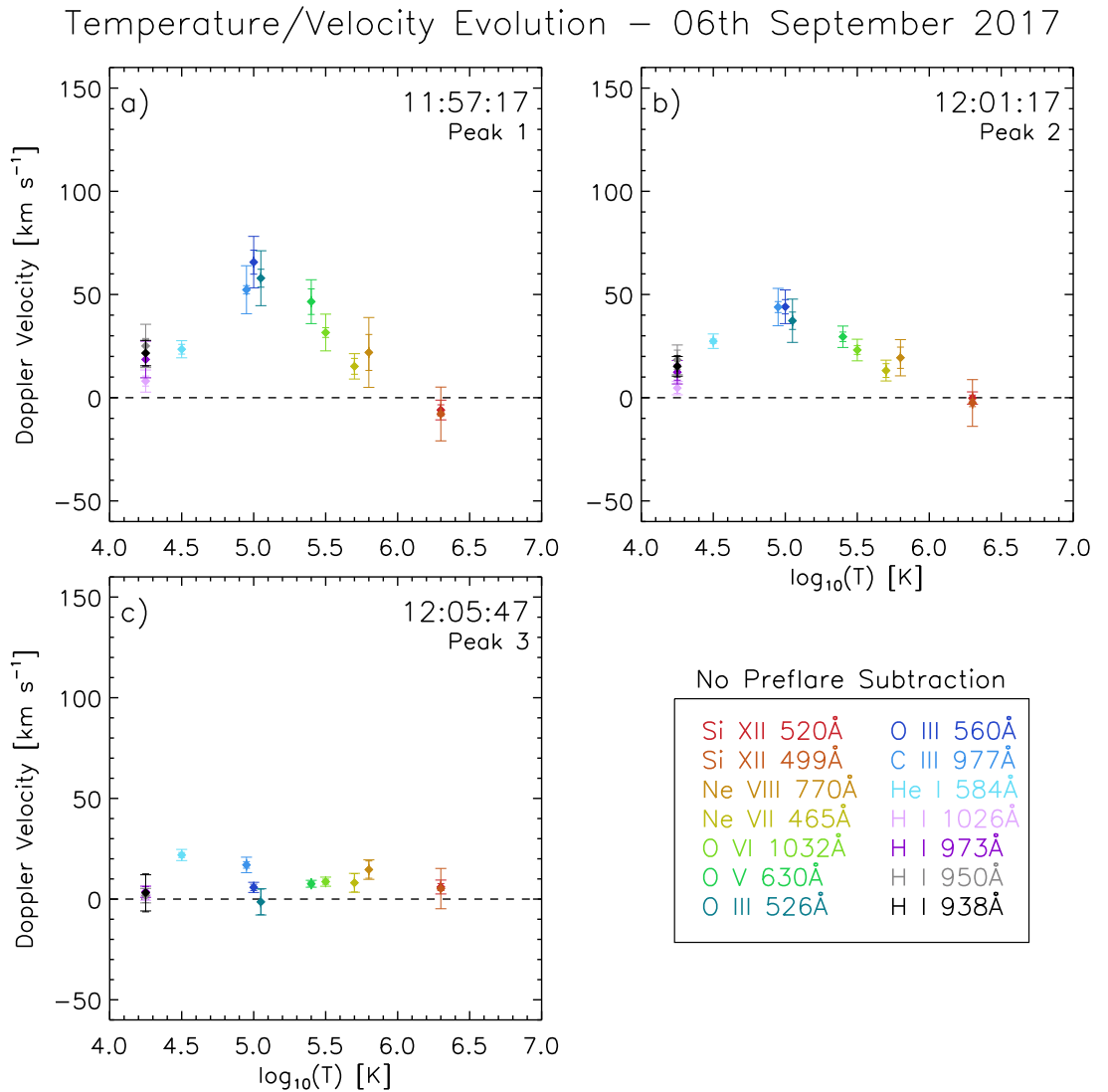


**Figure 6.8:** Doppler velocities (obtained using cross correlation) plotted as a function of temperature as in Figure 6.7, but obtained using Sun-as-a-star data (no preflare subtraction).

lines exhibit upflows during the first flare peak, these measurements again have rather large errors and are likely introduced by the difficulties in fitting Gaussians to these lines. When the Si XII lightcurves are at their maximum (Figure 6.7c), weak downflows are found in the lines.

While the velocity characteristics for some lines are rather variable, there does appear to be some form of dependency of the derived Doppler velocity on the

formation temperature of a given line. There is no evidence of upflow in any of the 12 lines that form at temperatures below 1 MK, with the only exception being found in the O III line 526 Å line, which may be affected by an unidentified blend. Downflow velocities appear to gradually increase with temperature between  $\log_{10}T=4.25 - 5.4$ , upon which they begin to diminish as the temperature increases beyond this limit. The Si XII lines are the only ones in our data that sample plasma temperatures above 1 MK, and indicate the possibility of both upflows and downflows, although beyond 12:01 their velocity signatures are weak ( $\sim 10 \text{ km s}^{-1}$ ). In Figure 6.8, the Sun-as-a-star counterpart to Figure 6.7 is shown, and it can be seen that the velocities obtained with no preflare subtraction display similar characteristics to those in flare-excess, although the downflow velocities peak at a slightly lower temperature than those in Figure 6.7.

The results found in Figures 6.7 and 6.8 are consistent with other studies. In Milligan & Dennis (2009), the velocity signatures of multiple EUV lines spanning a wide range of formation temperatures were determined using HINODE/EIS observations. Figure 5 of their paper shows that downflows were observed in many low-temperature lines, accompanied by much faster upflows in the high-temperature lines. Furthermore, they indicate that the transition between downflow and upflow occurs between 1.5 – 2 MK. Similarly, results from modelling reported by Liu et al. (2009) place this transition temperature between 1 – 2 MK. The observations reported in Kamio et al. (2005) also provide a baseline for comparison, in which strong downflows of  $87 \text{ km s}^{-1}$  were observed in O V, while no prominent velocities were observed in the T=1 MK Mg IX line.

When compared to the literature, our results are encouraging as we also find that downflows are a ubiquitous feature of the chromospheric lines in this flare. As in Kamio et al. (2005), we also find these signatures to be particularly strong in the O V line. Despite the challenges in fitting the T=2 MK Si XII lines, we also find that their derived flow signatures are close to what would be expected. While they only exhibit clear upflows at around the time of the first peak 11:57, the downflow signatures observed afterwards are very weak. As with the Mg IX line observed by Kamio et al. (2005), the lack of a dominant flow direction in these lines could be indicative of

their formation within the “intermediate” temperature range. Figure 5 of [Milligan & Dennis \(2009\)](#) and Figure 10 of [Liu et al. \(2009\)](#) support this idea, indicating that any upflows at temperatures of 2 MK would be weak.

It is worth reiterating that several of the lines studied in this chapter may still be affected by the presence of unidentified blends, but bearing this in mind, the velocity characteristics determined using these EVE lines are not in contradiction to other studies. While the range of temperatures sampled in this chapter is rather restricted towards low-temperature lines, the characteristics shown in Figure 6.7 are in agreement to those reported by other authors, and suggest a case of explosive evaporation during the X9.3 flare. Nonetheless, chapter 5 has shown that interpretation of these results should be done with caution. It has already been established that if central reversals are present in the EVE lines, the derived flow direction obtained from observations of the line centroid variations may not be indicative of the true dynamics of the situation. Keeping this in mind, but noting the appreciable number of EVE lines considered, it is encouraging that the expected hallmarks of explosive evaporation are found here.

# Chapter 7

## Conclusions

The work presented in this thesis provides an overview of several aspects relating to the dynamics of the flaring chromosphere. In particular, the strength of a combined approach incorporating both observations and modelling is emphasised. The overall aim of this work has been to investigate and assess the suitability of prevailing theories about chromospheric flow structure during flares. This has been done by applying analysis techniques to new observations, and by taking advantage of increasingly sophisticated flare modelling and radiative transfer codes. While some of our EVE observations verify the current paradigms relating to chromospheric evaporation and condensation, others do not. Furthermore, problems regarding interpretation of line shifts observed by this instrument have been identified as a result of simulating model line profiles.

In Chapter 3, EVE observations of Doppler shifted emission in 6 solar flares throughout solar cycle 24 were presented. Having drawn little attention in line-shift studies in the past, the hydrogen Lyman series were prioritised given their importance in the chromospheric radiation output. To provide a baseline for comparison, the C III 977 Å line was also included due to its strong flare signal. Based on an initial expectation that these lines should exhibit redshifts, three independent methods were used to measure the line centroid variations throughout the course of 6 M and X class flares.

While three of the flares studied confirmed the presence of redshifted emission

in the Lyman and C III lines, three exhibited blueshifts, indicating material upflows. While blueshifts during the 07th March 2011 event can convincingly be linked to the rapid ejection of material from the active region, it is more difficult to associate material ejection with the blueshifts observed during the 03rd November 2011 flare. It is even more challenging to explain the long-lived blueshifts during the the combined X5.4 and X1.3 07th March 2012 flares with a transient material ejection process. While weak upflow signatures may be explained by the “gentle evaporation” phenomenon, it is not overly convincing that these moderate to high strength flares would lead to such a subtle reaction in the chromosphere. Despite the lack of consensus on flow direction, it was generally found that the observed flow signatures corresponded to velocities of around  $20 - 30 \text{ km s}^{-1}$  in the Lyman lines, and that throughout the course of a given flare, the same flow direction was observed in all lines.

To shed light on the ambiguous dynamics suggested by observations, simulations and modelling were introduced in Chapter 4. Facilitated by the publicly-available grid of models, four different RADYN simulations were analysed. These models spanned a variety of beam characteristics, allowing us to examine the effects of altering the deposition height of the injected energy. It was found that in all simulations, the Lyman lines were affected by upflows initiated by the beam injection. Crucially, it was found that for low flux beams (F10), the Lyman lines were simultaneously centrally reversed and blueshifted. In the case of a high-flux, high- $\delta$  beam (3F10D8), an entirely separate blueshifted component in the Lyman lines was formed by the upwards acceleration of a dense slab of material. The highest-flux beam (F11) considered in this study also indicated a strengthened blue wing while the beam-injection is taking place. In each of the simulations considered, upflow signatures could be observed in the Lyman lines at certain times. Contrary to our initial expectations, the Lyman lines did not display a tendency to exhibit redshifts in any of the flare models, doing so only at late times in the evolution of the F11D3 model.

With the addition of another radiative transfer code (RH) in Chapter 5, synthesised Lyman line profiles for each of the flare simulations were calculated with the assumptions of partial frequency redistribution (PRD). Convolution of both the RA-

DYN and RH profiles with the EVE instrumental profile was performed, and Doppler velocities in the resulting lines were measured. This was particularly illuminating, as it was found that redshifts were observed in the synthetic velocity profiles when the Lyman lines exhibited both a central reversal and a blueshift before undergoing convolution. In cases where the line core is blueshifted, if it is also centrally reversed then this acts to remove a greater amount of irradiance in the blue wing relative to the red wing. Upon convolution with the EVE instrumental profile, the subtle detail in the line is lost and the red wing is accentuated as a result. In the context of Chapter 3, these instances of blueshifted absorption in the Lyman lines would be wholly indistinguishable from redshifted emission, and could very easily lead to misinterpretation of the corresponding flow direction.

In Chapter 5, the effects of incorporating a PRD treatment for the Lyman lines were examined. It was found that these effects were more important for calculation of the wing intensities in the lower order Lyman lines, with differences between the CRD and PRD solutions being less severe in Ly- $\gamma$  and Ly- $\delta$ . Unexpectedly, even the RH solutions while assuming CRD were found to be notably different from those computed by RADYN after the beam-injection phase stops. Furthermore, once the deposition of energy ceases, the RH profiles computed with CRD exhibit more similarity to the RH profiles assuming PRD than those from RADYN. This indicates an alternative factor in the solution process responsible for the differences between RADYN and RH, most likely related to statistical equilibrium.

It appears that while the electron beam is being deposited, the enhanced collisional and recombination rates allow the non-equilibrium level populations in RADYN to approximate those under the conditions of statistical equilibrium. RH, on the other hand, assumes that statistical equilibrium holds and iterates level populations towards this. This leads to agreement between the RADYN and RH profiles during beam injection. However, when the electron beam ceases, statistical equilibrium quickly becomes a poor assumption as the dynamics of the atmosphere continue to evolve too rapidly for non-equilibrium effects to be ignored. Ideally, future consideration of the Lyman lines should utilise a combination of both PRD and non-equilibrium effects.

---

At the end of Chapter 5, predictions were made of how the Ly- $\beta$  line may appear in observations made with the SPICE instrument on the upcoming Solar Orbiter. It was found that while the detailed features in the Ly- $\beta$  line from the 3F10D8 simulation are not retained after convolution with the SPICE instrumental line profile, the presence of central reversals in the line are subtly hinted at during certain times. It should be noted, however, that generally these are not visible unless the central reversal is particularly pronounced. More reliable observations of a potential central reversal in the Ly- $\beta$  line would require an instrumental line profile with a FWHM of less than  $\sim 0.25$  Å.

In Chapter 6, an in-depth case study of the strongest flare in solar cycle 24 was presented, which was observed by the EVE instrument. Building on the work outlined in Chapter 3, this X9.3 event presented a unique opportunity to measure line-centroid variations with excellent flare signal at high cadence. Because the simulated observations presented in Chapter 5 highlighted the problem with interpreting flow direction from EVE lines, a broader selection of spectral lines was examined in this chapter compared to that of our initial EVE observations in Chapter 3. A total number of 14 spectral lines in the EVE data were considered, sampling formation temperatures ranging from  $\sim 10$  kK to 2 MK. The methods used in Chapter 3 were used to determine line centroid variations throughout the course of the flare for each of the lines considered.

Redshifts were found to be widespread among the low-temperature species during the X9.3 event, and were observed clearly even in spectra that had not undergone preflare subtraction. Downflow velocities appeared to have a semi-quadratic dependency on formation temperature, with the most pronounced downflows occurring in the O v 630 Å line ( $\log_{10}(T)=5.4$ ). The only convincing signatures of upflow were found in the Si xii lines, formed at temperatures close to 2 MK, although these signatures transitioned into downflows by the time the Si xii lightcurves had reached their peak intensities. The Si xii line shapes also made it difficult for the Gaussian fitting method to correctly determine their line centroid positions (potentially due to unidentified blends), and so the velocities measured in these lines should be treated more cautiously than those of the low-temperature lines.

Despite the ambiguities present in the Si XII lines, the general picture observed during the X9.3 event agrees well with other studies of explosive evaporation. Downflows are consistently observed in the low-temperature lines, with the Si XII lines showing weaker signatures of both upflow and downflow. These observations are in line with the prevailing paradigm of explosive evaporation; hot material is pushed upwards at high speed and cool material condenses downwards, with a weaker dynamical response at an intermediate temperature between these two domains. Nonetheless, even with a wider sample of spectral lines, the findings described in Chapter 5 give us pause for thought; were any of the lines centrally reversed? If so, their respective asymmetries may have been misinterpreted as being produced in emission, and not in absorption. To obtain more robust determinations about the causes of line asymmetries during flares, observations with higher spectral-resolution are desired.

While many individual observations and simulations of the flaring chromosphere have been presented in this work, there are several key points that are worth emphasising:

- The work presented in this thesis is one of the first that provides a systematic and comprehensive study of the dynamic response of the hydrogen Lyman series during flares. For an instrument primarily concerned with measurements of the total solar irradiance, the quality of the EVE data should not be underestimated for spectral studies of flares. While the loss of detailed features in the lines observed by EVE warrants caution, we have observed 4 flares that agree well with current theories of the dynamics of the flaring chromosphere. The strongest flare in solar cycle 24 verifies the assumption that, during explosive evaporation, material of  $\sim 1$  MK temperatures is pushed upwards while lower-temperature material moves downwards. Observations of 3 other flares, however, do not match these expectations for the Lyman lines.
- RADYN simulations of flares, performed with a variety of beam parameters, suggest that upflows are a common feature of the flaring chromosphere. In addition to this, the line cores of the Lyman lines formed in the upflows

---

are blueshifted. According to simulations, the line cores are often centrally-reversed. However, as with observations, results from modelling should not be over-interpreted; flares are not 1-dimensional, single-threaded structures, and the inclusion of other heating mechanisms should be considered. Future work should consider applying the techniques of multi-threaded modelling.

- By simulating observations by the EVE instrument of synthetic Lyman line profiles, it has been found that a correct interpretation of line asymmetries requires knowledge of whether or not a line is centrally-reversed. As the EVE instrumental profile smoothes over the line core, the detailed information is lost, and we can no longer distinguish between blueshifted absorption and redshifted emission.
- It should also be re-iterated that there is a large discrepancy between simulated profiles from RADYN and RH even when CRD is assumed in the latter. The assumption of statistical equilibrium in RH is a more important factor in the calculation of Lyman line intensities than the frequency redistribution process, as the rapidly-evolving dynamics of the atmosphere are not fully encompassed. Future work should ideally incorporate non-equilibrium conditions within the RH framework.

Despite the progress made in this work, some questions persist; can EVE observations of upflows in the Lyman lines be fully attributed to ejection phenomena, or do they represent genuine instances of upflow in these lines? Could the observed blueshifted signatures be produced by redshifts acting on centrally-reversed line cores? Conversely, simulations suggest that these lines almost exclusively exhibit upflows during flares. Where, then, does that leave our current assumptions regarding chromospheric evaporation and condensation? The work presented in chapter 6 does provide some headway in this respect, but would benefit from incorporating Doppler shift measurements from Hinode/EIS for the same event to better constrain the plasma behaviour at high temperatures.

The work described here is by far the first, nor will be the last, study of the dynamical response of the chromosphere during flares. The hydrogen Lyman lines, however,

---

have been relatively unexplored in this respect in previous studies. Utilising both observations and modelling has proved essential; our observations remind us that “the data is the data”, in the sense that only observational data can provide tangible evidence for processes in the flaring atmosphere. On the other hand, simulations have prompted us to be cautious of over-interpretation of the observational data, and have emphasised that an observation will always at some extent be limited by the instrumentation.

The future direction of the work presented in this thesis will no doubt be aided by the next generation of space and ground-based observatories, in particular Solar Orbiter, Solar-C and the Daniel K. Inouye Solar Telescope (DKIST), both of which will permit examination of Doppler velocities in flare lines. Of particular interest will be the increased spectral resolution with which the SPICE instrument on Solar Orbiter will be able to observe the Ly- $\beta$  line of hydrogen. Observations of the C III 977 Å line will also be capable with SPICE, and greater context to flow observations will be enabled by the instrument having spatial resolution as a result of its slit imager. The planned Solar-C mission should also facilitate spectroscopic observations of the lower order Lyman series, with the intended wavelength bands on the proposed Large European Module for solar Ultraviolet Research (LEMUR) instrument covering Ly- $\alpha$  through Ly- $\gamma$ . DKIST will not observe the hydrogen Lyman lines, but will allow imaging spectroscopy of other Transition Region lines (such as He I and He II), along with measurements of polarisation as a function of wavelength.

Future observations will undoubtedly be enriched by insights from simulations, facilitated by the ever-improving and increasingly-sophisticated suites of numerical codes capable of exploring the complex physics and radiative processes of the flaring Sun. Further modelling should be driven by a multi-threaded approach, in which flares are better-approximated through the excitation of multiple threads throughout time. The radiative output is then synthesised by the emission from each of these threads. This will be an important consideration, as at a given time the flows in differing threads may be markedly different, and the overall Doppler shift in a given line will be an average.

A particular consideration in future work would be the benefit of incorporating

a non-equilibrium approach into RH, given that it already has the advantage of a large number of atom files and can easily be used to examine singular snapshots at a time. With this in mind, it may be interesting to use RH to synthesise C III 977Å profiles and compare them to EVE observations and those expected from SPICE. Consideration should also be given to exploring alternative sources of heating, such as Alfvén waves.

# Bibliography

- Abbett, W. P. & Hawley, S. L. 1999, *The Astrophysical Journal*, 521, 906
- Adams, T. F., Hummer, D. G., et al. 1971, *Journal of Quantitative Spectroscopy and Radiative Transfer*, 11, 1365
- Ajello, M., Albert, A., et al. 2014, *The Astrophysical Journal*, 789, 20
- Allred, J. C., Hawley, S. L., et al. 2005, *The Astrophysical Journal*, 630, 573
- Allred, J. C., Kowalski, A. F., et al. 2015, *The Astrophysical Journal*, 809, 104
- Antiochos, S. K. & Sturrock, P. A. 1978, *The Astrophysical Journal*, 220, 1137
- Aschwanden, M. J. 2005, *Physics of the Solar Corona. An Introduction with Problems and Solutions* (2nd edition)
- Aschwanden, M. J., Hudson, H., et al. 1996, *The Astrophysical Journal*, 464, 985
- Beck, J. G. 2000, *Solar Physics*, 191, 47
- Benz, A. O. 2008, *Living Reviews in Solar Physics*, 5, 1
- Berlicki, A., Heinzl, P., et al. 2005, *Astronomy and Astrophysics*, 430, 679
- Bian, N. H. & Kontar, E. P. 2011, *Astronomy and Astrophysics*, 527, A130
- Bray, R. J. & Loughhead, R. E. 1974, *The solar chromosphere*
- Brown, J. C. 1971, *Solar Physics*, 18, 489
- Brown, S. A., Fletcher, L., et al. 2018, *The Astrophysical Journal*, 862, 59

- Brown, S. A., Fletcher, L., et al. 2016, *Astronomy and Astrophysics*, 596, A51
- Bruzek, A. 1964, *The Astrophysical Journal*, 140, 746
- Carlsson, M. 2007, in *Astronomical Society of the Pacific Conference Series*, Vol. 368, *The Physics of Chromospheric Plasmas*, ed. P. Heinzel, I. Dorotovič, & R. J. Rutten, Heinzel
- Carlsson, M. & Stein, R. F. 1992, *The Astrophysical Journal, Letters*, 397, L59
- Carlsson, M. & Stein, R. F. 1997, *The Astrophysical Journal*, 481, 500
- Carlsson, M. & Stein, R. F. 2002, *The Astrophysical Journal*, 572, 626
- Carrington, R. C. 1859, *Monthly Notices of the Royal Astronomical Society*, 20, 13
- Castelli, J. P. & Richards, D. W. 1971, *Journal of Geophysics Research*, 76, 8409
- Charbonneau, P. 2014, *Annual Review of Astronomy and Astrophysics*, 52, 251
- Chen, H., Ma, S., et al. 2013, *The Astrophysical Journal*, 778, 70
- Chen, P. F. 2011, *Living Reviews in Solar Physics*, 8, 1
- Clette, F., Svalgaard, L., et al. 2014, *Space Science Reviews*, 186, 35
- Crotser, D. A., Woods, T. N., et al. 2007, in *Proceedings of the SPIE*, Vol. 6689, *Solar Physics and Space Weather Instrumentation II*, 66890M
- Culhane, J. L., Harra, L. K., et al. 2007, *Solar Physics*, 243, 19
- De Pontieu, B., Title, A. M., et al. 2014, *Solar Physics*, 289, 2733
- Del Zanna, G. & Woods, T. N. 2013, *Astronomy and Astrophysics*, 555, A59
- Delaboudinière, J. P., Artzner, G. E., et al. 1995, *Solar Physics*, 162, 291
- Dennis, B. R. & Schwartz, R. A. 1989, *Solar Physics*, 121, 75
- Dennis, B. R. & Zarro, D. M. 1993, *Solar Physics*, 146, 177
- Dere, K. P., Landi, E., et al. 1997, *Astronomy and Astrophysics, Supplement*, 125, 149

- Donnelly, R. F. & Kane, S. R. 1978, *The Astrophysical Journal*, 222, 1043
- Dorfi, E. A. & Drury, L. O. 1987, *Journal of Computational Physics*, 69, 175
- Doschek, G. A., Mariska, J. T., et al. 1994, *The Astrophysical Journal*, 431, 888
- Dzifčáková, E., Zemanová, A., et al. 2018, *The Astrophysical Journal*, 853, 158
- E. Bailey, J., Nagayama, T., et al. 2014, 517, 56
- Eastwood, J. P. 2008, *Philosophical Transactions of the Royal Society of London A: Mathematical, Physical and Engineering Sciences*, 366, 4489
- Emslie, A. G. 1978, *The Astrophysical Journal*, 224, 241
- Emslie, A. G., Dennis, B. R., et al. 2012, *The Astrophysical Journal*, 759, 71
- Emslie, A. G. & Sturrock, P. A. 1982, *Solar Physics*, 80, 99
- Fan, Y. 2009, *Living Reviews in Solar Physics*, 6, 4
- Fisher, G. H., Canfield, R. C., et al. 1985a, *The Astrophysical Journal*
- Fisher, G. H., Canfield, R. C., et al. 1985b, *The Astrophysical Journal*
- Fletcher, L. 1995, *Astronomy and Astrophysics*, 303, L9
- Fletcher, L., Dennis, B. R., et al. 2011, *Space Science Reviews*, 159, 19
- Fletcher, L. & Hudson, H. S. 2008, *The Astrophysical Journal*, 675, 1645
- Fletcher, L., Pollock, J. A., et al. 2004, *Solar Physics*, 222, 279
- Fludra, A., Griffin, D., et al. 2013, in *Proceedings of SPIE - The International Society for Optical Engineering*, Vol. 8862, 88620F
- Fontenla, J. M., Avrett, E. H., et al. 1990, *The Astrophysical Journal*, 355, 700
- Garcia, H. A. 1994, *Solar Physics*, 154, 275
- Golub, L., DeLuca, E., et al. 2007, *Solar Physics*, 243, 63

- Green, J. L., Boardsen, S., et al. 2006, *Advances in Space Research*, 38, 145
- Gustafsson, B. 1973, A FORTRAN program for calculating "continuous" absorption coefficients of stellar atmospheres (Uppsala Astronomiska Observatoriums Annaler)
- Handy, B., Acton, L., et al. 1999, *Solar Physics*, 187, 229
- Hathaway, D. H. 2015, *Living Reviews in Solar Physics*, 12
- Holman, G. D., Aschwanden, M. J., et al. 2011, *Space Science Reviews*, 159, 107
- Hoyng, P., Brown, J. C., et al. 1976, *Solar Physics*, 48, 197
- Hubeny, I. & Lites, B. W. 1995, *The Astrophysical Journal*, 455, 376
- Hubeny, I. & Mihalas, D. 2014, *Theory of Stellar Atmospheres*
- Hudson, H. S. 2000, *The Astrophysical Journal, Letters*, 531, L75
- Hudson, H. S., Wolfson, C. J., et al. 2006, *Solar Physics*, 234, 79
- Hudson, H. S., Woods, T. N., et al. 2011, *Solar Physics*, 273, 69
- Hundhausen, A. J. 1970, *Reviews of Geophysics and Space Physics*, 8, 729
- Ichimoto, K. & Kurokawa, H. 1984, *Solar Physics*, 93, 105
- Kamio, S., Kurokawa, H., et al. 2005, *The Astrophysical Journal*, 625, 1027
- Kane, S. R. & Anderson, K. A. 1970, *The Astrophysical Journal*, 162, 1003
- Kane, S. R. & Donnelly, R. F. 1971, *The Astrophysical Journal*, 164, 151
- Keller, C. U., Schüssler, M., et al. 2004, *The Astrophysical Journal, Letters*, 607, L59
- Kerr, G. S. & Fletcher, L. 2014, *The Astrophysical Journal*, 783, 98
- Kerr, G. S., Fletcher, L., et al. 2016, *The Astrophysical Journal*, 827, 101
- Kimball, D. 1960, *UAG-R109*

- Klimchuk, J. A. 2006, *Solar Physics*, 234, 41
- Kolotkov, D. Y., Pugh, C. E., et al. 2018, *The Astrophysical Journal, Letters*, 858, L3
- Kontar, E. P., Brown, J. C., et al. 2011, *Space Science Reviews*, 159, 301
- Kosugi, T., Makishima, K., et al. 1991, *Solar Physics*, 136, 17
- Kowalski, A. F., Hawley, S. L., et al. 2013, *The Astrophysical Journal, Supplement*, 207, 15
- Kretzschmar, M. 2011, *Astronomy and Astrophysics*, 530, A84
- Kuridze, D., Mathioudakis, M., et al. 2015, *The Astrophysical Journal*, 813, 125
- Landi, E., Del Zanna, G., et al. 2012, *The Astrophysical Journal*, 744, 99
- Leenaarts, J., Carlsson, M., et al. 2012, *The Astrophysical Journal*, 749, 136
- Lemaire, P., , et al. 1984, *Solar Physics*, 90, 63
- Lemaire, P., Gouttebroze, P., et al. 2004, *Astronomy and Astrophysics*, 418, 737
- Lemaire, P., Vial, J.-C., et al. 2015, *Astronomy and Astrophysics*, 581, A26
- Lemen, J. R., Title, A. M., et al. 2012, *Solar Physics*, 275, 17
- Lin, R., Dennis, B., et al. 2002, *Solar Physics*, 210, 3
- Liu, R., Titov, V. S., et al. 2014, *The Astrophysical Journal*, 790, 8
- Liu, W., Petrosian, V., et al. 2009, *The Astrophysical Journal*, 702, 1553
- MacKinnon, A. L. & Craig, I. J. D. 1991, *Astronomy and Astrophysics*, 251, 693
- Marsch, E. 2006, *Living Reviews in Solar Physics*, 3, 1
- Masuda, S., Kosugi, T., et al. 1994, *Nature*, 371, 495
- Mauas, P. J. D. & Gómez, D. O. 1997, *The Astrophysical Journal*, 483, 496
- McTiernan, J. M., Fisher, G. H., et al. 1999, *The Astrophysical Journal*, 514, 472

- Metcalf, T. R., Alexander, D., et al. 2003, *The Astrophysical Journal*, 595, 483
- Milkey, R. W. & Mihalas, D. 1973, 185, 709
- Milligan, R. O. & Dennis, B. R. 2009, *The Astrophysical Journal*, 699, 968
- Milligan, R. O., Kerr, G. S., et al. 2014, *The Astrophysical Journal*, 793, 70
- Mitalas, R. & Sills, K. R. 1992, *The Astrophysical Journal*, 401, 759
- Mosher, J. M., Acton, L. W., et al. 1979, in Bulletin of the AAS, Vol. 11, Bulletin of the American Astronomical Society, 710
- Ng, K.-C. 1974, *Journal of Chemical Physics*, 61, 2680
- Nordlund, Å., Stein, R. F., et al. 2009, *Living Reviews in Solar Physics*, 6, 2
- Owens, M. J. & Forsyth, R. J. 2013, *Living Reviews in Solar Physics*, 10, 5
- Paletou, F. 1995, *Astronomy and Astrophysics*, 302, 587
- Parenti, S. 2014, *Living Reviews in Solar Physics*, 11, 1
- Parker, E. N. 1958, *The Astrophysical Journal*, 128, 664
- Parker, E. N. 1965, *Space Science Reviews*, 4, 666
- Patsourakos, S., Georgoulis, M. K., et al. 2016, *The Astrophysical Journal*, 817, 14
- Pesnell, W. D., Thompson, B. J., et al. 2012, *Solar Physics*, 275, 3
- Peter, H. 2001, *Astronomy and Astrophysics*, 374, 1108
- Peterson, B. M., Wanders, I., et al. 1998, *Publications of the ASP*, 110, 660
- Pradhan, A. K. & Nahar, S. N. 2011, *Atomic Astrophysics and Spectroscopy*
- Prialnik, D. 2009, *An Introduction to the Theory of Stellar Structure and Evolution*
- Pulkkinen, T. 2007, *Living Reviews in Solar Physics*, 4, 1
- Qiu, J., Lee, J., et al. 2002, *The Astrophysical Journal*, 565, 1335

- Radziszewski, K., Rudawy, P., et al. 2007, *Astronomy and Astrophysics*, 461, 303
- Rathore, B. & Carlsson, M. 2015, *The Astrophysical Journal*, 811, 80
- Romano, P., Elmhamdi, A., et al. 2018, *The Astrophysical Journal, Letters*, 852, L10
- Rubio da Costa, F., Kleint, L., et al. 2016, *The Astrophysical Journal*, 827, 38
- Russell, A. J. B. & Fletcher, L. 2013, *The Astrophysical Journal*, 765, 81
- Rutten, R. 1993, Tech. rep., Sterrekundig Instituut Utrecht
- Rybicki, G. B. & Hummer, D. G. 1991, *Astronomy and Astrophysics*, 245, 171
- Rybicki, G. B. & Hummer, D. G. 1992, *Astronomy and Astrophysics*, 262, 209
- Schmidt, J. M., Cairns, I. H., et al. 2014, *Journal of Geophysical Research (Space Physics)*, 119, 6042
- Schmieder, B., Malherbe, J.-M., et al. 1990, 356
- Schwenn, R. 2006, *Living Reviews in Solar Physics*, 3, 2
- Sharykin, I. N. & Kosovichev, A. G. 2018, *ArXiv e-prints*
- Shea, M. & Smart, D. 2006, *Advances in Space Research*, 38, 313 , the Great Historical Geomagnetic Storm of 1859: A Modern Look
- Simões, P. J. A., Fletcher, L., et al. 2016, in *Astronomical Society of the Pacific Conference Series*, Vol. 504, Coimbra Solar Physics Meeting: Ground-based Solar Observations in the Space Instrumentation Era, ed. I. Dorotovic, C. E. Fischer, & M. Temmer, 197
- Smith, D. F. & Auer, L. H. 1980, *The Astrophysical Journal*, 238, 1126
- Solanki, S. K., Inhester, B., et al. 2006, *Reports on Progress in Physics*, 69, 563
- Stix, M. 2004, *The sun : an introduction*
- Svestka, Z. 1976, *Solar Flares*, 415

- Taroyan, Y. & Bradshaw, S. J. 2014, *Solar Physics*, 289, 1959
- Tousey, R., Bartoe, J. D. F., et al. 1973, *Solar Physics*, 33, 265
- Tsuneta, S., Acton, L., et al. 1991, *Solar Physics*, 136, 37
- Tsuneta, S., Ichimoto, K., et al. 2008, *Solar Physics*, 249, 167
- Tsurutani, B. T., Gonzalez, W. D., et al. 2003, *Journal of Geophysical Research: Space Physics*, 108, n/a, 1268
- Uitenbroek, H. 2001, *The Astrophysical Journal*, 557, 389
- Švestka, Z., Kopecký, M., et al. 1962, *Bulletin of the Astronomical Institutes of Czechoslovakia*, 13, 37
- van Driel-Gesztelyi, L. & Green, L. M. 2015, *Living Reviews in Solar Physics*, 12, 1
- Vernazza, J. E., Avrett, E. H., et al. 1973, *The Astrophysical Journal*, 184, 605
- Vernazza, J. E., Avrett, E. H., et al. 1981, *The Astrophysical Journal, Supplement*, 45, 635
- Viall, N. M. & Klimchuk, J. A. 2017, *The Astrophysical Journal*, 842, 108
- Vilmer, N., MacKinnon, A. L., et al. 2011, *Space Science Reviews*, 159, 167
- Wang, J., Simoes, P. J. A., et al. 2018, *ArXiv e-prints*
- Winebarger, A. R., DeLuca, E. E., et al. 2001, *The Astrophysical Journal, Letters*, 553, L81
- Wittmann, A. D. & Xu, Z. T. 1987, *Astronomy and Astrophysics, Supplement*, 70, 83
- Woods, T. N., Eparvier, F. G., et al. 2012, Extreme Ultraviolet Variability Experiment (EVE) on the Solar Dynamics Observatory (SDO): Overview of Science Objectives, Instrument Design, Data Products, and Model Developments, ed. P. Chamberlin, W. D. Pesnell, & B. Thompson (New York, NY: Springer US), 115–143
- Wolfson, M. 2000, *Astronomy & Geophysics*, 41

---

Wülser, J.-P., Canfield, R. C., et al. 1994, *The Astrophysical Journal*, 424, 459

Yan, X. L., Wang, J. C., et al. 2018, *The Astrophysical Journal*, 856, 79

Zirin, H. 1966, *The solar atmosphere*